

Resonant optical control of magnetism on ultrashort timescales

Hortensius, J.R.

DOI

[10.4233/uuid:7a9909e7-472d-4da9-8637-852e9e873577](https://doi.org/10.4233/uuid:7a9909e7-472d-4da9-8637-852e9e873577)

Publication date

2022

Document Version

Final published version

Citation (APA)

Hortensius, J. R. (2022). *Resonant optical control of magnetism on ultrashort timescales*. [Dissertation (TU Delft), Delft University of Technology]. <https://doi.org/10.4233/uuid:7a9909e7-472d-4da9-8637-852e9e873577>

Important note

To cite this publication, please use the final published version (if applicable). Please check the document version above.

Copyright

Other than for strictly personal use, it is not permitted to download, forward or distribute the text or part of it, without the consent of the author(s) and/or copyright holder(s), unless the work is under an open content license such as Creative Commons.

Takedown policy

Please contact us and provide details if you believe this document breaches copyrights. We will remove access to the work immediately and investigate your claim.

**RESONANT OPTICAL CONTROL OF MAGNETISM
ON ULTRASHORT TIMESCALES**

RESONANT OPTICAL CONTROL OF MAGNETISM ON ULTRASHORT TIMESCALES

Dissertation

for the purpose of obtaining the degree of doctor
at Delft University of Technology
by the authority of the Rector Magnificus, Prof.dr.ir. T.H.J.J. van der Hagen,
chair of the Board for Doctorates,
to be defended publicly on
Tuesday 8 March 2022 at 12:30 o'clock

by

Jorrit Rutger HORTENSIUS

Master of Science in Applied Physics,
Delft University of Technology, The Netherlands,
born in Schiedam, The Netherlands.

This dissertation has been approved by the promotors

Dr. A. D. Caviglia
Prof.dr. L. Kuipers

Composition of the doctoral committee:

Rector Magnificus,	chairperson
Dr. A. D. Caviglia,	Technische Universiteit Delft, promotor
Prof.dr. L. Kuipers,	Technische Universiteit Delft, promotor

Independent members:

Prof.dr. Y. M. Blanter,	Technische Universiteit Delft
Dr. R. Citro,	Università degli Studi di Salerno, Italy
Prof.dr. T. Kampfrath,	Freie Universität Berlin, Germany
Prof.dr. A. V. Kimel,	Radboud Universiteit
Prof.dr. J. -M. Triscone,	Université de Genève, Switzerland
Prof.dr. P. G. Steeneken,	Technische Universiteit Delft (<i>reserve member</i>)



Nederlandse Organisatie voor Wetenschappelijk Onderzoek



European Research Council
Established by the European Commission

Keywords: Ultrafast spectroscopy, femtosecond laser pulses, nonlinear phononics, ultrafast strain, ultrafast magnetism, magneto-optics, antiferromagnets, spin-wave dynamics

Printed by: Gildeprint, Enschede

Front & Back: Artist impression of propagating spin waves in an antiferromagnet. Image produced by Ella Maru Studio.

Copyright © 2022 by J.R. Hortensius

Casimir PhD Series 2022-05

ISBN 978-90-8593-516-2

An electronic version of this dissertation is available at
<http://repository.tudelft.nl/>.

CONTENTS

Summary	ix
Samenvatting	xi
1 Introduction	1
1.1 Ultrafast control of material properties	3
1.2 Research context and scope of this thesis	6
1.2.1 Ultrafast control of magnetic properties	6
1.2.2 Propagating excitations in insulating materials	9
1.3 Structure of this thesis	10
2 Magnetic order and spin waves	13
2.1 Magnetic moments and electron orbital states in crystal fields	14
2.1.1 Quenching the orbital moment	14
2.2 Magnetic interactions.	16
2.2.1 Exchange interaction	16
2.2.2 Zeeman interaction	18
2.2.3 Spin-orbit interaction	19
2.3 Magnetic anisotropy	20
2.3.1 Single-ion anisotropy	21
2.3.2 Two-ion anisotropy	21
2.3.3 Anisotropy in two-dimensional magnets.	22
2.4 Magnetization dynamics and spin waves	23
2.4.1 Uniform spin precession.	23
2.4.2 Dispersion relation.	25
2.5 Appendix: Magnetic dynamics in antiferromagnets.	27
3 Experimental techniques	31
3.1 All-optical pump-probe spectroscopy.	32
3.2 Tunable ultrashort laser pulses	32
3.2.1 Ultrafast Ti:sapphire amplifier	32
3.2.2 Tunable pulse frequency.	33
3.3 Detection methods	36
4 Nonlinear phononics and ultrafast strain wave generation in LaAlO₃	39
4.1 Nonlinear phononics	41
4.1.1 Phonon-polaritons and optical properties	41
4.1.2 Nonlinear coupling	44
4.2 Ultrafast lattice excitation in LaAlO ₃	47
4.3 Photo-induced structural dynamics.	47
4.4 Coherent oxygen octahedra rotations.	49

4.5	Tunable shear strain	51
4.6	Conclusions.	52
4.7	Methods	54
4.8	Supplementary Information	54
4.8.1	Temperature dependence of the E_g mode	54
4.8.2	DFT calculations on nonlinear lattice dynamics	55
4.8.3	Pump fluence and polarization dependence of the strain waves	61
5	Control of magnetic interactions via ultrafast resonant lattice excitation	63
5.1	Magnetic properties of DyFeO_3	64
5.2	Phonon-driven reconfiguration of the magnetic potential	67
5.3	Out-of-equilibrium metastable state	69
5.4	Ultrafast phonon-driven magnetic phase transition	71
5.5	Conclusions.	72
5.6	Methods	73
5.7	Supplementary Information	74
5.7.1	Optical absorption spectrum.	74
5.7.2	First-order spin reorientation and spin dynamics in DyFeO_3	75
5.7.3	Reconstructing the magnetic potential using the spin precession frequency	77
5.7.4	Effect of the laser fluence on the spin precession frequency and the anisotropy parameters.	80
5.7.5	Nonlinear lattice dynamics and their effect on the magnetic exchange interactions	81
6	Controlling the anisotropy of van der Waals antiferromagnet NiPS_3 via orbital resonances	87
6.1	Magnetic and optical properties of NiPS_3	89
6.2	Selective light-induced magnetic dynamics.	89
6.3	Excitation of an in-plane magnetic mode	92
6.4	Selection rules for the magnon excitation.	94
6.5	Conclusions.	96
6.6	Methods	96
6.7	Supplementary Information	97
6.7.1	Excitation of magnetic and phonon modes	97
6.7.2	Characterization of the sub-THz modes	97
6.7.3	Supporting spin dynamics theory	98
6.7.4	Relation between the spin-flop field and the magnon frequency.	101
6.7.5	Light-matter interaction in NiPS_3 and the resulting spin-dynamics	102
6.7.6	Fluence dependence of the magnon mode.	105
7	Broadband spin-wave emission in an insulating antiferromagnet	107
7.1	Introduction	108
7.2	All-optical generation and detection of coherent AFM spin waves	109
7.3	Optical confinement to generate propagating spin waves.	112
7.4	Spectral components of the broadband spin-wavepacket.	113
7.5	Spin-wave propagation distance	115

7.6	Conclusions.	116
7.7	Methods	116
7.8	Supplementary Information	117
7.8.1	Temperature-dependent spin-wave detection	117
7.8.2	Magneto-optical detection of propagating spin waves in antiferromagnets	117
7.8.3	Formalism on the generation of the magnon wavepacket	123
7.8.4	Propagating coherent acoustic phonon wavepacket	125
7.8.5	Temperature and magnetic field dependence of the magnon and phonon modes.	126
7.8.6	Polarization dependence of the magnon and phonon modes	128
8	Conclusion and Outlook	131
8.1	Nonlinear phononics and strain generation.	132
8.2	Controlling magnetic properties via resonant lattice excitation	133
8.3	Magnetic excitations in a van der Waals antiferromagnet	134
8.4	Propagating coherent antiferromagnetic spin waves	134
8.5	Concluding remarks	135
	References	136
	Acknowledgements	151
	Curriculum Vitæ	157
	List of Publications	159

SUMMARY

Excitation of optical transitions in solids using ultrashort pulses of light allows to selectively perturb microscopic degrees of freedom in order to change and control material properties on very short timescales. In this thesis we study how ultrafast resonant excitation of optical transitions can induce coherent structural dynamics in wide-bandgap insulators and control magnetic interactions, manipulate magnetic order and induce (propagating) spin dynamics in insulating antiferromagnets. In time-resolved all-optical pump-probe experiments, we use ultrashort pulses of light to target specific lattice vibrations, orbital resonances and electronic transitions in various insulating materials and optically probe the structural and magnetic dynamics on the picosecond timescale.

Chapter 1 provides an introduction to the field that studies ultrafast optical control of solids, with a focus on resonant optical control of magnetic properties and the generation of propagating excitations. Chapter 2 discusses the basic concepts of magnetic interactions, magnetic order and spin waves. In chapter 3 we briefly discuss the main experimental methods and experimental setups used in this work.

In chapter 4 we study the coherent structural dynamics initiated by ultrafast resonant excitation of an infrared-active lattice vibration in the wide-bandgap insulator LaAlO_3 . We observe the excitation of a coherent THz phonon mode, corresponding to rotations of the oxygen octahedra around a high-symmetry axis, and identify the underlying non-linear phonon-phonon coupling through density functional theory calculations. The resonant lattice excitation is also shown to generate both longitudinal and transverse strain wavepackets, the result of optically induced anisotropic strain.

In chapter 5 we demonstrate that light-driven infrared-active phonons can be used to control fundamental magnetic interactions and coherently manipulate magnetic states on picosecond timescales. Resonant optical excitation of lattice vibrations in the antiferromagnet DyFeO_3 results in nonthermal, ultrafast and long-living changes in the exchange interaction between the Dy orbitals and the Fe spins. We identify phonon-induced coherent lattice distortions as the underlying mechanism and show that we can use this change in magnetic interaction to induce picosecond coherent switching from a collinear antiferromagnetic ground state to a weakly ferromagnetic phase.

Having explored the structural and magnetic dynamics following excitation of lattice vibrations, we explore the effect of optical excitation of orbital resonances in the van der Waals antiferromagnet NiPS_3 in chapter 6. We demonstrate that ultrashort pulses of light, with the photon energy tuned in resonance with orbital transitions within the magnetic nickel d -orbital manifold, can excite a subterahertz magnon mode with two-dimensional behaviour. We show that this selective excitation results from a photoinduced transient magnetic anisotropy axis, which emerges in response to excitation of the ground-state electrons to orbital states with a lower orbital symmetry.

Finally, we show in chapter 7 that ultrashort pulses of light can generate a wavepacket of coherent propagating spin waves in insulating antiferromagnets. The nanometer confinement of ultrafast optical excitation in resonance with electronic charge-transfer transitions in the antiferromagnet DyFeO_3 creates a strongly non-uniform spatial spin excitation profile close to the material surface. This results in the emission of a broadband wavepacket of coherent subterahertz spin waves into the material. We optically probe individual spectral components of this spin-wavepacket with wavelengths down to 125 nm in a time-resolved fashion using the magneto-optical Kerr effect.

Chapter 8 provides the main conclusions of the work presented in this thesis. We reflect on unanswered questions and give possible directions for future research.

SAMENVATTING

Het aanslaan van optische overgangen in materialen met behulp van ultrakorte lichtpulsen maakt het mogelijk om selectief microscopische vrijheidsgraden te verstoren, met als doel om op hele korte tijdschalen controle te krijgen over materiaaleigenschappen. In deze thesis bestuderen we hoe ultrasnelle, resonante excitatie van optische overgangen kan leiden tot dynamische veranderingen in de kristalstructuur van materialen met een grote bandkloof en daarnaast in antiferromagneten de magnetische interactie kan controleren, de magnetische orde kan manipuleren en (voortbewegende) spin dynamica kan opwekken. In volledige optische ‘pump-probe’ experimenten met een tijdsresolutie van minder dan een picoseconde gebruiken we ultrakorte lichtpulsen om specifieke roostertrillingen, orbitaalresonanties en elektronische overgangen in verschillende niet-geleidende materialen aan te slaan en vervolgens de structurele en magnetische dynamiek op deze tijdschalen optisch te meten.

Hoofdstuk 1 geeft een korte introductie tot het veld dat de ultrasnelle optische controle over vaste stoffen bestudeert, met een focus op de resonante optische controle over magnetische eigenschappen en het genereren van voortbewegende excitaties. Hoofdstuk 2 bediscussieert de basisconcepten van magnetische interactie, magnetische orde en spingolven. In hoofdstuk 3 bediscussiëren we kort de belangrijkste experimentele methoden en opstellingen die in deze studie gebruikt zijn.

In hoofdstuk 4 bestuderen we de coherente dynamiek van de kristalstructuur als gevolg van de ultrasnelle resonante excitatie van een infrarood-actieve roostertrilling in het niet-geleidende LaAlO_3 met een grote bandkloof. We observeren het aanslaan van een coherente THz fonon, die gerelateerd is aan rotaties van de octaëders van zuurstofatomen rondom een as van hoge symmetrie, en bestuderen de onderliggende niet-lineaire fonon-fonon koppeling met behulp van dichtheidsfunctionaaltheorie berekeningen. Het resonante aanslaan van de roostertrilling resulteert daarnaast in golfpakketten van longitudinale en transversale vervorming, het gevolg van optisch opgewekte anisotrope vervorming.

In hoofdstuk 5 tonen we aan dat infrarood-actieve fonon die door licht worden aangedreven kunnen worden gebruikt om fundamentele magnetische interacties te beheersen en magnetische toestanden coherent te manipuleren op de tijdschaal van picosecondes. De resonant optische excitatie van roostertrillingen in de antiferromagneet DyFeO_3 resulteert in een niet-thermische, ultrasnelle en langlevende verandering in de uitwisselingsinteractie tussen de Dy orbitalen en de Fe spins. We stellen vast dat dit het gevolg is van een coherente vervorming van het kristalrooster. Tot slot laten we zien we deze verandering in de magnetische interactie kunnen gebruiken om in enkele picoseconden een overgang van een collineaire antiferromagnetische grondtoestand naar een zwakke ferromagnetische toestand te realiseren.

Na de dynamiek van de kristalstructuur en magnetische dynamiek na het aanslaan van roostertrillingen te hebben bestudeerd, onderzoeken we het effecten van optische excitatie van orbitaaltoestanden in de van der Waals antiferromagneet NiPS_3 in hoofdstuk 6. We tonen aan dat ultrakorte lichtpulslen, met de fotonenergie afgestemd op overgangen tussen verschillende d -orbitaaltoestanden van het magnetische nickel ion, een subterahertz magnon met twee-dimensionale kenmerken kunnen aandrijven. We laten zien dat deze selectiviteit het gevolg is van een kortstondige magnetische anisotropie-as die wordt opgewekt door het laser licht en ontstaat doordat elektronen vanuit de grondtoestand naar orbitaaltoestanden met een lagere orbitale symmetrie worden gebracht.

Tot slot laten we in hoofdstuk 7 zien dat ultrakorte lichtpulslen een golfpakket van coherente spingolven in isolerende antiferromagneten kunnen opwekken. Ultrasnelle optische excitatie in resonantie met elektronische overgangen die ladingsoverdracht met zich meebrengen wordt op de nanometer schaal opgesloten in de antiferromagneet DyFeO_3 . Dit creëert een sterk niet-uniform spin-excitatie profiel dicht bij het oppervlak van het materiaal en resulteert in het uitstralen van een breedbandig coherente golfpakket van subterahertz spingolven. Met een optische methode gebaseerd op het magneto-optische Kerr effect detecteren we de individuele componenten van dit spingolfpakket met golflengtes tot 125 nm en volgen we hun evolutie in de tijd.

Hoofdstuk 8 bevat de belangrijkste conclusies van het werk in deze thesis. We reflecteren op onbeantwoorde vragen en geven richtingen voor mogelijk vervolgonderzoek.

1

INTRODUCTION

"In the right light, at the right time, everything is extraordinary."

Aaron Rose

In this introductory chapter I provide an outline of the context and scope of the work presented in this thesis. It is a broad introduction to the field that studies control of macroscopic material properties by bringing materials out of equilibrium using ultrashort laser pulses, followed by a discussion on the importance of selective excitation of specific degrees of freedom in the material under study. This chapter specifically focuses on the resonant optical control of magnetic properties and the generation of propagating excitations. I conclude with a brief outline of this thesis.

We live in an era in which information and communications technology (ICT) has found its way into every aspect of our lives. The amount of information stored, transmitted and processed is ever-increasing and this trend does not appear to be changing in the near-future, with technologies such as the ‘Internet of Things’ still only in their infancy [1]. There are a few technological drivers that have underpinned the dramatic improvement of information technology. The most prominent example is the doubling of the transistor density on chips every two years for more than fifty years, following the so-called Moore’s law [2–4]. The downscaling of integrated circuits has been the result of technological progress and tremendous investments of time and money. In the coming years, despite increasing investments, these building blocks will reach their ultimate limit in terms of both speed and size [4, 5]. This provides a challenge, as society has not only become dependent on information technology itself, but also relies on its rapid development. In addition, the rise of information technology comes with a large increase in energy consumption: some models predict that the ICT’s electricity use could exceed 20% of the global electricity demand in 2030 [6]. These two factors are a threat to important economic and industrial sectors that are intimately linked to continued improvements in information technology [7]. Moreover, an upper limit to computing power seriously hinders the human ability to solve a set of increasingly complex problems that we are now facing. Faster supercomputers can play a key role in climate change modelling, health care and disease prevention and the development of new materials [8]. Research aimed at exploring radically different strategies to process and store information therefore plays a crucial role in overcoming these future challenges.

These societal and technological challenges, in combination with an improving description of the world around us, might very well have contributed to a paradigm shift that has taken place in the physical sciences. For many years, the central goal of condensed matter physics has been to understand and describe naturally occurring phenomena, both in macroscopic and microscopic terms. Over the past years, a new central goal has emerged, which is to experimentally realize new states of matter that are not found in nature [9–12]. Alongside answering fundamental scientific questions, control over and knowledge of potential ‘exotic’ phases also holds promise to create a new and radically different generation of data processing devices [9, 10, 13]. The complex interplay between different degrees of freedom in so-called correlated, or quantum, materials plays an important role in this artificial material quest. The electron orbitals, crystal lattice, electron spins and electron charges are interacting complex entities, together giving rise to a material ground state, exhibiting certain macroscopic properties, as exemplified in figure 1.1a. The interplay between the different degrees of freedom results in a delicate balance between the coexisting and competing ground states, making these materials highly sensitive to external influences.

One particular approach to create new ground states is to bring materials out of equilibrium and toward desired states by selectively perturbing microscopic degrees of freedom [14]. In this way, the system can be *dynamically* steered to a desired new state that is not accessible in thermodynamic equilibrium (see Fig. 1.1b). A type of external stimulus which has shown to be particularly successful in dynamically controlling material properties are sub-picosecond electric field transients [14, 15].

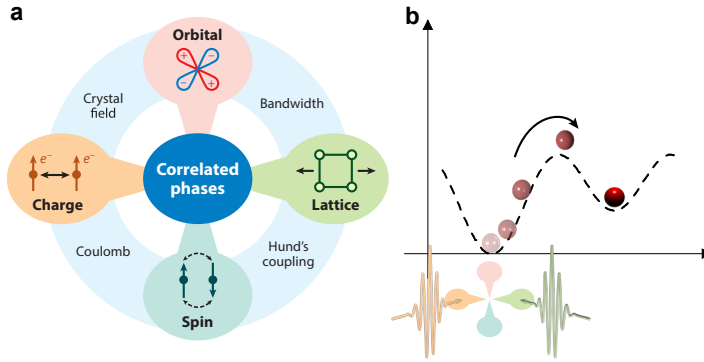


Figure 1.1: **Dynamical control of material properties.** **a**, The interplay between the different microscopic degrees of freedom in a solid gives rise to a correlated phase (figure from Ref. [16], Annual Reviews, with permission). **b**, By bringing one of the degrees of freedom out of equilibrium using an external stimulus, the material can be dynamically steered into a metastable state.

1.1. ULTRAFAST CONTROL OF MATERIAL PROPERTIES

EXCITING MATERIALS USING LIGHT

There are two intrinsically related reasons to focus on ultrashort bursts of light in the form of laser pulses as means to control materials:

- (i) Electromagnetic radiation (light) can couple to the excitations of many degrees of freedom in ordered states, provided that the radiation has the right frequency. Due to recent technological progress, laser pulses with central frequencies over a wide range can presently be generated by commercially available table-top laser setups [17–21]. Intense optical pulses with wavelengths spanning from the extreme ultraviolet (XUV) to the terahertz enable the resonant, and therefore selective, excitation of particular electronic transitions and a wide variety of collective modes. This in turn provides an extremely diverse experimental toolbox to manipulate materials, as different excitations enable different control techniques (see Fig. 1.2).
- (ii) The width of these laser pulses can be less than 100 fs (1 *femtosecond* (fs) = 10^{-15} s), which makes them the fastest stimuli available. This brings the advantage of *ultrafast* control over material properties and the possibility to monitor the dynamics of materials on their intrinsic timescales. A sub-picosecond time resolution makes it possible to ‘watch’ the energy flow between the interacting energy reservoirs and thus to study some of the most fundamental processes.

PROBING ULTRAFAST DYNAMICS

The most commonly used approach to excite materials and detect the effect of ultrashort pulses of light on their properties is time-resolved (optical) spectroscopy. The standard optical *pump-probe* experimental scheme uses one ultrashort *pump* pulse to

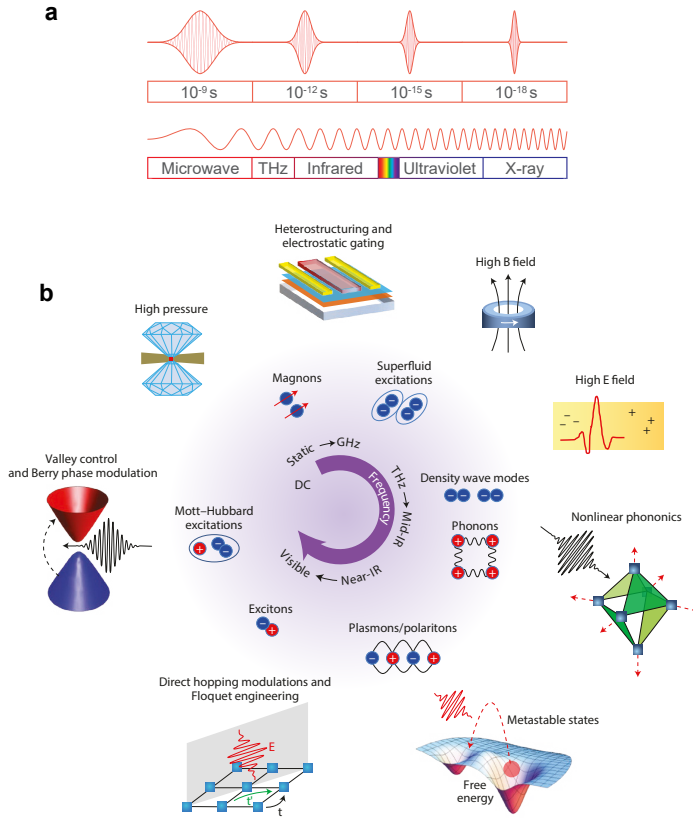


Figure 1.2: **Controlling materials over a broad frequency range.** **a**, The broad spectral frequency range over which ultrashort laser pulses can be created. **b**, Different methods and their associated frequencies that can be used to control materials through coupling to specific transitions and collective modes. Figure with permission from Ref. [22], APS (**a**), Ref. [14], Nature Publishing Group (**b**).

excite the material, followed by a second time-delayed *probe* pulse to monitor the time-evolution of the material's optical properties. By changing the delay time between the two pulses and analyzing the properties of the probe pulse after interaction with the excited medium, it is possible to temporally resolve the laser-induced phenomena on (sub)-picosecond timescales. The time-resolved spectroscopy can be extended by integrating femtosecond lasers with a multitude of other scattering probes such as X-ray diffraction [23], angle-resolved photoemission spectroscopy (ARPES) [24] or scanning probes like scanning tunneling microscopes (STM) [25] and scanning near-field microscopes (SNOM) [26]. The combination of several probing techniques is crucial to get a full understanding of the transient material state.

The dynamics and evolution of spectroscopic features following excitation of one of the microscopic degrees of freedom can be best understood by considering the equilib-

rium free-energy landscape of the material (see Fig. 1.3). Weak optical excitation can excite collective modes, which are oscillations of the material's order parameters around the stable minimum (ground state) (see Fig. 1.3a). By tracking these modes in the time-domain using a delayed (optical) probe one can (i) study the equilibrium properties of these collective modes and (ii) infer and disentangle the interaction between the different microscopic degrees of freedom directly after excitation. Sufficiently strong and efficient optical excitation can bring the system beyond the perturbative regime. This can result in strongly nonlinear dynamics and even dynamical effective interactions[22].

If the excitation is strong enough, the ultrashort laser pulse can lift the system over an energy barrier and drive it into a metastable state that is not accessible in equilibrium (see Fig. 1.3b). These metastable phases can persist for very long times[27] after the excitation. The phenomenon of optical switching between different material phases is quite universal, with examples range from light-induced insulator-metal transitions to magnetic phase transitions in different classes of materials. It constitutes the prototypical example of control over material properties using light and is often explored for its potential in future devices that could work at unprecedented speeds.

Finally, ultrafast photoexcitation can also affect the energy landscape itself. One could argue that this pathway forms the most 'out-of-equilibrium' instance of transient dynamics, as the excited oscillations of the order parameter in this case take place in an altered potential (see Fig. 1.3c). For large-amplitude oscillations, or when the energy barrier in the energy landscape is reduced to zero, the system can again be driven into an initially metastable state. If coherent oscillations of the order parameter persist in this altered landscape, their frequency should be changed. In chapter 5 we will see that the frequency softening can indeed serve as a measure of the transient landscape in an (antiferro)magnetic system.

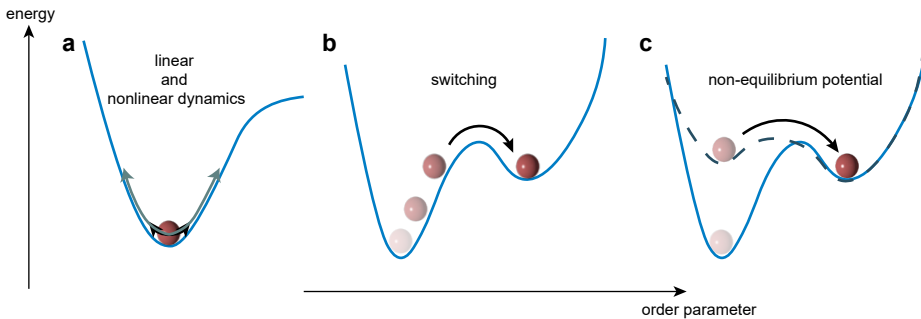


Figure 1.3: **Pathways through energy landscapes after laser excitation.** Laser excitation can drive different kinds of dynamics of the order parameter in the energy landscape. Weak excitation can drive oscillations in a stable minimum (ground state) (a). Strong excitation can bring the system in a metastable state either through large-amplitude oscillations (b), or via a transient change of the energy landscape itself (c).

1.2. RESEARCH CONTEXT AND SCOPE OF THIS THESIS

In the broad field concerning ultrafast control of matter and non-equilibrium dynamics, notable achievements include the optical excitation of coherent lattice and molecular vibrations [28], the ultrafast melting of magnetic order [29] and charge-density waves [30, 31], photo-induced insulator-to-metal transitions [27, 32, 33], switching between magnetically ordered phases [34], the light-induced enhancement of superconducting properties [35, 36] and the ultrafast switching of the magnetization direction [37, 38]. The wide variety of materials and their associated phases that have been subjected to phase-control experiments using light, reflects the broad applicability of laser pulses for material control. In line with this wide variety, this thesis concerns all-optical experiments on different materials using different excitation energies. Their common denominator is the selective perturbation of microscopic degrees of freedom in order to change and control material properties on very short timescales. The results can be subdivided in two main themes: control of magnetic properties and the generation of propagating excitations in insulating materials.

1.2.1. ULTRAFAST CONTROL OF MAGNETIC PROPERTIES

Magnetic materials have permeated our society for a long time and will probably continue to do so for many more years to come. Its use has evolved from the first application in early compasses, guiding the sea sailors in the Middle Ages in the right direction, to key component in modern magnetic hard drives used extensively for storing enormous amounts of data. The purpose of studies on ultrafast control of magnetic properties is therefore two-fold. Although highly fundamental in nature, studying microscopic interactions and phenomena on their natural timescales, these studies are also very relevant for future technological applications [39]. Using ultrashort pulses of light, the fundamental speed limits on magnetic switching and magnetic dynamics can be explored. The applications could range from vast improvements in the field of ‘conventional’ magnetic storage and information processing technologies [39] to novel terahertz (THz) spintronics applications [40].

A phenomenon that has acquired specific interest in recent years is the existence of intrinsically two-dimensional (2D) magnets. The first demonstration of layered 2D (van der Waals) magnets [41] attracted great interest, as it enabled a wide variety of both fundamental and application-based studies. Such ultrathin magnets do not only provide the best platform to study magnetism in the 2D limit, but also have the potential for improved efficiency in spintronic devices [42]. Optical techniques were shown recently to be able to probe the magnetic order in ferro- and antiferromagnets down to the monolayer limit [42], but could also be used to investigate and control the order on very short timescales [43].

The field of ultrafast magnetism was founded 25 years ago with the discovery of the sub-picosecond demagnetization of a thin Ni film by a 60 fs ultrashort laser pulse [29] (see Fig. 1.4a). This loss of magnetic order occurred orders of magnitude faster than predicted on the basis of spin-orbit and electron-lattice interaction times. While it sparked a debate on the exact physical mechanism underlying the ultrafast transfer of angular momentum [44], this demonstration showed that ultrafast manipulation of magnetic order

using light is possible. The laser-induced magnetization in metals is often captured in the simple phenomenological three-temperature model (see Fig. 1.4b): the spins, lattice and charge carriers form interacting energy reservoirs [39]. A laser-induced increase in the electron temperature will via different channels be transferred to the spin system, which results in an increase in the spin temperature and melting of the magnetic order.

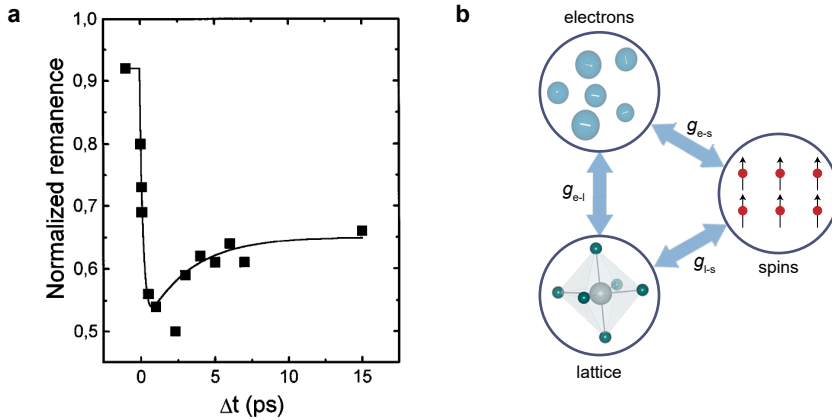


Figure 1.4: **Ultrafast demagnetization of a Ni film.** **a**, The transient remanent magneto-optical signal from a thin Ni film measured as a function of time after excitation with a 60 fs laser pulse. The transient signal demonstrates a loss of the magnetic order in the film within several picoseconds after excitation (figure with permission from Ref. [29], APS). **b**, The three-temperature model that describes the electrons, lattice and spins as three interacting reservoirs.

OPTICAL MANIPULATION OF MAGNETIC ORDER

In the years following the discovery of the ultrafast demagnetization using laser pulses, several works demonstrated and studied the optical excitation of coherent magnetic precession in ferromagnets in time-domain measurements [45]. The laser-driven sudden change in magnetic anisotropy due to absorbed heat triggers magnetic precession if this change occurs faster than the precession period. This precession with a frequency of several GHz takes place around a new equilibrium (see Fig. 1.5a): the ultrashort laser pulse affects the magnetic anisotropy and changes the effective magnetic field. Only a few years thereafter, the concept of laser-driven uniform magnetic precession was taken to a different class of magnetic materials: the antiferromagnets. These materials have intrinsic resonance frequencies up to hundreds of gigahertz, due to the exchange interaction between the oppositely oriented magnetic sublattices. Ultrashort pulses of light were shown to excite the antiferromagnetic spin dynamics (see Fig. 1.5b) [46, 47], where the phase of the precessional motion can be controlled by the polarization of the light [47, 48].

Coherent magnetic precession corresponds to spin oscillations around a minimum in the magnetic potential or energy landscape, which indicates a stable equilibrium po-

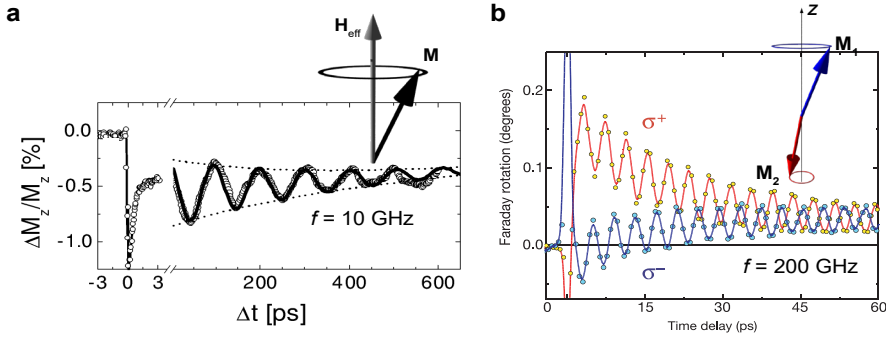


Figure 1.5: **All-optical excitation and detection of uniform spin precession.** **a**, Laser-induced coherent magnetic precession of the net magnetic moment around an effective field H_{eff} in a ferromagnetic Ni film. Due to the effect of the laser pulse, the direction of the effective field becomes different from the equilibrium direction. **b**, Optically-induced coherent spin precession in antiferromagnet. In an antiferromagnet the oppositely oriented magnetic sublattices precess around the easy-axis direction. Note the frequency difference between the spin precession in the ferro- and antiferromagnet. Figure with permission adapted from Ref. [45], APS (a), Ref. [47], Springer Nature (b).

sition (see Fig. 1.6a). As outlined in the previous section (see Fig. 1.3), the magnetic potential is a function of a certain coordinate or order parameter. In this case the parameter is often chosen to be φ , the angle between the net or sublattice magnetization and a certain crystallographic axis. The ability to excite spin oscillations using laser pulses hints at a more exciting and technologically relevant application: bringing the magnetic material from one magnetic configuration to the other (see Fig. 1.6b). As switching between two stable phases can be used to store information in binary memories, this may enable new technologies for faster magnetic recording [49]. To induce such a magnetic order-order phase transition at will in the fastest and most efficient way therefore forms an ongoing challenge. For ferromagnets and ferrimagnets this switching would correspond to (precessional) *magnetization reversal*: changing from one stable orientation of the net magnetization to another one. Also in antiferromagnets there can exist multiple stable orientations for the antiferromagnetic sublattices.

Indeed, there have been demonstrations of ultrafast magnetic order-order phase transitions in several types of magnetic materials. Magnetization reversal was studied in ferromagnets [50] and metallic ferrimagnets close to the compensation temperature [37, 51]. Similarly, spin-reorientation transitions were triggered on picosecond timescales in the rare-earth orthoferrite antiferromagnets [34, 52] and ferromagnetic order was generated by inducing an AFM-FM phase transition in FeRh [53, 54]. As laser-induced heating formed the basis of all these instances of magnetic order-order transitions, this stimulates to find less dissipative ways of switching.

RESONANT OPTICAL CONTROL OF MAGNETIC ORDER

Efficient pathways to control magnetic order crucially rely on the ability to manipulate the microscopic interactions that stabilize the macroscopic order. In this regard, excitation of optical resonances that involve degrees of freedom that are tightly coupled to the magnetic order might provide these pathways. Over the past decade there have ap-

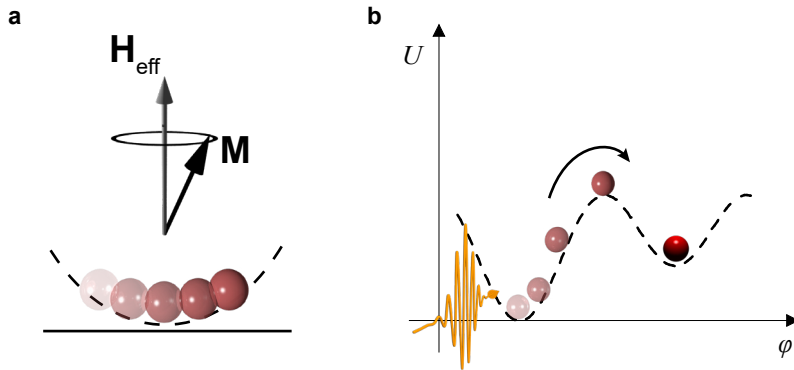


Figure 1.6: **Laser-induced magnetic dynamics.** **a**, Magnetic or spin precession corresponds to oscillations around a minimum in the magnetic potential. **b**, Magnetic potential as function of an order parameter φ . Large-amplitude precession can eventually bring the system to a metastable equilibrium.

peared several works that focus on the excitation of a specific degree of freedom and the effect on magnetism. One of the first examples concerned the resonant excitation of spin precession using intense terahertz pulses [55] that directly couple to the spins through their magnetic field component. Resonant excitation of infrared-active phonons led to ultrafast melting of magnetic order [56], the excitation of spin-precession [57], and was used to study spin-lattice coupling in ferrimagnetic yttrium iron garnet [58]. The net magnetization in a dielectric, transparent cobalt-doped ferrimagnetic garnet was switched to a different stable state using ultrashort pulses to resonantly pump the $d-d$ transitions of the cobalt ions [38], which are responsible for the strong magnetocrystalline anisotropy in the material. Terahertz electromagnetic pulses were used to directly excite electronic orbital transitions and induce large-amplitude coherent spin oscillations [59] and a subsequent ballistic spin-reorientation transition [60]. Finally, direct optical excitation of $d-d$ orbital transitions was used as a mechanism to resonantly change the exchange interaction in iron oxides [61]. These very recent successes invite for further studies on resonant excitation and their potential to induce magnetic dynamics and dynamically change magnetic properties on very short timescales.

1.2.2. PROPAGATING EXCITATIONS IN INSULATING MATERIALS

The concepts of coherent, uniform spin precession and laser-induced phase changes as discussed in the previous section and summarized in Fig. 1.6 occur locally and are restricted to the volume initially excited by the optical pulse. The generation of propagating modes is another topic of interest, as propagating excitations offer a compelling feature: they allow for the transport and processing of information. Specifically, the concept of short-wavelength spin waves as information carriers and key constituents of future wave-based computing devices [62–65] (see Fig. 1.7a) has attracted a lot of attention. The generation of spin waves with a varying degree of coherency and their subsequent propagation over macroscopic distances has been demonstrated in insulating ferrimag-

nets and studied heavily over the past years [66–68]. On the contrary, the generation of coherent short-wavelength propagating spin waves in antiferromagnets, has not been demonstrated. This is because the intrinsic resonance frequencies of antiferromagnets are orders of magnitude higher, which not only provides potential for future devices at THz frequencies, but also results in increased difficulty for coherent excitation.

The nature of normal modes, be it magnetic or vibrational, as determined by its wavelength and the dispersion relation (Fig. 1.7b), defines whether the excitation can propagate away from the excited volume. The light-induced generation of high-frequency, short-wavelength quasi-particles requires a broadband stimulus that can simultaneously provide the required momentum. It has been known for a long time that *confined* optical excitation can result in the emission of broadband propagating wavepackets of coherent acoustic phonons [69]. This observation led to the emergence of the field of picosecond ultrasonics [70] with demonstrations of strain-induced dynamical functionalities in oxides and potential to use the gigahertz to terahertz acoustic phonons for ultrafast light processing [71]. Apart from the direct applicability of dynamical strain in the form of propagating strain pulses, detection of these pulses can also inform us on the type and amplitude of the strain initially present in the optically excited volume.

As the optical absorption of materials is intimately connected to the presence of optically-active transitions, resonant optical excitation is inevitably confined to a volume close to the material's surface, the so-called skin depth. Additionally, resonant excitation can alter specific microscopic degrees of freedom, with the capability to induce excitations of significant amplitude. This makes it a powerful tool to excite broadband wavepackets of propagating quasi-particles, which will be the topic of chapter 4 and chapter 7.

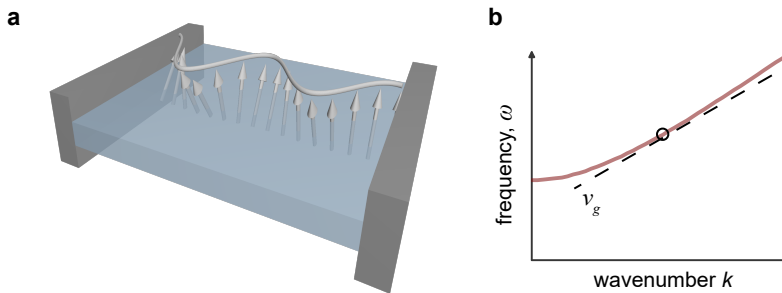


Figure 1.7: **Propagating spin excitations.** **a**, Short-wavelength propagating spin waves can be used to transport information. **b**, The dispersion relation defines the frequency and propagation velocity v_g of the excitation.

1.3. STRUCTURE OF THIS THESIS

In this thesis we explore how ultrafast resonant excitation of optical transitions can be used to induce localized and propagating structural dynamics in wide-bandgap insulators and control magnetic interactions and manipulate magnetic order in antiferromagnets. We do this by resonantly targeting specific lattice vibrations and orbital and

electronic transitions with ultrashort pulses of light. Chapter 2 and 3 provide the necessary background information and tools to understand the work in this thesis. **Chapter 2** discusses the basic concepts of magnetic order and spin waves that are important to this thesis. It also includes an introduction to magnetic interactions. **Chapter 3** gives a brief overview of the main experimental methods and the typical experimental setups that were used.

We then proceed with the core of this thesis, which consists of four works that study the structural and magnetic dynamics of various materials in response to resonant excitation of optically-active transitions:

- In **chapter 4** we introduce the concept of nonlinear phononics and study the coherent structural dynamics after resonant excitation of infrared-active optical phonons in LaAlO_3 . We show in this wide-bandgap insulator that ionic Raman scattering drives coherent rotations of the oxygen octahedra, which is the result of anharmonic phonon-phonon coupling. The resonant lattice excitation also generates longitudinal and transverse strain wavepackets, which are the result of anisotropic optically induced strain.
- In **chapter 5** we demonstrate that light-driven infrared-active phonons can be used to manipulate microscopic interactions on ultrashort timescales, which results in control over macroscopic magnetic states. When mid-infrared laser pulses are tuned to resonance with a lattice mode in the antiferromagnet DyFeO_3 , they can induce nonthermal, long-living changes of the exchange interaction between the Dy orbitals and the Fe spins. We identify nonlinear phonon-phonon coupling as the underlying mechanism. With this renormalized interaction we can tip the balance and induce picosecond coherent switching from a collinear antiferromagnetic to a weakly ferromagnetic phase.
- **Chapter 6** explores the effect of resonant excitation of orbital transitions within the magnetic nickel ion d -orbital manifold in the van der Waals antiferromagnet NiPS_3 . We demonstrate the selective excitation of a magnon mode with corresponding two-dimensional characteristics. We show that the excitation of this mode is the result of a transient photo-induced magnetic anisotropy, which emerges in response to photoexcitation of the electrons into states with lower orbital symmetry.
- **Chapter 7** describes how ultrashort pulses of light can be used to generate a wavepacket of coherent propagating spin waves in the insulating antiferromagnet DyFeO_3 . The nanometer confinement of laser pulses with photon energies above the material's bandgap creates a strongly non-uniform spatial spin-excitation profile. This results in the emission of a broadband wavepacket of coherent antiferromagnetic magnons, propagating from the sample surface into the material.

In **chapter 8** we summarize the main observations of this thesis, reflect on unanswered questions and provide perspectives for future research.

2

MAGNETIC ORDER AND SPIN WAVES

“Needle in a haystack’s easy — just bring a magnet.”

Keith DeCandido, in *The Zoo Job* (2013)

In this chapter we provide the theoretical background required to understand the results presented in the subsequent chapters. We introduce atomic magnetic moments in solids and discuss the most important fundamental magnetic interactions. After reviewing the different sources of magnetic anisotropy, the chapter ends with a derivation and comparison of the spin-wave dispersion relation in ferro- and antiferromagnets.

2.1. MAGNETIC MOMENTS AND ELECTRON ORBITAL STATES IN CRYSTAL FIELDS

Generating a macroscopic net magnetic moment requires the existence of microscopic ones. Understanding the origin of a net magnetic moment thus boils down to finding the small magnetic moments that constitute it. It turns out that it is the electron that possesses the microscopic magnetic moment and thus forms the small building block of magnetic materials.¹

The total magnetic moment of an electron consists of two contributions: an orbital magnetic moment and a spin magnetic moment. The orbital magnetic moment is related to the electron's orbital angular momentum \mathbf{l} , while the spin magnetic moment arises from the intrinsic (spin) angular momentum \mathbf{s} . In all atoms other than hydrogen, there is more than one electron present. This means that the total angular momentum (and therefore total magnetic moment) of a localized magnetic ion becomes a function of the moments of the many (interacting) electrons in the outer shell. The way in which the different types of angular momentum add up, depends on the relative magnitude of the orbit-orbit coupling, spin-orbit coupling and spin-spin coupling. For magnetic $3d$ transition metal ions, for which the spin-orbit coupling is quite weak, the Russell-Saunders coupling is applicable [72]. The orbital angular momenta \mathbf{l}_i of all electrons are first combined into the total orbital angular momentum \mathbf{L} and the spin angular momenta \mathbf{s}_i in the total spin angular momentum \mathbf{S} . The total angular momentum \mathbf{J} is then given as $\mathbf{J} = \mathbf{L} + \mathbf{S}$. For angular momentum states that are well-described by the Russell-Saunders coupling, Hund's rules can identify the ground state electronic configuration [73].

With the total angular momentum \mathbf{J} in the atom's ground state determined, the magnitude of the corresponding magnetic moment $\mu_{\mathbf{t}}$ is given by:

$$\mu_J = \langle \mu_{\mathbf{t}} \rangle = -g_J \mu_B \sqrt{J(J+1)}. \quad (2.1)$$

Here J is the total angular momentum quantum number, and g_J the Landé g -factor [73]. μ_B is the Bohr magneton defined by $\mu_B = \frac{e\hbar}{2m_e}$, with e and m_e the electron charge and mass, respectively and \hbar the reduced Planck constant.

2.1.1. QUENCHING THE ORBITAL MOMENT

In the previous section we have discussed the total magnetic moments of free atoms with full spherical symmetry. We can associate a certain energy E_0 with the Coulomb interactions leading to Hund's rules that determine the lowest-energy configuration of a multielectron ion. In real solids, however, the crystal environment in combination with spin-orbit coupling affects the systematics of the free atom electronic levels. We will focus on the $3d$ transition metal ions. In this class of materials, the $3d$ sub shell is not filled completely, with the electronic configuration given by $[\text{Ar}]3d^n 4s^2$, $1 \leq n \leq 10$ ². In their natural oxidation states, the $3d$ electrons determine the electronic and magnetic properties of these ions. In order to deduce the properties of the magnetic moments in solids,

¹The atomic nucleus also possesses a magnetic moment, but it is around 3 orders of magnitude smaller than the electron's magnetic moment and therefore often neglected.

²For zinc and chromium the $4s$ shell contains only one electron

we can treat the crystal field (energy E_{CF}) and the spin-orbit interaction (energy E_{SO}) between the spin and orbital angular momentum as perturbations with $E_0 > E_{CF} > E_{SO}$ as hierarchy of the different interactions.³ Specifically, this means that the Coulomb and exchange interaction within the magnetic atom are considered most important. As a result, we consider one-electron d orbitals [74]. When the $3d$ magnetic ions are surrounded by a regular octahedron of negatively charged ligands such as O^{2-} and S^{2-} (which is one of the most common environments in the broad class of transition metal oxides), the spherical symmetry is violated and the five-fold degenerate d levels are split into a lower triplet (t_{2g}) and higher doublet (e_g). This energy splitting Δ_{CF} (or associated energy E_{CF}) between the t_{2g} and e_g states is caused by the interaction of the d -electrons with the surrounding ligands [72]. The negatively charged anions induce a cubic potential, which leads to an increase in energy for wavefunctions with a large electron density in the direction of the octahedral corners (see Fig. 2.1).

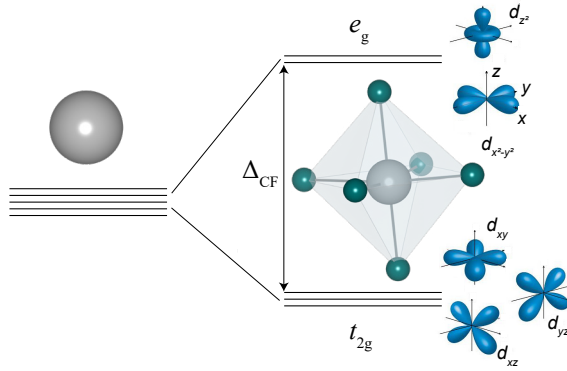


Figure 2.1: **Crystal field splitting.** Crystal field splitting of the five-fold degenerate electron d levels of the $3d$ -ion (grey) in an octahedral field into the e_g and t_{2g} manifolds. The angular distribution of the electron density for the conventional basis states is shown. Wavefunctions from Ref. [75].

The crystal field splits the five degenerate d -orbitals, which can be denoted by $|l = 2, l_z\rangle$, or $|l_z\rangle$ for short. An important consequence of the crystal field becomes apparent when looking at the expressions of the e_g and t_{2g} wavefunctions as linear superpositions of the basis states [72]:

$$\begin{aligned}
 e_g : \begin{cases} |z^2\rangle & = |0\rangle \\ |x^2 - y^2\rangle & = \frac{1}{\sqrt{2}} (|2\rangle + |-2\rangle) \end{cases} \\
 t_{2g} : \begin{cases} |xy\rangle & = \frac{-i}{\sqrt{2}} (|2\rangle - |-2\rangle) \\ |xz\rangle & = \frac{-i}{\sqrt{2}} (|1\rangle - |-1\rangle) \\ |yz\rangle & = \frac{i}{\sqrt{2}} (|1\rangle + |-1\rangle). \end{cases}
 \end{aligned} \tag{2.2}$$

³Deviations from this hierarchy and competition between E_0 and E_{CF} lead to the phenomenon of *high-spin* and *low-spin* states [72]

Here we used real combinations of the $|l_z\rangle$ as basis states for the t_{2g} manifold. Looking at the expressions in Eq. 2.2, we immediately see that the orbital angular momentum $l = 2$ for free atoms with spherical symmetry is quenched or reduced in an octahedral crystal field environment. In the e_g doublet, all diagonal matrix elements $\langle e_g | \mathbf{l} | e_g \rangle = 0$. Moreover, the off-diagonal matrix elements that are related to l_x and l_y operators are also 0, as these operators (or the linear combinations $l_{\pm} = l_x \pm il_y$) can only mix states with difference in angular momentum projection $\Delta l_z = \pm 1$. The same reasoning shows that for the t_{2g} triplet in the chosen basis the diagonal matrix elements are 0 and some off-diagonal matrix elements can have non-zero values.⁴

The magnetic moment of a state is given by the average value of the operator $\mu_B(\mathbf{L} + 2\mathbf{S})$. Applying a magnetic field along the z -direction, we see that the orbital contribution, linear in the expectation value of l_z , vanishes. Note that the levels still have a definite total angular momentum, but that the different vector components are no longer constants of motion. The consequence is that the contribution of the orbital magnetic moment is said to be 'quenched'. This can be experimentally confirmed by measuring the effective magnetic moment of these ions in magnetically dilute salts, where the ions experience octahedral crystal fields [76]. In the simple case of $3d$ ions in octahedral fields, the magnetic moment is mainly determined by the spin moment, with little orbital contribution.⁵

2.2. MAGNETIC INTERACTIONS

In the previous section we discussed the origin of isolated atomic magnetic moments. An ensemble of localized microscopic magnetic moments can only produce a macroscopic net magnetization if a large fraction of them are oriented in the same direction. More generally, in order for some sort of magnetic order to spontaneously appear and prevail over other types of magnetic ordering, there needs to be an associated energy gain. This requires the presence of interaction, either between the magnetic moments themselves or with an external magnetic field. In this section we discuss the different microscopic interactions that give rise to spontaneous magnetic order and the existence of preferred directions for the magnetic moments in solids. We have seen in the previous section that in many materials of interest this magnetic moment mainly comes from the spin angular momentum. For reasons of simplicity we will therefore assume in the rest of this section that the localized moments are carried completely by the *spins*.

2.2.1. EXCHANGE INTERACTION

With a rather simple calculation, it can be shown that the magnetic dipole interaction between the different localized moments is so weak that thermal excitation would destroy magnetic order at temperatures of several Kelvin [77]. There exist, however, many ferromagnetic materials that sustain their order up to room temperature. This implies the presence of a stronger interaction that keeps the magnetic moments ordered.

⁴More specifically, the triplet can be mapped onto the p -orbitals ($l = 1$), provided that the effective moment should actually taken to be negative [72].

⁵Spin-orbit coupling can result in orbital contributions, as we see in the following section.

DIRECT EXCHANGE

The first phenomenological explanation for the high ordering temperatures was proposed by Pierre Weiss in 1906, who explained ferromagnetism in terms a huge internal ‘molecular field’, proportional to the applied magnetic field. It took two more decades before it was found that the origin of this effective internal field lies in the *exchange* interaction between the different electrons. This interaction derives from a combination of Coulomb repulsion between the electrons that carry the spin and have overlapping wavefunctions, and the symmetrization postulate. As result of this interaction and a charge distribution that depends on the spin configuration, there is an energy difference between states with parallel and antiparallel spins. For a two-electron system, with spin \mathbf{S}_1 and \mathbf{S}_2 , this means that there is an energy difference between the singlet state ($S = 0$) and the triplet states ($S = 1$). This can be captured in a Hamiltonian of the following form, which is called the Heisenberg Hamiltonian:

$$\mathcal{H}_{\text{exch}} = A\mathbf{S}_1 \cdot \mathbf{S}_2, \quad (2.3)$$

with A the singlet-triplet energy splitting. More generally, the Heisenberg Hamiltonian is an exchange model that describes the effect of exchange interaction in a many-electron system (N electrons) in terms of the individual spin operators \mathbf{S}_i :

$$\mathcal{H}_{\text{exch}} = - \sum_{i \neq j}^N J_{ij} \mathbf{S}_i \cdot \mathbf{S}_j, \quad (2.4)$$

with J_{ij} the exchange integral that captures the exchange interaction between the different spins and depends on the overlap of the electronic wavefunctions (see Fig. 2.2a) and the sum over all pairs of spins. The coupling energy constant J_{ij} is positive for ferromagnetic, parallel coupling and negative for antiferromagnetic, antiparallel coupling. If this interaction occurs between electrons on neighbouring atoms, this is known as *direct* exchange.

SUPEREXCHANGE

The electrons that carry the magnetic moments in insulating materials such as many magnetic transition-metal (TM) oxides are localized. Moreover, the magnetic ions are often separated by non-magnetic ones, such as oxygen. As a result there is very little direct overlap between the $3d$ orbitals from nearest-neighbour magnetic ions. However, the $3d$ -orbitals of both these ions are hybridized with the $2p$ -orbitals of the oxygen ions. The non-magnetic oxygen ion therefore ‘connects’ the two magnetic ions and acts as a mediator that helps the magnetic ions to interact. We consider the situation that the $3d$ transition metal ions are magnetic and have a single localized d -electron or a half-filled shell (Fe^{3+} , Mn^{2+}). The oxygen atoms have filled p -orbitals and the TM-O-TM bond is 180° (see Fig. 2.2b). The d t_{2g} -orbitals hybridize in that case with the oxygen p -orbitals. Without considering hopping of electrons (spins) between the different ions, the ground state has one electron localized on each TM-ion, due to the strong Coulomb repulsion U between two electrons at one site. The two spins can be aligned either ferromagnetically or antiferromagnetically. Using second-order perturbation theory, starting from

the Mott-insulator ground state, the energy gain due to hopping with a small associated energy t can be calculated. The second-order process allowing electrons to hop to the other magnetic ion, is forbidden by the Pauli principle when the spins on nearest-neighbour magnetic ions are aligned. As a result there is only an energy gain $J \sim \frac{-t^2}{U}$ for the antiferromagnetic ground state, which is why it is favored over the ferromagnetic ground state. Summing up different hopping possibilities, the superexchange interaction effectively favours oppositely oriented spins on the magnetic ions and the exchange constant becomes $J = -\frac{2t^2}{U}$ [74].

In general, the different d -orbitals are split in the crystal field, can be only partially filled and TM-O-TM bonds can also have values close to 90° . The sign and strength of the exchange still follow regularities, which are formulated as the Goodenough-Kanamori rules [72]. In most cases of transition metal oxides with octahedral crystal environments and 180° TM-O-TM bonds, however, the exchange favours antiferromagnetic alignment.

There are several other type of exchange interactions. Some of them result in magnetic anisotropy, which is the topic of section 2.3.

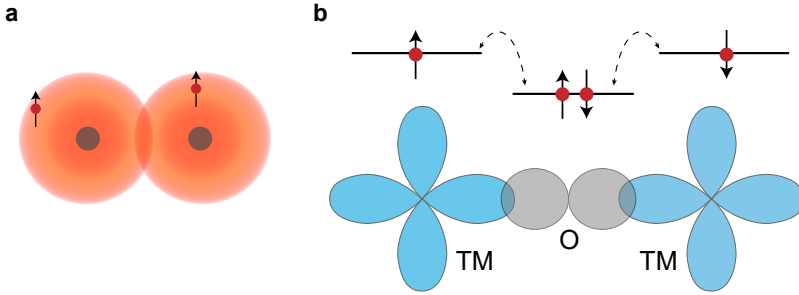


Figure 2.2: **Exchange interaction.** **a**, Direct exchange is the result of overlapping wavefunctions of the magnetic ions. **b**, Schematic illustration of the superexchange interaction in a $3d$ magnetic oxide. The $3d$ -ions have one unpaired electron and the oxygen shell is filled. Antiferromagnetic alignment allows for hopping through second-order processes, which reduces the overall energy.

2.2.2. ZEEMAN INTERACTION

Magnetic moments μ orient in external magnetic fields \mathbf{H} . This is due to the Zeeman interaction, which gives an energy

$$\begin{aligned} H_{Zee} &= -\mu_0 \mu \cdot \mathbf{H} \\ &= \frac{gJ\mu_0\mu_B}{\hbar} \mathbf{J} \cdot \mathbf{H}. \end{aligned} \quad (2.5)$$

Even in antiferromagnets, which possess no net magnetic moment in zero fields, this energy term can play an important role. Large applied fields result canting of the magnetic sublattices and in spin-flop transitions.

2.2.3. SPIN-ORBIT INTERACTION

In section 2.1.1 we argued that the magnetic moment of many $3d$ ions in solids (experiencing octahedral crystal fields) is determined by the spin only, as the orbital contribution is quenched. The interactions between the different spins is due to the exchange interaction, which is intrinsically isotropic. The reason that the spins can still 'feel' the crystal lattice, is the spin-orbit interaction that couples the spin and orbital magnetic moments.

Spin-orbit interaction describes the interaction between the spin angular momentum \mathbf{S} and the orbital angular momentum \mathbf{L} . \mathbf{S} and \mathbf{L} can either be single-electron angular momenta or represent the sum of coupled electron momenta. While the existence of their coupling with the correct factors follows naturally from the relativistic Dirac equation [78], we can picture spin-orbit coupling with a semi-classical model as well [74]. Consider the situation shown in figure 2.3, where an electron (mass m_e) moving in a circular orbit or radius r is associated with current loop I and has orbital magnetic moment $\mu_{\text{orb}} = -\frac{\mu_B}{\hbar} \mathbf{L} = -\frac{e}{2m_e} \mathbf{L}$. This results in a magnetic field \mathbf{H} in the center of the loop, which then interacts with the spin magnetic moment $\mu_s = -\frac{e}{m_e} \mathbf{S}$. θ is the angle between \mathbf{S} and \mathbf{L} in a vector model. The field in the center is given by $H_{\text{orbit}} = I/2r$. Using that a magnetic moment μ_{loop} of a current loop with current I and area $S = \pi r^2$ is given by $|\mu_{\text{loop}}| = IS$, this can be rewritten to

$$\mathbf{H}_{\text{orbit}} = \frac{\mu_{\text{orb}}}{2\pi r^3} = -\frac{e\mathbf{L}}{4\pi m_e r^3}. \quad (2.6)$$

The spin-orbit energy is then given by

$$E_{\text{so}} = -\mu_0 \mu_s \cdot \mathbf{H}_{\text{orbit}} = -\frac{e^2}{4\pi \epsilon_0 m_e^2 c^2 r^3} \mathbf{L} \cdot \mathbf{S} \quad (2.7)$$

with $\epsilon_0 = \frac{1}{c^2 \mu_0}$ the vacuum permittivity, c the speed of light and both \mathbf{L} and \mathbf{S} in units of \hbar .

An alternative derivation [77] considers the situation from the electron frame (with spin (orbital) angular momentum \mathbf{s} (\mathbf{l})), where the orbiting nucleus constitutes a magnetic field at the static position of the electron that acts on the spin magnetic moment. Including the relativistic Thomas factor ($\frac{1}{2}$) to account for the reference frames that accelerate with respect to each other, the correct expression for the intrinsic spin-orbit interaction can be obtained. This leads to an expression for the spin-orbit Hamiltonian of the form

$$\begin{aligned} H_{\text{so}} &= -\frac{1}{2} \mu_0 \mu_s \cdot \mathbf{H} \\ &= \frac{e\hbar^2}{2m_e c^2 r} \frac{dV}{dr} \mathbf{l} \cdot \mathbf{s} \end{aligned} \quad (2.8)$$

Here $V(r)$ is the potential energy corresponding to the electrostatic interaction between the nucleus and the electron. For an electron in the Coulomb field of a hydrogen-like atom with quantum numbers n, l , the spin-orbit coupling ξ_{nl} is given by integrating over the wavefunction. This results in $\xi_{nl} \sim Z^4 \frac{1}{n^3 l(l+1/2)(l+1)}$ and scales rapidly with the nucleus charge Z . The formalism can be extended to the resulting spin \mathbf{S} and angular momentum \mathbf{L} of a multi-electron system [76, 78]. This will give the term $H_{\text{SO}} = \lambda \mathbf{S} \cdot \mathbf{L}$, with $\lambda = \langle \xi \rangle / 2S$.

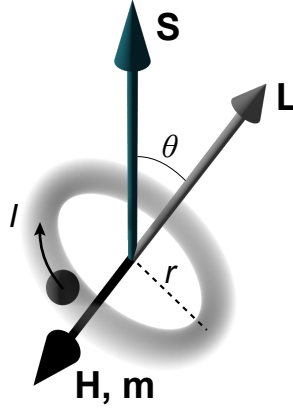


Figure 2.3: **Semi-classical spin-orbit coupling.** Schematic of a simple model to derive the spin-orbit coupling energy (Eq. 2.7). The electron orbiting the nucleus has an orbital angular momentum \mathbf{L} , orbital magnetic moment \mathbf{m} and causes a magnetic field \mathbf{H} in the center of the loop. This magnetic field interacts with the spin magnetic moment.

2.3. MAGNETIC ANISOTROPY

Magnetic anisotropy refers to the situation that in many magnetic materials the ferromagnetic or antiferromagnetic axis lies along some fixed crystallographic directions. This behaviour can be treated phenomenologically by expressions for the anisotropy energy density E_{an} of the form

$$E_{\text{an}} = K_1 \sin^2 \theta, \quad (2.9)$$

where θ is the angle between the magnetization vector (ferromagnets) or Néel vector (antiferromagnets) and the easy axis. K_1 is called the uniaxial anisotropy constant and depends on temperature. Deflecting the magnetic or antiferromagnetic order parameter from the easy axis comes with a certain energy cost. Eq. 2.9 only suffices to describe the simple uniaxial magnetic systems. Most magnetic materials exhibit anisotropy contributions of higher-order. In general, expressions like Eq. 2.9 need to remain invariant under all operations that together form the crystal symmetry group.

A general Heisenberg Hamiltonian (Eq. 2.4) might describe whether the system is ordered ferromagnetically or antiferromagnetically, it does not provide indications along which axis the spins will orient themselves. The exchange interaction itself is isotropic, and we need spin-orbit interaction to couple the spins to certain crystallographic or sample orientations. Regardless of the exact microscopic origin, a term in the Hamiltonian of the form $\xi_{nl} \mathbf{L} \cdot \mathbf{S}$ (see previous section), gives an energy gain if \mathbf{L} and \mathbf{S} are aligned (anti)parallel compared to perpendicular orientations. The orbital angular momentum \mathbf{L} does couple to the crystal field. This gives rise to the concept of magnetocrystalline anisotropy: preferential directions of the (spin) magnetic moments in the crystal. Below we describe a few interactions that result into magnetic anisotropy.

2.3.1. SINGLE-ION ANISOTROPY

The first contribution to anisotropy depends on the energy of a single ion in the crystal environment. It arises from the combination of the spin-orbit coupling and the electronic configuration of the anisotropic d -orbitals in the crystal field. As the spin-orbit interaction energy is much smaller than the intra-atomic exchange interaction and the crystal field-splitting, it can be treated using perturbation theory. The strength and exact expression of the single-ion anisotropy depend on the details of the electronic configuration and the occupation of different electronic levels ψ_n , with energy E_n . Using second-order perturbation theory, the effective anisotropic Hamiltonian for an electronic ground state corresponding to an orbital singlet, can be written as [78]:

$$\hat{H}_{\text{eff}} = -\lambda^2 \left(\Lambda_{xx} \hat{S}_x^2 + \Lambda_{yy} \hat{S}_y^2 + \Lambda_{zz} \hat{S}_z^2 \right), \quad (2.10)$$

with

$$\Lambda_{ii} = \sum_n^{\text{excited states}} \frac{\langle \psi_0 | \hat{L}_i | \psi_n \rangle}{E_n - E_0}. \quad (2.11)$$

Looking at the expressions in Eqs. 2.10 and 2.11, we see that anisotropy arises from the way the different electronic levels are mixed by the orbital angular momentum operator. Another effect of the spin-orbit coupling is that it recreates part of the orbital momentum that was quenched by the crystal field interaction.

An important note must be made here. For $4f$ (rare-earth) magnetic ions, the situation is completely different. For these magnetic ions, the crystal field energy is small compared to the spin-orbit interaction, and the magnetic moment consists of a large orbital component. The magneto-crystalline anisotropy is then calculated using first-order perturbation, with the crystal field as perturbation [79]. The resulting anisotropy is in general very large compared to the situation for magnetic transition metal ions.

2.3.2. TWO-ION ANISOTROPY

Two-ion anisotropy is the collective name given to anisotropy resulting from the interaction between two magnetic ions. It arises from different types of interaction, often competing within the same system, depending on which type of magnetic ions interact and the nature of the material. The most important ones are:

- **Dipolar interactions and shape anisotropy:** Pairs of magnetic moments can interact with each other through dipole-dipole coupling. While this coupling is in general weak compared to exchange interactions, it is long-range and highly anisotropic and can be decisive in determining the final preferred orientation. Due to the long-range character of this interaction, the orientation of a magnetic moment depends on the macroscopic magnetization orientation. This factor is referred to as shape anisotropy.
- **Indirect exchange:** In metallic materials, localized magnetic moments can be coupled through intermediary conduction electrons. While in the simplest approximation this interaction is isotropic, orbital contributions in $4f$ ions can lead to higher-order corrections [79].

- **Anisotropic (symmetric) exchange:** Anisotropic exchange is a general term that refers to a situation where the interaction strength between two spins depends on the orientation of the spins relative to their bond vector. This means that the terms instead of the isotropic Heisenberg Hamiltonian (Eq. 2.4) become of the form

$$J_{xx}S_{x,i}S_{x,j} + J_{yy}S_{y,i}S_{y,j} + J_{zz}S_{z,i}S_{z,j}, \quad (2.12)$$

with $\mathbf{S}_{i,j}$ the spin-operators of two neighbouring spins and the exchange parameters J_{ii} not necessarily equal. Microscopically, such terms can arise from third-order perturbation contributions. For example, for $3d$ S -type ions with a non-degenerate orbital ground state, this contribution can be evaluated and contains products containing the spin-orbit interaction in the two interacting ions combined with their exchange interaction [80]. The physical interpretation is as follows. The spins on both sites turn slightly due to spin-orbit interaction. This has an effect on the shape of the atomic electron shells, which then alters the exchange energy between the spins.

- **Antisymmetric exchange:** A special contribution to the total magnetic exchange is given by the antisymmetric exchange. This is a relativistic correction to the regular superexchange, and given by a term in the Hamiltonian of the form:

$$H^{DM} = \mathbf{D}_{ij} \cdot (\mathbf{S}_i \times \mathbf{S}_j). \quad (2.13)$$

In general the tensor \mathbf{D}_{ij} is determined by the crystal and magnetic symmetry and the orientation of the neighbouring magnetic ions. This term was introduced phenomenologically by Dzyaloshinskii [81] with a microscopic origin given by Moriya a few years later [82]. Moriya showed that taking into account spin-orbit interactions for both magnetic ions and the exchange interaction between them, second-order perturbation theory gives a term of this form, which is now conventionally referred to as Dzyaloshinskii-Moriya interaction (DMI). The most important effect of this interaction is that it favours non-collinear spin ordering. The competition between the superexchange and DMI-interaction leads to weak ferromagnetism: a slight canting of the spins results in a small, but measurable net magnetic component. Examples of weak ferromagnets are the rare-earth (R) orthoferrites RFeO_3 and $\alpha\text{-Fe}_2\text{O}_3$ hematite.

2.3.3. ANISOTROPY IN TWO-DIMENSIONAL MAGNETS

A system is considered to be magnetic if the microscopic magnetic moments order over long-range distances, with an associated spontaneous breaking of time-reversal symmetry. The interaction between the magnetic moments that drives the ordering competes with thermal fluctuations that tend to destroy this long-range order and become larger at higher temperature. Ultimately, at the ordering temperature T_C , the thermal fluctuations are victorious and the long-range order is indeed destroyed. The thermal fluctuations become more decisive as the dimensionality of the system is lowered. While ordering is possible in three-dimensional magnetically isotropic systems, thermal fluctuations destroy long-range magnetic order in the two-dimensional equivalent. The

Mermin-Wagner theorem [83] states that no finite-temperature ordering as a result of isotropic and short-ranged interactions is possible in two-dimensional magnets. However, if the spin dimensionality is lowered as well, for example by introducing anisotropy, which favours certain spin directions, a gap in the spin-wave spectrum opens. The frequency gap suppresses the effect of thermal fluctuations and a transition to a magnetically ordered phase becomes possible. This highlights the importance of anisotropy for the mere existence of magnetic 2D materials. Indeed, after many years of theoretical predictions, the existence of two-dimensional (mono-layer) magnetic materials was demonstrated very recently [41, 42].

2.4. MAGNETIZATION DYNAMICS AND SPIN WAVES

Ferro- and antiferromagnets have in common that at finite temperature the spontaneous magnetization (of the sublattices) decreases due to magnetic excitations. The lowest-energy magnetic excitations are called spin waves and can be thought of as spatial and temporal oscillations in the relative orientations of all spins on the lattice. These collective excitations were first predicted by Bloch in the case of the spins in a ferromagnet [84]. As the spin deviations spread over the whole lattice, they can be described by a wavevector \mathbf{k} , with an energy $\epsilon_{\mathbf{k}} = \hbar\omega_{\mathbf{k}}$. While we can visualize spin waves as classical excitations, they are a true quantum phenomenon and their quanta are called magnons. The relation between the wavevector \mathbf{k} and the frequency $\omega_{\mathbf{k}}$ is called the dispersion relation. One of the most interesting properties of antiferromagnets is the so-called *exchange enhancement* or *exchange amplification* of all antiferromagnetic dynamic parameters compared to those in ferromagnets. This exchange enhancement results in high magnetic resonance frequencies and spin wave velocities. In this section we discuss the different energy scales in ferro- and antiferromagnets and derive the dispersion relation using a semi-classical approach.

2.4.1. UNIFORM SPIN PRECESSION

FERROMAGNETS

Standard ferromagnetic materials are described by a non-zero average value of the spin density $\langle S \rangle$ or magnetization \mathbf{M} . The magnetization is related to the average spin density by $\mathbf{M} = -g\mu_B\langle S \rangle$. Here g is the Landé factor, which for ions in the s -state takes the value $g \approx 2$. The occurrence of a net magnetization has as result that time-reversal symmetry is broken, as $\mathbf{M} \rightarrow -\mathbf{M}$ under inversion of time.

Some phenomena in ferromagnets can be described using the continuum approach. Fortunately the most important dynamical processes fall in that category. We start by defining the magnetization

$$\mathbf{M} = \frac{1}{V} \sum_n \boldsymbol{\mu}_n, \quad (2.14)$$

The sum is taken over all microscopic magnetic moments $\boldsymbol{\mu}_n$ in the small, but macroscopic volume V , which in this case are the spin magnetic moments. The continuum approach now allows us to use classical theory to derive the dynamical properties of an isotropic ferromagnet [85]. We assume that the magnetization $\mathbf{M}(\mathbf{r}, t)$ is uniform or only changes very slowly in space, so that all microscopic magnetic moments in the volume

form a ‘macrospin’ \mathbf{M} . The equation of motion for \mathbf{M} in a magnetic field \mathbf{H} is then simply given by [85]:

$$\frac{d\mathbf{M}}{dt} = \gamma [\mathbf{M} \times \mathbf{H}] \quad (2.15)$$

and is called the *Landau-Lifshitz* equation. γ is the gyromagnetic ratio, the proportionality constant between the magnetic moment μ and the total angular momentum. This means that it is not necessarily equal to the spin g -factor, but often very close, as the small difference is due to the orbital magnetic moments. An important feature of Eq. 2.15 is that it follows that the magnitude $|\mathbf{M}|$ remains constant in time: \mathbf{M} precesses around the magnetic field direction with frequency $\omega_H = \gamma H$, which is called the ferromagnetic resonance. In the more general case of an anisotropic ferromagnet, the Landau-Lifshitz equation becomes

$$\frac{d\mathbf{M}}{dt} = \gamma [\mathbf{M} \times \mathbf{H}_{\text{eff}}], \quad (2.16)$$

with $\mathbf{H}_{\text{eff}} = -\frac{\partial U}{\partial \mathbf{M}}$ and $U = U_{\text{an}} + U_Z$ the magnetic energy density that contains an anisotropy (U_{an}) and Zeeman (U_Z) contribution. The exchange energy is neglected, as it does not enter the equation of motion [85]. The magnetization precesses around an effective magnetic field (see Fig. 2.4a) which is the sum of an anisotropy field $\mathbf{H}_{\text{an}} = -\frac{\partial U_{\text{an}}}{\partial \mathbf{M}}$ and the applied magnetic field \mathbf{H} . This causes a non-zero value of the ferromagnetic resonance (FMR) frequency $f = \frac{\gamma}{2\pi} H_{\text{an}}$ at zero applied field, due to the presence of anisotropy. The value of the FMR is usually in the several GHz range.

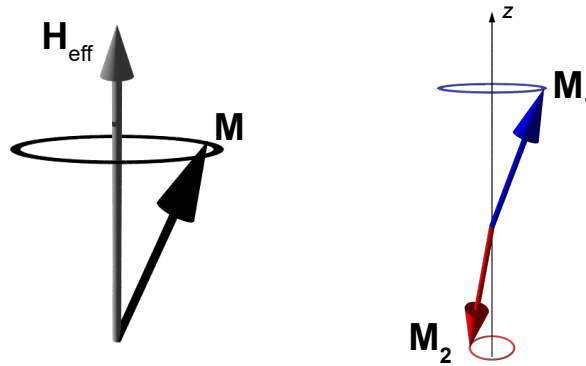


Figure 2.4: **Uniform spin precession.** **a**, In ferromagnets, the net magnetization \mathbf{M} precesses around an effective magnetic field \mathbf{H}_{eff} . **b**, In antiferromagnets, both magnetic sublattices precess around their equilibrium direction.

ANTIFERROMAGNETS

In antiferromagnetic materials, time-reversal symmetry is also broken, but there is no net macroscopic magnetic moment \mathbf{M} . The reason for this is the existence of a finite number n of magnetic sublattices, each with a net magnetization \mathbf{M}_i , which cancel each

other such that $\sum_i \mathbf{M}_i = 0$. We restrict ourselves to the simplest situation with two oppositely oriented magnetic sublattices \mathbf{M}_1 and \mathbf{M}_2 . In this case, it is the antiferromagnetic or Néel vector $\mathbf{L} = \frac{\mathbf{M}_1 - \mathbf{M}_2}{2}$ ⁶ that serves as order parameter. It is important to note that this does not exclude the presence of a small magnetic moment. Both an applied magnetic field \mathbf{H} and interactions of relativistic origin such as the Dzyaloshinskii-Moriya interaction can lead to canting of the magnetic moments \mathbf{M}_i and incomplete compensation.

Antiferromagnetic dynamics is qualitatively different from the dynamics in ferromagnets. The equations of motion are derived for the magnetic sublattices \mathbf{M}_1 and \mathbf{M}_2 . The magnetic energy density U_{AFM} contains in that case a term that derives its origin from the interaction between the two sublattices [85] that is given by [86–89]:

$$U_{\text{AFM, ex}} = \frac{1}{4M_0} H_{\text{ex}} \mathbf{m}^2. \quad (2.17)$$

Here M_0 is the sublattice magnetization, $\mathbf{m} = (\mathbf{M}_1 + \mathbf{M}_2)/M_0$ and H_{ex} is the amplitude of the exchange field \mathbf{H}_{ex} , which can be on the order of 10^6 Oersted. In the equations of motions for the magnetic sublattices this now gives a very large effective field. The full derivation is given in appendix 2.5, but the most important result is stated here: in zero magnetic field, the antiferromagnetic resonance is $\omega = \gamma \sqrt{H_{\text{ex}} H_{\text{an}}}$. As typically $\sqrt{H_{\text{ex}}/H_{\text{a}}} \sim 30\text{--}100$, this is the first manifestation of the exchange enhancement of dynamical parameters. In antiferromagnets with ordering temperatures of several hundred Kelvin, which is not uncommon, this will give frequencies in the THz range.

2.4.2. DISPERSION RELATION

Uniform spin precession corresponds to a spin wave with infinite wavelength, i.e. $k = 0$. The spins can also precess with a phase difference between neighbouring spins (see Fig. 2.5a), which corresponds to a travelling spin wave. The frequency of these spin wave modes is determined by the dispersion relation, the relation between the wavevector \mathbf{k} and the frequency ω of the spin wave at this wavevector.

FERROMAGNETS

We can add a nonuniform term U_{ex} to the energy of exchange interaction of a ferromagnet, to account for the increased exchange energy when neighbouring magnetic moments are not aligned:

$$U_{\text{ex}} = \frac{1}{2} \sum_{i=1}^3 \sum_{j=1}^3 q_{ij} \frac{\partial \mathbf{M}}{\partial x_i} \frac{\partial \mathbf{M}}{\partial x_j}, \quad (2.18)$$

with q_{ij} the components of a tensor \mathbf{q} . This is the lowest-order term that takes deviations from a uniform magnetization into account. For an isotropic ferromagnet this then takes the form

$$U_{\text{ex}} = q \nabla^2 \mathbf{M} \quad (2.19)$$

Working out the equations of motions, this gives a dispersion [85]

$$\omega^2 = \left(\omega_{0,\text{FM}} + \eta k^2 \right) \left(\omega_H + \eta k^2 + \omega_{\text{dip}} \sin^2 \theta_k \right). \quad (2.20)$$

⁶Following convention, we use the symbols \mathbf{L} and \mathbf{l} for the Néel vector and its normalized version, respectively. Unfortunately these are the same symbols that are conventionally also used for angular momentum. From this point onwards, \mathbf{l} and \mathbf{L} will always refer to the (normalized) Néel vector in this thesis.

$\omega_{0,\text{FM}} = \gamma H_0$ is the spin-wave gap due to the internal magnetic field H_0 (taking into account the geometrically dependent demagnetization field). $\omega_{\text{dip}} = \gamma \mu_0 M_0$ results from the anisotropy of dipolar interaction, and θ_k is the angle between the wavevector \mathbf{k} and the static magnetization \mathbf{M}_0 . $\eta = \gamma M_0 q$ is often referred to as a nonuniform exchange constant or spin stiffness. Most important to note is:

- For $\omega_{0,\text{FM}}, \omega_{\text{dip}} \ll \eta k^2$ ($\ll \eta \frac{\pi^2}{a^2}$) the dispersion becomes quadratic:

$$\omega \sim \eta k^2. \quad (2.21)$$

This approximate dispersion is plot in Fig. 2.5b, with a small spin-wave gap.

- The group velocity in this regime is equal to $v_g = \frac{\partial \omega}{\partial k} = 2\eta k$. Using the quantum mechanical derivation of the spin wave dispersion [85], we find that $\eta = \frac{1}{3} \frac{ZSJ}{\hbar} a^2 \sim \frac{J}{\hbar} a^2$, with Z the number of nearest neighbours, J the exchange integral, S the spin quantum number and a the lattice parameter.

ANTIFERROMAGNETS

In the case of antiferromagnets, the full dispersion consists of two branches and (for wavenumber $k \ll \frac{\pi}{a}$, a the lattice parameter) is given by (see section 2.5):

$$\omega^{1,2}(k) = \sqrt{\left(\omega_0^{(1,2)}\right)^2 + c^2 k^2}, \quad (2.22)$$

There are some differences with the dispersion relation for ferromagnets. As mentioned before, the antiferromagnet spin-wave gap $\omega_0^{1,2}$ will be much larger than for ferromagnets. The characteristic velocity c can have values up to tens of km/s in antiferromagnets with high Néel temperatures. In Fig. 2.5b we can see that the physical sense of this quantity is that it equals the limiting spin wave group velocity $v_{\text{AFM},g} = \frac{\partial \omega}{\partial k}$. This value can be estimated as $c \approx \frac{J}{\hbar} a$ [87]. Comparing this to the ferromagnetic group velocity given by $v_{\text{FM},g} = 2\eta k \sim \frac{J}{\hbar} a^2 k$, we find that $v_{\text{AFM},g} \gg v_{\text{FM},g}$ for $k \ll \frac{1}{a}$. We conclude see that the spin-wave velocity is another example of an exchange enhanced dynamical parameters in antiferromagnets compared to ferromagnets.

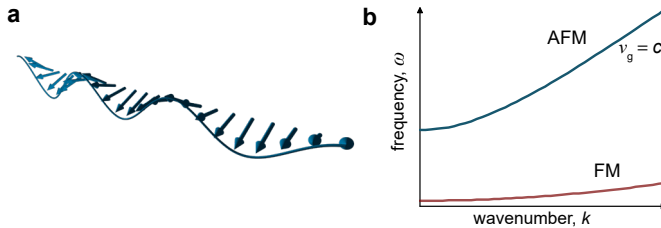


Figure 2.5: **Spin-wave dispersion.** **a**, Localized spins precessing around an (effective) magnetic field with a phase difference between neighbouring spins constitute a spin wave with non-zero wavenumber. **b**, The spin-wave dispersion for ferro- (FM) and antiferromagnets (AFM). The AFM spin-wave frequency is orders of magnitude larger than for ferromagnets and the dispersion converges to a linear form with limiting group velocity $v_g = c$.

2.5. APPENDIX: MAGNETIC DYNAMICS IN ANTIFERROMAGNETS

In antiferromagnetic materials there is no net macroscopic magnetic moment \mathbf{M} . The reason for this is the existence of a finite number n of magnetic sublattices, each with a net magnetization \mathbf{M}_i , which cancel each other such that $\sum_i \mathbf{M}_i = 0$. In order to describe spin dynamics in antiferromagnets, we restrict ourselves to the simplest example of an antiferromagnet consisting of two oppositely oriented magnetic sublattices \mathbf{M}_1 and \mathbf{M}_2 , such that $|\mathbf{M}_1| = |\mathbf{M}_2| = M_0$, with M_0 the saturation magnetization: $M_0 = Ng\mu_B\hbar S$, with N the number of spins per unit volume and S the spin of the magnetic ions.

Regardless of the presence or absence of a small magnetic moment $\mathbf{M} = \mathbf{M}_1 + \mathbf{M}_2$, the antiferromagnetic order is best described by introducing the antiferromagnetic vector or Néel vector $\mathbf{L} = \mathbf{M}_1 - \mathbf{M}_2$. This vector serves as an order parameter for the antiferromagnetic order. The equations of motion for the two magnetic sublattices (ignoring dissipation) are obtained from the Landau-Lifshitz equation [90]:

$$\frac{d\mathbf{M}_{1,2}}{dt} = \gamma \mathbf{M}_{1,2} \times \mathbf{H}_{\text{eff},1,2}. \quad (2.23)$$

$\gamma = g\mu_B/\hbar$ is the gyromagnetic ratio and $\mathbf{H}_{1,2}^{\text{eff}}$ represents the effective fields that acts on the sublattice magnetizations $\mathbf{M}_{1,2}$ and are given by the functional derivative of the total magnetic energy density $w(\mathbf{M}_1, \mathbf{M}_2)$ with respect to $\mathbf{M}_{1,2}$:

$$\mathbf{H}_{1,2}^{\text{eff}} = -\frac{\partial w(\mathbf{M}_1, \mathbf{M}_2)}{\partial \mathbf{M}_{1,2}}. \quad (2.24)$$

Now we introduce the vectors $\mathbf{m} = \mathbf{M}/2M_0$ and $\mathbf{l} = \mathbf{L}/2M_0$, which are normalized variants of the magnetization \mathbf{M} and Néel vector \mathbf{L} . It follows that

$$\mathbf{l}^2 + \mathbf{m}^2 = 1, \quad \mathbf{m} \cdot \mathbf{l} = 0 \quad (2.25)$$

Substituting the expressions from Eq. 2.24 into these definitions leads to the following equations of motion [89]:

$$\begin{aligned} 2M_0 \frac{\partial \mathbf{m}}{\partial t} &= \gamma [\mathbf{m} \times \mathbf{H}_m] + \gamma [\mathbf{l} \times \mathbf{H}_l], \\ 2M_0 \frac{\partial \mathbf{l}}{\partial t} &= \gamma [\mathbf{m} \times \mathbf{H}_l] + \gamma [\mathbf{l} \times \mathbf{H}_m], \end{aligned} \quad (2.26)$$

where the effective magnetic fields $\mathbf{H}_{m,l}$ are defined as:

$$\mathbf{H}_m = -\frac{\partial w}{\partial \mathbf{m}}, \quad \mathbf{H}_l = -\frac{\partial w}{\partial \mathbf{l}}. \quad (2.27)$$

As the dynamics of the normalized irreducible vectors is completely determined by the energy density w , we need to take a closer look at this quantity. A general expression [86–89] is given by:

$$w(\mathbf{m}, \mathbf{l}) = M_0 H_{\text{ex}} \mathbf{m}^2 - 2M_0 \mathbf{m} \cdot \mathbf{H}_0 + \frac{\alpha}{2} (\nabla \mathbf{l})^2 + w_0(\mathbf{l}) + w_D. \quad (2.28)$$

Here, H_{ex} is the so-called exchange field of the AFM, a crucial characteristic of any AFM. This quantity is defined as the minimum value of the external magnetic field \mathbf{H}_0

for which the magnetizations for the two magnetic sublattices becomes parallel, such that $|\mathbf{M}| = 2M_0$ and $\mathbf{L} = 0$. Note that as this field needs to overcome the direct exchange between the two sublattices, it typically has very large values, up to 1000 T. α is the inhomogeneous exchange energy constant, and $w_0(\mathbf{l})$ the anisotropy energy density. In this expression we already made use of the condition $|\mathbf{m}| \ll |\mathbf{l}|$ and omitted terms the terms with $(\nabla\mathbf{m})^2$ and ignored the dependence of the anisotropy energy density w_0 on \mathbf{m} . This assumes sufficiently weak magnetic fields: $|\mathbf{H}| \ll H_{\text{ex}}$.

The first two terms are universal, in the sense that they have the same form for all AFMs. The first term accounts for the isotropic exchange between the magnetic sublattices. As we will see later, the presence of this term (including the large constant H_{ex}) is what leads to exchange amplification of the dynamical parameters compared to ferromagnets. The second term is the Zeeman energy of the net magnetic moment in an external applied field \mathbf{H}_0 . The third term accounts for spatial variations of the magnetization of the sublattices \mathbf{M}_1 and \mathbf{M}_2 . It has the same meaning as for ferromagnets. It is important to note that $\alpha \sim H_{\text{ex}}M_0a^2$, with a the lattice parameter. The fourth term accounts for anisotropy of the antiferromagnet. The fifth term is special, as it is bilinear in the components of \mathbf{m} and \mathbf{l} [87]: $w_{\text{D}} = D_{ij}m_i l_j$. In general the tensor $D_{ij}(\mathbf{l})$ is determined by the AFM symmetry and can depend on the antiferromagnetic vector \mathbf{l} [91]. This term was introduced phenomenologically by Dzyaloshinskii [81] with a microscopic origin given by Moriya a few years later [82]. Moriya showed that taking into account exchange and spin-orbit interactions, this gives a term of the form $w_{\text{D}} = H_{\text{D}} [\hat{\mathbf{d}}(\mathbf{m} \times \mathbf{l})]$, which is called the standard antisymmetric form. The direction of the unit vector $\hat{\mathbf{d}}$ is determined by the symmetry of the AFM. Contributions of this form are now conventionally referred to as Dzyaloshinskii-Moriya interaction (DMI). The DMI is responsible for canting of the sublattice magnetization, resulting in a weak magnetic moment $\mathbf{m} \sim (H_{\text{D}}/H_{\text{ex}})\mathbf{l}$. Note that the contribution of the DMI interaction can also be included by a term $2M_0\mathbf{m} \cdot \mathbf{H}_{\text{D}}$ using an effective Dzyaloshinskii field \mathbf{H}_{D} . The parameter H_{D} is the amplitude of this effective Dzyaloshinskii field and can be much larger than the anisotropy field, but is still much smaller than the exchange field H_{ex} [89, 91].

Of course the resulting equations of motion take a different form for different antiferromagnetic systems. However, it is insightful to study the behaviour for simplest case, setting the applied magnetic field equal to zero and using that the exchange field H_{ex} is significantly larger than all other effective fields. This results in $|\mathbf{m}| \ll |\mathbf{l}|$. In this case a compact and closed equation of motion for the vector \mathbf{l} can be obtained, which is called the sigma model equation [88]: a set of equations independent of \mathbf{m} .

The equation of motion for the antiferromagnetic vector \mathbf{l} can first be rewritten, using the expression for the energy density in Eq. 2.28. All terms in this expression are bilinear in the components of \mathbf{m} and \mathbf{l} , meaning that it contains terms of the form $m_i m_j$, $l_i m_j$ and $l_i l_j$. By grouping those terms and using the relative sizes of the constants involved, several terms can be omitted. For example, the term containing the inhomogeneous exchange with constant $\alpha \sim M_0 H_{\text{ex}} a^2 \ll M_0 H_{\text{ex}}$ is negligible in the long wavelength ($\lambda \gg$

a) limit. This leaves us with the following form of Eq. 2.26 [89]:

$$\begin{aligned} \frac{1}{\gamma} \frac{\partial \mathbf{l}}{\partial t} &= \frac{1}{2M_0} [\mathbf{m} \times \mathbf{H}_l] + \frac{1}{2M_0} [\mathbf{l} \times \mathbf{H}_m] \\ &\approx H_{\text{ex}}(\mathbf{l} \times \mathbf{m}) + (\mathbf{H}^{(\text{eff})} \times \mathbf{l}), \end{aligned} \quad (2.29)$$

where $\mathbf{H}^{(\text{eff})} = \mathbf{H}_0 + \mathbf{H}_D$.

In small magnetic fields $|\mathbf{H}_0| \ll H_{\text{ex}}$, this leads to the following expression for the magnetization [88, 89]

$$\mathbf{m} = \frac{1}{H_{\text{ex}}} \left[\mathbf{H}^{(\text{eff})} - \mathbf{l}(\mathbf{H}^{(\text{eff})} \cdot \mathbf{l}) \right] + \frac{1}{H_{\text{ex}}\gamma} \frac{\partial \mathbf{l}}{\partial t} \times \mathbf{l}. \quad (2.30)$$

This expression gives two important insights:

- The Dzyaloshinskii field can lead to a net equilibrium magnetization, even when the applied field is zero, given by the first term.
- The second term shows that a dynamical net magnetization component can emerge due to dynamics of the antiferromagnetic vector, even when a net magnetization is absent in equilibrium.

Substituting this expression into Eq. 2.29 gives the desired dynamic equation for \mathbf{l} .

However, a more compact form of this equation can be obtained by considering the Lagrangian density \mathcal{L} of an AFM which has the form [87, 89, 91]:

$$\mathcal{L} = \int d\mathbf{r} \left\{ \frac{M_0}{\gamma^2 H_{\text{ex}}} \left(\frac{\partial \mathbf{l}}{\partial t} \right)^2 - \frac{2M_0}{\gamma H_{\text{ex}}} \left(\mathbf{H}^{(\text{eff})} \cdot \left[\mathbf{l} \times \frac{\partial \mathbf{l}}{\partial t} \right] \right) - \frac{\alpha}{2} \left(\frac{\partial \mathbf{l}}{\partial x_i} \right)^2 - w_r(\mathbf{l}) \right\}, \quad (2.31)$$

with $w_r(\mathbf{l})$ a potential energy term containing contributions from the anisotropy energy $w_a(\mathbf{l})$ and the external field:

$$w_r(\mathbf{l}) = w_a(\mathbf{l}) + \frac{M_0}{H_{\text{ex}}} \left[(\mathbf{H}_0 \cdot \mathbf{l})^2 - \mathbf{H}_0^2 \right] \quad (2.32)$$

While the expression in Eq. 2.31 looks complex, it is again insightful to consider different terms and take a look at a simple mechanical analogy, for which the langrangian is given by $\mathcal{L} = T + G - W$, with T, G, W the kinetic, gyroscopic and potential energy term respectively. Now this first term, quadratic in the time derivative $\left(\frac{\partial \mathbf{l}}{\partial t} \right)$ determines the so-called inertial properties of AFM spin dynamics. This in contrast to ferromagnets, where this term is absent in the Lagrangian. The result is that antiferromagnetically coupled spins have inertia, which means that a short stimulus can trigger inertial spin motion [92]. The second term is the gyroscopic term, linear in $\frac{\partial \mathbf{l}}{\partial t}$, also present for ferromagnets. Its presence depends on the effective magnetic field $\mathbf{H}^{(\text{eff})}$. The last two terms describe the potential energy of the AFM and contain contributions of spatial variation

of the sublattice magnetization and relativistic corrections in w_r . Now making some assumptions, we can derive expressions for the frequencies of the spin dynamics. Setting $\mathbf{H}_0 = 0$ and neglecting the contribution of the Dzyaloshinskii field \mathbf{H}_D to the dynamics, which is valid if \mathbf{H}_D is of the form $H_D(\hat{\mathbf{d}}(\mathbf{m} \times \mathbf{l}))$ [87–89], the Lagrangian Eq. 2.31 leads to the following sigma model equation for the antiferromagnetic vector \mathbf{l} [89]:

$$\frac{1}{\omega_{\text{ex}}} \left(\mathbf{l} \times \frac{\partial^2 \mathbf{l}}{\partial t^2} \right) = \frac{\gamma \alpha}{2M_0} (\mathbf{l} \times \nabla^2 \mathbf{l}) - \frac{\gamma}{2M_0} \left(\mathbf{l} \times \frac{\partial w_a}{\partial \mathbf{l}} \right) \quad (2.33)$$

We study the linear case, where the deviation of \mathbf{l} from its equilibrium position is small. We consider the vector \mathbf{l} , with l_i its projections along the unit vectors $\hat{\mathbf{e}}_i$. In the quadratic approximation, the potential energy term then has the form

$$w_a = M_0(H_{a1}l_1^2 + H_{a2}l_2^2), \quad (2.34)$$

with $H_{a1,2}$ the anisotropy fields.

Equation 2.33 then reduces to the set of equations for the two components for \mathbf{l}

$$\begin{aligned} \frac{\partial^2 l_1}{\partial t^2} - c^2 \nabla^2 l_1 + \left(\omega_0^{(1)} \right)^2 l_1 &= 0 \\ \frac{\partial^2 l_2}{\partial t^2} - c^2 \nabla^2 l_2 + \left(\omega_0^{(2)} \right)^2 l_2 &= 0 \end{aligned} \quad (2.35)$$

Here the characteristic velocity $c = \gamma \sqrt{\frac{\alpha H_{\text{ex}}}{2M_0}}$ and frequencies $\omega_0^{(1)} = \gamma \sqrt{H_{\text{ex}} H_{a1}}$, $\omega_0^{(2)} = \gamma \sqrt{H_{\text{ex}} H_{a2}}$ are introduced. The plane-wave solution to equations 2.35 provides a relation between the frequency $\omega^{(1,2)}$ and the wavenumber k . This dispersion relation for the two magnon branches of the system is then given by [87]:

$$\omega^{(1,2)}(k) = \sqrt{\left(\omega_0^{(1,2)} \right)^2 + c^2 k^2}, \quad (2.36)$$

There are some differences with the dispersion relation for ferromagnets. First of all, the spin-wave gap $\omega_0^{(1,2)}$ will be much larger than for ferromagnets, as in that case the uniform spin precession frequency is given by $\omega_{\text{FM}} = \gamma \sqrt{H_{a1} H_{a2}}$. As typically $\sqrt{H_{\text{ex}}/H_{\text{an}}} \sim 30$ -100, this is the first manifestation of the exchange enhancement of dynamical parameters. In antiferromagnets with ordering temperatures of several hundred Kelvin, which is not uncommon, this will give frequencies in the THz range. The characteristic velocity c can have values up to tens of km/s in AFM with high Néel temperatures. In Fig. 2.5 we can see that the physical sense of this quantity is that it is the limiting spin wave group velocity $v_g = \frac{\partial \omega}{\partial k}$. The spin-wave velocity is another example of an exchange enhanced dynamical parameters in antiferromagnets compared with ferromagnets.

3

EXPERIMENTAL TECHNIQUES

*“It doesn't matter how beautiful your theory is,
it doesn't matter how smart you are.
If it doesn't agree with experiment, it's wrong.”*

Richard Feynmann

In this chapter we give a brief overview of the different experimental setups and optical techniques that form the basis for the work presented in this thesis. While the schematics look rather compact, the realization of these setups involves many optical components to control the direction, beamsize and polarization of the light pulses. Careful alignment of the setup is crucial to reduce noise and allow for correct interpretation of the data.

Time-resolved spectroscopy is the study of dynamical processes using spectroscopic techniques. The type of dynamical processes that can be studied is defined by, among many other factors, the sensitivity and spatial and temporal resolution of the spectroscopic technique. The highest time-resolution is given by ultrafast optical spectroscopy techniques that use sequences of ultrashort pulses of light (femtosecond duration) in order to study dynamical processes on very short timescales in a wide variety of material systems. This field of research has greatly expanded over the last decades due to technological process that enabled the generation of high-stability ultrashort pulses of electromagnetic radiation in a very wide frequency range [17–21].

The most conventional technique to study ultrafast dynamical processes is pump-probe spectroscopy. After excitation with a strong external stimulus (the pump), the system is monitored through its interaction with a probe. By repeating this process after starting in the same ground state and changing the delay between the moment of excitation and probing, we get a full time-resolved picture of the system's response to the stimulus. In this thesis we perform all-optical experiments, in which a strong laser pulse excites the system and the weaker probe pulse measures transient changes in the material's optical properties. In this chapter we give a short overview of the experimental setup and techniques that are used in these experiments.

3.1. ALL-OPTICAL PUMP-PROBE SPECTROSCOPY

The generic scheme used for all-optical pump-probe experiments is shown in Fig. 3.1. The first step is to divide the output of an (amplified) pulsed laser system (repetition rate f) into two beams with a large difference in power. The large-power pulses can be down converted in frequency through several nonlinear processes and then used to excite the system and bring it out of equilibrium. The other, weaker, pulses are delayed in time and used to monitor the optical properties of the material after excitation through changes in the probe's transmission or polarization plane. The difference in arrival time between the pulses is precisely controlled by sending the probe pulse via a mechanical delay line, which consists of a retroreflector on a moving stage. The delay line allows to control the delay time with a precision of less than ~ 6 fs (displacement $\Delta x < 1 \mu\text{m}$) over a total range of more than a nanosecond. In order to monitor the effect of the pump pulse, the probe signal coming from the excited material needs to be compared directly to the situation in which the pump beam was absent. The standard scheme uses an optical chopper system (Thorlabs) in the optical path of the pump that is synchronized with the laser and works at half the repetition rate $\frac{1}{2}f$. This means that every second pump pulse is blocked and detection of the signal at frequency $\frac{1}{2}f$ allows to only measure the pump-induced changes which reduces the noise substantially. This detection is performed using a standard lock-in scheme at frequency $\frac{1}{2}f$, where a boxcar can be included for increased noise reduction.

3.2. TUNABLE ULTRASHORT LASER PULSES

3.2.1. ULTRAFAST TI:SAPPHIRE AMPLIFIER

The key component in the experimental setup described in the previous section is the amplified pulsed laser system that generates the high-power ultrashort light pulses. We

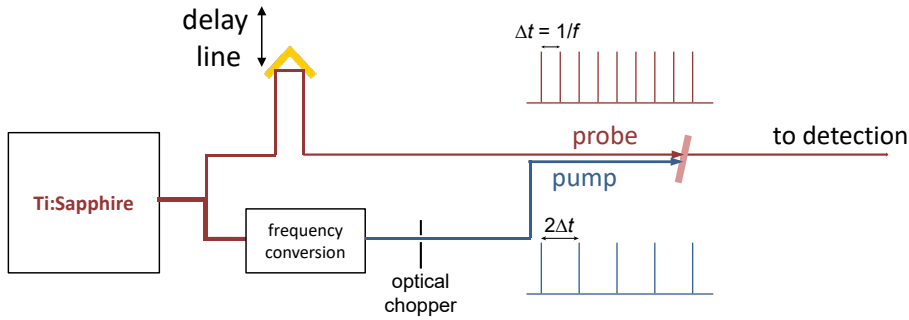


Figure 3.1: **All-optical pump-probe setup.** In an all-optical pump-probe experiment the output pulses (frequency f) of a powerful amplified Ti:Sapphire laser system are split into two beams. A small portion is sent via a mechanical delay line and used as a probe of the pump-induced structural and magnetic dynamics. A large fraction of the light is used to obtain ultrashort pulses of light in a wide range of frequencies and will be used as excitation pulses. The chopper in the pump path is synchronized with the laser and operates at a frequency $\frac{1}{2}f$, effectively blocking every second pulse.

use a commercially available table-top system (*Astrella*, Coherent) that provides pulses at a central wavelength of 800 nm (photon energy 1.55 eV), with a duration of 100 fs and pulse energy of more than 7 mJ at a repetition rate f of 1 kHz. The system consists of a mode-locked seed laser and a regenerative amplifier module.

The Ti:sapphire seed laser provides broadband ultrashort pulses with central frequencies around 800 nm at a repetition rate of 80 MHz. In order to obtain high-power ultrashort pulses, the regenerative amplifier module is crucial. Using the chirped pulse amplification (CPA) technique [93], the pulses are stretched temporally using a system of gratings before they are amplified inside a cavity. By lengthening the pulses and thereby reducing the peak power, energy can be extracted from the Ti:sapphire gain medium inside the cavity, while avoiding damage to this medium. After amplification, the high-energy pulses are recompressed back to nearly the original duration. The large increase in energy per pulse comes at the cost of a much lower repetition rate, which is set by the 1 kHz repetition rate of the amplifier module.

3.2.2. TUNABLE PULSE FREQUENCY

OPTICAL PARAMETRIC AMPLIFIER

While the Ti:sapphire amplifier has the ability to provide high peak power ultrashort pulses of light, the central frequency of these pulses cannot be changed. An optical parametric amplifier (OPA) forms the core component in the system used to obtain ultrashort pulses of light in a wide range of frequencies. The OPA consists of several stages in order to generate these high-amplitude pulses at different frequencies. The output of the amplifier that enters the OPA is split in a weak and strong beam (see Fig. 3.3). The weak beam is used to generate a white light continuum inside a sapphire crystal. The strong beam and the white light continuum are combined inside a nonlinear β -barium borate (BBO) crystal. Due to the nonlinearity of the crystal, electric fields at different frequencies can interact to produce a time-varying polarization with mixed frequency compo-

nents. The induced polarization can therefore emit radiation at these new frequency components. Optical parametric amplification [18] is the specific nonlinear process in which energy from a strong pump beam (frequency ω_p) is transferred to a weak signal beam at the desired frequency ω_s in a nonlinear crystal. In addition, a third beam (the idler beam) at frequency ω_i is created, with $\omega_i < \omega_s < \omega_p$. Aside from energy conservation,

$$\hbar\omega_p = \hbar\omega_s + \hbar\omega_i \quad (3.1)$$

the momentum conservation (or phase matching) condition must be satisfied in order for the process to be efficient:

$$\hbar\mathbf{k}_p = \hbar\mathbf{k}_s + \hbar\mathbf{k}_i, \quad (3.2)$$

with $\mathbf{k}_p, \mathbf{k}_s, \mathbf{k}_i$ the wavevectors in the crystal of the pump, signal and idler beam respectively. Rewritten in terms of the refractive index n , the phase matching condition is given by

$$n_p = \frac{n_i\omega_i + n_s\omega_s}{\omega_p}. \quad (3.3)$$

In negative uniaxial birefringent materials ($n_e < n_o$ the refractive indices of the extraordinary (e) and ordinary (o) axes), this phase matching condition can be met for some combinations of frequencies by polarizing the pump beam along the extraordinary axis with the lower refractive index. In the system used for the experiments in thesis, the process relies on type II phase matching, where either the signal or idler beam is polarized parallel to the pump beam and the other one perpendicular to it. In order to achieve phase matching over a wide range of frequencies, the angle θ_{pm} between the wavevector of the beams and the optical axis is adjusted by rotating the crystal [18] (see Fig. 3.2). This means that the phase matching condition plays a crucial role as it allows to selectively amplify the frequency component within the white light continuum by changing the angle θ_{pm} to satisfy this condition only for the component at the desired signal frequency.

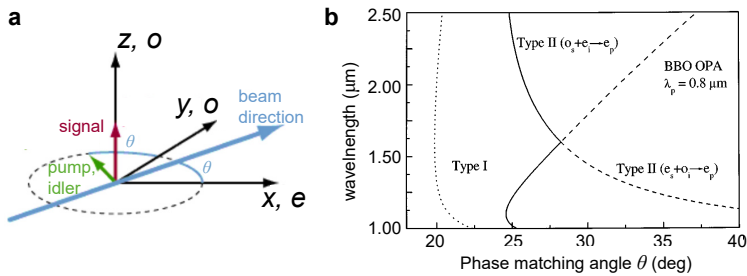


Figure 3.2: **Angular phase matching.** **a**, Angular phase matching of optical parametric amplification in a uniaxial birefringent crystal with two ordinary (o) and one extraordinary (e) axis with refractive index $n_e < n_o$. The pump, signal and idler beam are propagating in the xy plane, with an angle θ between wavevector \mathbf{k} and the extraordinary x -axis. The signal polarization is oriented along an ordinary direction. By rotating the crystal around the z -axis, the pump and idler encounter a changing effective extraordinary refractive index $n_{e'}(\theta)$. Figure adapted from Ref. [94]. **b**, The angle tuning curves for a BBO OPA with pump wavelength $\lambda_p = 800$ nm for type I phase matching (dotted curve) and type II phase matching (solid curve: idler and pump parallel, dashed curve: signal and pump parallel). Figure with permission from Ref. [18], AIP Publishing.

We use a commercially available dual OPA (TOPAS twins, Light Conversion) to obtain two independently tunable outputs with a single white light seed (see Fig. 3.3). The OPA delivers pulses with a duration of less than 100 fs, and, by considering both the signal and idler beams, an output range of $\lambda = 1.1\text{--}2.7\ \mu\text{m}$ (0.45–1.1 eV). The photon energy of these output pulses can then be doubled or tripled using second and third harmonic generation by focusing them in a BBO crystal (see Fig. 3.3). This means that we can cover the range of wavelengths in the range $0.34\text{--}2.7\ \mu\text{m}$ (0.45–3.3 eV)

MID-INFRARED GENERATION

Alternatively, the signal output beams of the two OPAs can be combined in a nonlinear GaSe crystal to generate low-frequency radiation using difference frequency generation (DFG) (see Fig. 3.3). DFG is a process that differs from optical parametric amplification only in the initial conditions. Initially, two powerful beams at frequency ω_1 and ω_2 are present with $\omega_2 < \omega_1$. The beam at ω_1 loses power to the beam at ω_2 and a newly generated beam at frequency $\omega_{\text{MIR}} = \omega_1 - \omega_2$. Similar to the situation with optical parametric amplification described in the previous section, we use a type-II angular phase matching process to achieve efficient conversion in the GaSe crystal. The signal outputs have the same polarization and the newly generated beam has a polarization perpendicular to this. By taking signal outputs that are relative close in energy and fulfilling the phase matching condition, the DFG process will generate linearly polarized, carrier-envelope-stable mid-infrared (MIR) pulses [20] with wavelengths in the range $5\text{--}19\ \mu\text{m}$ (65–250 meV). The MIR-pulses are selected by a germanium filter that blocks the OPA output and other residual beams.

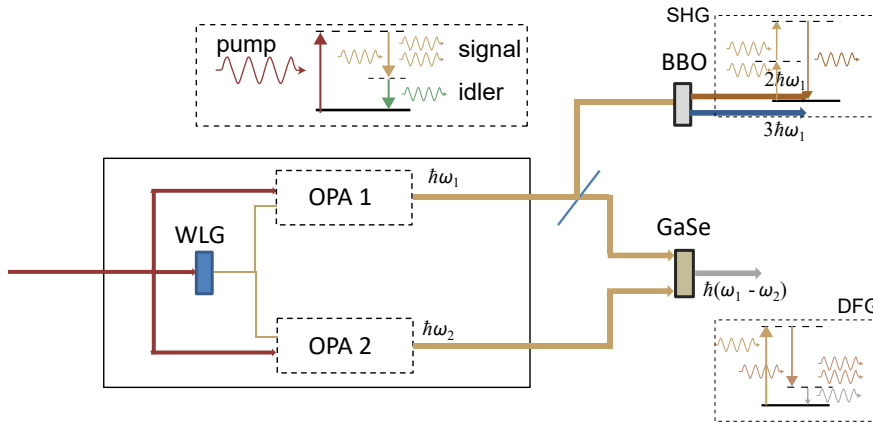


Figure 3.3: **Frequency conversion.** A large fraction of the amplified laser system is used inside the TOPAS twins to pump the two OPAs. A small fraction of the light is used to generate white light (WLG) in a sapphire crystal and sent into the two OPAs. The pulse at the desired wavelength is amplified through optical parametric amplification (see inset) in a β -barium borate (BBO) crystal. The output beams can either be combined to generate MIR-pulses by difference frequency generation (DFG) in a GaSe crystal (see inset), or a single output beam can be doubled or tripled in frequency inside another BBO crystal using second and third harmonic generation (SHG, THG) (see inset).

3.3. DETECTION METHODS

In order to determine the (magneto-)optical response of the sample under study, we track the transient changes in reflection and rotation of the polarization plane of the reflected or transmitted probe pulse (see Fig. 3.4). The pump beam is focused to a spot that is usually a few times larger than the focused probe pulse. The rotation of the polarization plane is determined through a scheme that uses a Wollaston Prism (WP) to split the probe into two orthogonally polarized rays s and p . These rays with intensities I_s and I_p are focused onto the photodiodes D1 and D2 of a balanced amplified silicon photodetector (PDB210A, Thorlabs), which outputs the difference $I^- = I_s - I_p$ and the sum $I^+ = I_s + I_p$. The half-wave plate in front of the WP rotates the polarization plane of the light in order to balance the two beams in equilibrium. The pump-induced difference in intensity I^- is a measure of the rotation $\Delta\theta_F$ or $\Delta\theta_K$ of the polarization of the probe pulse, while the sum provides the total reflected or transmitted intensity. With the time-dependent total transmitted intensity $I_0(t)$ we can expand the signals in the small polarization rotation angle $\Delta\theta_F$:

$$\begin{aligned} I^- &= I_0(t) \cos^2\left(\frac{\pi}{4} + \Delta\theta_F\right) - I_0(t) \sin^2\left(\frac{\pi}{4} + \Delta\theta_F\right) = 2I_0(t)\Delta\theta_F \\ I^+ &= I_0(t) \cos^2\left(\frac{\pi}{4} + \Delta\theta_F\right) + I_0(t) \sin^2\left(\frac{\pi}{4} + \Delta\theta_F\right) = I_0(t). \end{aligned} \quad (3.4)$$

These two output signals can therefore be used to extract the transient polarization rotation $\Delta\theta_F$ and total transmitted or reflected intensity $I_0(t)$.

For more sensitive detection of changes in the intensity of the probe pulse, we use a differential detection scheme. This requires comparison between intensities of the probe pulse reflected by or transmitted through the sample and a stable reference beam. The probe pulse and reference beam are sent to the two different diodes of the balanced amplified photodetector. This gives a typical sensitivity of $\Delta R/R \sim 5 \cdot 10^{-5}$, when measuring for 1 second and the given 1 kHz repetition rate of the system.

MAGNETO-OPTICAL DETECTION

The interaction of light with matter can be affected by the magnetic state of the material, usually characterized by the magnetization. Macroscopically, it can be ascribed to the anti-symmetric off-diagonal components of the dielectric tensor [95]. The Faraday effect and Kerr effect are the two most well-known magneto-optical phenomena that describe changes to light propagating through (Faraday) or reflecting from (Kerr effect) magnetic materials. The Faraday effect causes a rotation of a linearly polarized light beam θ_F , proportional to the projection of the magnetization \mathbf{M} on the direction of propagation \mathbf{k} :

$$\theta_F = V\mathbf{M} \cdot \mathbf{e}_{\mathbf{k}}. \quad (3.5)$$

The Verdet constant V is a material-dependent empirical proportionality constant that depends on the probe wavelength and temperature, $\mathbf{e}_{\mathbf{k}}$ is the unit vector in the direction of wavevector \mathbf{k} . The effect can be understood when looking at the decomposition of the linearly polarized beam into left- and right-circularly polarized components:

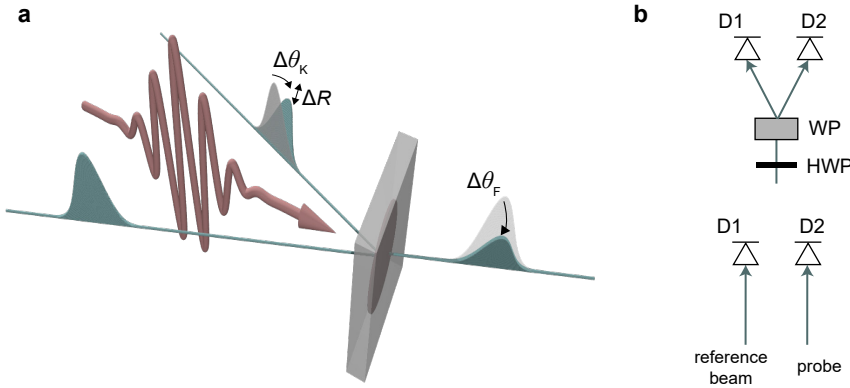


Figure 3.4: **Detecting transient changes in optical properties.** **a**, After excitation with a pump pulse (red), the optical properties of the material can be affected through various mechanisms. The optical probe experiences changes in the reflection ΔR and transmission ΔT and rotation of its polarization. **b**, (top) The small changes in the polarization of the probe pulse are detected in a scheme with a half-wave plate (HWP), Wollaston Prism (WP) and balanced photodiodes D1, D2. (bottom) Transient changes in the reflection are measured by comparing the intensity of the reflected probe with an unaffected reference beam.

$$\mathbf{e}_x = \frac{1}{2} \begin{pmatrix} 1 \\ -i \end{pmatrix} + \frac{1}{2} \begin{pmatrix} 1 \\ +i \end{pmatrix} = \frac{1}{2} \mathbf{e}^+ + \frac{1}{2} \mathbf{e}^-.$$

The different circularly polarized components experience different refractive indices n_{\pm} , which results in rotation of the linear polarization.

The optical anisotropy of a magnetized material also affects the reflection of light from its surface. The different phenomena that arise are generally referred to as the magneto-optical Kerr effect (MOKE). The polar and longitudinal Kerr effect rely on a non-zero projection of the wavevector \mathbf{k} on the out-of-plane (polar Kerr effect) and in-plane (longitudinal Kerr effect) magnetization. These effects can also be ascribed to a different refractive index for oppositely oriented circularly polarized components.

In addition to these well-known effects, there exist several other so-called quadratic magneto-optical effects such as magnetic linear dichroism and magnetic linear birefringence [96].

PHONON DETECTION

After excitation of optically-active vibrational modes, e.g. through stimulated Raman scattering processes, a second time-delayed probe pulse can be coherently scattered by the vibrational distortion. This is most easily understood by considering that the optical Raman-active mode affects the linear susceptibility, due to the phonon-induced change in the electronic polarizability of individual ions [97, 98]. Impulsive excitation of this Raman mode then results in a time-dependent light scattering, which can be experimentally detected either through the effect on the probe pulse spectrum, or by monitoring the transient reflectivity or polarization of the probe.

For a long time it has been known that light can inelastically scatter with thermal acoustic phonons and teach us about the elastic properties of materials, such as the sound velocity [99]. In the 1980s, this technique was brought to the ultrafast timescales, when it was discovered that ultrashort pump laser pulses can generate broadband coherent acoustic wavepackets and time-delayed probe pulses can be used to detect them [69]. Applied to transparent materials, the technique was referred to as picosecond acoustic interferometry [100]. The detection relies on interference between probe light reflected from the surface and light scattered by the propagating acoustic wavepacket in the material. This results in an oscillating intensity of the total reflected light, with a frequency f given by [101]:

$$f = \frac{2nv_s \cos(\theta)}{\lambda}, \quad (3.6)$$

with n the refractive index of the material at the probe wavelength λ , θ the refracted angle of incidence and v_s the speed of sound. More generally, the opto-acoustic detection process relies on interference between the probe pulse and the spatial strain distribution, which gives sensitivity to an acoustic phonon with a wavenumber $k_a = 2k_p$, with k_p the probe wavenumber inside the medium in case of normal incidence and neglecting probe absorption [102]. The frequency of the oscillation in the reflected probe intensity is then equal to the intrinsic frequency of this acoustic phonon.

4

NONLINEAR PHONONICS AND ULTRAFAST STRAIN WAVE GENERATION IN LaAlO_3

"Somewhere, something incredible is waiting to be known."

Sharon Begley

In this chapter we study the concept of nonlinear phononics in the insulator LaAlO_3 , characterised by its large optical bandgap. We give a brief introduction to the linear optical properties of insulating ionic materials close to an infrared(IR)-active phonon resonance and introduce the effects of nonlinear coupling between different phonon modes. We then perform time-resolved all-optical pump-probe experiments to study ultrafast lattice dynamics initiated by impulsive light excitation tuned in resonance with the highest-energy IR-phonon in LaAlO_3 . Aside from the excitation of octahedral rotations, expected within the framework of nonlinear phononics, we observe the generation of propagating longitudinal and transverse acoustic wavepackets. The wavepackets result from anisotropic strain, optically induced by the resonant lattice excitation. The efficient generation of dynamical shear strain close to the phonon resonance hints at the strong connection between optically excited IR-phonons and acoustic deformations and opens excited perspective for ultrafast material control. The observations described in this chapter provide essential insights for the understanding of the ultrafast phonon-induced magnetic phase transition studied in chapter 5 and antiferromagnetic spin-wavepackets, which is the topic of chapter 7.

Parts of this chapter have been published in npj Quantum Materials 5, 95 (2020) by J. R. Hortensius, D. Afanasiev, A. Sasani, E. Bousquet and A. D. Caviglia [103].

DFT calculations were performed by A. Sasani and E. Bousquet

Epitaxy can be used to impose misfit strain capable of altering the properties of materials. Notable examples include the enhancement of ferroelectric and ferromagnetic order [12] and even the engineering of artificial multiferroics at room temperature [104]. Whereas static strain engineering is a well-established paradigm [105–107], ultrafast strain engineering has emerged only recently as an effective method to manipulate functional properties of oxides [71, 108], control collective excitations [52, 109–111], induce changes in the band topology [112, 113] and drive optoelectronic phase switching [114, 115]. The generation of strain pulses traditionally relies on opto-acoustic conversion processes either in the functional material itself or in opto-acoustic transducers, often involving electronic excitation [70] and accompanied by excessive dissipation of coherent heat.

Infrared-active (IR-active) phonons are low-energy elementary excitations of the crystal lattice that can directly couple to electromagnetic waves. Compared to electronic excitation, resonant driving of the phonons thus represents an alternative and more direct route to excite the lattice, avoiding the production of excessive heat and providing applicability in wide-bandgap insulators. This novel approach has gained momentum over the last decade due to a dramatic progress in nonlinear optics allowing for the generation of pulses of mid-infrared radiation with electric field strengths exceeding 100 MV/cm [20]. The mid-infrared pulses, tuned in resonance with the IR-active phonons have proven to be a powerful approach in controlling material properties on ultrashort timescales, with demonstrations of ultrafast insulator-metal transitions [116], melting of magnetic order [56] and most interestingly and controversially: transient superconductivity [35, 36]. In line with static and ultrafast strain engineering, ultrashort pulses of light have also been tuned in resonance with an IR-active atomic vibration of a substrate, in order to transform the structural and electronic properties of an epitaxial thin film [114]. This mechanism, applied extensively to insulating lanthanum aluminate (LaAlO_3) substrates, governs ultrafast metal-insulator transitions [114], ultrasonic magnetic dynamics [117], and sonic lattice waves [118] in various thin films of strongly correlated oxides. However, the nature of the nonlinear lattice dynamics initiated in the substrate material is not yet fully understood.

Most of these and other demonstrations have been subsumed under the umbrella of *nonlinear phononics* [119]. This is a qualitative description, starting from the concept of Ionic Raman scattering [120, 121], in which the excitation of an IR-active phonon mode results in a sub-picosecond lattice distortion along the coordinate of a coupled Raman mode. It is this transient displacement along a Raman coordinate that has been identified as the crucial effect that underlies the observed control of functional collective properties after resonant phonon excitation [35, 36, 116, 119, 122].

In this chapter we study the concept of nonlinear phononics in the wide-bandgap insulator LaAlO_3 . We begin with a quick overview of the concept of nonlinear phononics [119]. We describe the optical properties of insulating materials close to IR-active phonon resonances and introduce the methodology of nonlinear phonon-phonon coupling. We then proceed to show that in LaAlO_3 , impulsive optical excitation at the photon energy tuned in resonance with a polar stretching of the Al-O bonds drives a non-polar rotational mode of oxygen octahedra via ionic Raman scattering. The resonant lattice ex-

citation also induces anisotropic strain, which generates propagating longitudinal and transverse acoustic wavepackets. Importantly, shear strain wavepackets are found to be produced with extraordinary efficiency close to the phonon resonance. These results uncover an hitherto unknown microscopic feature of ultrafast strain engineering that opens wide perspectives for material control via optically tunable strain.

4.1. NONLINEAR PHONONICS

4.1.1. PHONON-POLARITONS AND OPTICAL PROPERTIES

Transverse IR-active optical phonons can interact with transverse electromagnetic waves. When the electromagnetic waves and the phonon mode are close in frequency, this interaction will have a profound effect on the way these electromagnetic waves travel through the material. This is reflected in the material's optical properties close to the phonon resonance frequency.

IR-active phonons can be considered as quantized, charged harmonic oscillators [123] with mass M , resonance frequency ω_T and effective charge Q . We assume that these charged harmonic oscillators are not damped and evenly distributed in the (isotropic) material and can find the displacement \mathbf{u} in response to a spatially (coordinate \mathbf{r}) and temporally (time t) varying electric field $\mathbf{E}(\mathbf{r}, t) = \mathbf{E}_0 e^{i(\mathbf{k}\cdot\mathbf{r} - \omega t)}$ with wavenumber \mathbf{k} through the oscillator's equation of motion

$$M \frac{d^2 \mathbf{u}}{dt^2} = -M\omega_T^2 \mathbf{u} + Q\mathbf{E}. \quad (4.1)$$

Here \mathbf{k} is the wavenumber of the plane wave electric field. Since all charged harmonic oscillators have the same displacement \mathbf{u} , they produce a macroscopic polarization

$$\mathbf{P} = NQ\mathbf{u}, \quad (4.2)$$

with N the density of harmonic oscillators. The displacement vector \mathbf{D} of the material is given by

$$\mathbf{D} = \epsilon_0 \mathbf{E} + \mathbf{P} = \epsilon_0 \epsilon \mathbf{E}, \quad (4.3)$$

where ϵ is called the dielectric function of the material. This gives for the contribution of the crystal lattice to the dielectric function [123]

$$\epsilon_l = 1 + \frac{NQ^2}{\epsilon_0 M(\omega_T^2 - \omega^2)}, \quad (4.4)$$

Aside from interacting with the crystal lattice, electromagnetic waves can also interact with the valence electrons. In order to account for these valence electrons, we introduce their contribution to the dielectric function $\epsilon_e(\omega)$. Assuming that the bandgap E_b is much larger than the energy of the radiation $\hbar\omega$ close to the phonon energy, the radiation field appears to be static ($\omega = 0$) for the valence electrons. This means that the electronic contribution $\epsilon_e(\omega)$ can be approximated by $\epsilon_e(0)$. In the region of frequencies with $\omega_T \ll \omega \ll E_b/\hbar$, the radiation field oscillates too fast for the lattice resonances to respond ($\epsilon_l \rightarrow 1$) and the total dielectric function ϵ is then constant and defined to be $\epsilon = \epsilon_l + \epsilon_e := \epsilon_\infty$. This is called the high-frequency dielectric constant, since it is the value

at frequencies much higher than the phonon resonance frequency ω_T . Including this value in the total dielectric function we obtain for $\omega \ll E_b/\hbar$ [123]:

$$\epsilon(\omega) = \epsilon_\infty + \frac{\omega_T^2(\epsilon_{st} - \epsilon_\infty)}{\omega_T^2 - \omega^2}. \quad (4.5)$$

Here we introduced the variable $\epsilon_{st} := \epsilon(0)$, the low-frequency dielectric constant. Generalized to a collection of phonon modes (charged harmonic oscillators) with different resonance frequencies, the different contributions to the dielectric function of the form Eq. 4.5 will add up. Note that this model neglects any dissipation as we started with an ideal, undamped harmonic oscillator (Eq. 4.1).

4

With the dielectric function at hand, we can now consider the Maxwell equations to calculate the material's optical response close to the phonon frequency. First we consider the electric displacement \mathbf{D} which satisfies

$$\nabla \cdot \mathbf{D} = 0 \quad (\epsilon(\mathbf{k} \cdot \mathbf{E}_0) = 0). \quad (4.6)$$

This equation has two solutions

1. Transverse field ($\mathbf{k} \cdot \mathbf{E}_0 = 0$)

This implies that the electric field is perpendicular to the wavevector. The response of the phonons (charged harmonic oscillators) is then given by the dielectric function $\epsilon(\omega)$. The resonance frequency of the medium equals the resonance frequency ω_T of the phonon.

2. Longitudinal field ($\mathbf{k} \parallel \mathbf{E}_0$ or $\epsilon = 0$)

When $\mathbf{k} \cdot \mathbf{E}_0 \neq 0$, $\epsilon(\omega)$ needs to vanish in order to satisfy Eq. 4.6. Using Eq. 4.5, we see that this is the case at the frequency ω_L , defined by:

$$\omega_L^2 = \omega_T^2 \frac{\epsilon_{st}}{\epsilon_\infty}. \quad (4.7)$$

PHONON-POLARITONS

In order to proceed and obtain the dispersion curve of a coupled light wave and lattice vibration, we need to consider all four Maxwell equations in an insulating non-magnetic medium. We consider transverse electromagnetic plane wave solutions (wavevector \mathbf{k} , $k = |\mathbf{k}|$) with electric components $\mathbf{E}(\mathbf{r}, t)$ and magnetic component $\mathbf{H}(\mathbf{r}, t)$. The Maxwell equations lead to the relation [123]:

$$k^2 = \omega^2 \epsilon, \quad (4.8)$$

the dispersion of a transverse electromagnetic wave in a lossless, non-magnetic medium. Now substituting the expression for the dielectric constant (Eq. 4.5) gives the following relation between wavenumber k and frequency ω :

$$k^2 = \omega^2 \left(\epsilon_\infty + \frac{\omega_T^2(\epsilon_{st} - \epsilon_\infty)}{\omega_T^2 - \omega^2} \right). \quad (4.9)$$

Rewriting this relation gives a fourth order equation in ω with a solution given by [124]:

$$\omega^2 = \frac{\omega_T^2 \epsilon_{st} + c^2 k^2}{2\epsilon_\infty} \pm \frac{1}{\epsilon_\infty} \sqrt{\left(\frac{\omega_T^2 \epsilon_{st} + c^2 k^2}{2}\right)^2 - c^2 k^2 \omega_T^2 \epsilon_\infty} \quad (4.10)$$

The two positive solutions to this equation form the coupled *phonon-polariton* dispersion relation (frequency ω as function of wavenumber k), shown in Fig. 4.1. For every wavenumber k , there are two solutions for ω , giving two dispersion branches. The two branches originate from the ‘original’ photon and phonon dispersion; the coupling leads to an avoided crossing and the frequencies are altered. It is important to note that this plot only depicts a very small part of the Brioullin zone, so we can consider $k \approx 0$ at the avoided crossing. Without the phonon resonance, the photon dispersion would be given by $\omega = \frac{c}{\sqrt{\epsilon_\infty}} k$, determined by the contribution from the valence electrons and propagating at velocity $\frac{c}{\sqrt{\epsilon_\infty}}$. The phonon-polariton dispersion converges to this dispersion for large k and ω : light at frequencies much higher than the phonon resonance frequency is not affected by the phonon. Interesting to see is that the phonon also affects the polariton dispersion for $\omega \ll \omega_T$, where the photon-like dispersion shows a velocity of $\frac{c}{\sqrt{\epsilon_{st}}}$. As $k \rightarrow 0$, the upper branch converges to the constant value ω_L . For large k , the lower branch converges to the constant value ω_T and there are no solutions for $\omega_T < \omega < \omega_L$. This remarkable result indicates that light with these frequencies cannot propagate into the material, which leads to a high reflection, as we will see below.

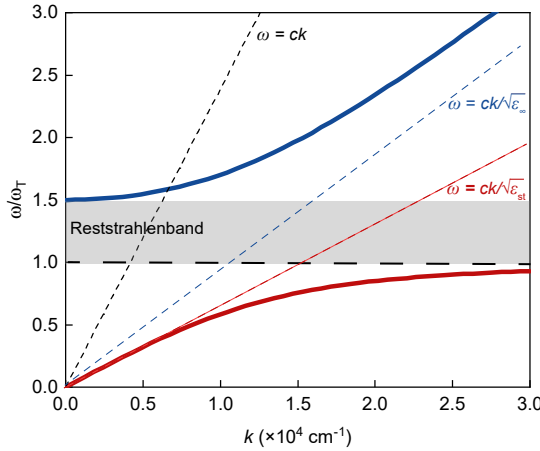


Figure 4.1: **Phonon-polariton dispersion.** Schematic diagram of the dispersion curves of the uncoupled light wave (black small-dashed line) and transverse optical phonon (large-dashed line at $\omega = \omega_T$). The coupling leads to the phonon-polariton dispersion, consisting of an upper- and lower-polariton branch (solid lines). The blue dashed line, indicating the $\omega = ck/\sqrt{\epsilon_\infty}$ indicates the dispersion of light in the medium without any coupling to the IR-active phonon. The red dashed line ($\omega = ck/\sqrt{\epsilon_{st}}$) indicates the combined effect of electrons and phonons on electromagnetic waves with low frequencies. Parameters: $\frac{\epsilon_\infty}{\epsilon_{st}} = 1.5^2$.

LATTICE ABSORPTION AND REFLECTION

In figure 4.1 we see that for frequencies $\omega_T < \omega < \omega_L$, there are no solutions to the wave equation in the material. This is exactly the region where $\epsilon(\omega) < 0$. We now proceed to study the linear optical properties of the material close to this region.

We add a damping term $\gamma \frac{du}{dt}$ to the equation of motion (Eq. 4.1) for the charged harmonic oscillators (phonons). This changes the expression for the dielectric constant (Eq. 4.5), which then becomes complex, into

$$\begin{aligned}\epsilon(\omega) &= \epsilon_1(\omega) + i\epsilon_2(\omega) \\ &= \epsilon_\infty + \frac{\omega_T^2(\epsilon_{st} - \epsilon_\infty)}{\omega_T^2 - \omega^2 - i\gamma\omega}\end{aligned}\quad (4.11)$$

The linear optical response of the material is best captured by considering the complex refractive index $\tilde{n}(\omega) = n(\omega) + i\kappa(\omega) = \sqrt{\epsilon(\omega)}$. The real part n determines the speed of light in a material (c/n), while the imaginary part κ is directly related to the absorption coefficient α by $\alpha = \frac{4\omega\kappa(\omega)}{c}$. By equating the real and imaginary parts, we see that the dielectric permittivity and the refractive index are related by

$$\begin{aligned}\epsilon_1 &= n^2 - \kappa^2 \\ \epsilon_2 &= 2n\kappa\end{aligned}\quad (4.12)$$

These relations can be inverted to calculate the complex refractive index from the dielectric permittivity. The real and imaginary part of \tilde{n} are shown in Fig. 4.2a. We see that the imaginary part κ peaks at the phonon resonance frequency ω_T , which means that the optical absorption is largest. In the region $\omega_T < \omega < \omega_L$, the real part n is very close to 0.

The reflectivity R of the material, is calculated from the complex refractive index as

$$R = \left| \frac{1 - \tilde{n}}{1 + \tilde{n}} \right|^2 \quad (4.13)$$

and plot in Fig. 4.2b for different values of the damping constant γ . The reflectivity rises from nearly 0 at ω_L to nearly $R = 1$ at ω_T . This region with high reflectivity is called the *Reststrahlenband*.

4.1.2. NONLINEAR COUPLING

In the previous section, we considered the phonons as quantized charged harmonic oscillators. This Lorentz model of an oscillator allowed us to derive the linear optical properties of a material close to a phonon resonance. In present-day experiments, ultrashort pulses of light with frequencies in the 15–50 THz range can be generated by commercially available technology (see chapter 3). These pulses of light can resonantly excite lattice vibrations to large amplitudes in oxide materials [116, 119]. In response to these short intense laser pulses, the phonon dynamics becomes nonlinear, and anharmonic contributions start to play a role [122]. This allows to excite Raman-active phonons via scattering with IR-active phonons, a mechanism that was proposed more than 50 years ago [120, 121] and coined ionic Raman scattering (IRS). This process is comparable to impulsive stimulated Raman Scattering (ISRS), but in this case the IR-active phonons rather than electronic states serve as the intermediate states for Raman

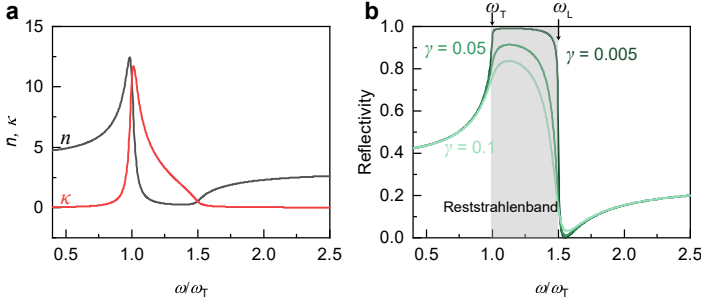


Figure 4.2: **Linear optical properties close to the phonon resonance.** **a, b,** Plot of the real (n) and imaginary (κ) part of the refractive index \tilde{n} (**a**) and the resulting reflectivity R of the material (**b**). For small damping, nearly all light in the frequency range between ω_T and ω_L is reflected. Parameters: $\gamma/\omega_T = 0.05$ (refractive index), $\epsilon_{st} = 4.5^2, \epsilon_\infty = 3^2$.

scattering. This means that the effect is mediated by phonon-phonon coupling instead of electron-phonon coupling.

In order to describe the nonlinear coupling between different phonon modes, we consider the potential energy surface of the material in terms of the displacement along both infrared-active (IR) and Raman-active (R) phonon coordinates Q_i , $i = \text{IR, R}$. We use a simple model with a single IR-active and R-active mode, with resonance frequencies ω_T and ω_R respectively, and investigate the effect of coupling between these modes. Important to note is that in this thesis we only consider centrosymmetric materials, which indeed allows us to make a distinction between odd-parity infrared-active modes and even-parity Raman-active modes. First considering only the IR-active mode, the potential energy can be expanded as function of the parameter Q_{IR} :

$$U_{\text{IR}} = \frac{1}{2}\omega_T^2 Q_{\text{IR}}^2 + \alpha Q_{\text{IR}}^3 + \beta Q_{\text{IR}}^4 + \dots, \quad (4.14)$$

where ω_T is the phonon transverse optical resonance frequency and α and β are the material- and mode-specific expansion coefficients.

A very similar expansion can be made for the potential energy in terms of the displacement along the coordinate of the Raman-active mode. Now including anharmonic phonon-phonon interactions, the potential surface energy becomes

$$U(Q_{\text{IR}}, Q_{\text{R}}) = \frac{1}{2}\omega_T^2 Q_{\text{IR}}^2 + \frac{1}{2}\omega_R^2 Q_{\text{R}}^2 - c Q_{\text{R}} Q_{\text{IR}}^2 + \dots \quad (4.15)$$

Here we ignore terms quadratic and higher-order in Q_{R} , as only the IR-driven mode can be resonantly excited by the laser pulse and driven to large amplitudes. As the material is centrosymmetric, the cubic anharmonic coupling $c Q_{\text{R}} Q_{\text{IR}}^2$ is the lowest order coupling term that is allowed by symmetry. Moreover, the existence of this term imposes additional restrictions on the symmetry of the modes. The coupling is only symmetry-allowed when the product of the irreducible representations Γ_i of the phonon modes contains the totally symmetric representation of the crystal's point group [122, 125, 126]: $[\Gamma_{\text{IR}} \times \Gamma_{\text{IR}}] \times \Gamma_{\text{R}} \supset \text{A}_{1g}$. In practice, this has some important consequences. A

non-degenerate IR-mode can only couple to a totally symmetric Raman mode. When two IR modes are excited simultaneously, or when the IR-mode is (doubly) degenerate, coupling to other Raman modes becomes possible [126].

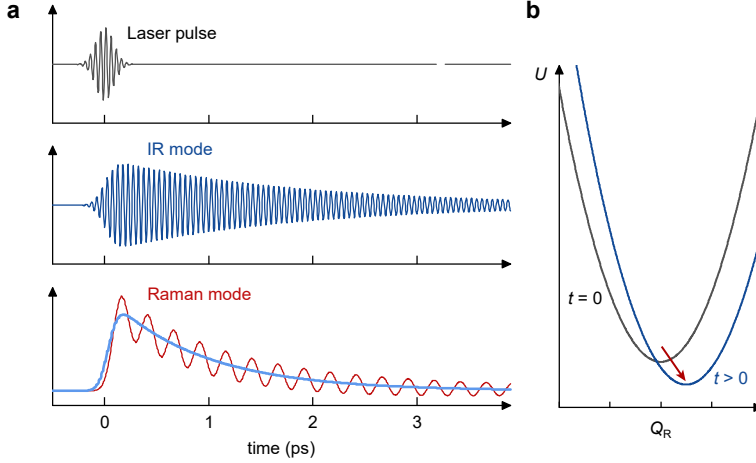


Figure 4.3: **Nonlinear phononics.** **a**, An ultrafast laser pulse (top panel) tuned in resonance with an IR-active phonon can drive the IR-mode to large amplitudes (middle panel). As a result of nonlinear coupling, a coupled Raman mode will oscillate around a displaced equilibrium (bottom panel). **b**, Total energy as function of the Raman mode amplitude before ($t = 0$) and shortly after ($t > 0$) excitation of the IR-mode. Figure inspired by [127].

Given that the coupling is allowed, this energy term can result in a force F_R on the Raman-mode, as $F_R = -\frac{\partial U}{\partial Q_R}$. The force from the laser field that drives the IR-mode is given by $F_I = F \sin(\omega_L t) e^{-\frac{t^2}{2\sigma^2}}$, with F the amplitude, ω_L the driving frequency and σ the duration of the light pulse. The equations of motion for the two modes (including damping) are then given by

$$\begin{aligned} \frac{d^2 Q_{IR}}{dt^2} + \gamma_{IR} \frac{dQ_{IR}}{dt} + \omega_T^2 Q_{IR} &= 2cQ_R Q_{IR} + F_I(t) \\ \frac{d^2 Q_R}{dt^2} + \gamma_R \frac{dQ_R}{dt} + \omega_R^2 Q_R &= cQ_{IR}^2. \end{aligned} \quad (4.16)$$

The term $2cQ_R Q_{IR}$ can often be ignored, as it is very small compared to the driving field. The solutions to Eqs. 4.16 are shown in Fig. 4.3a. The ultrashort laser pulse resonantly drives the IR-active mode. The Raman mode experiences an effective forcing field cQ_{IR}^2 , which has a rectified, non-zero average value. This rectified component is proportional to the envelope of the IR-displacement and causes a transient displacement along the coordinate of the Raman mode. In the impulsive limit, when the displacive force rises quickly compared to the Raman mode frequency ω_R , the Raman mode starts oscillating around a displaced position. The displaced position, which signals a deformed lattice structure, survives for the duration of the lifetime of the IR mode. The displacement can also be visualized in terms of a transient energy potential surface as function

of the Raman coordinate Q_R , where the potential is changed due to the effective force provided by the coupling to the driven IR mode (see Fig. 4.3b). The transient potential has a minimum at a different position from the equilibrium potential.

4.2. ULTRAFAST LATTICE EXCITATION IN LaAlO₃

We investigate light-induced structural dynamics in LaAlO₃, an insulating substrate utilized extensively in oxide electronics for the epitaxy of correlated materials, including high- T_c cuprate superconductors [128], magnetoresistive manganites [129] and nickelates [130]. At room temperature, LaAlO₃ exhibits a distorted perovskite structure (rhombohedral space group $R\bar{3}c$, see Fig. 4.4a). To resonantly drive the lattice vibrations in (001) LaAlO₃ single crystals, we use ultrashort pump pulses in the mid-IR frequency range. We tune the photon energy of the pump pulses continuously across the closely lying highest-frequency E_u and A_{2u} infrared-active phonon resonances [131, 132]. Schematics of the atomic motion corresponding to the E_u and A_{2u} mode are shown in Fig. 4.4b and Fig. 4.10. The energy was tuned in the experimentally accessible range of 70–180 meV (17–41 THz) and allowed us to compare dynamics excited in the optical transparency window (> 130 meV) with structural transient dynamics induced by pulses tuned in resonance with the lattice vibrational modes centered at 81 meV. A high efficiency of ionic Raman scattering is anticipated in LaAlO₃ as mutual coupling between optical phonon modes exists and even results in a small negative Lyddane-Sachs-Teller splitting between longitudinal and transversal optical modes [133]. The large bandgap of LaAlO₃ (5.6 eV [134]) as well as the absence of electronic in-gap states [135] ensures the purely structural nature of the photoinduced response.

To track the ensuing dynamics of the lattice, time-resolved optical reflectivity and birefringence measurements are performed using near-infrared probe pulses. The two complementary experimental techniques are schematically illustrated in Fig. 4.4c. In the first scheme we monitor the transient differential reflectivity ΔR . The structural dynamics initiated by the pump pulse modulate the sample's dielectric function resulting in a perturbation of the refractive index n , which is imprinted on the ΔR signal. In the second scheme we track the transient optical birefringence $\Delta\theta_B$. The phonon modes of LaAlO₃ are intrinsically highly anisotropic, meaning that coherent dynamics of these modes can also modify the off-diagonal components of the permittivity tensor, thereby resulting in a transient birefringence.

4.3. PHOTO-INDUCED STRUCTURAL DYNAMICS

Measurements of transient changes to both the reflectivity and birefringence, using pump pulses at the photon energy tuned in resonance with the infrared-active phonon modes, $h\nu \approx 85$ meV (21 THz), reveal multiple oscillatory responses at frequencies significantly below the one of the pump, see Fig. 4.5a,b. The highest-frequency oscillation is centered at 1.1 THz and is assigned to the Raman-active E_g soft mode of LaAlO₃ [132, 136] associated with a rhombohedral instability of the $R\bar{3}c$ lattice structure (see section 4.8.1). This mode comprises rotations of the oxygen octahedra around an axis perpendicular to the [111] pseudocubic direction as shown in Fig. 4.5c. The longer time delay further reveals oscillatory components at two discrete frequencies f_{TA} and f_{LA} in the GHz fre-

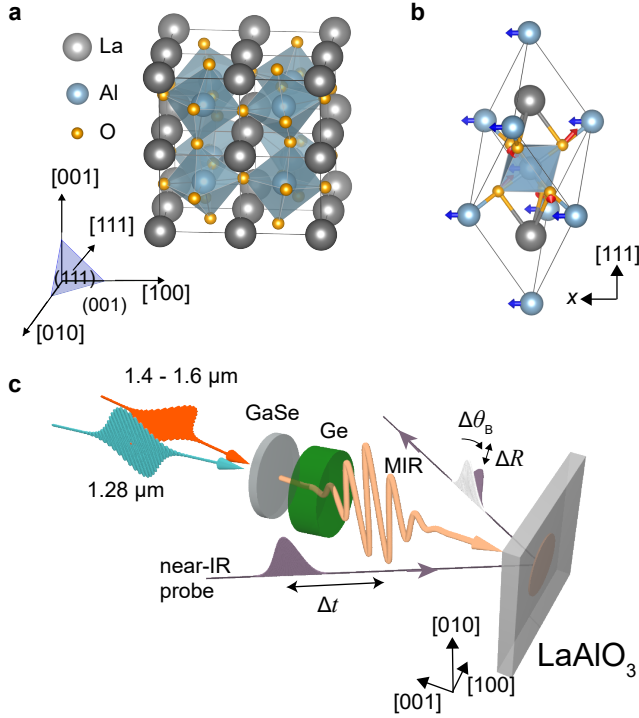


Figure 4.4: **Crystal structure and experimental geometry.** **a**, The crystal structure of LaAlO_3 , with indications of the different crystallographic directions. The rhombohedral distortion from the high-temperature cubic phase is due to out-of-phase rotations of the oxygen octahedra about the $[111]_{\text{pc}}$ axis. **b**, Atomic motion corresponding to the infrared-active E_u stretching mode, polarized in the (111) plane in the x -direction. **c**, Schematic illustration of the experimental scheme. The mid-IR pulse is generated by difference frequency mixing of two near-infrared pulses in a GaSe crystal, after which the mid-IR pulses are filtered by a germanium (Ge) filter. Following the mid-IR excitation, the transient changes in optical properties are probed with a time-delayed near-infrared pulse ($\lambda = 800 \text{ nm}$, $h\nu = 1.55 \text{ eV}$). The pump-induced changes to the reflection intensity ΔR and rotation $\Delta\theta_B$ of the polarization plane are monitored.

quency range. This pattern originates from interference between light pulses reflected at the crystal surface and reflections from an acoustic wavefront propagating into the bulk (Fig. 4.5d). In transparent materials, the frequency of the oscillations f is related to the refractive index n of the material at the probe wavelength [135], the speed of sound v_s , the angle θ w.r.t. the sample normal and the wavelength λ of the probe by the relation [101] $f = 2nv_s \cos(\theta)/\lambda$. In our experiments we vary the angle of incidence of the probe beam and find that, while the frequency of the E_g mode remains unchanged, the frequency of the GHz oscillations decreases in agreement with the relation shown above. We extract the corresponding propagation velocities, obtaining $v_{\text{LA}} = 6.67 \text{ km/s}$ and $v_{\text{TA}} = 4.87 \text{ km/s}$, and find that they match the speed of longitudinal acoustic (LA) and transverse (TA) phonons in LaAlO_3 propagating in the $[001]$ direction [137]. This acousto-optic conversion is strongly peaked at a phonon wavenumber k_a determined by the probe wavenumber [102]. This experiment is sensitive to a specific frequency

component of the generated strain pulse at $k_a = 3.2 \cdot 10^5 \text{ cm}^{-1}$. Our experiments show that optical excitation with ultrashort resonant mid-IR pulses initiates coherent structural dynamics in both the acoustic and optical branches of the phonon spectrum. Although the optical excitation of a broadband longitudinal acoustic wavefront is expected from electrostriction in LaAlO_3 [138] and/or optical absorption [70], the optical generation of shear strain requires the presence of an equilibrium or light-induced structural anisotropy. We discuss this aspect below, after the analysis of the THz Raman-active mode.

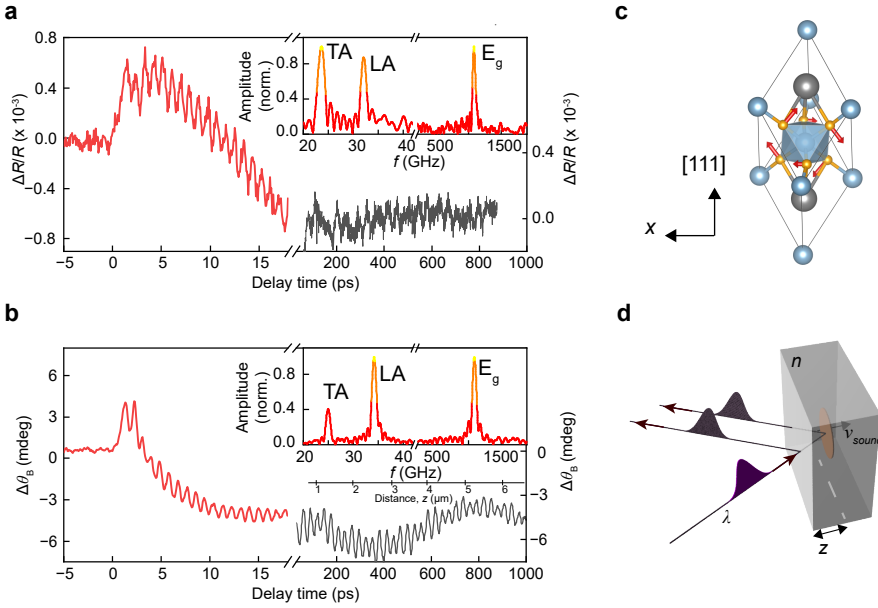


Figure 4.5: **Photo-induced structural dynamics.** **a, b**, Transient changes in the intensity of the reflected 1.5 eV probe pulse $\Delta R/R$ (**a**) and the polarization rotation $\Delta\theta_B$ of the probe pulse (**b**) after excitation of the LaAlO_3 substrate with a mid-infrared pump pulse of 86 meV (**a**) and 89 meV (**b**) and a fluence of $10 \text{ mJ}/\text{cm}^2$ ($T = 10 \text{ K}$). The insets show the Fourier spectra of the signals. The top axis in (**b**) shows the distance z which the longitudinal sound wave has travelled at that time. **c**, The real-space atomic motion corresponding to the excited E_g mode indicated with arrows. **d**, A schematic picture of a strain wave propagating with speed v_{sound} leading to interference between probe light (wavelength λ) reflected at the interface and scattered at the strain wave, depending on the distance z that the strain wave has propagated.

4.4. COHERENT OXYGEN OCTAHEDRA ROTATIONS

In our experiments only the lowest-energy Raman-active E_g optical phonon mode was observed. The frequencies of the remaining higher-energy modes (e.g. of A_g symmetry) lie outside the bandwidth of our excitation pulses and thus cannot be excited in the experiment. To unveil the mechanism of excitation of the E_g mode, we vary the pump photon energy across the phonon absorption band. Fig. 4.6a compares time-resolved transient reflectivity $\Delta R/R$ induced by pumping close to the phonon resonance

($h\nu = 85$ meV) with off-resonant pumping ($h\nu = 124$ meV), revealing a striking selectivity of the low-energy mode excitation. The inset in figure 4.6a shows that the amplitude of the excited Raman E_g mode measured for various pump photon energies increases strongly and peaks at 95 meV close to the absorption peak attributed to the E_u phonon mode centered at 81 meV.

Recently, ionic Raman scattering (IRS) or nonlinear phononics, was proposed as a mechanism to resonantly and nonthermally activate coherent low-energy Raman-active (nonpolar) phonon modes upon exciting infrared-active (polar) lattice vibrations [119]. This mechanism relies on the anharmonicity of the lattice potential, which leads to a nonlinear response when large-amplitude infrared-active ionic vibrations Q_{IR} are excited. The anharmonicity causes a short-living net distortion of the lattice along a Raman coordinate Q_R accompanied by coherent oscillations of the corresponding Raman-active mode around this displaced metastable position (see Fig. 4.3a). In the general case the nonlinear coupling can be described by introducing an invariant nonlinear term $\alpha' Q_{IR}^2 Q_R$ in the lattice potential, with α' defining the strength of the coupling and Q_R corresponding to the normal coordinate of a Raman phonon mode. Despite the strong correlation between the phonon absorption and the E_g mode amplitude, we note that the largest amplitude is observed at a pump photon energy shifted from the peak of the linear phonon absorption. Moreover, the lineshape of the amplitude as function of the pump photon energy is significantly broader than the linear absorption. These observations indicate that the excitation of the E_g mode is more efficient at the reststrahlen band, where the absorption processes are not dominant and the optical response of the medium is non-dissipative.

To verify and study this nonlinear coupling in the specific case of LaAlO_3 , we perform a symmetry analysis and density functional theory (DFT) calculations with the ABINIT code [139] to fit a nonlinear phonon-phonon model potential of bulk $R\bar{3}c$ LaAlO_3 (see section 4.7 and section 4.8.2). The DFT calculations show that the coupling between the A_{2u} and E_g mode is negligible and confirm a strong coupling between the E_u and E_g mode. In the case of rhombohedral LaAlO_3 , with a high-symmetry three-fold rotation axis along the pseudocubic [111] direction, the IR-active E_u mode has two orthogonal components (E_u^x, E_u^y) oriented in the natural rhombohedral plane (pseudocubic (111)) (see inset Fig. 4.4a for a schematic including the different orientations). The coupling term is given by $\alpha' = \alpha \cos(2\theta)$, with α a material-dependent constant and θ the angle between the laser polarization projected onto the (111) plane and the x -component of the E_u mode.

In Fig. 4.6c we show the DFT results for the evolution of the effective coupling coefficient α' with respect to the pump polarization angle ϕ , oriented in the (001) plane, such that $\phi = 0$ corresponds to the pump polarization oriented along the [100] axis. In order to calculate the coupling constant α' , the laser polarization in the pseudocubic (001) plane needs to be projected on the (111) plane. As a result α' evolves as a non-trivial periodic function with extrema around $\phi = 0^\circ$ and 112.5° (see section 4.8.2). To verify this behavior, we measured the amplitude of the E_g oscillation for the pump polarization plane oriented along several pseudocubic crystallographic directions, as shown in Fig. 4.6b.

Figure 4.6c summarizes the observations, showing a good agreement with predictions of the nonlinear phonon model built from DFT. Together with the dependence on the pump photon energy, this confirms that excitation of the E_g Raman-active mode is governed by the IRS mechanism. Moreover, these selection rules are another strong indication that these lattice dynamics are not driven by the absorption, but are rather non-dissipative and rely on the resonant enhancement of the scattering process [119]. The relevance of this mechanism is further corroborated by measurements of the fluence dependence of the oscillation amplitude (see figure 4.12), revealing a linear increase in the E_g mode amplitude [28]. These findings are therefore a clear manifestation of the efficient nonlinear phononics mechanism in a wide bandgap insulator in conditions promoting exclusively coherent phonon-phonon coupling. In this sense IRS differs substantially from regular impulsive stimulated Raman scattering (ISRS) in which excitation of coherent phonons is mediated by virtual electronic transitions [28]. Note that the observation of the net structural distortion along the E_g coordinate responsible for the oscillations is not feasible in an all-optical experiment alone and requires use of time-resolved X-ray diffraction [140].

4.5. TUNABLE SHEAR STRAIN

The Fourier analysis (FFT) of the light-induced coherent strain waves as a function of the pump photon energy is summarized in Fig. 4.7a. We observe that acoustic waves are excited both in the optical transparency window, and in the reststrahlen band. The inset of Fig. 4.7a shows that upon reaching the reststrahlen band, the amplitudes of both strain waves experience a pronounced growth indicating an enhancement at the phonon resonance. The dependence of the strain waves on the pump fluence and polarization are given in section 4.8.3. The relation between the resonant excitation of IR-active phonons and the generation of macroscopic strain [142] and strain wavepackets has been an understudied subject.

Conventionally, the generation of strain in the transparency window is described by electrostriction [70, 143], even though there exist only a few experimental observations of this mechanism [144]. Large static electrostriction effects have been found in the case of thin LaAlO_3 films on SrTiO_3 [138]. In this regard the observation of strain waves after excitation in the transparency window is a remarkable observation, but can still be explained by electrostriction. In principle, the enhancement of the TA and LA mode amplitudes close to the phonon resonance could simply originate from an increased photon absorption and the anisotropic elastic response of [001] LaAlO_3 , as this crystal cut is different from the high-symmetry [111] direction, providing a coupling between shear and transversal strain. However, analyzing the strain wave amplitudes, we observe that the presence of the phonon resonance also dramatically renormalizes the ratio r between the amplitudes of the TA and LA modes (see Fig. 4.7b). Our experiments indicate that while their ratio r is around 0.2 in the transparency window, it shows a pronounced increase up to 2 in the reststrahlen band. As seen in the inset of Fig. 4.7a, the renormalization is due to a strong enhancement in the generation of the TA strain wave, which seemingly occurs at the expense of the LA phonon mode. Such an evolution of the ratio with photon energy cannot be explained by direct TA mode excitation via dissipative effects due to an increased photon absorption, especially as the peak of the ratio does not

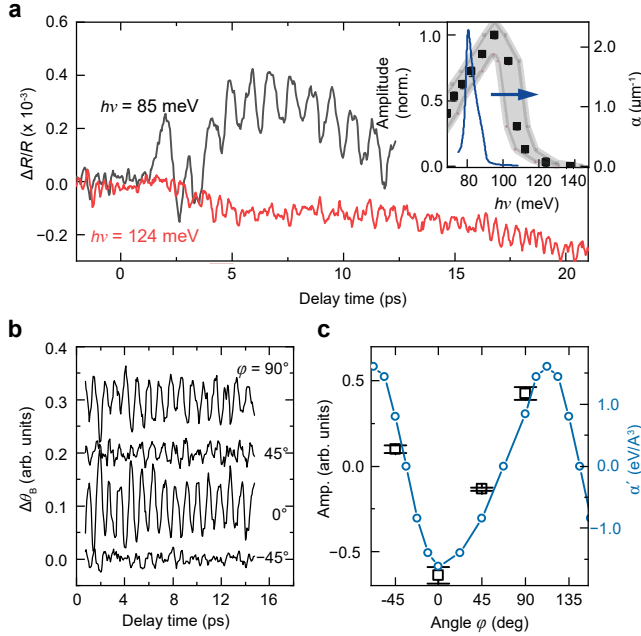


Figure 4.6: **Light-induced excitation and dynamics of oxygen octahedra rotations.** **a**, Time resolved reflectivity changes of the probe pulse after mid-IR excitation at different photon energies. Inset: the amplitude of the coherent phonon oscillations at 1.1 THz, as extracted from fitting an exponentially damped sine function to the transient reflectivity changes for different pump photon energies. The thick blue solid line indicates the linear absorption due to the E_u phonon mode, data taken from Ref. [114, 141]. The spectral full width at half maximum of the excitation pulses is indicated by the shaded band. **b**, Time-resolved transient polarization rotation of the probe pulse after excitation with the pump pulses with a changing polarization of ϕ degrees with respect to the pseudocubic [100] axis (pump: $h\nu = 89$ meV). **c**, Amplitude of the observed E_g mode excitation (square markers) as extracted by fitting sine functions to the data in (b) and DFT calculated coupling of the excited phonons to the E_g mode (blue circles) vs pump polarization angle ϕ with a sine fit. The error bars account only for the uncertainty of the fit.

coincide with the phonon absorption peak. Strikingly, the ratio peaks at a higher photon energy, comparable to the position of the maximum amplitude of the E_g mode (see inset Fig. 4.6a). We propose that this relative and absolute increase in TA mode generation is the result of a phonon-driven enhancement of the coupling between TA and LA modes, in combination with an ionic enhancement of the electrostriction [142]. In section 4.8.2 we quantify the elastic constants of LaAlO_3 using DFT and show that, out of equilibrium, the distortion along the E_g Raman coordinate driven by the rectification of the phonon field, alters the off diagonal elastic constants. This change of elastic constants shows that the anisotropic E_g mode can transfer longitudinal strain into shear strain.

4.6. CONCLUSIONS

Using a combination of time-resolved reflectivity and polarimetry we have studied coherent structural dynamics in LaAlO_3 induced by ultrashort excitation of a selected IR-

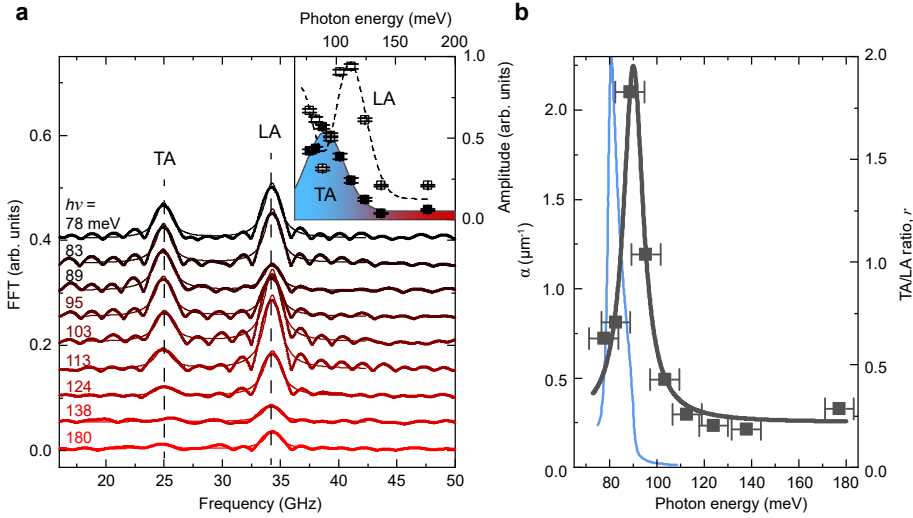


Figure 4.7: **Tunable shear strain.** **a**, Fourier transforms of the measured polarization rotation signals corresponding to strain wave propagation after excitation with different pump energies. Inset: Pump photon energy dependent amplitude of the two oscillations corresponding to LA and TA strain waves for fixed pump and probe polarizations as obtained from the Fourier transforms shown in panel a. The solid and dashed lines are guides to the eyes. The errorbars account for the uncertainty of the fit. **b**, Linear absorption due to the infrared active phonon modes, as taken from Ref. [114] (left axis) and ratio r of the TA and LA mode amplitudes (right axis) vs photon energy at constant incident fluence. The black line serves as a guide to the eye. The spectral full width at half maximum of the excitation pulses is indicated by the errorbars.

active phonon mode. Our experimental and theoretical analysis uncovers a previously unknown remarkable feature associated with the excitation of the crystal lattice. In addition to the displacement along a Raman coordinate and coherent THz atomic vibrations, expected within a nonlinear lattice excitation regime, we observe an efficient generation of shear strain wavepackets. Shear strain following resonant pumping of the crystal lattice in LaAlO_3 is likely to be a key element of the metal-insulator transitions, ultrasonic magnetic dynamics and sonic lattice waves observed in recent years. Importantly, the ratio between the longitudinal and transversal strain waves can be tuned by the pump photon energy in vicinity of the phonon resonance, which hints at a close relation between nonlinear lattice dynamics, coherent lattice symmetry breaking and (shear) strain generation. Tunable shear strain available on the ultrafast timescales via resonant lattice excitation can be exploited for material control using a wide array of perovskite wide-bandgap anisotropic substrates beyond LaAlO_3 . Since equilibrium shear strain is an important element for ferroelectric [12], flexoelectric [145], piezoelectric and magnetoelectric effects, we envision opportunities for ultrafast manipulation of collective excitations in solids.

The effects of macroscopic strain after resonant excitation of phonon resonances in insulating materials is a seemingly universal mechanism that invites further study. The effect might also play an important role in phonon-induced changes in macroscopic properties taking place on longer timescales than expected from nonlinear phononic

effects. In this regard, in finding the exact microscopic origin of a phenomenon induced by resonant phonon excitation, it is crucial to be able to distinguish strain effects from effects resulting from nonlinear phononics mechanisms.

4.7. METHODS

SAMPLE AND EXPERIMENTAL SETUP

In our experiments we use commercially available 5×5 mm (001) LaAlO_3 single crystals with a thickness of 0.5 mm from Crystec GMBH. The mid-infrared pulses (200 fs) are generated in a 0.35 mm thick GaSe crystal by difference frequency mixing the output of two optical parametric amplifiers (OPAs). The OPAs share the same white light, generated in a sapphire crystal, by the output of a laser amplifier (800 nm, 100 fs, 5 mJ, 1 kHz), which ensures carrier-envelope-phase (CEP)-stability of the pulses [20]. A small part of the laser output is used to probe the structural dynamics. The transient differential reflectivity ΔR is monitored using a balanced photodetector. The optical birefringence θ_B is tracked using an optical polarization bridge (Wollaston prism) and a balanced photodetector. In both experimental configurations, the probe pulses were focused to a spot with a diameter of $80 \mu\text{m}$. The spatial overlap between the pump and probe pulses is obtained by co-propagation of the beams, using an off-axis parabolic mirror, which focuses the pump beam to a spot of about $150 \mu\text{m}$.

DFT CALCULATIONS

The DFT calculations and symmetry analysis were performed by A. Sasani and E. Bousquet. We simulated the $R\bar{3}c$ phase of LaAlO_3 through density functional theory (DFT) [146, 147] as implemented in the ABINIT package (Ver 8.10.2) [148, 149]. We used Norm-conserving pseudopotentials [150] to account for the interaction of the nuclei and the electrons. These pseudopotentials were downloaded from the Pseudodojo website [151]. For La we considered $5s$, $5p$, $5d$, $6s$ and $4f$ as valence states and for Al and O the valence states were considered to be $3s$, $3p$ and $2s$, $2p$ respectively. We used the PBEsol GGA functional for the exchange correlation interaction [152] and all the calculations were done with a $5 \times 5 \times 5$ mesh of k -points for sampling of reciprocal space and a cut-off energy on the plane wave expansion of 45 Hartree. To calculate the phonons, we used density functional perturbation theory as implemented in ABINIT [153, 154].

4.8. SUPPLEMENTARY INFORMATION

4.8.1. TEMPERATURE DEPENDENCE OF THE E_g MODE

In order to confirm that the observed oscillation at 1.1 THz corresponds to the Raman-active E_g mode, we tracked the frequency and lifetime of the excited oscillations as a function of temperature. In Fig. 4.8 we summarize the experimental findings. Although the frequency f of the oscillation demonstrates only weak softening upon temperature increase, its lifetime demonstrates a strong temperature dependence. This behavior, as well as the exact value of its frequency, are cogent hallmarks of the E_g Raman-active vibration, a soft-mode of the rhombohedral-to-pseudocubic structural transition in LaAlO_3 at $T \approx 750$ K [155]. The temperature-dependent lifetime is the result of a decay

into acoustic phonon modes [156]. We also note that in our experiment the amplitude of the E_g mode shows a pronounced decay upon temperature increase. These observations cannot be the result of a temperature-dependent oscillator strength of the excited infrared-active E_u phonon mode, as the optical properties of LaAlO_3 close to the phonon resonance are nearly temperature-independent in this temperature range [131] and might be the result of a temperature-dependent coupling coefficient between the E_u and E_g modes.

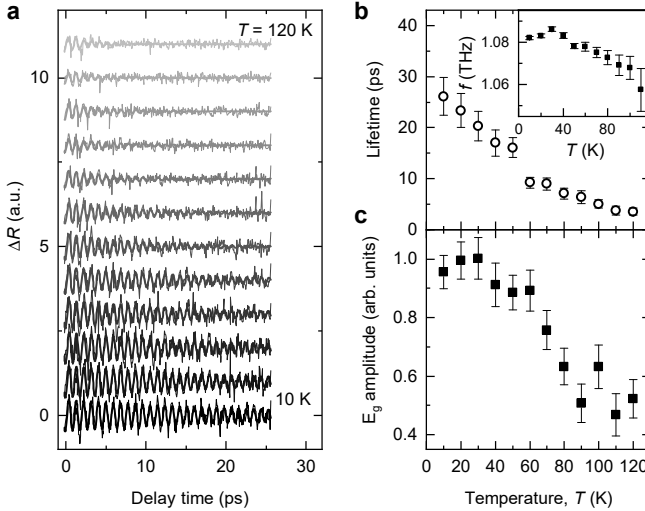


Figure 4.8: **Temperature dependence of the E_g mode.** **a**, Time-resolved measurements of the transient change in reflectivity of the probe pulse after excitation of the sample at different temperatures ($h\nu = 89$ meV). The thicker solid lines represent damped sine fits. **b,c**, Lifetime (**b**), frequency f (inset (**b**)) and amplitude (**c**) of the E_g mode oscillations vs. the temperature T , extracted using the fits of the data in panel **a**. All errorbars account only for the uncertainty of the fit of the oscillations.

4.8.2. DFT CALCULATIONS ON NONLINEAR LATTICE DYNAMICS

The technical details of the calculation are given in section 4.7.

PHONONS

The relaxed lattice parameters are shown in Table 4.1, together with experimental and DFT calculation values available from literature. There is a good agreement between all of them, besides the usual underestimation of the bandgap given by GGA functionals.

Table 4.2 shows the calculated phonon frequencies for the lowest-frequency Raman active (E_g , A_{1g} , A_{2g}) and highest-energy infrared active (A_{2u} and E_u) modes relevant to our study. The calculated phonon frequencies are in good agreement with reported experimental values.

PHONON-PHONON COUPLING MODEL

In our experiment, the resonant amplification of the E_g mode amplitude is observed when the pump photon energy is around 85 meV with the propagation vector in the [001]

Table 4.1: Calculated and experimental ground state parameters of the $R\bar{3}c$ phase of LaAlO_3 . The first column shows the lattice parameter a , the second shows the angle Θ between the lattice vectors, the third reports the energy band gap and the last column shows the oxygen octahedral rotation angle around the [111] axis.

	a (Å)	Θ (°)	bandgap (eV)	$\phi_{[111]}$ (°)
this work	5.337	60.2	4.16	5.97
DFT	5.29[133]	60.1[133]	3.88[133]	5.9[157]
EXP	5.357[158]	60[158]	5.5[159]	6[158]

Table 4.2: Phonon labels of the $R\bar{3}c$ phase of LaAlO_3 and their frequencies as calculated in this work (column 2), experimentally measured (column 3) and previously DFT calculated (column 4).

Irrep	Freq. (meV)	Exp	DFT[160]/ DFT[133]
$E_g(1)$	3.82	4.22[136]	4.09/ 2.91
$E_g(2)$	18.89	18.84[136]	18.10/ 19.40
A_{1g}	22.97	16.37[132]	15.99/ 20.36
$A_{2g}(1)$	16.84		17.48/ 17.91
$A_{2u}(3)$	79.78		77.74/ 83.19
$E_u(5)$	81.66	81.45[161]	78.98/ 84.43

pseudocubic direction. As can be seen from Fig. 4.9a this direction makes a 55° angle with the high symmetry [111] crystallographic axis. This means that the polarization has one component in the [111] direction and one in the (111) plane (from a symmetry point of view, every vector in this space group can be written through the A_{2u} -[111] and E_u -(111) irreducible representation). Considering the phonon mode energies, the laser can only excite the highest frequency A_{2u} and E_u phonon modes. Hence, we only focus on the excitation of the $A_{2u}(3)$ and $E_u(5)$ modes (from this point on referred to as A_{2u} and E_u respectively) and their coupling to lower frequency modes. All the other modes are lower in energy and cannot be excited directly by the laser. We further show that although the light can couple to the A_{2u} mode, its excitation cannot account for our experimental findings.

Since the calculations are done in a rhombohedral setting while the orientation of the pump polarization plane is located in the (001) pseudocubic plane, this needs to be taken into account when comparing the results of the calculations to experimental results. Figure 4.9b shows the projection of the in-plane vectors of the pseudocubic system to the x, y axes in the (111) plane. Rotating the laser polarization from the [100] to the [010] direction in the pseudocubic setting corresponds to rotating the polarization direction from x in the (111) plane by 120° . Rotating the laser polarization from [010] to [-100] corresponds to rotation of the polarization from 120° to $-x$ which is a 60° angle. This leads to two different functions to describe the connection between results of the experiment to the theory.

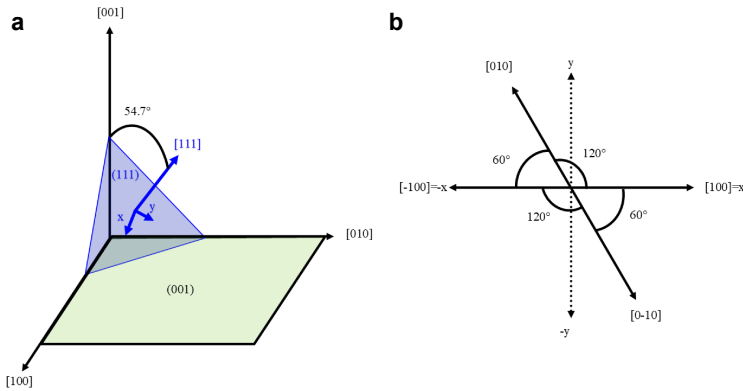


Figure 4.9: **Crystallographic orientations.** **a**, Schematic view of the lattice planes and directions of pseudocubic and rhombohedral cells. The surface of the sample is [001] oriented but the crystallographic rhombohedral main axis is along the [111] direction. **b**, projection of the pseudocubic directions onto rhombohedral coordinates in the (111) plane

Phonon modes

The E_u mode is a two-dimensional degenerate phonon mode and depending on the orientation of the polarization plane of the excitation pulse, we can excite different linear combinations of these two degenerate modes. These modes can be excited along the two main axes (orthogonal x and y , see Fig. 4.9a) or through a linear combination of them. Hence, for the E_u mode we studied 3 different cases:

- (i) E_u^x polarized in the x direction in the (111) plane (P1(9)) (Fig. 4.10c),
- (ii) E_u^y polarized in the y direction in the (111) plane (P2(5)) (Fig. 4.10d),
- (iii) E_u^{xy} with symmetry C1(1), a linear combination of the E_u^x and E_u^y modes, making a 45° angle with the x or y directions.

The A_{2u} mode is not degenerate and is polarized in the [111] direction perpendicular to the (111) plane as presented in Fig 4.10b.

We studied the nonlinear coupling of the form $\alpha Q_{IR} Q_R^2$ of the IR-active E_u and A_{2u} modes with several low frequency modes Raman (R) modes (results not shown here), where we found that all the modes except $E_g(1)$ (the lowest frequency one) have negligible coupling to them. Hence, from this point we focus on the coupling between the E_u , A_{2u} and $E_g(1)$ modes (from now on referred as E_g). The E_g mode is also doubly degenerate and therefore can have two different symmetries in which the modes could be excited depending on its orientation (E_g^a and E_g^b with P1(15) symmetry shown in Fig. 4.10 and E_g^{ab} with C1(2) symmetry (similar to Fig 4.10b with different orientation). Here, E_g^a and E_g^b are rotated 60° with respect to each other.

E_u and E_g coupling

To study the coupling of E_u and E_g modes, we can first consider 3 special cases:

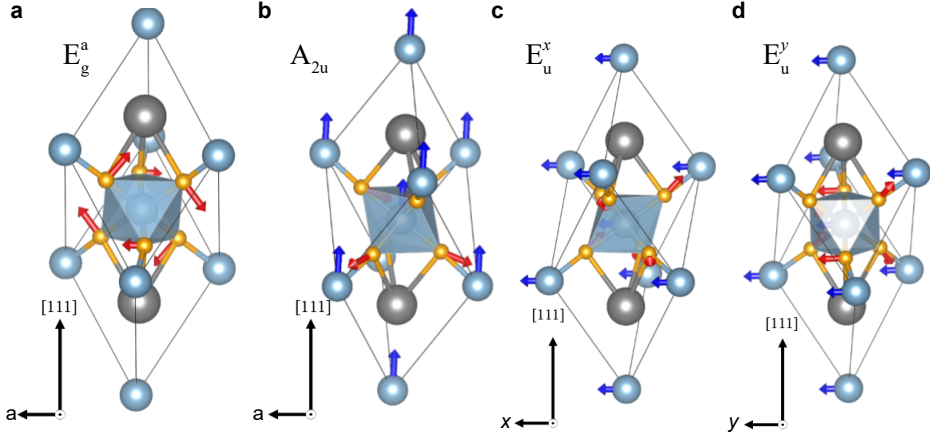


Figure 4.10: **Real-space atomic motion for different phonon modes.** Schematic pictures of phonon modes vibrations for the E_g mode (a), A_{2u} mode (b) and E_u modes (c and d).

- (i) ($E_u^x \neq 0$ with $E_u^y=0$) mode with E_g^a and E_g^{ab} modes,
- (ii) ($E_u^y \neq 0$ with $E_u^x=0$) mode with E_g^a and E_g^{ab} modes,
- (iii) (E_u^{xy} with $E_u^y = E_u^x$) mode with the E_g^a mode.

For cases (i) and (ii), we can consider the nonharmonic potential given in Eq. 4.17 and fit the results with DFT calculations.

$$V(Q) = aQ_{E_u}^2 + bQ_{E_u}^4 + a'Q_{E_g}^2 + b'Q_{E_g}^3 + c'Q_{E_g}^4 + \alpha Q_{E_g} Q_{E_u}^2 + \beta Q_{E_g}^2 Q_{E_u}^2 \quad (4.17)$$

In the general case where we have the E_u polar modes excited in two directions, we define an effective α' parameter, which is a function of the laser polarization direction and can be written as follows:

$$\alpha' = -\alpha \cos 2\theta, \quad (4.18)$$

where $\theta = \arccos\left(\frac{Q_{E_u^x}}{\sqrt{Q_{E_u^x}^2 + Q_{E_u^y}^2}}\right)$.

The results of the fit are shown in Table. 4.3 where we obtain that the constant $\alpha \approx 1.61$. For the E_u^{xy} case (iii) (with $E_u^y = E_u^x$), the α' parameter is zero and the higher order couplings are not large enough to create any considerable dynamics. This situation occurs when the polarization component of the laser in the (111) plane is exactly between the x and y axis ($\theta = 45^\circ$).

Fig. 4.11 shows the evolution of the potential energy V as a function of the E_g^a mode condensation amplitude for different amplitudes of E_u^x (Fig. 4.11a) and E_u^y (Fig. 4.11b)

Table 4.3: Coupling coefficients between E_g^a mode and $E_u^x \neq 0$ with $E_u^y=0$ (shown as E_u^x), $E_u^y \neq 0$ with $E_u^x=0$ (shown as E_u^y) or $E_u^x = E_u^y$ (shown as E_u^{xy}). The units are $\text{eV}/\text{\AA}^n$, where n is the order of the coupling.

	a	b	a'	b'	c'	α'	β
E_u^x	13.418	11.049	0.027	0.077	1.075	-1.611	-3.922
E_u^y	13.425	10.895	0.028	0.079	1.074	1.616	-4.802
E_u^{xy}	13.422	10.95	0.028	0.073	1.076	-0.001	-4.406

modes. The modes E_u^x and E_u^y tend to displace the minimum of the E_g^a mode toward different directions. These behaviours are due to opposite signs of the α' coefficients that couples the two E_u^x and E_u^y modes to the E_g^a mode. Hence, this shifts the minimum of the energy in two different directions, which could be the reason why we observe oscillations of the E_g modes in the experiments with different phases for excitation with 0° (exciting E_u^x mode) and 90° polarization (mainly exciting the E_u^y mode) of the laser. A minimum horizontally shifted from 0\AA , means that excitation of the E_u^x and E_u^y modes quasi-statically freezes the E_g^a mode (lowering the symmetry), which is the characteristic of nonlinear phononics [119].

To further understand the effects of polarization direction of the laser on the E_g^a mode, we have analysed the evolution of α' with respect to the polarization angle ϕ in the (001) plane. Figure 4.6c shows the results with α' changing in an oscillatory manner. The evolution of α' with the angle ϕ is not trivial and has two regimes. The origin of these two regimes is the polarization in the (001) plane which has to be projected on the (111) plane, which results into two types of periodicity, one of 60° and one of 120° (see Fig. 4.9b).

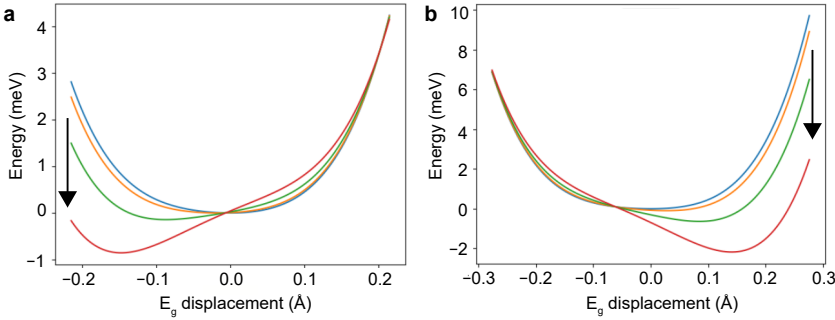


Figure 4.11: **E_g mode displacement.** The potential energy V as a function of the E_g^a mode displacement for different amplitudes of the E_u mode (E_u^x (a), E_u^y (b)). The arrows show the direction of increasing E_u mode amplitude, with amplitudes of 0, 0.03, 0.06 and 0.09 \AA respectively.

We also studied the coupling of the E_u modes with the E_g^b mode. The results are similar to the ones presented for the E_g^a case with the difference that the b' coefficient is positive in the E_g^a case while it is negative in the E_g^b case. However, the effects of this bi-quadratic coefficient b' are smaller than the third order α coefficient.

Fluence dependence of the E_g mode

We measured the dependence of the observed oscillations corresponding to the non-polar E_g mode as a function of the pump fluence at the resonance conditions (with the pump photon energy of 89 meV). As shown in Fig. 4.12, the oscillation amplitude depends linearly on the pump fluence. This observation, combined with the resonant character, indicates a quadratic dependence of the E_g mode amplitude on the amplitude of the pump driven E_u mode.

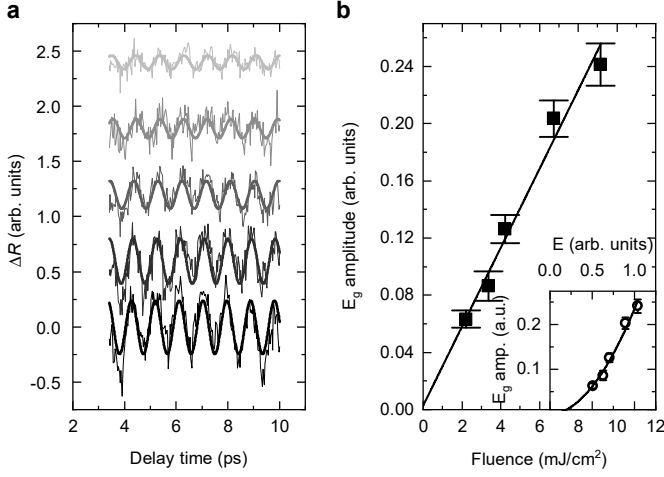


Figure 4.12: **Pump fluence dependence of the E_g mode.** **a**, Time-resolved measurements of the transient change in reflectivity of the probe pulse after excitation of the sample at a pump energy of 89 meV with different fluences (offset for clarity). The thicker solid lines represent sine fits. **b**, Amplitude of the E_g mode oscillations vs. pump fluence, extracted using the fits of the data in panel a. Inset: Amplitude of the E_g mode vs. pump electric field E with a power fit giving $E^{1.93 \pm 0.15}$. Errorbars account for the uncertainty of the fits in panel a.

A_{2u} and E_g coupling

Unlike the E_u mode, the A_{2u} mode has no degeneracy and it could couple to different directions of the E_g mode (E_g^a and E_g^b and E_g^{ab} modes). We fitted Eq. 4.17 to study the A_{2u} mode coupling with E_g mode where α is equal to zero (it is not allowed by symmetry, as the A_{2u} mode is non-degenerate). The resulting fitted coefficients are shown in Table 4.4.

Table 4.4: coupling coefficients between the A_{2u} mode and E_g^a , E_g^b and E_g^{ab} modes. The units are $\text{eV}/\text{\AA}^n$, with n the order of the coupling.

	a	b	a'	b'	c'	β
E_g^a	12.81	8.01	0.027	0.078	1.059	-3.161
E_g^b	12.81	8.00	0.027	-0.084	1.062	-3.159
E_g^{ab}	12.82	8.02	0.027	-0.012	-0.012	-3.167

In this case the only coupling term between the polar mode and the E_g mode is the higher order bi-quadratic β coefficient, which is smaller than the E_u case such that the

dynamics resulting from the A_{2u} excitation can be neglected.

STRAIN WAVES

In the experiment, both longitudinal acoustic (LA) and transverse acoustic (TA) waves are observed after resonant optical phonon excitation. Although exciting the LA mode is straightforward, exciting the TA mode is not evident in nearly-isotropic materials. We have studied two possible origins to excite the TA mode: (i) by having the crystal with off-axis orientation with respect to the sample surface or (ii) through the phonon-phonon coupling that induces anisotropic strain.

In case (i), the experimental set-up is such that the LaAlO_3 sample surface is oriented in the pseudocubic [001] direction, which makes an angle of 55° with respect to the proper rhombohedral [111] high symmetry direction (as can be seen in Fig. 4.9a). This is evidenced from the calculated elastic constants of both the pseudocubic and the rhombohedral phases reported in Table 4.5. We can see that the transition from pseudocubic to $R\bar{3}c$ phase creates anisotropy compared to the pseudocubic elasticity with a pronounced splitting between the rhombohedral xy directions and the z direction. In this case the shear strain will be excited due to anisotropy arising from off-axis orientation of the crystal.

In the second case (ii) the phonon-phonon coupling induced by the laser excites the E_g mode, which in turn can induce an out-of-equilibrium anisotropy into the elasticity. To further show the effect of this dynamically induced phonon induced stress, we relaxed the lattice parameters by keeping the E_g mode frozen in the crystal and compared the resulting elastic constants with respect to the ones of pseudocubic and rhombohedral LaAlO_3 (Table 4.5). It is seen that the anisotropy arising from the E_g mode condensation has a strong impact on the C_{35} and C_{51} elastic constants. These off-diagonal constants indeed couple longitudinal and shear strain, which makes it likely that they contribute to the strain conversion when energy of the pump photon is swiped across the E_u phonon resonance.

4.8.3. PUMP FLUENCE AND POLARIZATION DEPENDENCE OF THE STRAIN WAVES

In this work, the strain waves were measured for different photon energies. These strain wave amplitudes increased linearly with pump fluence, as shown in Fig. 4.13a for all photon energies. In addition the strain waves were measured for different pump polarization. The time-resolved traces are shown in Fig. 4.13b. No strong dependence of the TA/LA ratio r on the pump polarization is observed.

Table 4.5: Elastic constants of LaAlO_3 (in the respective coordinate systems) for the pseudocubic, rhombohedral ($R\bar{3}c$) and rhombohedral with the E_g mode condensed. The amplitude of the distortion is 0.13 \AA . Units are in (GPa)

	pseudocubic	Rhombo	Rhombo+ E_g
C_{11}	366	404	410
C_{22}	366	404	394
C_{33}	366	406	406
C_{12}	130	124	124
C_{23}	130	98	97
C_{31}	130	98	100
C_{44}	161	124	123
C_{55}	161	124	124
C_{66}	161	140	140
C_{46}	0	-22	-23
C_{51}	0	22	18
C_{52}	0	-22	-22
C_{35}	0	0	-4

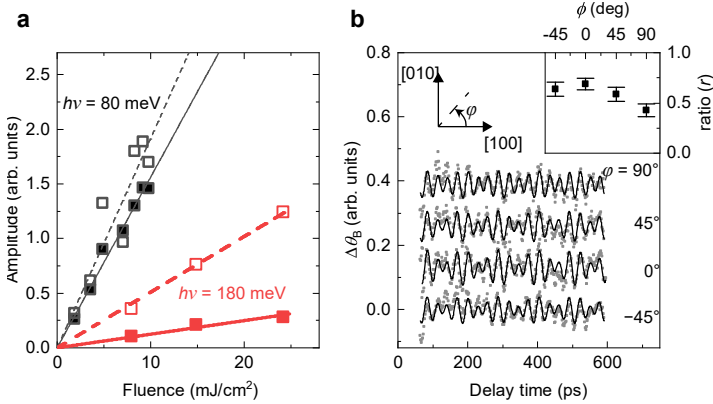


Figure 4.13: **Pump fluence and polarization dependence of the strain waves.** **a**, The amplitude of the LA (open markers) and TA (filled markers) strain wave amplitudes vs pump fluence for resonant and non-resonant excitation with linear fits (solid and dashed lines). **b**, Time-resolved measurements of the transient polarization rotation of the probe pulse after excitation of the sample with different orientation of the pump polarization at a pump energy of 89 meV. The black solid lines are best fits using a sum of two sines, to account for the two frequencies. inset: Ratio r of the different acoustic pulses for different pump polarization as extracted from fitting the FFT spectra from the data in (b). The errorbars account for the uncertainty due to the fits of the Fourier peaks.

5

CONTROL OF MAGNETIC INTERACTIONS VIA ULTRAFAST RESONANT LATTICE EXCITATION

"The most exciting phrase to hear in science, the one that heralds new discoveries, is not 'Eureka!' but 'That's funny'."

Isaac Asimov

In the previous chapter we introduced resonant ultrafast excitation of infrared-active phonons as a powerful technique to control functional material properties through transient structural deformations. In this chapter we show that light-driven phonons can be utilized to coherently manipulate macroscopic magnetic states. Intense mid-infrared electric field pulses, tuned to resonance with a phonon mode of the antiferromagnet DyFeO₃, induce ultrafast and long-living changes of the fundamental exchange interaction between rare-earth orbitals and transition metal spins. This nonthermal lattice control over the magnetic exchange, which defines the very stability of the macroscopic magnetic state, allows us to perform picosecond coherent switching between competing antiferromagnetic and weakly ferromagnetic spin orders.

This chapter has been published with minor differences in Nature Materials **20**, 607 (2021) by D. Afanasiev, J. R. Hortensius, B. A. Ivanov, A. Sasani, E. Bousquet, Y. M. Blanter, R. V. Mikhaylovskiy, A. V. Kimel and A. D. Caviglia [162].

DFT calculations were performed by A. Sasani and E. Bousquet

The ability to control macroscopic states of matter by light on the fastest possible timescale crucially relies on finding efficient routes to manipulate the various microscopic interactions defining the very stability of the cooperative state [14]. In magnetism, these interactions either involve the electrons of only one magnetic ion (single-ion magnetic anisotropy [38, 59]), or rely on a mutual interaction between pairs of magnetic ions (two-ion anisotropy [163]). Despite the intrinsic differences, both of these interactions originate from the same electrostatic Coulomb repulsion, which is strongly sensitive to the lattice symmetry and the electronic overlap. Terahertz control of magnetism is a thriving field, but its main focus until now has been limited either to the direct excitation of spins by the magnetic field component of the single-cycle terahertz pulse [55] or to resonant pumping of the electronic degrees of freedom [59, 60]. Resonant pumping of infrared-active phonons with multi-terahertz pulses in the mid-infrared spectral (MIR) range has emerged as a low-energy route to drive large-amplitude net structural distortions. These coherent lattice distortions, emerging on the timescale of several picoseconds, modulate the spatial overlap of the electronic wavefunctions and have been shown to transiently melt charge [164] and orbital ordering [165], drive insulator-to-metal phase transitions [116] and even enhance superconducting correlations in high- T_c cuprates [35, 36]. Although pioneering experiments have demonstrated that driving optical phonons can also affect magnetism [57, 58, 166, 167], no coherent switching of the spin orientation or coherent light-induced magnetic symmetry breaking has been shown so far.

Here we investigate phonon-induced magnetism (phonomagnetism) in dysprosium orthoferrite (DyFeO_3), a material where a strong exchange interaction between the spin of the transition metal (TM) ion and the orbital momentum of the rare-earth (RE) ion leads to a distinctive first-order spin-reorientation phase transition accompanied by a change of the magnetic symmetry from the antiferromagnetic (AFM) to the weakly ferromagnetic (WFM) [168]. We show that a sub-ps pulse of an intense multi-terahertz electric field, tuned in resonance with a phonon mode (see Fig. 5.1a), drives a coherent spin-reorientation, developing long-living WFM order within a half-cycle of the spin precession. Phonon-induced magnetism emerges via a non-equilibrium metastable state (see Fig. 5.1b), inaccessible not only via a thermodynamic transformation but also via optical pumping of the high-energy electronic transitions. We experimentally and theoretically demonstrate that phonomagnetism originates from phonon-induced lattice distortions that modify the RE-TM exchange interaction within a few picoseconds.

5.1. MAGNETIC PROPERTIES OF DyFeO_3

The magnetic insulator DyFeO_3 crystallizes in a perovskite orthorhombic structure (see Fig. 5.2a) and exhibits antiferromagnetic order of the iron spins set by the Fe-Fe isotropic exchange interaction. Although the rare-earth Dy^{3+} magnetic moments only order below 4K, they play a crucial role in determining the magnetic properties of the iron spins at much higher temperatures ($< 100\text{K}$).

While the singlet state of the Fe^{3+} ion (${}^6\text{S}$ ground state) results in negligible single-ion magnetic anisotropy, its anisotropic exchange interaction with the large angular momentum of the dysprosium (${}^6\text{H}_{15/2}$ ground state) mediates the strong coupling of the iron spins to the crystal lattice, thereby setting up the magneto-crystalline anisotropy [168].

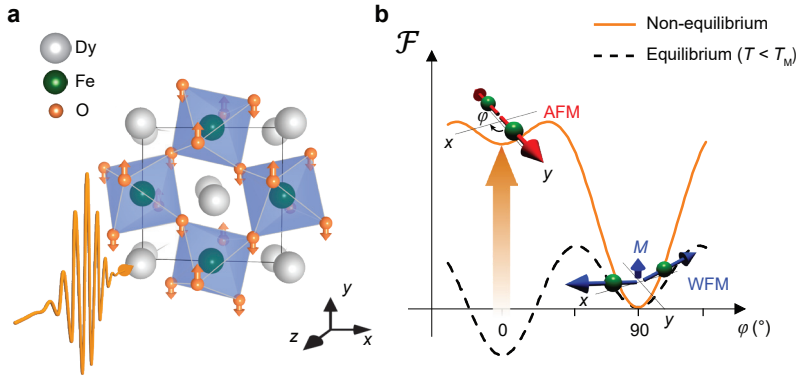


Figure 5.1: **Phonon-driven reconfiguration of the magnetic potential in DyFeO_3 .** **a**, The eigenmode of the laser-excited B_u phonon mode; orange arrows indicate the atomic motion of the oxygen ions. **b**, The magnetic potential \mathcal{F} as a function of the angle φ the spins form with the y -axis before (dashed black) and after (solid orange) phonon excitation. The red and blue arrows depict the spin configurations corresponding to the antiferromagnetic (AFM) and weakly ferromagnetic (WFM) magnetic phases. The orange arrow highlights the destabilization of the AFM ground state together and the reduction of the potential barrier separating the phases.

Around 51 K DyFeO_3 experiences a spontaneous spin-reorientation transition, in which the spins rotate in the xy -plane, accompanied by the emergence of a small net magnetic moment. This transition can also be induced by a magnetic field applied in the crystallographic z -direction and detected using the magneto-optical Faraday-rotation (see Fig. 5.2b). The thermal population of the two lowest Dy^{3+} Kramers doublets (energy gap $\Delta E = 6.4$ meV, corresponding temperature $T \approx 75$ K) changes the orbital state of the rare-earth ion and therefore directly links the origin of the first-order phase transition to the Fe-Dy exchange interaction.

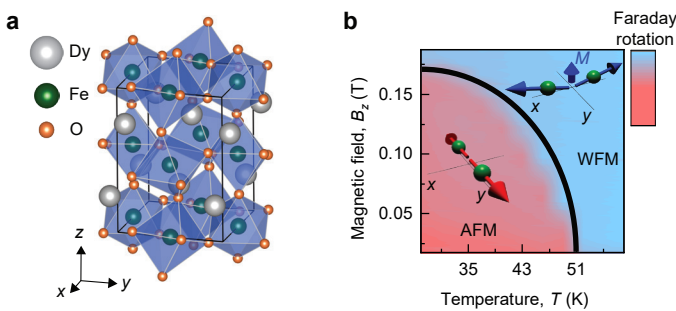


Figure 5.2: **The magnetic properties of DyFeO_3** **a**, Crystal structure of DyFeO_3 . **b**, Phase diagram of the magnetic states of DyFeO_3 as a function of the magnetic field B_z applied along the z -axis and temperature T as measured by hysteresis loops using the static magneto-optical Faraday effect.

In order to describe this spin-reorientation transition, we introduce the normalized

net magnetization \mathbf{m} and Néel vector \mathbf{l}

$$\mathbf{l} = \frac{\mathbf{M}_1 - \mathbf{M}_2}{2M_0}, \quad \mathbf{m} = \frac{\mathbf{M}_1 + \mathbf{M}_2}{2M_0}, \quad (5.1)$$

where $\mathbf{M}_{1,2}$, with $|\mathbf{M}_{1,2}| = M_0$, are the individual magnetizations of the antiferromagnetically coupled magnetic sublattices. Due to the planar character of the spin reorientation in DyFeO₃, the unit vector \mathbf{l} can be written as $\mathbf{l} = (\sin \varphi, \cos \varphi, 0)$, with φ the angle between the spins and the y -axis. The anisotropy energy can be written as function of the different components of \mathbf{l} and the temperature-dependent anisotropy parameters and rewritten in terms of φ (see section 5.7.2). The spin-reorientation is then described by the magnetic potential \mathcal{F} which depends on the temperature and the angle φ [168, 169]:

$$\mathcal{F}(\varphi, T) = \frac{1}{2}K_2(T) \cos^2 \varphi - \frac{1}{4}K_4 \cos^4 \varphi \quad (5.2)$$

5

K_2, K_4 are phenomenological anisotropy constants of very different microscopic origin. While K_2 originates from the temperature-dependent anisotropic exchange interaction between the iron and dysprosium ions, K_4 is the nearly temperature-independent magnetic anisotropy of the iron ion, with contributions of different origin (dipole, direct spin-orbit coupling and Dzyaloshinskii-Moriya interaction (DMI)) [170]. This potential function features two characteristic minima at $\varphi = 0^\circ, 90^\circ$ in a broad temperature range (see Fig. 5.3a), indicating the presence of two ordered (meta)stable states. At the Morin temperature $T_M = 51$ K, the direction of the magnetic easy-axis for the iron spins and Néel vector \mathbf{l} changes abruptly between the y - and x -crystal axis, as the relative potential energy of the two minima changes sign. This first-order phase transition is accompanied by a change in magnetic symmetry, from a collinear AFM, to a canted WFM state characterized by the emergence of a net magnetization \mathbf{m} . The evolution of the magnetic landscape close to the phase transition also has a pronounced effect on the frequency f of the antiferromagnetic spin precession mode, the soft mode of the Morin phase transition (see Fig. 5.3b). The reason for this is the sensitivity of the soft-mode to the local curvature of the magnetic potential:

$$f^2 \propto \left. \frac{\partial^2 \mathcal{F}}{\partial \varphi^2} \right|_{\varphi=\varphi_0}, \quad (5.3)$$

both in the AFM ($\varphi_0 = 0^\circ$) and WFM ($\varphi_0 = 90^\circ$) phase.

The height of the potential barrier separating the two competing states, as well as their relative energy, is controlled by the strength of the Fe-Dy exchange through the parameter K_2 . This interaction is presumably not only sensitive to the temperature but also to changes in the crystal environment, both via direct modulation of the Fe-Dy electronic overlap and via structurally-driven changes in the orbital state of the RE $4f$ multiplet [59, 171]. In our study we consider light-induced oscillations of atoms driven far from their equilibrium positions in order to control the strength of the Fe-Dy exchange [172, 173] and to realize lattice control of the spin arrangement on the ultrafast timescale.

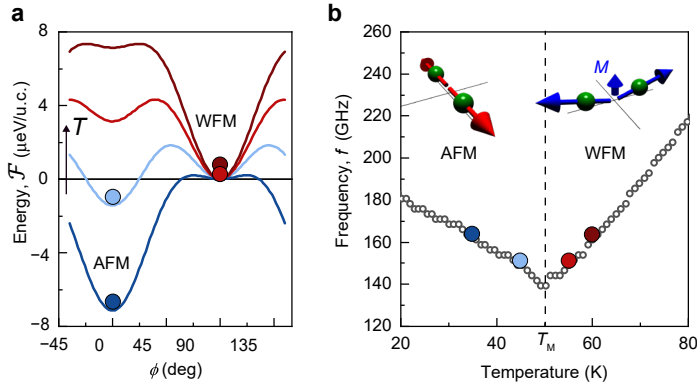


Figure 5.3: **Temperature-dependent magnetic potential of DyFeO₃.** **a**, Evolution of the magnetic potential with temperature T across the Morin temperature. The position of the solid ball indicates the system's ground state. **b**, Frequency of the equilibrium soft mode as a function of temperature. The balls indicating the ground state in panel **a** are mapped on the temperature-dependent soft-mode frequency.

5.2. PHONON-DRIVEN RECONFIGURATION OF THE MAGNETIC POTENTIAL

In our experiments we investigate spin dynamics in single crystals of z -cut DyFeO₃. The phonon excitation is provided by an intense (electric field in excess of 10 MV/cm), phase locked mid-infrared impulsive source (250 fs, 1 kHz), tunable in a broad photon energy range from 65 to 250 meV (16–60 THz). This energy range covers the highest frequency infrared-active TO phonon mode (B_u) centered at 70 meV, associated with periodic stretching of the Fe-O bonds (see Fig. 5.1a and Fig 5.16). The ensuing spin dynamics are measured in a conventional pump-probe scheme, by tracking the polarization rotation θ_R , imprinted by the magneto-optical Faraday effect, on co-propagating near-infrared probe pulses at the photon energy of 1.55 eV. Therefore the Faraday rotation probes the magnetization along the normal direction in our experimental geometry. This also allows to measure the net magnetic component resulting from canting of the magnetic sublattices in the course of antiferromagnetic spin precession (see section 5.7.2). Similarly to Refs. [174, 175], we use this precession frequency as probe of the magnetic potential (see section 5.7.3).

Figure 5.4a and 5.4b show light-induced dynamics of the Faraday signal in the AFM and WFM phases revealing coherent oscillations, corresponding to spin precession around their respective equilibria. These dynamics are induced by pump pulses tuned in resonance with the lattice vibrational mode ($h\nu = 85$ meV). As a control experiment, we excite magnon oscillations via impulsive stimulated Raman scattering (ISRS) [48] using pulses tuned away from lattice or electronic resonances ($h\nu = 165$ meV). We note that the frequencies of the magnon oscillations excited by ISRS match exactly with the tabulated values reported in the literature [169, 175] and therefore serve as in-situ probe of the curvature of the potential \mathcal{F} at equilibrium. A comparison of the Fourier spectra (insets

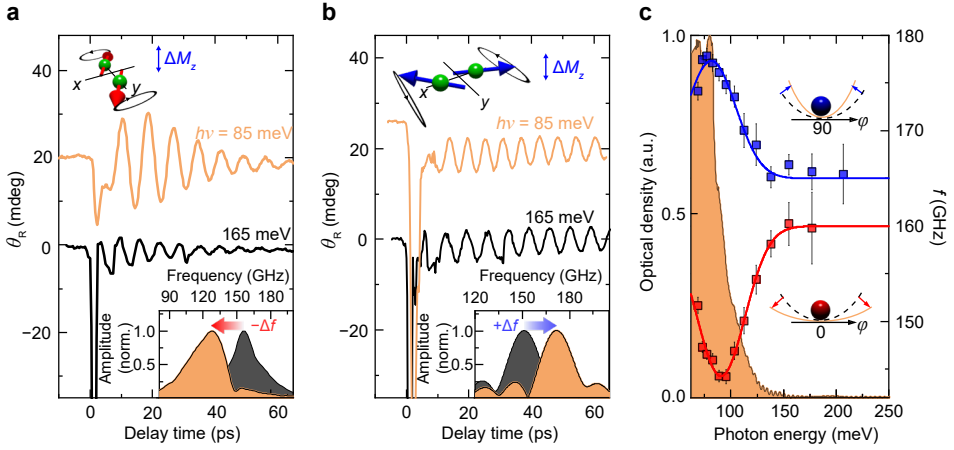


Figure 5.4: **Phonon-driven reconfiguration of the magnetic potential in DyFeO₃.** **a,b,** Time-resolved transient rotation of the probe polarization plane θ_R after light excitation with photon energy of 85 meV (orange traces) and 165 meV (black traces) performed in the AFM (**a**) and WFM (**b**) phases. The bottom insets show the normalized amplitude spectra of the soft mode oscillations. The top insets are schematics of the corresponding spin precessions, with the resulting oscillating magnetic component ΔM_z . **c,** Central frequency of the excited soft mode as a function of the photon energy of the pump pulse in the two magnetic phases. The solid lines serve as a guide to the eye. The background, shaded, curve shows the sample's optical density. The insets schematically indicate changes in the local curvature of the magnetic potential.

5

in Fig. 5.4a and 5.4b) reveals that the frequency of the spin precession excited by pulses in resonance with the lattice mode is shifted as compared to the equilibrium value. The sign of the shift Δf depends on the initial magnetic configuration, being red in the AFM phase and blue in the WFM phase. To underscore the resonant character of the frequency shift, we tune the photon energy of the pump pulse across the phonon resonance and extract the central frequency of the spin oscillations (Fig. 5.4c). The data acquired in both magnetic phases show that the onset of the frequency shift closely follows the spectrum of the linear absorption of the B_u phonon mode, revealing a correlation between light-driven phonon and spin dynamics. These observations contain important information on the effects of the phonon-pumping on the magnetic potential, as the frequency serves as a measure of the magnetic potential curvature, following the relation in Eq. 5.3. The red shift indicates a flattening of the potential energy in vicinity of the AFM minimum ($\varphi = 0^\circ$), which may lead to a phase instability. The blue shift observed in the WFM phase points at an increased curvature of the potential and enhanced phase stability in vicinity of the WFM minimum ($\varphi = 90^\circ$).

Time-resolved Fourier analysis indicates that the oscillations are chirped and the change in frequency occurs already within a half-cycle of the first spin oscillation, defining an upper bound for the phonon-driven changes in the magnetic potential of about 5 ps (see Fig. 5.5). This time is an order of magnitude shorter than reported in Ref. [175], where the heat-driven dynamics of the magnetic potential were governed by the interaction of incoherent acoustic phonons with the Dy³⁺ electrons. Thus, the observed ultrafast response excludes heat-driven spin-lattice relaxation as the origin of the initial

kinetics. Remarkably, the change in frequency persists for a time $\tau > 100$ ps, exceeding the precession period by nearly an order of magnitude. We also note that the value of τ closely follows the characteristic equilibrium decay time of the spin precession (see inset Fig. 5.5b).

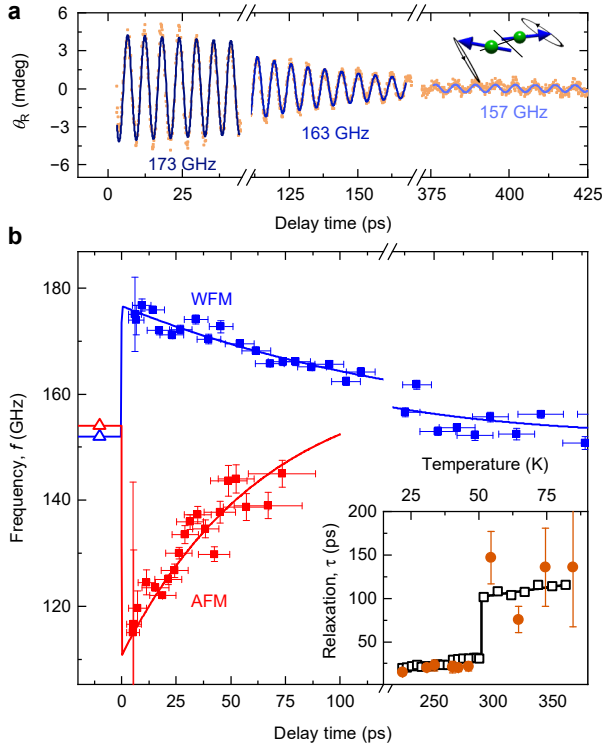


Figure 5.5: **Ultrafast dynamics of the soft mode frequency.** **a**, Spin precession after resonant phonon excitation ($h\nu = 85$ meV) in the weakly ferromagnetic (WFM) phase. The solid lines are sine fits to extract a time varying frequency f . **b**, The resulting dynamics of the frequency f as measured in the AFM (red, $T = 43$ K) and WFM (blue, $T = 57$ K) phases. The solid lines are guides to the eye. The triangular markers at $t < 0$ correspond to reference measurements performed at a pump photon energy of 165 meV. Inset: Relaxation time τ of the pump-induced frequency change across the Morin temperature T_M (orange markers) imposed on the equilibrium decay time of the spin precession (black markers).

5.3. OUT-OF-EQUILIBRIUM METASTABLE STATE

As shown in Fig. 5.6a, measurements of the frequency of the magnetic mode at equilibrium as a function of temperature reveal a cusp-like evolution in proximity to T_M , in excellent agreement with Ref. [169]. In contrast, the temperature-dependent frequencies of the magnons launched via resonant phonon excitation are characterized by a pronounced discontinuity at T_M of more than 50 GHz (see Fig. 5.6a). The discontinuity is accompanied by magnetic responses at frequencies well below the minimum equilibrium value (140 GHz). Although the heat capacity of DyFeO_3 changes by a factor of

20 between 10 and 60 K [176], the magnitude of the observed frequency change is nearly temperature-independent in the range 10–80 K, providing another indication that a non-thermal process is at play.

From the analysis of the temperature dependence of the magnon frequencies, we map out the magnetic potential \mathcal{F} (see section 5.7.3) before ($t < 0$) and after ($t > 0$) laser excitation (see Fig. 5.6b). One can see that phonon-pumping significantly increases the energy of the AFM state, simultaneously lowering the potential barrier, such that close to T_M the AFM phase may lose its stability. We note that the frequency difference between the excited phonon (17 THz) and the magnon (0.2 THz) rules out direct phonon-magnon coupling.

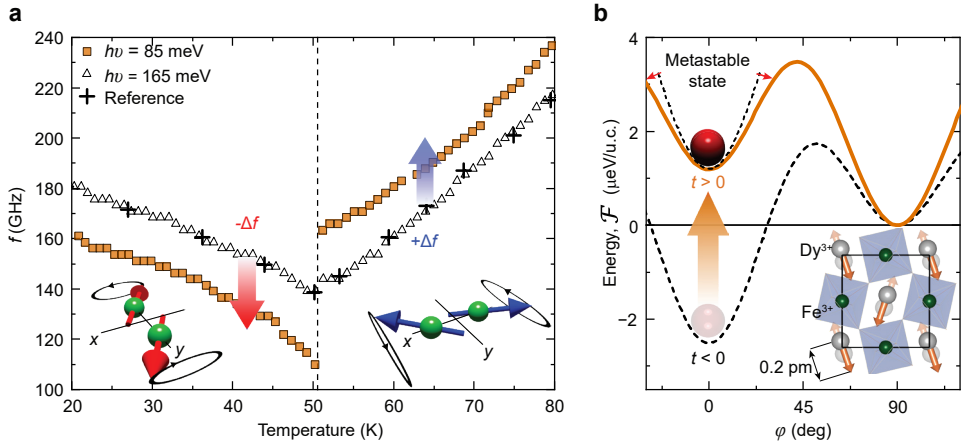


Figure 5.6: **Out-of-equilibrium metastable magnetic state.** **a**, Spin precession frequency f as a function of temperature across the Morin phase transition for different photon energies of the pump excitation. Reference values: [169] **b**, Reconstructed magnetic potential \mathcal{F} before ($t < 0$) (dashed black) and after ($t > 0$) (solid orange) the phonon-pumping. The position of the red ball represents the energy state of the system. Inset: The eigenmode of the A_g lattice distortion considered as a driving force for the dynamics of the magnetic potential. The orange arrows depict the motions of the Dy^{3+} ions, antipolar in the adjacent layers.

To describe our experimental findings, we propose a simple phenomenological model that indicates that all the changes of the magnetic potential can be explained by a renormalization of a single value parametrizing the strength of the Fe-Dy exchange by about $5 \mu\text{eV/u.c.}$ (see section 5.7.3 and Fig. 5.13). In order to identify the microscopic pathways that connect the light-driven optical phonons with the transient changes in the Fe-Dy exchange, we use density functional theory (DFT) calculations (see section 5.6 and 5.7.5 for details). The computations suggest the presence of a transient coherent lattice distortion in response to resonant pumping of the B_u mode. This distortion has the same lifetime as the infrared-active mode (~ 1 ps) and emerges as a consequence of an anharmonic interaction of different phonon modes, generally known as ionic Raman scattering or nonlinear phononics [122], which rectifies and transfers the large-amplitude excitation of the B_u polar mode into a finite time distortion along the coordinate of a coupled, Raman-active A_g phonon mode (see inset Fig. 5.6b and Fig. 5.15). This lattice

distortion involves antipolar motions of the heavy Dy^{3+} ions reaching values of about 0.2 pm for the pump fluences employed in our experiment (see section 5.7.5). The DFT results also show that such displacements can alter the Fe-Dy exchange integral by about $1\text{--}2\ \mu\text{eV/u.c.}$, consistent with the estimation of the phenomenological model (see section 5.7.5). The long-living effect of the distortion on the Fe-Dy exchange is presumably governed by the spin-lattice interaction, which also defines the lifetime of the spin precession (see inset Fig. 5.5).

5.4. ULTRAFAST PHONON-DRIVEN MAGNETIC PHASE TRANSITION

To demonstrate the potential of the phonomagnetism for ultrafast control of magnetic states we transiently modify the RE-TM exchange interaction in proximity to T_M . Two distinct regimes of the magnetization dynamics are observed above and below a critical fluence $I_c = 10\ \text{mJ/cm}^2$ (see Fig. 5.7a,b). For fluences below I_c the pump drives a nearly harmonic response of the spins, mainly influencing its amplitude and frequency. However, upon exceeding the value of I_c , the course of the magnetization dynamics changes dramatically. A long-lived ($>250\ \text{ps}$) offset, odd parity with respect to the sign of the applied field, develops within a half-period of the spin precession ($<5\ \text{ps}$), marking the coherent emergence of a transient magnetization ΔM . As the temperature is varied, it becomes apparent that the induced magnetization peaks nearly at T_M and completely vanishes for $T > T_M$ (see Fig. 5.7c). The presence of a well-defined fluence threshold, as well as the observation of the phonon-induced macroscopic magnetization inherent to the WFM phase, are clear signatures that phonon pumping drives the coherent reorientation of spins accompanied by a change in the magnetic symmetry.

It is important to compare the observed kinetics of the ultrafast phase transition launched via the phonon-pumping with those driven via a dissipative mechanism. Therefore, we perform an auxiliary experiment in which we excite the sample with visible light with a photon energy of 2.3 eV and 3.1 eV, above the charge-transfer electronic gap [177] (see section 5.7.1). Here the optical absorption is large ($\alpha \gg 1000\ \text{cm}^{-1}$), and the transition is expected to be driven by the heat deposited in the medium. In Fig. 5.8 we compare the spin-reorientation transition obtained in DyFeO_3 via conventional ultrafast heating (excitation with photon energy 2.3 eV and 3.1 eV, above the material's band gap) with the phonomagnetism discussed here. Note that especially at 3.1 eV the optical absorption is significantly larger than the optical absorption due to phonons at 85 meV. Ultrafast heating results in a net magnetization that develops on a time scale of 50–100 ps, consistent with the spin-lattice relaxation time [175]. The slow dynamics can be explained by the slow heat transfer from the excited electrons to the $4f$ electrons of Dy^{3+} , which determine the dynamics of the magnetic potential [178]. This kinetics stands in sharp contrast with the one induced by phonon pumping, where the potential is altered on a timescale shorter than a single-cycle of the coherent spin precession, below 5 ps, indicating its coherent character. This leads us to conclude that a very different mechanism from regular heating is at play in the case of phonon pumping.

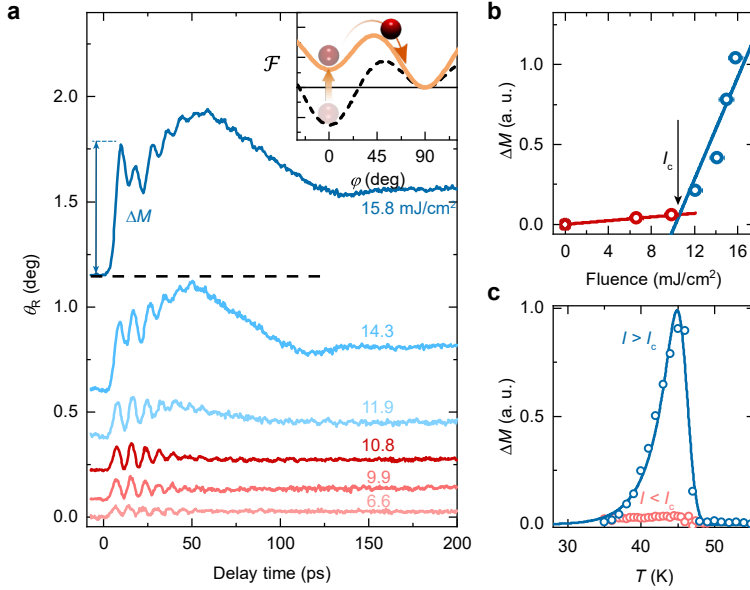


Figure 5.7: **Ultrafast phonon-induced magnetic phase transition.** **a**, Time-resolved dynamics of the polarization rotation θ_R at $T = 45$ K for various fluences of the pump. Each trace is obtained by subtracting individual traces obtained for opposite polarities of the external magnetic field to highlight magnetic components of the dynamics. Inset: Schematics of the ballistic reorientation in the altered magnetic potential \mathcal{F} . **b**, Amplitude of the transient magnetization ΔM as a function of the pump fluence I . **c**, ΔM as a function of the sample temperature for fluences I above (blue curve) and below (red curve) the threshold I_c . a. u., arbitrary units.

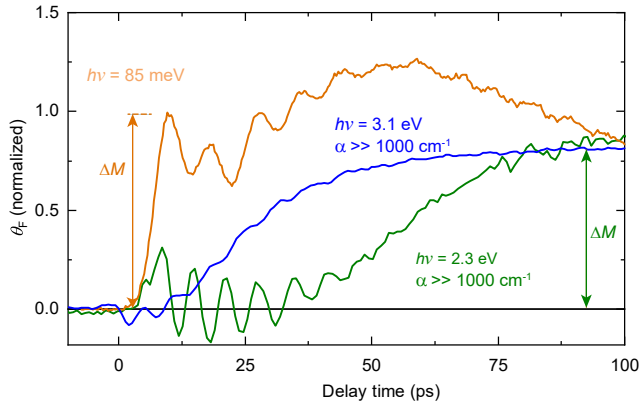


Figure 5.8: **Heat-induced vs. phonon-driven magnetic phase transition in DyFeO_3 .** Time-resolved Faraday rotation of the probe pulse after above-bandgap electronic excitation with a pump pulse with photon energy of 2.3 eV (green trace) and 3.1 eV (blue trace). The kinetics of the phonon-induced phase transition after excitation at 85 meV (orange trace) are shown for comparison. α is the absorption coefficient.

5.5. CONCLUSIONS

By resonantly pumping infrared-active phonons with strong-field ultrashort multi-terahertz pulses of light, we have investigated a new route to reshape magnetic potentials and

initiate ultrafast coherent magnetic phase transitions. Using a phenomenological description and first-principles calculations, we have demonstrated that the mechanism is based on a phonon-driven change of the exchange interaction between the rare-earth and transition metal ions. We anticipate that a similar mechanism will be active in other magnetic materials featuring anisotropic exchange interactions such as rare-earth based compounds (manganites, vanadates, and orthochromites) and type-II multiferroics [179]. Our findings fill the gap between manipulation of magnetism with single-cycle terahertz pulses [55, 59] and ultrashort pulses at optical frequencies [39], highlighting new avenues for the manipulation of ferroic order on ultrafast timescales and providing a new platform for magnonics and antiferromagnetic spintronics [180].

5.6. METHODS

SAMPLE AND EXPERIMENTAL SETUP

We used a monocrystalline, 63 μm -thick DyFeO_3 sample grown by floating-zone melting. The sample is cut perpendicularly to the z -crystallographic axis in the form of a thin slab. The sample was kept in a dry-cycle cryostat (Montana Instruments) which allowed to cool it down to 10 K, far below T_M . Static bias fields up to $B_{\text{ext}} = 700$ mT from an electromagnet were applied within the (xz) -plane of the crystal at an angle of about 70° relative to the z -axis to provide a single domain magnetic state of the sample.

The intense pump pulses with wavelengths in the mid-infrared (MIR) spectral range used in this experiment, were generated via difference frequency generation (DFG) in a GaSe crystal using the output beams of two commercially available, independently tunable optical parametric amplifiers (OPAs) integrated into a single housing (Light Conversion, TOPAS-Twins). The OPAs were pumped by a commercially available amplified Ti:Sapphire laser system (Coherent, Astrella) delivering pulses at a 1 kHz repetition rate with a duration of 100 fs and a photon energy of 1.55 eV ($\lambda = 800$ nm). The OPAs were seeded by the same white light generated in a sapphire crystal, which ensures separately tunable, but phase-locked output pulses [20] with photon energies in the range 0.45–1.1 eV ($\lambda = 2.7$ – 1.1 μm). As a result, when the pulses are mixed in the GaSe crystal, the generated MIR pulses are carrier envelope phase (CEP) stable [181], linearly polarized and their energy lies in the range from 65–250 meV ($\lambda = 19$ – 5 μm) with an average pulse duration of around 250 fs.

To generate pump pulses in the visible spectrum with a photon energy larger than the electronic band gap, we used a β -barium borate (BBO) single crystal to double or triple the photon energy of a single OPA output. This provided tunable excitation pulses with energies in the range of 0.9–3.3 eV. In the experiments, the mid-infrared pulses were focused onto the sample surface to a spot with a diameter of about 150 μm , using an off-axis parabolic mirror. The pump-induced dynamics were measured in a transmission geometry. The polarization rotation θ_R of the linearly polarized probe pulse, imprinted by the magneto-optical Faraday effect, was measured with the help of a polarization bridge (Wollaston prism) and a pair of balanced Si photodetectors. The loss function of the sample in the MIR spectral range was measured using a Nicolet 6700 Fourier transform infrared (FTIR) spectrometer. The optical absorption in the visible spectral range was measured using a halogen lamp and an Ocean Optics spectrometer.

The optical setup is described in more detail, including a figure, in chapter 3.

DFT CALCULATIONS

We simulated the *Pnma* phase of DyFeO₃ through density functional theory (DFT) [146, 147] and its projected augmented wave (PAW) [182] flavour as implemented in the ABINIT package [148, 183]. The PAW atomic potentials used for Fe and O were downloaded from the GBRV pseudopotential library [184] with 3s, 3p, 3d, 4s and 2s, 2p considered as valence states for Fe and O respectively. For Dy we used the PAW atomic potential from M. Topsakal et al. [185] where the valence states are 4f, 5s, 5p and 6s (with f electrons in the valence). We used the PBEsol GGA functional [152] for the exchange correlation interaction and Hubbard corrections [186] on both Fe and Dy of respectively 4 and 7 eV have been used to have the closest possible properties with respect to experiments (lattice constants). All the calculations were done with a 6x6x4 mesh of *k*-points for the reciprocal space and a cut-off energy on the plane wave expansion of 36 Hartree and 72 Hartree for the second finer grid inside the PAW spheres. To calculate the phonons, the frozen phonon technique has been used through the phonopy software [187].

5

5.7. SUPPLEMENTARY INFORMATION

5.7.1. OPTICAL ABSORPTION SPECTRUM

DyFeO₃ is an insulator with a large optical bandgap. At the photon energies above 2.1 eV, the optical absorption is dominated by the dipole-active charge-transfer electronic transitions from the O²⁻ to the Fe³⁺ ions [177] (see Fig. 5.9). The several broad absorption peaks below 2.1 eV correspond to optical transitions due to spin-forbidden *d-d* transitions within the Fe³⁺ multiplet. The optical losses at photon energies below 150 meV are due to absorption and reflection of the nearly degenerate, highest-frequency TO-phonon modes, with B_{1u} and B_{3u} symmetries and the dipole moment oriented along the *x*- and *y*-axis respectively. The eigenvectors of the atomic motion comprising these phonon modes are shown as inset in Fig. 5.9.

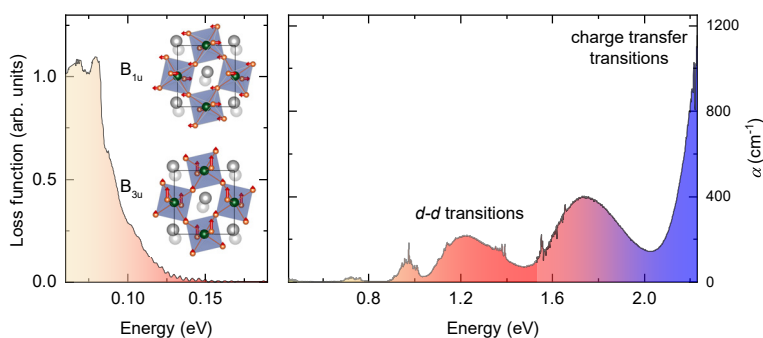


Figure 5.9: **Optical absorption spectrum.** **a**, Loss function and optical absorption for the 63 μm thick (001) DyFeO₃ sample in a broad energy range. The B_{1u} and B_{3u} phonon modes are nearly degenerate and dominate the loss function at energies below 0.15 eV.

5.7.2. FIRST-ORDER SPIN REORIENTATION AND SPIN DYNAMICS IN DyFeO_3 SPIN REORIENTATION

Below the Néel temperature $T_N = 650$ K, the Fe^{3+} spins in DyFeO_3 are ordered antiferromagnetically. The magnetic phase diagram of DyFeO_3 includes a collinear antiferromagnetic (AFM) phase with the spins oriented along the y -axis and a weakly ferromagnetic (WFM) phase with the spins oriented along the x -axis [144, 170, 188–192]. The AFM phase is stabilized at low temperatures ($T < T_M = 51$ K) and can be transformed to the WFM phase either by an increase in temperature or by application of an external magnetic field along the z -crystallographic axis [144]. The spin reorientation occurs in the (xy) crystallographic plane and thus can be fully parametrized by an angle φ that the spins form with the y -axis [168, 169]. It proceeds as a first-order phase transition and demonstrates a very narrow (< 0.2 K) temperature hysteresis [144, 170], due to a high sensitivity of the spin-reorientation transition to lattice deformations and crystal defects. These factors contribute to a prompt nucleation of the new magnetic phase, once the energy balance between the AFM and the WFM states changes its sign, making the hysteresis extremely narrow in vicinity of T_M .

The following discussion heavily builds on section 2.5. To describe the phase transition we introduce the normalized net magnetization and Néel vector:

$$\mathbf{l} = \frac{\mathbf{M}_1 - \mathbf{M}_2}{2M_0}, \quad \mathbf{m} = \frac{\mathbf{M}_1 + \mathbf{M}_2}{2M_0}, \quad (5.4)$$

where $\mathbf{M}_{1,2}$, with $|\mathbf{M}_{1,2}| = M_0$ are the individual magnetizations of the antiferromagnetically coupled magnetic sublattices that are related to the mean values of the atomic spins $\mathbf{s}_{1,2}$ as $\mathbf{M}_{1,2} = g\mu_B\mathbf{s}_{1,2}/v_0$, with v_0 the volume per iron ion, g the Landé factor and μ_B the Bohr magneton. The Dzyaloshinskii effective field in DyFeO_3 is given by:

$$\mathbf{H}_D = H_D[\mathbf{e}_y \times \mathbf{l}], \quad (5.5)$$

with \mathbf{e}_y a unit vector along the y -axis, corresponding to the even C_2 crystal axis in DyFeO_3 . As H_D is large ($\sim 1 \times 10^5$ Oe), the external field \mathbf{H}_0 can be neglected from this point on. Due to the planar character of the spin reorientation in DyFeO_3 , the unit vector \mathbf{l} can be written as $\mathbf{l} = (\sin\varphi, \cos\varphi, 0)$ (with φ the angle between the spins and the y -axis). Putting this in Eq. 2.30, we find that the normalized static magnetization $\mathbf{m}^{(\text{static})}$ is given by:

$$\mathbf{m}^{(\text{static})} = \frac{H_D}{H_{\text{ex}}}[\mathbf{e}_y \times \mathbf{l}] = -\frac{H_D}{H_{\text{ex}}}\sin\varphi\mathbf{e}_z. \quad (5.6)$$

It is thus clearly seen that the net magnetization is absent when the spins are aligned along the y -axis ($\varphi_0 = 0^\circ$, AFM phase) and is oriented along the z -axis when the spins are oriented along the x -axis ($\varphi_0 = 90^\circ$, WFM phase).

The spontaneous spin-reorientation between these two states is governed by the dependence of the energy of the magneto-crystalline anisotropy on the temperature T . To describe the behavior of spins in DyFeO_3 in the vicinity of the Morin transition, the anisotropy energy should include a large number of invariants, both quadratic and bi-quadratic with respect to components of the vector \mathbf{l} . However, due to the planar character, it can be effectively reduced to terms quadratic and biquadratic in l_y , such that the

anisotropy energy reads [168, 169]:

$$w_a^{\text{planar}}(\mathbf{l}) = \frac{1}{2}K_2(T)l_y^2 - \frac{1}{2}K_4l_y^4 \quad (5.7)$$

Note that the magnetic anisotropies defined by the parameters $K_2 > 0$ and $K_4 > 0$ are of very different microscopic origin. While K_2 originates from the temperature-dependent anisotropic exchange interaction between the iron and dysprosium ions, K_4 is the nearly temperature-independent magnetic anisotropy of the iron ion, with contributions of different origin (dipole, direct spin-orbit coupling and Dzyaloshinskii-Moriya interaction (DMI)) [170]. Written in terms of the angle φ , this energy acquires the form of the double well magnetic potential $\mathcal{F}(\varphi, T)$ considered in the main text:

$$\mathcal{F}(\varphi, T) = \frac{1}{2}K_2(T)\cos^2\varphi - \frac{1}{4}K_4\cos^4\varphi \quad (5.8)$$

SPIN DYNAMICS IN VICINITY OF THE SPIN-REORIENTATION

Starting from the Landau-Lifshitz equations for the two magnetic sublattices (Eq. 2.26) and using the expression for the Dzyaloshinskii field (Eq. 5.5) we can arrive at an expression for the normalized magnetization \mathbf{m} (Eq. 2.30)

$$\mathbf{m} = \frac{H_D}{H_{\text{ex}}}[\mathbf{e}_y \times \mathbf{l}] + \frac{1}{\omega_{\text{ex}}} \left[\frac{\partial \mathbf{l}}{\partial t} \times \mathbf{l} \right], \quad (5.9)$$

with $\omega_{\text{ex}} = \gamma H_{\text{ex}}$. The first term again gives the equilibrium magnetization, Eq. 5.6. Even though the equilibrium net magnetization $m = 0$ in the AFM phase, a dynamical component (second term) emerges due to dynamics of the antiferromagnetic vector. In the AFM phase this dynamical contribution is the only source of the magnetization along the z -axis probed by the magneto-optical Faraday effect in our experiments. Substituting Eq. 5.9 into the Landau-Lifshitz equation for \mathbf{m} (Eq. 2.26), we obtain an equation for dynamics of the vector \mathbf{l} alone:

$$\mathbf{l} \times \left(\frac{\partial^2 \mathbf{l}}{\partial t^2} + \omega_{\text{ex}} \frac{\gamma}{2M_0} \frac{\partial w_a}{\partial \mathbf{l}} \right) = 0 \quad (5.10)$$

It can be shown that for any ground state with the \mathbf{l} vector parallel to crystal axis, like the AFM phase with $\mathbf{l}_{\text{AFM}} = \mathbf{e}_y$, $\mathbf{m}_{\text{AFM}} = 0$ or the WFM phase with $\mathbf{l}_{\text{WFM}} = \mathbf{e}_x$, $\mathbf{m} = (H_D/H_{\text{ex}})\mathbf{e}_z$, Eq 5.10 allows for two classes of simple dynamical solutions with planar oscillations of the vector \mathbf{l} within two orthogonal crystal planes, containing the ground state direction of \mathbf{l} [193]. For these planar regimes, it is indeed sufficient to consider in the anisotropy energy $w_a(\mathbf{l})$ only terms quadratic and biquadratic in components of the vector l that lie in the corresponding planes. In particular, this leads to the expression for the planar anisotropy energy w_a^{planar} introduced in Eq. 5.7.

In the linear approximation these two regimes correspond to two normal modes of spin dynamics. Namely, for the AFM state ($\mathbf{l} = \mathbf{e}_y$ in the ground state) one mode corresponds to non-zero values of $l_z(t)$ and $m_x(t)$, and the other mode to non-zero values of $l_x(t)$ and $m_z(t)$. The second one is the soft mode near the Morin phase transition and

the main subject of our research. For the WFM phase ($\mathbf{l}_{\text{WFM}} = \mathbf{e}_x$, $\mathbf{m}_{\text{WFM}} = (H_D/H_{\text{ex}})\mathbf{e}_z$ in the ground state) these two modes are usually called the quasi-FM (q-FM) mode and quasi-AFM (q-AFM) mode. The q-AFM mode, where \mathbf{l} is moving in the xy -plane, is the soft mode near the Morin phase transition. This mode has non-zero $l_x(t)$ and only one time-dependent component of magnetization, $m_z(t)$. For the soft-mode oscillations, the magnetization has a time-dependent z -component in both magnetic phases that allows using Faraday effect for their detection in z -cut samples. The motions of \mathbf{l} and \mathbf{m} for the soft-modes in both phases are schematically shown in Fig. 5.10a,b.

The character of the motion of spins (and the related magnetization of the sublattices $\mathbf{M}_{1,2}$) can be easily restored through the equations $\mathbf{s}_1 = s(\mathbf{m} + \mathbf{l})$ and $\mathbf{s}_2 = s(\mathbf{m} - \mathbf{l})$, $s = |\mathbf{s}_{1,2}|$. Contrary to the planar motions of \mathbf{l} and \mathbf{m} , the motion of the spins and sublattice magnetization is elliptic, as shown in Fig. 5.10c,d

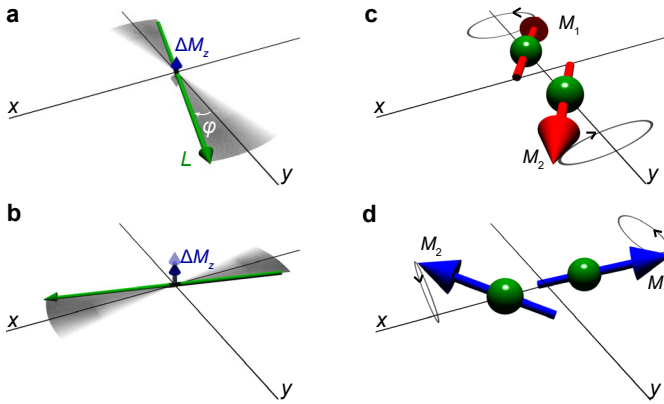


Figure 5.10: **Soft mode spin dynamics in DyFeO₃.** **a,b**, Planar motion of the Néel vector \mathbf{L} corresponding to the soft spin precessional mode in the AFM **(a)** and WFM **(b)** phase. The resulting oscillation of a net magnetization component ΔM_z is shown by the blue arrow. **c, d**, Precessional motion of the magnetic sublattices $\mathbf{M}_{1,2}$ corresponding to the same magnetic mode in the AFM **(c)** and WFM **(d)** phase.

5.7.3. RECONSTRUCTING THE MAGNETIC POTENTIAL USING THE SPIN PRE-CESSION FREQUENCY

EQUILIBRIUM POTENTIAL

Using the equilibrium magnetic potential $\mathcal{F}(\varphi, T)$, given by Eq. 5.8 and shown in Fig. 5.11a, the frequency of the antiferromagnetic spin precession f , the soft mode of the phase transition, in the AFM ($T < T_M$, $\varphi_0 = 0^\circ$) and the WFM ($T > T_M$, $\varphi_0 = 90^\circ$) phases can be obtained from the relation [91]:

$$\begin{aligned} \frac{\omega^2(T)}{\omega_{\text{ex}}^2} &= \frac{\gamma}{2M_0} \left. \frac{\partial^2 \mathcal{F}(\varphi, T)}{\partial \varphi^2} \right|_{\varphi=\varphi_0} \\ &= \frac{\gamma}{2M_0} \begin{cases} -K_2(T) + K_4, & T < T_M \quad (\varphi_0 = 0^\circ) \\ K_2(T), & T > T_M \quad (\varphi_0 = 90^\circ) \end{cases} \end{aligned} \quad (5.11)$$

Here, $\omega = 2\pi f$, with ω and f the angular and regular spin precession frequency, respectively; M_0 is the saturation magnetization of one magnetic sublattice; ω_{ex} is the so-called exchange frequency, defined as the angular frequency of the spin precession in the effective field H_{ex} of the Fe-Fe exchange interaction. For our definition of the exchange field H_{ex} ($H_{\text{ex}} = 12.8$ MOe for orthoferrites); $\omega_{\text{ex}} = \gamma H_{\text{ex}}$, γ is the gyromagnetic ratio. Only planar dynamics of the Néel vector is considered ($\theta = 90^\circ$).

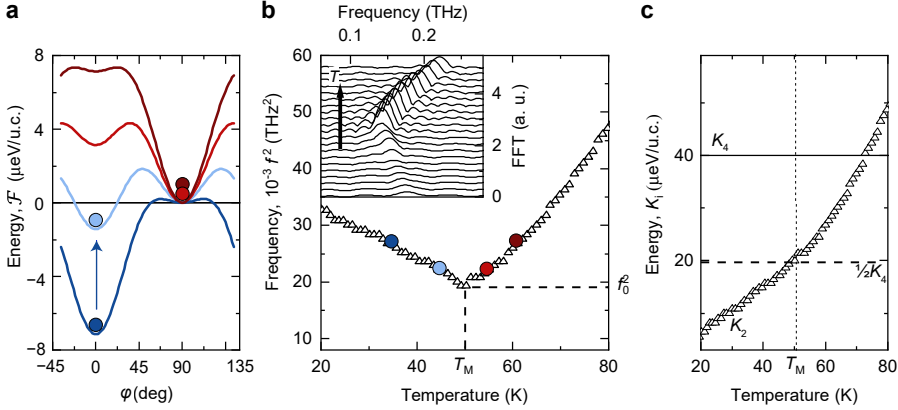


Figure 5.11: **The temperature-dependent magnetic potential.** **a**, Evolution of the magnetic potential with temperature (blue indicates low temperature) across the Morin temperature. The position of the solid ball indicates the system's ground state. **b**, Squared frequency of the equilibrium soft mode as a function of temperature. The balls indicating the ground state in panel **a** are mapped on the temperature dependence to match the frequency with the potential and the ground state. Inset: Fourier spectra of the equilibrium oscillatory magnetic dynamics after ISRS excitation at different temperatures T (offset for clarity, arrow indicates increasing temperature T). **c**, The anisotropy parameters K_2 and K_4 as extracted from the temperature dependence of the equilibrium soft mode precession frequencies.

Inversely, using the frequency of the spin precession one can obtain absolute values of the anisotropy parameters K_2 and K_4 and recover their temperature evolution. Using the assumption that the anisotropy K_4 is nearly temperature-independent, one can determine its magnitude relatively to K_2 :

$$2K_2(T_M) = K_4, \quad (5.12)$$

valid at $T = T_M$. Hence, the absolute value of K_4 using Eq. 5.11 is:

$$K_4 = \frac{4M_0}{\gamma} \frac{\omega_0^2(T_M)}{\omega_{\text{ex}}}, \quad (5.13)$$

The value of ω_0^2 can be found at the intersection of the squared frequency branches corresponding to the AFM and WFM phases. This value can be obtained from temperature dependence of the magnon frequency: $f_0(T_M) = 0.1386$ THz ($\omega_0 = 0.8704$ THz) (see Fig. 5.11b). To obtain the absolute value of the K_4 anisotropy we used the following material parameters: $H_{\text{ex}} = 12.8$ MOe, $\omega_{\text{ex}} = \gamma H_{\text{ex}} = 35.84$ THz, $M_0 = 392$ G resulting in $K_4 = 299$ erg/cm³, in close agreement with Ref. [169]. Using the volume of a single unit cell

(u.c.), comprising four formula units, this gives $K_4 \approx 40 \mu\text{eV/u.c.}$. The temperature evolution of the anisotropic exchange represented by the parameter K_2 can be extracted using:

$$K_2(T) = \begin{cases} K_4 - \frac{4M_0}{\gamma\omega_{\text{ex}}} \omega^2(T), & T < T_M \\ \frac{4M_0}{\gamma\omega_{\text{ex}}} \omega^2(T), & T > T_M \end{cases} \quad (5.14)$$

The temperature evolution of the K_2 and K_4 anisotropy parameters at equilibrium is summarized in Fig. 5.11c.

NON-EQUILIBRIUM POTENTIAL

Our experiment shows that resonant pumping of the B_u mode alters the magnetic potential represented by the function \mathcal{F} . This effect can originate from a phonon-driven renormalization of either the K_2 or K_4 anisotropy, such that:

$$\begin{aligned} K_2 &:= K_2 + \Delta K_2 \\ K_4 &:= K_4 + \Delta K_4 \end{aligned} \quad (5.15)$$

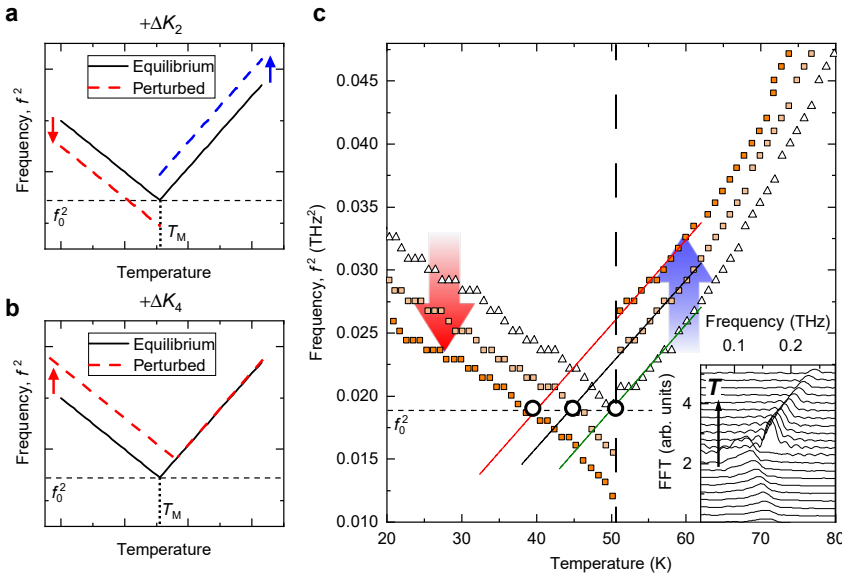


Figure 5.12: **Changing the soft-mode frequency.** **a, b**, Schematic of the squared spin precession frequencies for the altered anisotropy parameters $K_2 + \Delta K_2$ (**a**) and $K_4 + \Delta K_4$ (**b**), indicated by dashed lines, following Eq. 5.15. The temperature dependence of the squared spin precession frequency for the equilibrium values of the phenomenological constants K_2 and K_4 is indicated by the solid black line. **c**, The extracted frequencies after excitation off-resonantly (black open triangles) and on-resonantly at different fluences (filled square markers). Inset: Fourier spectra of the oscillatory magnetic dynamics after resonant phonon-excitation for different temperature T (offset for clarity), showing a pronounced frequency gap across the Morin transition.

From Eq. 5.11 one can see that the ΔK_2 contribution results in an antisymmetric shift of the squared magnon frequency across the Morin transition as exemplified in

Fig. 5.12a. In contrast, the ΔK_4 contribution changes the squared frequency exclusively in the low-temperature AFM phase (see Fig. 5.12b). Our experiment clearly demonstrates that the frequency shift is present in both phases and is strongly antisymmetric, underscoring that the phonon pumping is altering the value of the K_2 anisotropy but not of K_4 . One can also see that the value f_0^2 as defined above is independent of the laser fluence (Fig. 5.12c) and matches the value at equilibrium. Following Eq. 5.13, this also suggests the insensitivity of the K_4 anisotropy to the phonon pumping. Equation 5.11 allows also to exclude a long-living (more than a period of the spin precession) influence of the phonon pumping on the strength of the Fe-Fe exchange interactions represented by the parameter H_{ex} . This possibility is excluded as such a change would induce a frequency shift with the same sign for both magnetic phases, which does not agree with the experimental data. Using the frequencies of the spin precession obtained for the resonant pumping of the phonon mode we recovered the absolute values of the out-of-equilibrium anisotropies (Fig. 5.13a). One can see that phonon-pumping substantially enlarges the magnitude of the K_2 anisotropy, which parametrizes the strength of the Fe-Dy exchange interaction. The value of ΔK_2 is continuous at T_M , nearly temperature-independent and reaches values up to $6 \mu\text{eV}/\text{u.c.}$ To illustrate the impact of modulation of the Fe-Dy exchange on the profile of the magnetic potential we reconstructed the potential before and after the phonon pumping, see Fig. 5.13b,c. It is clearly seen that in both magnetic phases the phonon-pumping is increasing the energy of the AFM state and lowering the potential barrier towards switching from the AFM to the WFM state, thereby destabilizing the AFM state as a ground state.

5.7.4. EFFECT OF THE LASER FLUENCE ON THE SPIN PRECESSION FREQUENCY AND THE ANISOTROPY PARAMETERS.

The frequencies of the spin precession as function of the pump fluence were extracted from the time-resolved waveforms for a pump photon energy tuned in- (85 meV) and off-resonance (165 meV) with the phonon mode. The results are shown in Fig. 5.14a. For the in-resonance excitation, the frequency of the magnon changes linearly with fluence for both magnetic phases. One can see that for the off-resonance excitation, the magnon frequency is nearly independent of the pump fluence. We extracted the values of the ΔK_2 anisotropy for the in-resonance excitation using Eq. 5.14 and plotted it in Fig. 5.14b. A clear linear dependence on the pump fluence is observed, independent of the sample's magnetic ground state. The linear dependence of ΔK_2 on the pump fluence implies a quadratic dependence on the amplitude of the electric field of the pump pulse. This can be easily understood considering the expansion of ΔK_2 in a series of the normal phonon coordinate Q_{IR} of the B_{1u} mode:

$$K_2(Q_{\text{IR}}) = K_2 + \Delta K_2 = K_2 + A_1 Q_{\text{IR}} + A_2 Q_{\text{IR}}^2 + \dots, \quad (5.16)$$

with $A_{1,2}$ phenomenological constants. The phonon coordinate Q_{IR} is defined as $Q_{\text{IR}} = Q_0 \sin(\Omega_{\text{IR}} t)$, where Q_0 and Ω_{IR} are the amplitude and the angular frequency of the B_{1u} mode, respectively. As the frequency of the infrared-active phonon is significantly higher than the one of the spin precession ($\Omega_{\text{IR}} \ll \omega$), Eq. 5.16 has to be time-averaged (integrated). The averaging shows that the phonon-induced additive ΔK_2 is determined by the rectified part of the phonon-coordinate, which depends quadratically on the am-

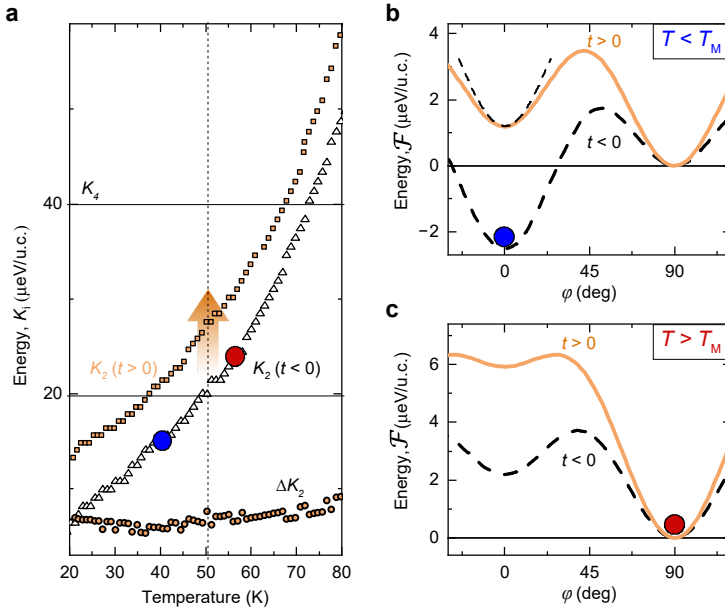


Figure 5.13: **Change of the magnetic potential after phonon-pumping.** **a**, The anisotropy parameters K_2 and K_4 before and after the phonon pumping and the pump-induced change ΔK_2 as extracted from the temperature dependence of the soft mode precession frequencies. **b,c**, Equilibrium (black, dashed line, $t < 0$) and reconstructed transient magnetic potential (orange line, $t > 0$) after excitation of the phonon mode in the AFM (**b**) and WFM (**c**) phase. The position of the balls indicate the magnetic ground state of the system before excitation.

plitude Q_0 , such that:

$$\Delta K_2 = \frac{1}{2} A_2 Q_0^2 \propto I, \quad (5.17)$$

where I is the fluence/intensity of the laser pulse tuned in the resonance with the phonon mode.

5.7.5. NONLINEAR LATTICE DYNAMICS AND THEIR EFFECT ON THE MAGNETIC EXCHANGE INTERACTIONS

To find a possible physical origin of this quadratic dependence we performed an extensive set of DFT simulations to find microscopic sources of such a nonlinear lattice-driven response.

CALCULATED IR AND RAMAN-ACTIVE MODE FREQUENCIES

In Table 5.1, we report the calculated IR and Raman-active mode frequencies in DyFeO_3 . Both the Raman and IR active modes are in good agreement with the experiments and previous DFT calculations done by Weber et al. [194]. The few small deviations between our results and the previous calculations can be due to the use of different lattice parameters (experimental cell parameters were used by Weber et al. while we used relaxed

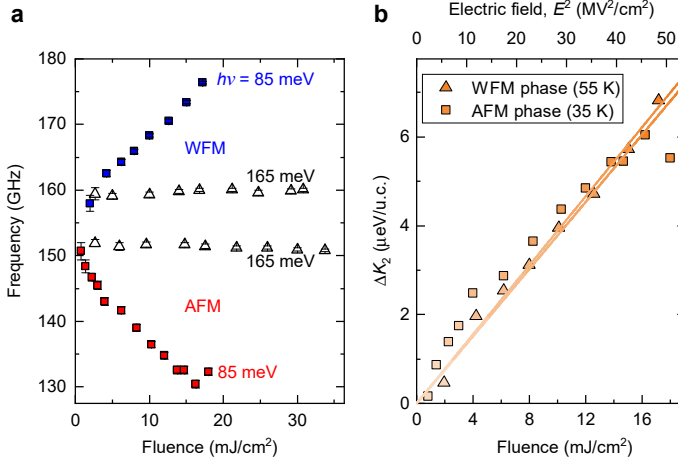


Figure 5.14: **Fluence dependence of the spin precession frequency and K_2 anisotropy.** **a**, Frequency of the spin oscillation as function of the laser fluence. The open and solid markers correspond to measurements at a pump photon energy of 165 meV and 85 meV respectively. The red and blue data points correspond to the sample being in the AFM and WFM phases, respectively. **b**, The phonon-induced additive ΔK_2 to the K_2 anisotropy as a function of the pump fluence in the AFM (square markers) and the WFM (triangular markers) phase after resonant phonon-excitation, with linear fits.

5

PBEsol cell parameters), to the different PAW atomic potentials or because we used f -electrons in the valence for Dy.

Table 5.1: **DyFeO₃ phonon mode frequencies.** Calculated energies of the DyFeO₃ IR-active (left) and Raman-active (right) phonon modes. first column: mode label of the $Pnma$ structure with f electrons in the core; second column: calculated energy. Reference DFT (Ref.) and experimental (Exp.) energy values reported in Ref. [194] given in the third and fourth column.

Phonon mode	Ω_{IR} (meV)	Phonon mode	Ω_{R} (meV)	Ref.	Exp.
B _{1u} (1)	13.14	A _g (1)	13.27	13.89	14.01
B _{1u} (2)	21.70	A _g (2)	16.49	16.74	17.36
B _{1u} (3)	31.00	A _g (3)	30.87	32.48	32.36
B _{1u} (4)	34.47	A _g (4)	40.67	41.16	42.28
B _{1u} (5)	39.92	A _g (5)	50.58	52.32	52.32
B _{1u} (6)	43.02	A _g (6)	50.58	51.45	51.70
B _{1u} (7)	48.72	A _g (7)	51.20	52.32	52.32
B _{1u} (8)	61.62	A _g (8)	59.51	60.75	61.49
B _{1u} (9)	67.32	B _{1g} (1)	16.86	16.74	–
B _{2u} (1)	18.84	B _{1g} (2)	30.38	31.00	–
B _{2u} (2)	20.08	B _{1g} (3)	43.76	44.51	44.76
B _{2u} (3)	32.23	B _{1g} (4)	51.95	52.94	52.94
B _{2u} (4)	37.19	B _{1g} (5)	73.27	73.52	–
B _{2u} (5)	43.52	B _{2g} (1)	13.27	13.51	13.76
B _{2u} (6)	60.75	B _{2g} (2)	19.22	19.96	20.21
B _{2u} (7)	65.34	B _{2g} (3)	36.95	38.56	40.29
B _{3u} (1)	12.40	B _{2g} (4)	43.15	43.52	–
B _{3u} (2)	23.18	B _{2g} (5)	58.77	59.76	61.25
B _{3u} (3)	29.01	B _{2g} (6)	65.34	66.21	–
B _{3u} (4)	35.95	B _{2g} (7)	75.63	75.88	77.36
B _{3u} (5)	38.31	B _{3g} (1)	14.88	15.25	–
B _{3u} (6)	41.16	B _{3g} (2)	38.06	38.56	–
B _{3u} (7)	52.57	B _{3g} (3)	51.70	52.57	53.68
B _{3u} (8)	63.73	B _{3g} (4)	56.41	57.03	58.77
B _{3u} (9)	65.09	B _{3g} (5)	78.98	78.98	79.22

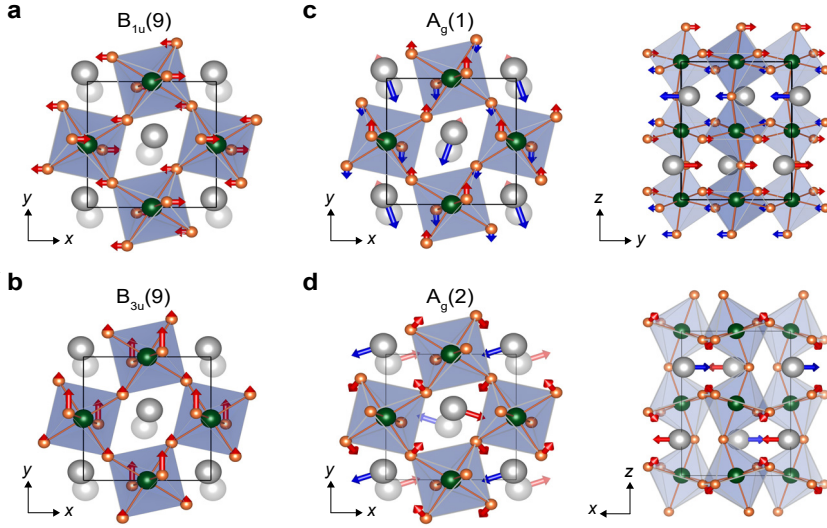


Figure 5.15: **Highest and lowest frequency phonon modes.** Schematic picture in which the arrows depict the polar components of the eigenvectors of the highest-frequency infrared-active, orthogonally polarized $B_{1u}(9)$ (a) and $B_{3u}(9)$ (b) phonon modes and the eigenvectors of the $A_g(1)$ (c) and $A_g(2)$ (d) phonon modes, as viewed from two different directions. Grey/green/orange spheres represent dysprosium/iron/oxygen atoms. The oxygen octahedra are drawn in light-blue. The presence of red and blue colored arrows for a type of atom indicates opposite movement.

LASER EXCITATION AND NONLINEAR PHONON-PHONON COUPLING MODE

To simulate an excitation of the phonon mode with an ultrashort laser pulse we consider the laser field to be a Gaussian function:

$$E(\omega) = \frac{E_0}{2\pi\sigma_\omega} e^{-\frac{(\omega-\omega_0)^2}{2\sigma_\omega^2}}. \quad (5.18)$$

We set the central frequency ω_0 ($\hbar\omega_0 = 81$ meV) and the frequency broadening σ_ω to match the experiment and consider the peak amplitude strength of the electric field $E_0 = 10$ MV/cm. The electric field excites the $B_{1u}(9)$ and $B_{3u}(9)$ modes having the highest frequencies. These two modes are polar in the x - and y -directions and correspond to a stretching of the oxygen bonds, see Fig. 5.15a,b. We study different possibilities of phonon-phonon coupling that can cause a change in the magnetic exchange interactions. One possibility is the nonlinear coupling of the IR modes to other phononic modes, dubbed nonlinear phononics [119, 122]. According to this mechanism when large-amplitude atomic vibrations are excited, a nonlinear response sets in, causing a net shift of the lattice energy potential along a Raman-active normal mode coordinate for a time given by the lifetime of the infrared-active phonon. The ensuing net distortion of the unit cell can consequently change the magnetic interactions of Fe and Dy and result in a spin reorientation. To determine the relevant nonlinear phonon-phonon couplings, we use the potential energy $V(Q)$ containing several anharmonic phonon-phonon interactions:

$$V(Q) = \frac{1}{2}\omega_{\text{IR}}^2 Q_{\text{IR}}^2 + \frac{1}{2}\omega_{\text{R}}^2 Q_{\text{R}}^2 + C_{\text{R}} Q_{\text{R}}^3 + \gamma_1 Q_{\text{R}} Q_{\text{IR}}^2 + \gamma_2 Q_{\text{R}}^2 Q_{\text{IR}}^2 + \frac{1}{4}d_{\text{IR}} Q_{\text{IR}}^4 + \frac{1}{4}d_{\text{R}} Q_{\text{R}}^4 \quad (5.19)$$

In Eq. 5.19 Q_X are mode amplitudes of phonon mode X ($X = \text{IR}, \text{R}$) with eigenfrequencies ω_X . C_{R} , γ_1 , d_{IR} , d_{R} and γ_2 are coefficients fitted against DFT data in the spirit of Ref. [125]. We consider the highest IR frequency $B_{1u}(9)$ mode excited by the laser and its coupling to each A_g mode because they are the first order couplings coming into play in the 20 atoms perovskite $Pnma$ phase. The A_g mode label being invariant under all the symmetry operations of the crystal, any coupling order with this mode is allowed such that the lowest order is of the type $Q_{A_g} Q_{B_{1u}}^2$. As one can see in Table 5.2, of all the coupling orders, the γ_1 parameter gives the strongest coupling with the B_{1u} mode. Fitting the coupling coefficients between the $B_{1u}(9)$ mode and the A_g modes, we find that the second lowest frequency $A_g(2)$ mode (see its schematic representation in Fig. 5.15d) gives the strongest coupling γ_1 , closely followed by the first one $A_g(1)$ (Fig. 5.15c)

Table 5.2: DFT fitted coupling coefficients of Eq. 5.19 for B_{1u} coupling with $A_g(1)$ and $A_g(2)$ modes. The units are $(\text{meV}/\sqrt{\text{u}\text{\AA}})^2$.

Coupled modes	C_{R}	d_{IR}	d_{R}	γ_1	γ_2
$B_{1u}-A_g(1)$	-0.004	0.0072	0.000	0.0681	0.000
$B_{1u}-A_g(2)$	0.003	0.0072	0.000	0.1246	0.000

The main difference between the $A_g(1)$ and $A_g(2)$ modes is in the way the antipolar motions of Dy ions are involved. Using the high symmetry reference cubic perovskite we can observe that the $A_g(1)$ mode is dominated by the cubic X point antipolar motion mode of Dy atoms (with coordinate $[1/2, 0, 0]$ of the cubic Brillouin zone and symmetry label X_5^-), while the $A_g(2)$ mode is dominated by the R point mode (coordinate $[1/2, 1/2, 1/2]$ of the cubic Brillouin zone and symmetry label R_4^-). By doing the same analysis for the $B_{1u}(9)$ mode, we find that this polar mode is dominated by the M_2^+ cubic mode label involving oxygen octahedral rotations ($a^0 a^0 b^+$) in Glazer notation [195]) plus the polar mode label Γ_4^- (with polarization direction along the x direction) plus R_4^- antipolar motions of the Dy atoms. Note that the Dy atoms have a very small amplitude contribution to the mode eigenvector due to the fact that at high frequency they are much less involved in the phonon vibrations. The fact that the $B_{1u}(9)$ allows, by symmetry, antipolar motions of Dy of the same type as the $A_g(2)$ mode (R_4^- label for both) can explain why this $A_g(2)$ mode has a larger coupling with the $B_{1u}(9)$ mode than the $A_g(1)$ mode.

The dynamics of the $A_g(1)$ and $A_g(2)$ modes in response to the laser excitation of the B_{1u} mode is shown in Fig. 5.16. One can see that although the laser field drives the B_{1u} atomic motions with zero average displacement about the equilibrium crystal structure, the $A_g(1)$ and $A_g(2)$ are rectified. The periodic motion is not around the equilibrium value of zero, but rather around a non-zero value which signals a distorted unit cell as compared to the equilibrium. This net distortion quickly decays, as its lifetime is defined by the lifetime of the coherent infrared-active phonon mode (several picoseconds). The displacement of the $A_g(1)$ mode reaches a value of $Q = 0.015 \sqrt{\text{u}\text{\AA}}$ (see Fig. 5.16). Using the eigenvector containing the atomic motion corresponding to this mode (partly shown

in Table 5.3) and the atomic mass of the Dy ion (162.5 u), this amplitude can be converted into an atomic displacement. This is done by multiplying the eigenvector component of a Dy ion with the A_g displacement and dividing by the square root of the Dy mass leads to an atomic displacement of around 0.2 pm.

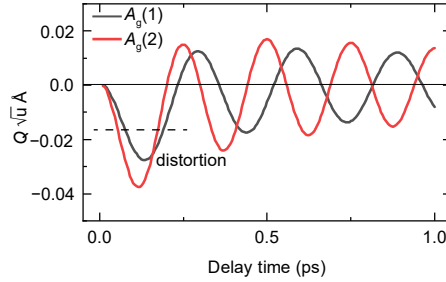


Figure 5.16: **DFT simulations of the phonon dynamics.** Time-evolution of the Raman-active phonons $A_g(1)$ and $A_g(2)$ following the resonant excitation of the B_{1u} mode.

5

Table 5.3: Part of the normalized $A_g(1)$ eigenvector corresponding to Dy^{3+} ion motion for the four different Dy ions in a unit cell in the three crystallographic directions x , y , z .

	Dy ₁	Dy ₂	Dy ₃	Dy ₄
x	-0.165	0.165	0.165	-0.165
y	0.465	0.465	-0.465	-0.465
z	0	0	0	0

MAGNETIC EXCHANGE INTERACTIONS

To study how the indirectly driven A_g modes can change the magnetic interaction between Fe and Dy, we used a Green's function method to calculate the superexchange interaction as a function of the A_g modes amplitude following the scheme of Korotin et al. [196] as implemented in the TB2J code [197]. We report the evolution of the Fe-Dy and Fe-Fe superexchange with respect to both $A_g(1)$ and $A_g(2)$ mode amplitudes. We observe that the two Raman-active modes can drive different modifications of the Fe-Dy superexchange interaction, which can be decomposed into eight contributions related to the eight Fe ions surrounding one Dy ion as shown in Fig. 5.17a,b. Table 5.4 summarizes the normalized variation of exchange with respect to the amplitude of the mode ($\frac{1}{J} \frac{dJ}{dQ}$) for both Fe-Dy and Fe-Fe superexchanges. One can see that A_g modes affect much more the Fe-Dy exchange than the Fe-Fe one, making the Fe-Fe exchange variation being negligible.

To have the net change in exchange interaction between each ion and its neighbours, we summed all the exchanges and fit the data with a linear equation. Figure 5.17c shows the change in this net superexchange for the $A_g(1)$ and $A_g(2)$ modes. As can be seen, the $A_g(2)$ mode has nearly the same influence on the Fe-Dy exchange as the $A_g(1)$ mode. Both interactions result in a change with same sign and the final change in the superex-

Table 5.4: Summary of the absolute values (second column) and normalized variations $dJ_i/(J_i dQ)$ of the Fe-Dy and Fe-Fe exchange interactions as a function of the normal phonon coordinates of the $A_g(1)$ (third column) and $A_g(2)$ modes (fourth column).

Label	Exchange (meV)	$\frac{dJ_i}{(J_i dQ)}$ $A_g(1)$	$\frac{dJ_i}{(J_i dQ)}$ $A_g(2)$
J_1	-0.987	-0.011	-0.047
J_2	-0.197	0.077	0.060
J_3	-0.814	0.022	-0.050
J_4	-0.256	-0.129	-0.081
J_5	-0.963	0.041	-0.067
J_6	-0.090	0.059	0.607
J_7	-0.938	-0.001	0.084
J_8	-0.217	0.037	0.289
Fe-Fe		0.001	0.001

5

change will be the sum of the two contributions. $Q = 0.015 \sqrt{u} \text{\AA}$ for both modes leads to a change in the Fe-Dy exchange interaction of around $1.5 \mu\text{eV}$.

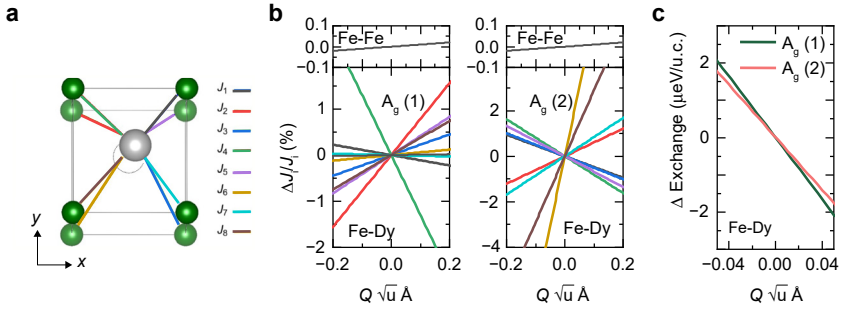


Figure 5.17: **Fe-Dy anisotropic exchange as function of A_g mode amplitudes.** **a**, The Fe-Dy superexchange as decomposed into eight contributions related to the eight Fe ions surrounding one Dy ion. The grey/green balls correspond to Dy/Fe ions. The empty dashed black circle corresponds to the equilibrium Dy atom as if not displaced from the high-symmetry cubic position. **b**, Variations $dJ_i/(J_i)$ in the superexchange interactions between Dy and Fe (bottom) and in the Fe-Fe exchange (top) as a function of the distortions along the $A_g(1)$ (left) and $A_g(2)$ (right) mode coordinate. **c**, Change in the net superexchange interaction between each Dy ion and its eight Fe neighbours for $A_g(1)$ (red line) and $A_g(2)$ (blue line). The result is obtained by summing up the eight contributions shown in panel **b** and **c** and using the absolute values of the exchange interactions.

6

CONTROLLING THE ANISOTROPY OF VAN DER WAALS ANTIFERROMAGNET NiPS_3 VIA ORBITAL RESONANCES

“Insight must precede application.”

Max Planck

In this chapter we explore the effect of resonant excitation of orbital resonances on the anisotropy in the van der Waals antiferromagnet NiPS_3 . Anisotropy plays a crucial role in the stabilization of two-dimensional long-range magnetic order, as the Mermin-Wagner theorem dictates that in reduced dimensions isotropic spin interactions cannot retain long-range correlations. By tuning the photon energy in resonance with an orbital transition between crystal-field split levels of the nickel ions, we demonstrate the selective activation of a sub-THz magnon mode with markedly two-dimensional behaviour. The pump polarization control of the magnon amplitude confirms that the activation is governed by the photoinduced magnetic anisotropy axis emerging in response to photoexcitation of ground state electrons to states with a lower orbital symmetry. Our results show that the excitation of orbital resonances is a viable route to manipulate magnetic order in low-dimensional (anti)ferromagnets.

This chapter has been published with minor differences in Science Advances 7, eabf3096 (2021) by D. Afanasiev, J. R. Hortensius, M. Matthiesen, S. Mañas-Valero, M. Šiškins, M. Lee, E. Lesne, H. S. J. van der Zant, P. G. Steeneken, B. A. Ivanov, E. Coronado and A. D. Caviglia [198].

The NiPS_3 crystal was synthesized by S. Mañas-Valero and E. Coronado. B. A. Ivanov developed the theoretical formalism to describe the magnetization dynamics.

The recent discoveries of van der Waals (vdW) two-dimensional (2D) layered magnets have led to a surge of interest due to their potential applications in constructing atomically-thin spin-processing devices and non-volatile magnetic memories [199, 200]. Unique phenomena and effects are foreseen in 2D magnetic systems due to their reduced dimensionality [201]. In contrast to three-dimensional magnets, long-range magnetic order cannot exist in two dimensions at any finite temperature without the presence of magnetic anisotropy [41, 202]. In 2D magnets, the anisotropy not only sets a preferred direction for spins but also protects the magnetic order against dimensionality-enhanced thermal spin fluctuations. This intimate relationship between magnetic order and anisotropy in 2D motivates the ongoing search for efficient pathways to manipulate the magnetic anisotropy in such systems. As the magnetic anisotropy in most materials is determined by the coupling of electronic orbitals and spins, stabilizing and controlling 2D magnetism is actively pursued through the manipulation of orbital degrees of freedom, using, for example, mechanical strain [203–205] and electrostatic gating [206, 207]. However, a large anisotropy is normally associated with an unquenched orbital moment, which is limited to specific oxidation states and to low-symmetry crystal environments, most notably for rare-earth ions [208]. In most 2D magnets, magnetism arises from transition metal ions, which typically have a quenched orbital moment in their ground state. In these systems magnetic anisotropy originates from the spin-orbit driven mixing of the ground state with higher-energy orbital states with unquenched momentum, a rather small effect. Optical pumping of the electronic transition towards the higher-level orbital states (orbital resonances) provides the most direct access to the admixing and subsequent control of the magnetic anisotropy as manifested by the excitation of spin precession in 3D magnets [59, 61, 209, 210], even to the extent of the sub-cycle coherent switching of the spin orientation [38, 60, 211]. Resonant pumping of orbital transitions in two-dimensional magnets, characterized by the subtle interplay between anisotropy and magnetic order, offers unique insights into dynamics of their highly-nontrivial elementary excitations, such as for example topological magnons [43, 212].

Here we study resonant optical control of magnetism in nickel phosphorus trisulfide NiPS_3 , a novel van der Waals layered magnet with XY-type antiferromagnetism [213–215]. The energetic competition between charge-transfer and Coulomb repulsion makes this system an intriguing example of a strongly correlated 2D magnet, with pronounced spin-charge correlations [216], spin-orbit entangled excitons [217], and strong spin-lattice coupling [218, 219]. We optically pump NiPS_3 using ultrashort pulses of light and probe the ensuing spin dynamics on the picosecond timescale. Continuously varying the pump photon energy across orbital resonances, we identify a transition to the orbital state responsible for the anisotropic magnetic properties in equilibrium. By resonant optical pumping of this transition we demonstrate the selective activation of a hitherto unreported two-dimensional magnon mode with a THz frequency demonstrating the XY-critical scaling with temperature. By studying the mode's excitation as a function of the pump polarization and photon energy, we show that the activation indeed proceeds as a result of the light-induced magnetic anisotropy emerging in response to the resonant photoexcitation of the higher energy orbital states of Ni^{2+} electrons. We also find that optical pumping in the region of optical transparency impulsively activates another high-

frequency coherent mode, a previously unreported candidate for the complementary magnon mode in NiPS₃.

6.1. MAGNETIC AND OPTICAL PROPERTIES OF NiPS₃

NiPS₃ crystallizes in the monoclinic space group $C/2m$ [220] (see Fig. 6.1a). In the ab plane, it features a network of edge-sharing NiS₆ octahedra arranged on a honeycomb lattice, each having a small trigonal distortion perpendicular to this plane (Fig. 6.1b). Below the Néel temperature $T_N = 155$ K, the magnetic moments of Ni²⁺ ions arrange into a complex compensated antiferromagnetic pattern. The pattern is formed by zig-zag ferromagnetic spin chains along the a -axis, which are coupled antiferromagnetically within the single layer [221] (Fig. 6.1a). A large spacing $c = 6.63$ Å between adjacent layers leads to a negligible orbital overlap between the magnetic ions of different layers, thereby suppressing interlayer exchange such that the antiferromagnetic order acquires a 2D character already in the bulk form.

The orientation of magnetic moments in NiPS₃ is governed by a biaxial magneto-crystalline anisotropy consisting of two distinct contributions: a dominant easy-plane anisotropy which locks the orientation of the spins to a magnetic plane (xy), slightly inclined from the crystallographic ab -plane; and a secondary weaker anisotropy which orients the spins in the magnetic (xy)-plane along the x -axis. Microscopically, the easy-plane anisotropy develops as a result of a zero-field splitting ($D \approx -1.1$ meV [222]) of the ³A_{2g} ground state of the Ni²⁺ ion ($S = 1$) in the crystal field of the trigonally distorted NiS₆ octahedra (see Fig. 6.1b). Note that ³A_{2g} is an orbital singlet and alone cannot develop the splitting. The splitting and anisotropy arise indirectly as a consequence of spin-orbit driven intermixing of the ground state with the first excited orbital triplet state ³T_{2g}, which is split by the trigonal lattice distortion [222, 223] into a set of low-symmetry doublets ³E_g and singlets ³A_{1g} separated by an energy gap of around 110 meV, as schematically shown in Fig. 6.1b. Although there are no reports on the origin of the in-plane magnetic anisotropy along the x -axis in NiPS₃, it likely stems from a rhombic distortion of the NiS₆ octahedra, which further splits the ³A_{2g} levels. Hence, an anisotropic Hamiltonian considering not only the axial distortion of the octahedron, but also an in-plane distortion may be needed to take this observation into account (see section 6.7.3).

The orbital resonances in NiPS₃ correspond to a pair of d - d transitions ³A_{2g} → ³T_{2g} and ³A_{2g} → ³T_{1g} emerging within the ³F ground state multiplet of the Ni²⁺ ion split by the octahedral crystal field (O_h) (see Fig. 6.1b). In NiPS₃ these transitions result in a pair of two broad optical absorption bands centred at 1.07 eV (³A_{2g} → ³T_{2g}) and 1.73 eV (³A_{2g} → ³T_{1g}). Note that in contrast to other transition metal ions, the d - d resonances in Ni²⁺ are spin-parity allowed ($\Delta S = 0$), i.e. they do not involve a spin-flip, and thus cannot directly affect the exchange interaction between adjacent spins.

6.2. SELECTIVE LIGHT-INDUCED MAGNETIC DYNAMICS

To selectively address the orbital resonances, we employed ultrashort (~ 100 fs) pump pulses with photon energy tunable in a broad spectral range of 0.1–0.9 eV. The pump-induced dynamics were measured by tracking the intensity I and the rotation of the polarization plane θ of time-delayed co-propagating near-infrared probe pulses at a pho-

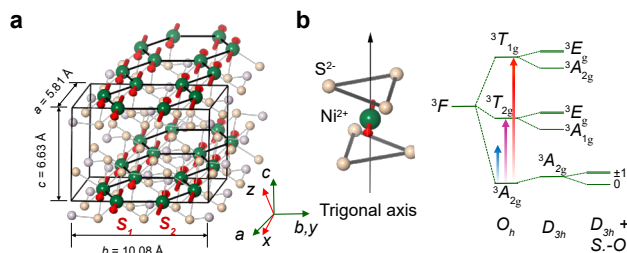


Figure 6.1: **Magnetic properties of the antiferromagnet NiPS₃.** **a**, Crystallographic and magnetic structure of NiPS₃. Green/fade orange/light pink spheres represent nickel/sulphur/phosphorous atoms. The green and red triple vectors are crystallographic and magnetic frames, respectively. **b**, Left: Ni²⁺ ion in the trigonally distorted octahedral sulphide environment. Right panel: Crystal field splitting of the ground state and first excited triplet state for Ni²⁺ ion (*O_h*: octahedral field) in a trigonally distorted octahedral environment (*D_{3h}*); S.-O.: spin-orbit coupling. (0, ±1) correspond to the projection of the spin moment along the trigonal distortion axis. The coloured arrows represent the different photon energies of the optical excitation used in the experiment.

ton energy of 1.55 eV, as schematically shown in Fig. 6.2a. Whereas I is considered as a measure of the non-magnetic components of the dielectric tensor, θ is sensitive to the magnetic order via magneto-optical effects, such as the Faraday effect and magnetic linear birefringence. The sample was cooled down to 10 K well below T_N and pumped using linearly polarized pulses at variable photon energies. The time-resolved polarization rotation θ reveals a striking sensitivity of the pump-induced dynamics to the photon energy of the excitation (see Fig. 6.2b,c). When excited at the ${}^3A_{2g} \rightarrow {}^3T_{2g}$ resonance ($h\nu = 0.97$ eV), θ displays a damped oscillation as a function of the pump-probe time delay Δt , with frequency $f_1 = 0.30$ THz (see Fig. 6.6 for the Fourier spectra). No coherent oscillations were observed when exciting at the higher photon energy ($h\nu = 1.8$ eV) corresponding to the ${}^3A_{2g} \rightarrow {}^3T_{1g}$ resonance. Detuning the photon energy below the absorption lines of the resonances ($h\nu = 0.8$ eV) shows no signal associated with the frequency f_1 , but reveals instead another higher-frequency mode at $f_2 = 0.92$ THz. We found no match for the frequencies of these oscillations in the phonon spectrum of NiPS₃, well studied in recent years [218, 219, 224], which hints at a magnetic origin.

To understand the significance of the orbital resonances, we tracked the ultrafast dynamics while varying the pump photon energies across the subgap states down to the phonon Reststrahlen band edge at 0.1 eV. The amplitudes of both oscillations at $f_{1,2}$ were retrieved and their relative values (normalized on the pump fluence) plotted as a function of the pump photon energy. Figure 6.3a shows that the f_2 mode is excited in the broad window of optical transparency 0.1–0.9 eV, indicating the off-resonant character of the excitation and impulsive stimulated Raman scattering process (ISRS) as a plausible mechanism. In striking contrast the excitation of the lower-frequency f_1 mode only occurs in a relatively narrow photon energy range, showing a pronounced resonance with the ${}^3A_{2g} \rightarrow {}^3T_{2g}$ transitions, see Fig. 6.3a. The lineshape of the resonance reveals a fine structure indicative of the trigonal splitting of the ${}^3T_{2g}$ manifold (${}^3E_g, {}^3A_{1g}$) (see Fig. 6.1b). Despite a nearly order of magnitude stronger optical absorption, no oscillations were seen upon resonant pumping of the ${}^3A_{2g} \rightarrow {}^3T_{1g}$ higher energy orbital resonance, underscoring the sensitivity of the oscillations to the photoexcitation of the

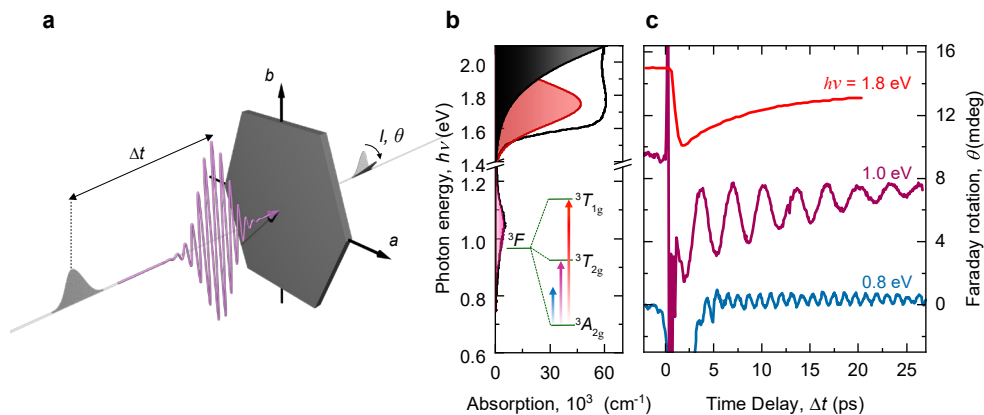


Figure 6.2: **Ultrafast light-induced dynamics in NiPS₃.** **a**, Schematic of the time-resolved pump-probe experiment. The pump (pink) and near-infrared probe (grey) pulses are collinearly focused onto the sample with variable time delay Δt . The pump induced dynamics is measured by tracking the pump-induced polarization rotation θ and intensity I of the probe pulses. **b**, Optical absorption spectrum of NiPS₃ displaying ${}^3A_{2g} \rightarrow {}^3T_{2g}$ and ${}^3T_{2g} \rightarrow {}^3T_{1g}$ absorption bands due to the d - d orbital resonances of Ni²⁺ ions (in pink and red respectively), and the onset of the above bandgap absorption due to Ni-S charge transfer transitions (black band). **c**, Experimentally detected polarization rotation signal θ as a function of the delay time, after excitation with pump pulses at various photon energies.

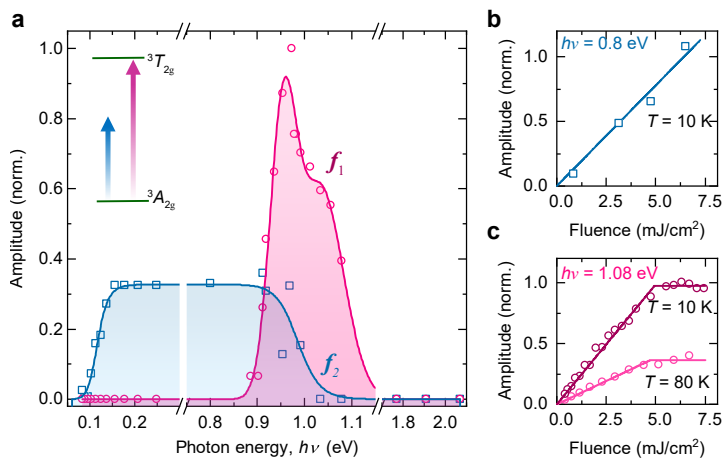


Figure 6.3: **Selective excitation of the light-induced coherent dynamics.** **a**, Amplitudes of the coherent oscillations corresponding to the modes at frequencies $f_{1,2}$ normalized to the maximal value of the f_1 mode as a function of the pump photon energy. Solid lines are guides to the eye. Inset: Schematic illustration of the optical transition at which the f_1 mode is observed. **b, c**, Amplitude of the oscillation as a function of the pump fluence for the f_2 (**b**) and f_1 mode (**c**). The solid lines are linear fits, including saturation.

${}^3T_{2g}$ states. Remarkably, whereas the amplitude of the mode at f_2 reveals a linear dependence on the pump fluence (Fig. 6.3b), the amplitude of the f_1 mode saturates above

5 mJ/cm (Fig. 6.3c), indicating a possible saturation of the ${}^3A_{2g} \rightarrow {}^3T_{2g}$ transition.

6.3. EXCITATION OF AN IN-PLANE MAGNETIC MODE

The temperature (T) dependence of the frequencies $f_{1,2}$ evidences that these modes are indeed sensitive to the magnetic ordering. Figure 6.4a shows that as T increases, the damping of the first mode goes up while the frequency f_1 gradually decreases and ultimately converges to zero at a temperature close to T_N . Although the application of a relatively weak in-plane magnetic field H up to 7 kOe produced no observable shift in f_1 (see section 6.7.2), the observation of the critical softening is a strong indication that the oscillation is of magnetic origin [225, 226]. The softening can be characterized by a power law $f_1(T) \propto (T_N - T)^\beta$ (see Fig. 6.4c), with $T_N \approx 155$ K, in full agreement with literature data, and a critical exponent $\beta = 0.23 \pm 0.01$ valid down to the temperature $T_0 = 0.65T_N$ (see Fig. 6.8). Note that the β value also matches remarkably well with the critical exponent of the XY-model ($\beta_{XY} = 0.23$) previously proposed to describe the temperature evolution of the 2D magnetic ordering in NiPS₃ [227–229]. This observation is unambiguous and at the same time surprising indication of the intrinsically 2D character of the mode observed in the bulk form of NiPS₃.

The temperature-evolution of the higher-frequency oscillation at f_2 is significantly different. As T increases, the central frequency f_2 shows a slight increase, which above 75 K is followed by a steep, nearly linear, softening. A linear extrapolation of the frequency decrease versus T suggests that a complete softening of the mode occurs at $T = 170$ K, in proximity to T_N (see Fig. 6.4d). The softening indicates that the oscillation is either of magnetic origin itself or strongly sensitive to the magnetic ordering. This is further corroborated by the significant increase of the damping constant upon heating. Such highly damped behaviour is typical for soft modes in the vicinity of their associated phase transitions [230].

We now analyze the spin dynamics in NiPS₃ from a phenomenological theory perspective. Two magnon modes are expected in a compensated antiferromagnet with a biaxial magnetic anisotropy [90, 231]. The modes correspond to orthogonal deflections of the Néel vector defined as $\mathbf{L} = S(\mathbf{S}_1 - \mathbf{S}_2)$, where $S = S(T)$ is the average value of the Ni²⁺ spin and $\mathbf{S}_{1,2}$ is a pair of antiferromagnetically coupled spins. In equilibrium, \mathbf{L} is oriented along the x -axis, and deflections are expected in (\parallel) and out (\perp) of the magnetic easy-plane (xy), in such a way that the dynamical components ΔL_y and ΔL_z emerge (see Fig. 6.4e,f). The frequencies $f_{\parallel,\perp}$ of the magnons are defined by the geometric mean of the respective magnetic anisotropy ($D_{\parallel,\perp}$) and exchange energy J_{ex} and in addition proportional to $S(T)$ (see section 6.7.3):

$$\omega_{\parallel,\perp} \sim S(T) \sqrt{D_{\parallel,\perp} J_{\text{ex}}} \quad (6.1)$$

Hence, both should experience a power law temperature scaling inherent to the magnetic order parameter \mathbf{L} similarly to the one observed for the f_1 mode. As the out-of-plane anisotropy is typically more substantial for easy-plane antiferromagnets such as NiPS₃, $f_{\parallel} \ll f_{\perp}$ is expected. Note that although there is no net magnetization in the ground state: $\mathbf{M} = S(\mathbf{S}_1 + \mathbf{S}_2) = 0$, a finite magnetization component $\mathbf{M} \propto [\dot{\mathbf{L}}, \mathbf{L}]$ emerges due to the dynamics of the Néel vector \mathbf{L} (see section 2.5). As a consequence, the in- and

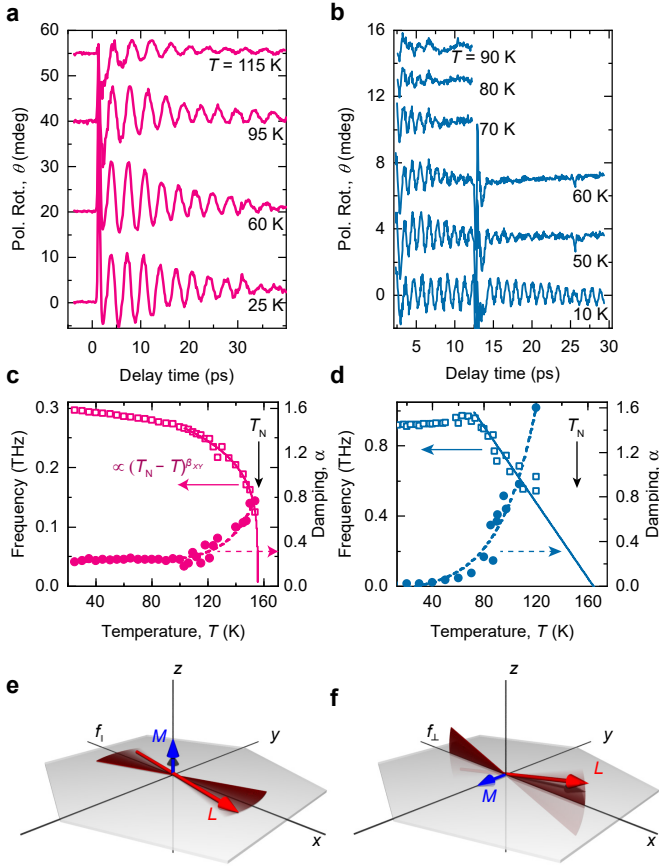


Figure 6.4: **Critical behavior of the light-induced coherent dynamics.** **a, b**, Temperature dependence of the time-resolved polarization rotation after pump-induced excitation with photon energies of 1.08 eV (**a**) and 0.2 eV (**b**). Irregularities around a time delay of 13 ps in (**b**) are related to an artifact of the measurement setup. **c, d**, Frequency (left axis) and damping factor α (right axis) of the oscillations as extracted from the damped sine fits of the time-domain data in panel **a** and **b**. The solid lines represent the best fit of $(T_N - T)^\beta$ (**c**), which gives $T_N = (15 \pm 5)$ K and $\beta = 0.23$, and a linear function (**d**) to the frequency data. **e, f**, Schematics of the in-plane (**e**) and out-of-plane (**f**) magnon modes.

out-of-plane magnetic modes can be fully described by the orthogonal pairs (L_y, M_z) and (L_z, M_y) , respectively.

In Ref. [232] it was recently shown that the application of an in-plane magnetic field larger than $H_{sf} = 100$ kG promotes a spin-flop transition in NiPS_3 during which the spins suddenly rotate in the easy-plane and in addition cant along the field orientation. It can be easily shown (see section 6.7.4) that the magnitude of the spin-flop field H_{sf} is a direct measure of the frequency of the in-plane dynamics $f_{\parallel} = 2\pi\gamma H_{sf} = 280$ GHz, where $\gamma/2\pi = 28 \times 10^{-4}$ GHz/G is the gyromagnetic ratio. This estimate agrees particularly well with f_1 and thus provides another strong indication that the coherent oscillation excited

upon resonant pumping of the ${}^3A_{2g} \rightarrow {}^3T_{2g}$ transition is the in-plane magnon mode characterized by L_y and M_z and a two-dimensional critical scaling. We note that even though there is an oscillating out-of-plane magnetic component M_z , the experimentally observed oscillations show a strong phase- and amplitude-dependence on the orientation of the probe polarization plane with respect to the crystal axes, indicating that the detection of this mode is given by linear magnetic birefringence due to the L_y component rather than Faraday rotation, sensitive to M_z [233].

Having identified $f_{\parallel} = f_1$, we propose that the higher frequency oscillation at f_2 can be assigned to the complementary out-of-plane magnon ($f_{\perp} = f_2$). Indeed, our phenomenological theory (see section 6.7.5) suggests that excitation of the out-of-plane magnon mode with linearly polarized light is possible in NiPS₃ due to the low-symmetry (monoclinic) distortion of the crystal lattice. However, these assumptions do not agree with the recently reported, mutually conflicting, values for the zone-center magnon at the significantly higher frequencies of 1.69 and 2.4 THz from Ref. [234] and [217] respectively. To unambiguously establish the origin of the coherent mode f_2 , time-resolved measurements in high magnetic fields $H \geq H_{sf}$, are of primary importance.

6.4. SELECTION RULES FOR THE MAGNON EXCITATION

To further our understanding of the excitation mechanism of the in-plane (f_1) magnon and its relation to the light-induced magnetic anisotropy, we varied the orientation of the pump polarization plane, set by the azimuthal angle ϕ (see Fig. 6.5a). Although the optical absorption at the ${}^3A_{2g} \rightarrow {}^3T_{2g}$ orbital resonance is nearly independent of ϕ , the amplitude and phase of the induced magnetic oscillations are strongly affected by variation of the angle. Figure 6.5b shows that the amplitude of the excited magnon follows a clear π -periodic sinusoid with maxima corresponding to the polarization oriented at $\pm 45^\circ$ with respect to the orientation of the Néel vector \mathbf{L} . This dependence can be understood as follows: the incident linearly polarized light, at normal to the (*ab*)-crystal plane, promptly induces a magnetic anisotropy axis directed along the orientation of the pump polarization plane. The axis breaks the magnetic symmetry in the basal plane (*xy*), providing an in-plane magnetic torque sufficiently short to impulsively trigger planar spin motion (see Fig. 6.5c). The validity of this scenario is further supported by a phenomenological theory based on symmetry considerations and general principles of light-matter interactions in a magnetic medium (see section 6.7.5).

The azimuthal dependence of the oscillation amplitude on the orientation of the pump polarization allows us to attribute the excitation of the in-plane magnon mode to an ultrafast light-induced change of the magnetocrystalline anisotropy. This anisotropy emerges in response to resonant optical excitation of the Ni²⁺ electrons to the ${}^3T_{2g}$ orbital state, characterized by an unquenched net angular momentum. To estimate the lifetime of the photoinduced anisotropy we performed a time-resolved analysis of the frequency of the spin precession at various fluences of the incident pump. A long-living change in the anisotropy should renormalize the magnon frequency within the lifetime of the excited state in agreement with Ref. [162, 235] and Eq. 6.1 and thus can be seen as a measure of the magnetic anisotropy relaxation. Consequently, exciting with greater fluence would amplify this effect: the spin precession frequency would scale with the fluence. In contradiction to this, we observe that fluence affects only the amplitude but

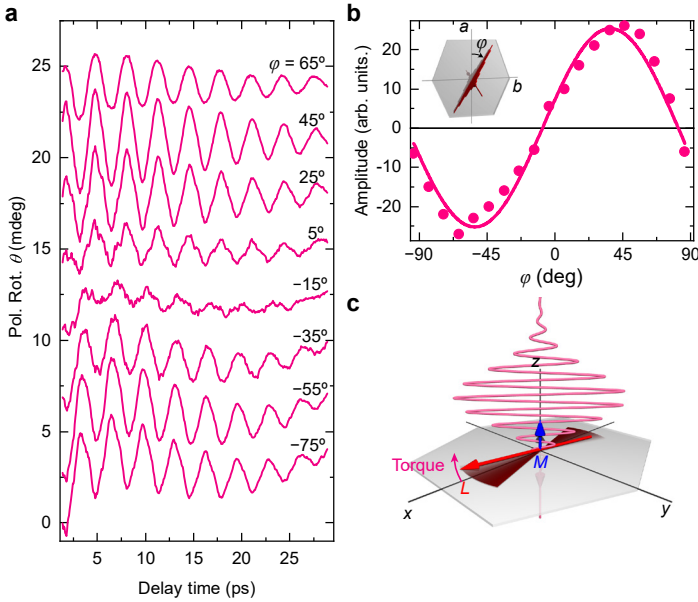


Figure 6.5: **Selection rules for the excitation of the in-plane magnetic mode.** **a**, Pump-induced rotation of the probe polarization plane as a function of pump-probe delay time Δt for different orientations of the linear polarization of the pump. The pump photon energy is 1.0 eV. **b**, The amplitude of the oscillations as a function of the azimuthal angle ϕ between the pump polarization plane and the a -crystal axis. **c**, Schematics showing that the electric field of light acts as an instantaneous photo-magnetic anisotropy (dashed line) with a direction along the light polarization plane, resulting in torque and subsequent oscillations of the Néel vector L and net magnetization M .

not the frequency of the spin precession (see Fig. 6.12), which indicates that the lifetime of the anisotropy is at least shorter than the period of the spin precession (<3 ps). The short lifetime of the anisotropy can originate from the short-lived photoexcited state, whose lifetime is given by the natural width of the ${}^3A_{2g} \rightarrow {}^3T_{2g}$ absorption line (0.2 eV) and is on the order of 20 fs. Interestingly, the observed polarization control of the spin precession is strongly reminiscent of the inverse Cotton-Mouton effect [48], a particular variant of the magnetic ISRS also widely considered as an instantaneous photo-induced magnetic anisotropy [236, 237]. In the magnetic ISRS scenario, the pump photon is scattered in an event wherein an electron momentarily gains orbital angular momentum from the higher-level orbital states typically having energy higher than the incident photon. Our experimental results can be thus interpreted alternatively as being indicative of the resonant enhancement of the scattering process upon approaching the transition to the higher-level ${}^3T_{2g}$ orbital state, underlining the strong impact of the low-symmetry trigonal ${}^3T_{2g}$ states on the magnetic anisotropy of NiPS₃. Indeed, several works reported that magnetic ISRS processes in iron-based compounds can be significantly enhanced in the vicinity of the d - d transitions, see for example Refs. [209, 210]. Our experiment shows that almost no magnon excitation is observed for the photon energies below the ${}^3A_{2g} \rightarrow {}^3T_{2g}$ resonance, contrary to what is expected for the ISRS process. The resonant

enhancement picture must thus assume that the magnon amplitude falls below our detection limit away from the resonance. Regardless of the exact microscopic nature of the driving mechanism, we emphasize the crucial role of the d - d transitions for optical control of magnetic anisotropy in NiPS₃.

6.5. CONCLUSIONS

In conclusion, our work establishes selective pumping of orbital resonances as an efficient pathway to control magnetic anisotropy and to reveal high-frequency two-dimensional coherent spin dynamics in van der Waals layered antiferromagnets. While ultrafast control of the magnetic anisotropy and sub-THz spin dynamics is demonstrated here in bulk lamellar NiPS₃, due to advances in exfoliating techniques and strong magneto-optical responses observed in our experiments, we anticipate the applicability of the suggested approach to atomically thin antiferromagnets [218, 238]. Such systems can serve as an excellent testbed for the theoretical XY-model, with further possibilities such as revealing dynamics of nontrivial topological vortex states associated with the Berezinskii-Kosterlitz-Thouless transition [201, 218].

6.6. METHODS

SAMPLE

Crystals of NiPS₃ were grown by chemical vapor transport. First, polycrystalline NiPS₃ was synthesized by mixing powders of S (99.998%, from Sigma-Aldrich), P (> 99.99%, from Sigma-Aldrich) and Ni (99.99%, from Sigma-Aldrich) in a stoichiometric ratio, pressed into a pellet and sealed in a quartz ampoule ($P \sim 5 \times 10^{-5}$ mbar, length: 25 cm, internal diameter: 1.5 cm). The ampoule was kept at 400°C for twenty days and cooled down slowly (0.07 °C/min). Next, the previous material was mixed with iodine (99.999% anhydrous beads from Sigma-Aldrich; $[I_2] \sim 5$ mg/cm³), sealed in an evacuated quartz ampoule ($P \sim 5 \times 10^{-5}$ mbar, length: 50 cm, internal diameter: 1.5 cm) and placed in a three-zone furnace in a gradient of temperatures of 700 °C/650 °C/675 °C for 28 days. Phase and compositional purity were verified by powder X-ray diffraction and ICP-OES (Inductively Coupled Plasma - Optical Emission Spectrometry). The materials were handled inside an argon glove-box to avoid any possible oxidation. Exact details about temperature gradients and characterization of crystals from the same batch as the ones studied in this work can be found in Ref. [203].

EXPERIMENTAL SETUP

The pump pulses at the photon energies of 0.8–1.9 eV (~100 fs) were obtained using an optical parametric amplifier (OPA), and to access energies below 0.4 eV (~200 fs) we used difference frequency generation (DFG) by mixing the outputs of two OPAs in a GaSe crystal [239]. The pump pulses at a 500 Hz repetition rate were focused on the sample surface to a spot with a diameter of 200 μm. The time-delayed co-propagating near-infrared probe pulses at a photon energy of 1.55 eV were focused to a spot of 130 μm such that the spatial overlap between pump and probe pulses was satisfied.

6.7. SUPPLEMENTARY INFORMATION

6.7.1. EXCITATION OF MAGNETIC AND PHONON MODES

Figure 6.6 shows the Fourier spectra of the time-resolved polarization rotation after excitation at different pump photon energies at or close to the ${}^3A_{2g} \rightarrow {}^3T_{2g}$ absorption line. The sub-THz modes correspond to the modes with frequency f_1 and f_2 as discussed in section 6.2. The amplitude spectrum also reveals the presence of high-frequency modes, with frequencies between 4 and 7.5 THz. These modes correspond to previously reported A_g phonon modes in NiPS₃ [218, 219, 224, 238].

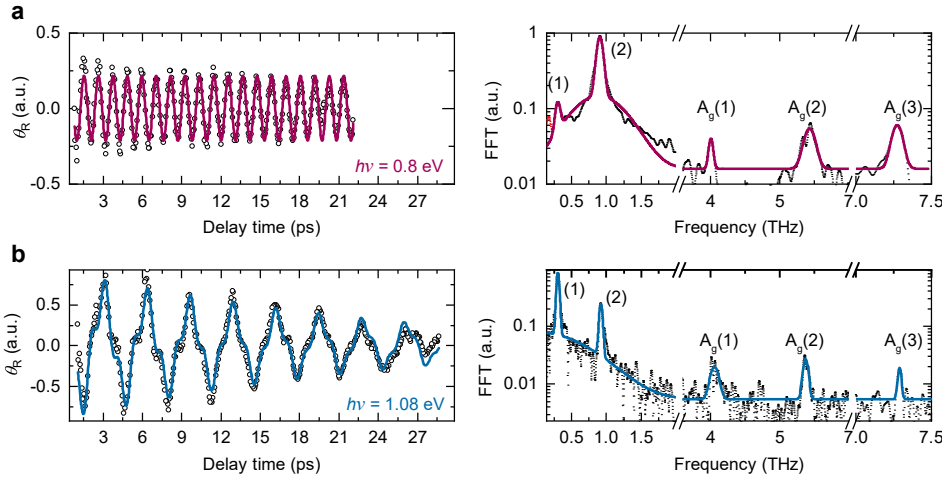


Figure 6.6: **Light-induced magnetic and phonon modes.** **a,b**, Transient polarization rotation θ_R as a function of the delay time between the pump and the probe pulse (left) and the corresponding FFT spectrum (right) after excitation with pump pulses at a photon energy of 0.8 eV (**a**) and 1.08 eV (**b**).

6.7.2. CHARACTERIZATION OF THE SUB-THZ MODES

In order to identify the origin of the sub-THz oscillations, we perform additional measurements. We perform the experiment in different magnetic fields. Fig. 6.7 shows the pump-induced dynamics in different applied magnetic fields. Both the mode at frequency f_1 (Fig. 6.7a) and at frequency f_2 (Fig. 6.7b) are not sensitive to the magnetic field applied in this range. Moreover, we plot the frequency of the f_1 -mode vs. temperature on a log-log scale in Fig. 6.8. The linear fit of the high-temperature data points gives the value of the critical exponent $\beta = 0.23$. A deviation from this scaling law occurs for temperatures below $T_0 = 0.65T_N$.

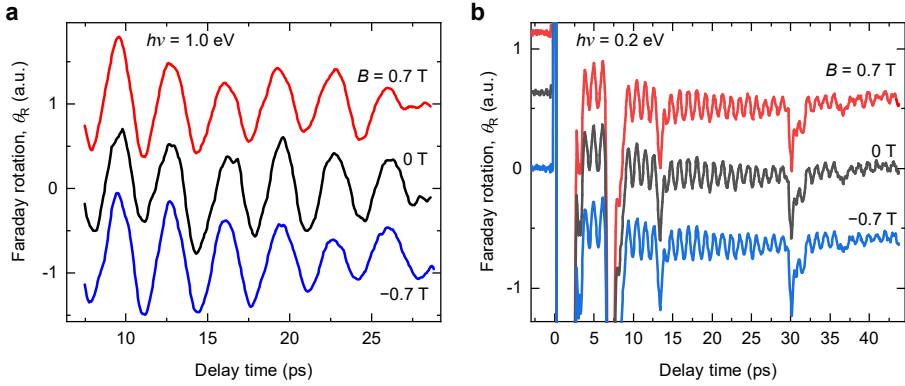


Figure 6.7: **Magnetic field dependence.** **a, b,** Pump-induced polarization rotation for different values of the external magnetic field applied in the sample (*ab*) plane, after excitation at a pump photon energy of 1.0 eV (**a**) and 0.2 eV (**b**). The traces for different magnetic fields are shifted for clarity.

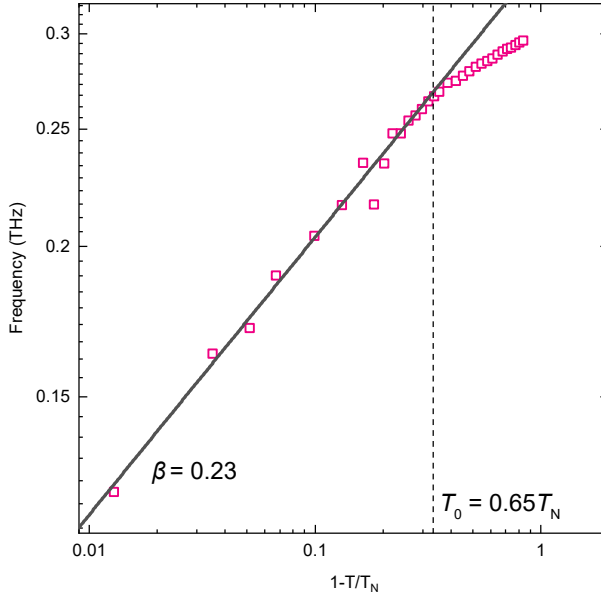


Figure 6.8: **Temperature-dependence.** The magnon frequency f_1 for different temperatures on a *log-log* scale. The solid line is a linear fit to the high-temperature datapoints close to the Néel temperature T_N and provides the value of the critical exponent $\beta = 0.23$.

6.7.3. SUPPORTING SPIN DYNAMICS THEORY

In this section we show that for an anisotropic magnetic Hamiltonian with both an axial distortion and an in-plane distortion there are two magnon modes. We derive the frequencies of these magnon modes in terms of anisotropy parameters, in order to relate

them to (known) material parameters. The derivation of antiferromagnetic dynamics closely follows the one in section 2.5 in chapter 2.

We start with an expression for the magnetic energy density in terms of the normalized variants \mathbf{l} and \mathbf{m} of the conventional Néel vector \mathbf{L} and net magnetization \mathbf{M} (see section 2.5):

$$w = 2zJS^2\mathbf{m}^2 + 2D_{\perp}S^2(l_z^2 + m_z^2) + 2D_{\parallel}S^2(l_y^2 + m_y^2) - 2g\mu_B\mathbf{S}\mathbf{H} \cdot \mathbf{m}. \quad (6.2)$$

The first term concerns the exchange energy between coupled spins, the second and third term reflect the anisotropy energy and the final term involves the Zeeman energy.

- $J > 0$ – phenomenological constant describing the (antiferromagnetic) exchange interaction between neighbouring spins.
- z is the number of nearest neighbours with antiparallel alignment of the spins.
- $D_{\perp}, D_{\parallel} > 0$ – phenomenological constants describing the strength of the out-of-plane (\perp) and in-plane anisotropy (\parallel). The form of the magnetic anisotropy term is chosen such that the spins are oriented along the x axis in the ground state and accounts for distortions of the magnetic site along the main symmetry axis (z) and in the perpendicular xy plane.
- g – value of the Landé factor for the Ni^{2+} magnetic moment
- μ_B – Bohr magneton
- \mathbf{H} – external magnetic field

$S(T)$ is the temperature-dependent averaged value of a single spin, whose temperature behaviour in vicinity of T_N is typically described by a power law scaling such that:

$$S(T) \sim (T_N - T)^{\beta}, \quad (6.3)$$

with β the scaling power and $S \approx 1$ at low temperatures.

Note that the exchange and Zeeman terms in the expression in Eq. 6.2 agree with Eq. 2.28 in chapter 2, using that the sublattice magnetization $M_0 = g\mu_B S = \gamma\hbar S$ and the exchange field $H_{\text{ex}} = \frac{2SzJ}{\gamma\hbar}$ [90].

The corresponding equations of motion for \mathbf{m} and \mathbf{l} derive from the Landau-Lifshitz equations for the magnetic sublattices (Eq. 2.26). Neglecting the applied magnetic field (and again using $M_0 = \gamma\hbar S$) this gives:

$$\begin{cases} 2\hbar S \frac{d\mathbf{m}}{dt} = \left[\mathbf{m} \times \frac{\partial w}{\partial \mathbf{m}} \right] + \left[\mathbf{l} \times \frac{\partial w}{\partial \mathbf{l}} \right] \\ 2\hbar S \frac{d\mathbf{l}}{dt} = \left[\mathbf{m} \times \frac{\partial w}{\partial \mathbf{l}} \right] + \left[\mathbf{l} \times \frac{\partial w}{\partial \mathbf{m}} \right] \end{cases} \quad (6.4)$$

In the ground state, the (normalized) Néel vector \mathbf{l} is oriented along the x -axis, such that

$$\mathbf{l} = l_0 \mathbf{e}_x, \quad \mathbf{m} = 0,$$

where $l_0 = \pm 1$ accounts for the time-reversal symmetry of the Néel state. From $\mathbf{m}^2 + \mathbf{l}^2 = 1$ one obtains $\mathbf{l} \cdot \partial \mathbf{l} = 0$. This means that the dynamics of the Néel vector is reduced to transverse deviations $\tilde{\mathbf{l}} = (\tilde{l}_y, \tilde{l}_z)$ of \mathbf{l} from the equilibrium value:

$$\mathbf{l} = l_0 \mathbf{e}_x + \tilde{\mathbf{l}} \quad (6.5)$$

Here we consider small-amplitude oscillations of the Néel vector. In the linear approximation we can get a simple, closed expression for the equations of motions for \mathbf{l} and \mathbf{m} without resorting to the Lagrangian. Substituting Eq. 6.5 into Eq. 6.4 results in a pair of coupled differential equations for the deviations $\tilde{\mathbf{l}}, \tilde{\mathbf{m}}$:

$$\begin{aligned} 2\hbar S \dot{\tilde{\mathbf{m}}} &= \left[l_0 \mathbf{e}_x \times \frac{\partial w}{\partial \tilde{\mathbf{l}}} \right] = 2l_0 \left(0, -2D_\perp S^2 l_z, 2D_\parallel S^2 l_y \right) \\ 2\hbar S \dot{\tilde{\mathbf{l}}} &= \left[l_0 \mathbf{e}_x \times \frac{\partial w}{\partial \tilde{\mathbf{m}}} \right] = 2l_0 \left(0, -2(zJ + D_\perp) S^2 m_z, 2(zJ + D_\parallel) S^2 m_y \right) \end{aligned} \quad (6.6)$$

These equations can be split into two pairs of linear differential equations for (l_y, m_z) and (l_z, m_y) :

$$\begin{cases} \hbar \frac{dm_z}{dt} = 2D_\parallel l_0 S l_y \\ \hbar \frac{dl_y}{dt} = -2(zJ + D_\perp) l_0 S m_z \end{cases} \quad \begin{cases} \hbar \frac{dm_y}{dt} = -2D_\perp l_0 S l_z \\ \hbar \frac{dl_z}{dt} = 2(zJ + D_\parallel) l_0 S m_y \end{cases} \quad (6.7)$$

Reducing these two systems of first-order linear differential equations to single second-order differential equations, we obtain two equations describing the in- and out-of-plane spin dynamics:

$$\begin{aligned} \ddot{l}_y + \left(\frac{l_0 S}{\hbar} \right)^2 4(zJ + D_\perp) D_\parallel l_y &= 0 \\ \ddot{l}_z + \left(\frac{l_0 S}{\hbar} \right)^2 4(zJ + D_\parallel) D_\perp l_z &= 0 \end{aligned} \quad (6.8)$$

The corresponding frequencies of the in-plane and out-of-plane oscillatory motion are then given by:

$$\begin{aligned} \omega_\perp &= \frac{2S}{\hbar} \sqrt{D_\parallel (zJ + D_\perp)} \approx \frac{2S(T)}{\hbar} \sqrt{(D_\parallel zJ)} \\ \omega_\parallel &= \frac{2S}{\hbar} \sqrt{D_\perp (zJ + D_\parallel)} \approx \frac{2S(T)}{\hbar} \sqrt{(D_\perp zJ)}, \end{aligned} \quad (6.9)$$

where the approximation $zJ \gg D_{\perp, \parallel}$ was used. Eq. 6.9 shows that the frequencies of the in-plane magnon and out-of-plane magnons are governed by the strength of the corresponding anisotropies. This means that the magnon frequencies can be used to estimate D_\perp and D_\parallel if the strength of the antiferromagnetic exchange parameter J is known. As mentioned before, $H_{\text{ex}} = \frac{2S z J}{\gamma \hbar}$ [90]. If we substitute $H_{\text{a},(1,2)} = \frac{2S D_{\perp, \parallel}}{\gamma \hbar}$ [90], we see that the frequencies are equivalent to the obtained frequencies for antiferromagnetic dynamics in chapter 2.

Note that the frequencies are proportional to the average spin value $S(T)$ and are thus subjected to a similar power law scaling (Eq. 6.3). The temperature-dependence of the anisotropy constants $D_{\perp, \parallel}$ can contribute to the total temperature-dependence of the magnon frequency. As we observed in the experiments (section 6.3) that $f_{\parallel} = f_{\perp} \sim S(T)$, we can conclude that the mode is of magnetic origin and that $D_{\parallel}(T)$ is independent of temperature.

6.7.4. RELATION BETWEEN THE SPIN-FLOP FIELD AND THE MAGNON FREQUENCY

We consider a magnetic field $\mathbf{H} = H_x \mathbf{e}_x$ applied along the x -direction. Using Eq. 6.2, this gives for the magnetic energy:

$$w = 2zJS^2 \mathbf{m}^2 + 2D_{\perp} S^2 (l_z^2 + m_z^2) + 2D_{\parallel} S^2 (l_y^2 + m_y^2) - 2g\mu_B S H_x m_x. \quad (6.10)$$

In the magnetic (xy)-plane we introduce an angle θ that the vector \mathbf{l} forms with the x -axis (see Fig. 6.9) such that:

$$\begin{aligned} \mathbf{m} &= m (\mathbf{e}_x \sin \theta - \mathbf{e}_y \cos \theta) \\ \mathbf{l} &= \sqrt{1 - m^2} (\mathbf{e}_x \cos \theta - \mathbf{e}_y \sin \theta) \end{aligned} \quad (6.11)$$

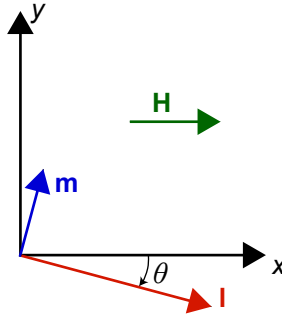


Figure 6.9: **Spin-flop experimental geometry.** The vector \mathbf{l} makes an angle θ with the magnetic x -axis in the xy -plane. The magnetic field is oriented in the x -direction.

Substituting this expression into Eq. 6.10 gives:

$$w = 2zJS^2 m^2 + 2D_{\parallel} S^2 \left[(1 - m^2) \sin^2 \theta + m^2 \cos^2 \theta \right] - 2g\mu_B S H_x m \sin \theta. \quad (6.12)$$

Minimizing w with respect to m gives:

$$m(\theta) = \frac{g\mu_B H_x \sin \theta}{2(zJ + D_{\parallel} \cos 2\theta)}. \quad (6.13)$$

Now substituting this into the expression for the magnetic energy w (Eq. 6.12) gives:

$$w(\theta) = -\frac{1}{2} \frac{(g\mu_B H_x) \sin^2 \theta}{(zJ + D_{\parallel} \cos 2\theta) S} + D_{\parallel} S^2 \sin^2 \theta. \quad (6.14)$$

Eq. 6.14 can be minimized with respect to the angle θ . Depending on the strength of the magnetic field, two different solutions exist:

1. For $H_x < H_1 = \frac{2S\sqrt{D_{\parallel}(zJ+D_{\perp})}}{g\mu_B}$, the collinear AFM phase is stable and $\theta = 0$, $m_x = 0$.
2. For $H_x > H_2 = \frac{2S\sqrt{D_{\parallel}(zJ-D_{\perp})}}{g\mu_B}$, the canted AFM phase is stable and $\theta = \frac{\pi}{2}$, $m_x = \frac{g\mu_B H_x}{2(zJ-D_{\parallel})}$.

Note that $H_1 > H_2$ and for $H_2 < H_x < H_1$, the canted and collinear phases coexist. Importantly, the higher field H_1 at which the collinear phase becomes unstable is directly related to the frequency of the in-plane spin precession:

$$H_1 = \frac{\hbar\omega_{\parallel}}{g\mu_B}$$

and thus can serve to estimate its value:

$$\hbar\omega_{\parallel} = g\mu_B H_1$$

6.7.5. LIGHT-MATTER INTERACTION IN NiPS₃ AND THE RESULTING SPIN-DYNAMICS

To account for the observed interaction between the Ni²⁺ spins and the ultrashort pulses we write the free energy term W_{int} in a quadratic form with respect to the electric field of light \mathbf{E} and the antiferromagnetic vector \mathbf{l} :

$$W_{\text{int}} = C_{ikpq} E_i E_k l_p l_q,$$

which is allowed by the magnetic and crystallographic point group of NiPS₃. Here C_{ikpq} are the components of the magnetoelectric susceptibility tensor C .

In the monoclinic system with C_2 symmetry along the y -axis, such as NiPS₃, the tensor C reads (in Voigt notation):

$$C = \begin{pmatrix} C_{11} & C_{12} & C_{13} & C_{14} & 0 & 0 \\ C_{21} & C_{22} & C_{23} & C_{24} & 0 & 0 \\ C_{31} & C_{32} & C_{33} & C_{34} & 0 & 0 \\ C_{41} & C_{42} & C_{43} & C_{44} & 0 & 0 \\ 0 & 0 & 0 & 0 & C_{55} & C_{56} \\ 0 & 0 & 0 & 0 & C_{65} & C_{66} \end{pmatrix}, \quad \begin{pmatrix} 1 \\ 2 \\ 3 \\ 4 \\ 5 \\ 6 \end{pmatrix} = \begin{pmatrix} xx \\ zz \\ yy \\ xz \\ yz \\ xy \end{pmatrix}.$$

The electric field \mathbf{E} of the laser pulse at normal incidence to the surface of the sample (ab -plane) is $\mathbf{E} = (E_a, E_b, 0)$. Projecting this electric field \mathbf{E} on the (xyz) magnetic reference frame gives $\mathbf{E} = (E_x, E_y, E_z) = (E_a \cos \gamma, E_b, E_a \sin \gamma)$, where γ is the angle between the x -axis and the a -axis in the ac plane.

Considering that in the linear approximation $l_x l_y$ and $l_x l_z$ are the only non-zero products of the Néel vector components that can contribute to the excitation of the spin dynamics, we find:

$$W_{\text{int}} = (AE_a^2 + BE_b^2) l_x l_z + GE_a E_b l_x l_y,$$

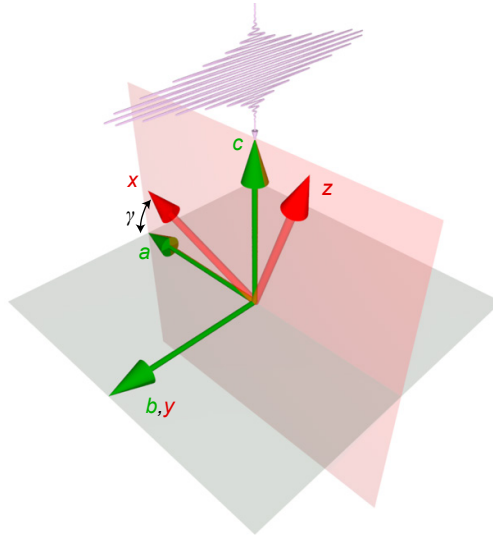


Figure 6.10: **Experimental geometry.** Relative orientation of the laser polarization with respect to the magnetic (xyz) and crystallographic (abc) reference planes.

6

where

$$\begin{aligned} A &= C_{14} \cos \gamma^2 + C_{24} \sin \gamma^2 + C_{44} \sin \gamma \cos \gamma \\ B &= C_{34} \\ G &= C_{56} \sin \gamma + C_{66} \cos \gamma. \end{aligned}$$

In our experiments, the laser light is linearly polarized, with the polarization plane oriented at an angle ϕ with respect to the crystallographic a -axis and therefore

$$\mathbf{E} = (E_0 \cos \phi, E_0 \sin \phi, 0),$$

$E_0(t) \approx E_0 \delta(t)$ is the time-dependent component of the electric field of the laser pulse. Thus, the interaction energy reduces to

$$W_{\text{int}} = \frac{1}{2} E_0^2(t) \left[((A+B) + (A-B) \cos 2\phi) l_x l_z + G \sin 2\phi l_x l_y \right]. \quad (6.15)$$

The W_{int} is anisotropic with respect to the components of the \mathbf{l} vector and thus during its presence in the medium, the light acts on the spins as an effective magnetic anisotropy. This action generates a torque $\frac{\partial W_{\text{int}}}{\partial t}$ which leads to a time-dependent force term $F_{y,z}(t)$ on the right-hand side of the equations of the motion (Eq.6.6):

$$\begin{cases} 2\hbar S \dot{m}_z &= l_0 (2D_{\parallel} S^2 l_y + F_y(t) l_0) \\ \hbar \dot{l}_y &= -2(zJ + D_{\perp}) l_0 S m_z \end{cases} \quad \begin{cases} 2\hbar S \dot{m}_y &= -l_0 (2D_{\perp} l_0 S^2 l_z + F_z(t) l_0) \\ \hbar \dot{l}_z &= 2(zJ + D_{\parallel}) l_0 S m_y, \end{cases} \quad (6.16)$$

with

$$\begin{aligned} F_y(t) &= G \sin 2\phi \cdot E_0^2(t) \\ F_z(t) &= \frac{1}{2} [(A+B) + (A-B) \cos 2\phi] E_0^2(t) \end{aligned} \quad (6.17)$$

The corresponding equations of the spin motion (Eq. 6.8) is then given by:

$$\begin{aligned} \ddot{l}_y + \omega_{\parallel}^2 l_y &= -\frac{(zJ + D_{\perp})l_0}{2\hbar^2} F_y(t) \\ \ddot{l}_z + \omega_{\perp}^2 l_z &= -\frac{(zJ + D_{\parallel})l_0}{2\hbar^2} F_z(t). \end{aligned} \quad (6.18)$$

Considering that duration of the pump pulse ($\Delta t \sim 100$ fs) is much shorter than the period of spin oscillations, $\Delta t \ll \frac{2\pi}{\omega_{\parallel,\perp}}$, the real pulse shape can be replaced by the Dirac delta function $\delta(t) : E_0^2(t) \rightarrow I_0 \delta(t)$, where $I_0 = \int E_0^2(t) dt$ is the integrated pulse intensity. This substitution clearly shows that action of the pump pulse is reduced to a nearly instantaneous force/torque impulsively launching the spin dynamics.

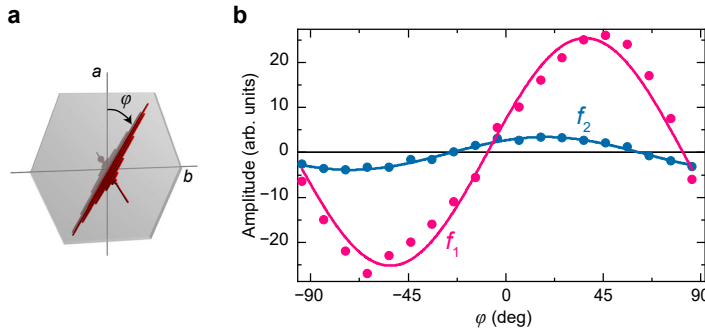


Figure 6.11: **Pump polarization dependence.** **a**, Schematic showing the geometry of the experiment. **b**, The amplitude of the oscillations with frequency f_1 and f_2 as a function of the azimuthal angle ϕ between the pump polarization plane and the a -axis.

One can see that to excite the in-plane dynamics l_y of the Néel vector, the polarization of light has to be oriented off the a and b axis of the crystal and reaches maxima of opposite sign at $\phi = \pm 45^\circ$ in perfect agreement with our experiment and the ultrafast Inverse Cotton-Mouton effect. Interestingly, the formulas also clearly show that excitation of the out-of-plane dynamics l_z of the Néel vector is also possible at the normal incidence. Note, the excitation is allowed only because of the monoclinic distortion as the excitation relies on the non-zero components A, B , each depending on the monoclinic terms C_{i4} of the magnetoelectric susceptibility tensor C .

Remarkably, the dependence of the magnon amplitude on the orientation of the pump pulse is expected to be the same as for the in-plane mode but 45° degrees shifted (compare $\sin 2\phi$ and $\cos 2\phi$ in Eq. 6.17). In the experiment, an 180° dependence of the coherent oscillation at f_2 was also observed. However, only a 22° shift was observed as

compared to the f_1 mode, see Fig. 6.11. The discrepancy can be explained by the birefringence of the crystal which influences the linear polarization of the incident pump light.

6.7.6. FLUENCE DEPENDENCE OF THE MAGNON MODE

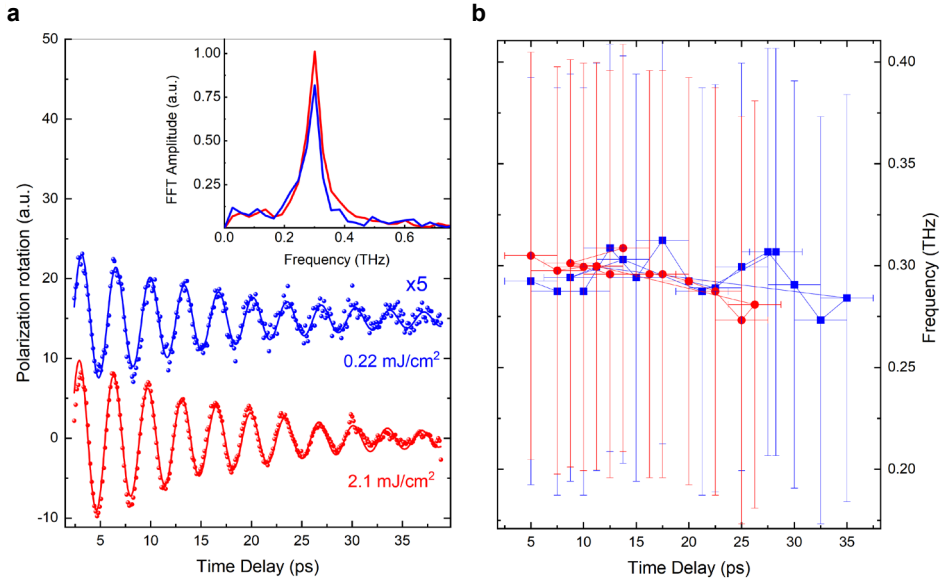


Figure 6.12: **Pump fluence dependence.** **a**, Time-resolved dynamics of the in-plane magnon mode for two significantly different fluences of the pump excitation at $T = 10$ K. Solid lines are damped sine fits to the experimental data. Inset shows FFT amplitude of the time-varying signals. **b**, Time-resolved dynamics of the frequency of the magnon mode. The data points are obtained via sine fit of the individual data segments presented in (a) using a sliding time window with a width of 5 ps. The horizontal error bars are derived from the width of the sliding window.

7

BROADBAND SPIN-WAVE EMISSION IN AN INSULATING ANTIFERROMAGNET

"Surprise is the greatest gift which life can grant us."

Boris Pasternak

In chapter 4 we observed that confined resonant excitation can generate broadband phonon wavepackets in wide-bandgap insulators. Ultrashort pulses of light have been routinely used to excite uniform spin precession in antiferromagnets, as we also observed in chapter 5 and 6. In this chapter we combine these concepts and demonstrate the efficient emission and detection of a nanometer-scale wavepacket of coherent propagating magnons in the insulating antiferromagnet DyFeO₃ using ultrashort pulses of light. The subwavelength confinement of the laser field due to large absorption creates a strongly non-uniform spin excitation profile, enabling the propagation of a broadband continuum of coherent THz spin waves. The wavepacket contains magnons with a shortest detected wavelength of 125 nm that propagate with supersonic velocities of more than 13 km/s into the material. This source of coherent short-wavelength spin carriers opens up new prospects for THz antiferromagnetic magnonics and coherence-mediated logic devices at THz frequencies.

This chapter has been published with minor differences in Nature Physics **17**, 1001 (2021) by J. R. Hortensius, D. Afanasiev, M. Matthiesen, R. Leenders, R. Citro, A. V. Kimel, R. V. Mikhaylovskiy, B. A. Ivanov, and A. D. Caviglia [240].

The theoretical formalism of the spin-wave detection was developed by R. Leenders and R. V. Mikhaylovskiy. B. A. Ivanov developed the general theoretical framework describing the spin-wave propagation.

7.1. INTRODUCTION

Antiferromagnetic insulators (AFMs) are prime candidates to replace ferromagnets (FMs) as active media in the quest towards high-speed spin transport and large spectral bandwidth operation [180, 241, 242]. Integration of AFMs in future wave-based technologies [62, 67, 243] crucially requires the realization of coherent (ballistic) transport of antiferromagnetic spin waves over large distances [244]. In this regard, non-uniform spin-wave modes with short wavelengths ($\lambda_m < 100$ nm) are of particular importance: they can operate at THz clock rates, exhibit high propagation velocities and enable the miniaturization of devices down to the nanoscale. Phase-coherent ballistic spin transport in AFMs is also interesting from a fundamental point of view, as it is anticipated to be a prerequisite for the occurrence of exotic phenomena such as magnetic solitons [91], Bose-Einstein condensates [245, 246] and spin-superfluidity [247–249]. Such prospects motivate a search for efficient methods for the excitation, manipulation, and detection of short-wavelength coherent antiferromagnetic magnons.

Conventional methods of linear spin-wave excitation use spatially varying oscillating magnetic fields. However, the high frequency of THz resonances inherent to antiferromagnetic dynamics make traditional field sources based on microstrip lines or coplanar waveguides impractical to be used in antiferromagnetic media. As a result, recent demonstrations of magnon-mediated spin transport in antiferromagnets were limited to either diffusive propagation of incoherent magnons [250–252] or evanescent spin-wave modes [253]. The experimental generation of coherent propagating short-wavelength magnons, which enables phase-coherent transport in an antiferromagnet, has so far remained elusive.

7

Ultrashort pulses of light have been routinely used to generate and to control large-amplitude THz spin precession [46, 47, 55] in antiferromagnets. The small photon momentum, however, poses a problem: it gives rise to a large momentum mismatch with short-wavelength spin waves. Consequently, optical techniques have so far been restricted to the generation of $k = 0$ uniform antiferromagnetic magnons and/or pairs of mutually coherent magnons at the edges of the Brillouin zone [254], for which group velocities are (near-)zero and no spatial transport of energy and angular momentum takes place. Here we overcome this problem and present an all-optical method to excite and detect a broadband wavepacket of short-wavelength coherent propagating magnons in an insulating antiferromagnet. Optical excitation of intense charge-transfer electronic transitions in the prototypical antiferromagnet DyFeO₃ with ultrashort pulses of light provides strong confinement of the light field, which creates a narrow exponential profile of deflected spins near the sample surface. This nanoscale magnetic non-uniformity serves as a source of short-wavelength coherent spin waves propagating into the sample bulk, as illustrated in Figure 7.1a. Using k -selective magneto-optical Bragg detection we map out spectral components of the magnon wavepacket and reveal magnon modes with nanoscale wavelengths, supersonic group velocities and an estimated propagation length of more than 1 μm .

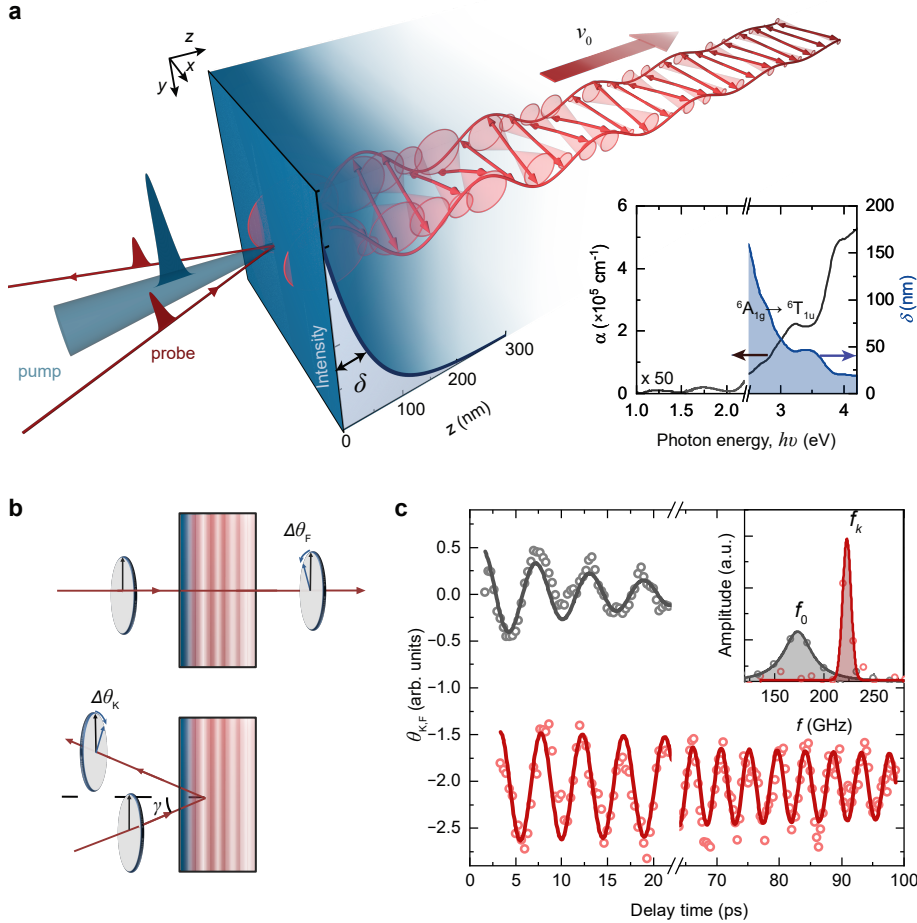


Figure 7.1: **All-optical generation and detection of coherent antiferromagnetic spin waves.** **a**, Schematic of the generation of propagating AFM spin waves after optical pumping. The optical penetration depth δ of the light defines the excited region and the width of the magnetic non-uniformity. Inset: Absorption coefficient α (left axis) and corresponding penetration depth δ (right axis) for DyFeO₃ as function of photon energy $h\nu$ (see Methods). ${}^6A_{1g} \rightarrow {}^6T_{1u}$: the charge-transfer transition of interest. **b**, Schematics for the optical detection mechanisms of spin waves in transmission (top) and reflection (bottom) geometries, via transient changes in the Faraday rotation (θ_F) and Kerr rotation (θ_K) respectively; γ is the angle of incidence. **c**, Time-resolved polarization rotation of a near-infrared probe pulse after excitation with pump pulses with a photon energy of 3.1 eV ($\delta = 50$ nm) as measured in the transmission (black) and reflection (red) geometries. The thick solid lines are exponentially damped sine fits. Inset: Fourier spectra of the oscillations with Lorentzian fits (thick solid lines), with central frequencies f_0 and f_k . a.u.: arbitrary units.

7.2. ALL-OPTICAL GENERATION AND DETECTION OF COHERENT ANTIFERROMAGNETIC SPIN WAVES

Dysprosium orthoferrite (DyFeO₃) is a charge-transfer antiferromagnetic insulator with Néel temperature $T_N = 645$ K, exhibiting one of the strongest observed interactions be-

tween spins and ultrashort laser pulses [47, 162, 255]. The optical spectrum of DyFeO₃ is dominated by a set of intense electronic O-Fe ($2p - 3d$) charge-transfer (CT) transitions. The absorption due to these transitions sets in above 2 eV, and promptly brings the absorption coefficient α to values as high as $5 \times 10^5 \text{ cm}^{-1}$ (see inset Fig. 7.1a) [256], corresponding to penetration depths (δ) of less than 50 nm.

In our experiments we study a 60 μm thick slab of z -cut DyFeO₃. The sample is excited with 100 fs pump pulses which have photon energy tunable in the spectral range of 1.5–3.1 eV, covering the lowest energy ${}^6A_{1g} \rightarrow {}^6T_{1u}$ charge-transfer electronic transition [256]. We use time-delayed probe pulses at various photon energies below the charge-transfer gap ($h\nu < 2 \text{ eV}$) to detect the photo-induced magnetic dynamics in two complementary transmission and reflection geometries (see Fig. 7.1b). In both geometries, the pump-induced rotation of the probe polarization plane, originating from the Faraday effect (θ_F) or the magneto-optical Kerr effect (MOKE) (θ_K), is tracked as a function of the pump-probe time delay. Note that while the Faraday transmission geometry is routinely used in pump-probe experiments for detecting uniform ($k = 0$) spin precession in antiferromagnets [47], the reflection geometry has been shown to enable detection of finite- k coherent excitations such as propagating acoustic wavefronts [69, 103]. As shown below we demonstrate that the reflection geometry can also be used to probe the dynamics of short-wavelength propagating coherent spin waves.

Following the optical pumping in the regime of strong absorption ($h\nu = 3.1 \text{ eV}$), the time-resolved dynamics reveal high-frequency oscillations in the hundreds of GHz range (see Fig. 7.1c). The frequencies f_0 and f_k of the oscillations observed in the transmission and reflection geometry respectively, are substantially different: $f_k > f_0$ (see inset Fig. 7.1c). Notably, the decay time of the oscillations also differs by nearly an order of magnitude.

To identify the origin of the oscillations, we track their central frequency as a function of temperature. The antiferromagnetic state in DyFeO₃ adopts two distinct spin configurations, sharply separated by a first-order phase transition at the so-called Morin temperature $T_M \approx 50 \text{ K}$ [144]. At $T < T_M$, the antiparallel iron spins are oriented along the y -axis and arranged in a compensated collinear AFM pattern. Above T_M , the spins experience a reorientation towards the x -axis accompanied by a mutual canting and stabilization of a canted AFM phase (see Fig. 7.2a). The temperature dependence of the oscillation frequency exhibits a characteristic cusp-like softening with a minimum at T_M (see Fig. 7.2b and Fig. 7.7). This frequency softening is an unambiguous hallmark of the quasi-antiferromagnetic (q-AFM) magnon branch in DyFeO₃ and is caused by strong temperature variations of the magneto-crystalline anisotropy in the vicinity of T_M [169]. Indeed, the frequencies f_0 observed in the transmission geometry match values reported in literature for the zone-centre ($k = 0$) q-AFM magnon [169].

To explain the physical origin of the oscillation at frequency f_k seen in the MOKE experiment, we refer to the dispersion relation for magnons. In both magnetic phases, below and above T_M , the magnon spectrum ω_k in DyFeO₃, is given by [193]:

$$\omega_k = \sqrt{\omega_0^2 + (v_0 k)^2}, \quad (7.1)$$

where $v_0 \approx 20 \text{ km/s}$ is the limiting group velocity of the spin waves [193]. This disper-

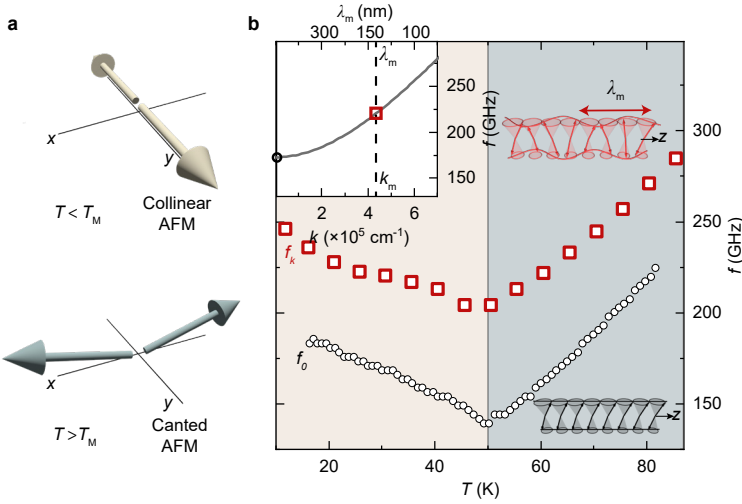


Figure 7.2: **Temperature evolution of the spin-wave frequencies.** **a**, The orientation of iron spins in the collinear AFM (top) and canted AFM (bottom) phase. **b**, Temperature (T) dependence of the central frequency of the oscillatory dynamics as measured in the reflection geometry (f_k , red square markers) compared with the $k = 0$ magnon T -dependence, as measured in transmission geometry (f_0 , black circle markers). The pump photon energy $h\nu = 3.1$ eV. See also Fig. 7.7. Left top inset: The AFM magnon dispersion of DyFeO₃. The dashed line indicates the $k_m = 4.2 \times 10^5 \text{ cm}^{-1}$ magnon to which the probe is sensitive. Right insets: Schematic illustration of the spin wave corresponding to the oscillatory dynamics at the different frequencies.

sion relation is shown as an inset to Fig. 7.2b. At small wavenumbers $k\nu_0 \ll \omega_0$, it has a quadratic form due to the magnon gap $\omega_0 = 2\pi f_0$, arising from magneto-crystalline anisotropy. At larger wavenumbers $\nu_0 k \gg \omega_0$, the dispersion relation becomes dominated by the exchange interaction (exchange regime), and thus takes a linear form typical for antiferromagnets [193]. Based on the form and properties of the dispersion relation we identify the MOKE signal at f_k as a finite- k magnon on the q-AFM branch: it follows the characteristic temperature dependence of the f_0 zone-center magnon mode and has a nearly temperature-independent blueshift. The detection geometry implies that the magnon wavevector k is perpendicular to the sample surface, and its magnitude can be deduced from Eq. 7.1 to be $k = 4.2 \times 10^5 \text{ cm}^{-1}$ ($\lambda = 2\pi/k \approx 140 \text{ nm}$) (see Figure 7.2b).

By considering the modulation of the material's dielectric tensor due to the propagating coherent spin waves, the attribution of the f_k oscillation to a finite- k magnon on the q-AFM branch can be further supported. A spin wave with a propagation vector along the z -axis causes a perturbation of the magnetic order and a corresponding periodic modulation of the off-diagonal components of the dielectric tensor [168], resembling the magneto-optical analogue of a dynamical volume phase grating. As a result, the polarization rotation of the reflected probe beam with wavenumber k_0 becomes subject to a Bragg condition:

$$k_m = 2k_0 n(\lambda_0) \cos \gamma', \quad (7.2)$$

where $n(\lambda_0)$ is the optical refractive index of the medium at the probe wavelength λ_0 , γ'

is the refracted angle of incidence of the probe, and k_m is the normal projection of the k -vector of the probed magnon (see section 7.8.2). Using Eq. 7.2 we find that a probe pulse at a central wavelength of 680 nm ($n \approx 2.39$) [256] and normal incidence ($\gamma' = 0$) is sensitive to propagating magnons with wavenumber $k_m \approx 4.2 \times 10^5 \text{ cm}^{-1}$. Note that this independent estimation agrees with the magnon wavenumber retrieved using the measured frequency and the known dispersion relation (Eq. 7.1).

7.3. OPTICAL CONFINEMENT TO GENERATE PROPAGATING SPIN WAVES

The generation of finite- k coherent magnons is anticipated to rely strongly on the confinement provided by the optical penetration depth δ , which is highly dispersive near the charge-transfer band. In particular, changing the pump photon energy between 2.4 and 3.1 eV provides a variation in the penetration depth between 300 and 50 nm, while the real part of the refractive index (influencing the pump wavelength) changes by only 5% (see Fig. 7.6). Therefore, the amplitude of the finite- k magnon is expected to vary strongly as function of the pump photon energy. The time-resolved MOKE signals obtained in the reflection geometry for different photon energies of the pump excitation, are shown in Fig. 7.3a. The Fourier transforms of the signals (Fig. 7.3b) show that the spectra are composed of two components, corresponding to the zone-centre and finite- k ($k_m = 3.7 \times 10^5 \text{ cm}^{-1}$) magnon modes. One can see that with increasing photon energy (i.e. decreasing penetration depth), the amplitude of the finite- k magnon mode increases dramatically (see Fig. 7.3c). The obtained dependence clearly shows that the finite- k magnon is nearly absent for penetration depths larger than 150 nm, a value close to the wavelength λ_m of the probed magnons, and grows dramatically for shorter penetration depths.

We model this observation using a simple assumption: the ultrashort light pulse promotes a spin excitation that is strongly non-uniform along the direction of incidence z . The excitation leads to a nearly instantaneous deflection of spins by an angle $\phi(z)$ with the spatial distribution following the optical absorption profile given by the Beer-Lambert law: $\phi(z, t = 0) = \phi_0 e^{-z/\delta}$, where $\phi_0 \sim I_0/\delta$ is proportional to the intensity of the pump pulse I_0 , and inversely proportional to the light penetration depth (see section 7.8.3). The strongly non-uniform spin perturbation distributes the initial deflection among magnon modes at different wavenumbers k , with the amplitudes A_k given by the reciprocal space image of the initial excitation (see inset Fig. 7.3c):

$$A_k \sim \frac{I_0}{1 + (k\delta)^2}, \quad (7.3)$$

This expression not only agrees well with the observations of Fig. 7.3c ($k_m = 3.7 \times 10^5 \text{ cm}^{-1}$, $\lambda_m = 170 \text{ nm}$), where it is plotted as a best fit to the pump intensity I_0 , but also confirms the intuitive interpretation that a stronger confinement shifts the spectral amplitude of the excited magnon wave packet towards larger k .

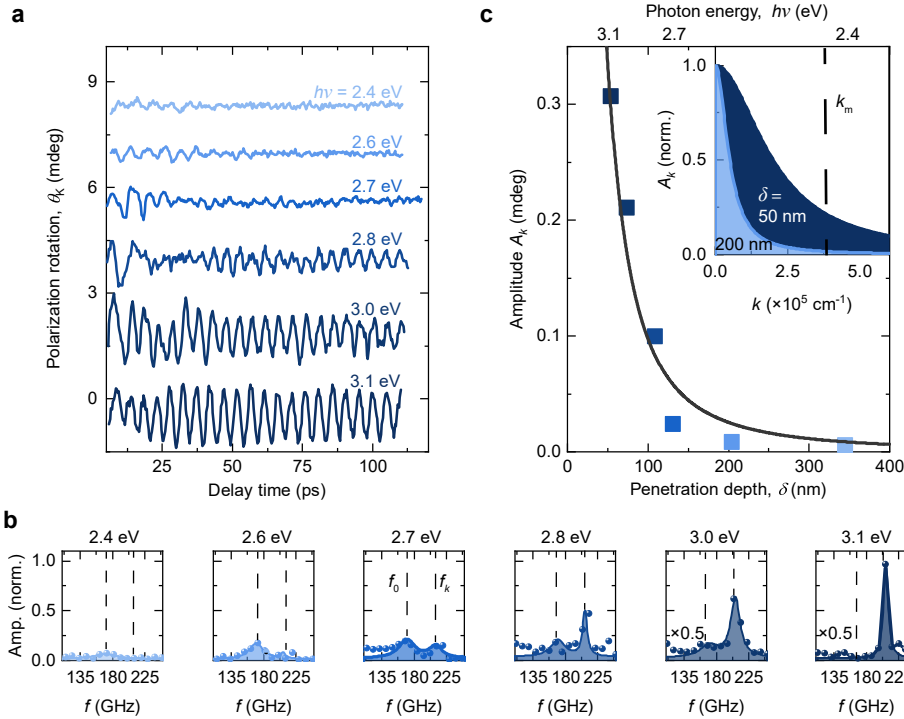


Figure 7.3: **Confinement of the light as a necessary condition for the generation of finite- k spin waves.** **a**, Time-resolved signals of the polarization rotation of the near-infrared probe pulse after excitation with pump pulses with increasing photon energy as measured in the reflection geometry. **b**, Fourier amplitude spectra of the time-resolved signals from panel **a**. **c**, Amplitude of sine fit oscillations corresponding to the AFM propagating spin wave to the data from panel **a** vs. penetration depth of the excitation pulse (color markers correspond to traces in panel **a**). The solid line is a theory fit using Eq. 7.3. Inset: distribution of the light-induced coherent magnon as a function of the wavenumber k . The distribution is provided for the excitation with pump pulses with $\delta = 50 \text{ nm}$ (dark blue, broadband distribution) and 200 nm (light blue, narrowband). The probe is selectively sensitive to $k_m = 3.7 \times 10^5 \text{ cm}^{-1}$, indicated by the dashed line.

7.4. SPECTRAL COMPONENTS OF THE BROADBAND SPIN-WAVEPACKET

The excited spin-wave continuum forms a broadband magnon wavepacket, in which individual spectral components propagate independently, each adhering to the dispersion relation $\omega_k = 2\pi f_k$ (Eq. 7.1). In order to visualize the time evolution of the wavepacket, we make use of the linearized sine-Gordon equation for the space- (z) and time- (t) dependent amplitude of the spin deflections $\phi(z, t)$ [193] (see section 7.8.3). The evolution of the spin dynamics is described by:

$$\phi(z, t) = \frac{2}{\pi} \int_{-\infty}^{\infty} dk [A_k \cos kz \cos \omega_k t] \quad (7.4)$$

and is shown in Fig. 7.4a. The dispersion promptly smears out the initial exponential profile of the spin excitation, simultaneously forming a spin-wave front that propagates into the bulk, already after around 10 ps. This front is composed of short-wavelength

magnons with $k \gtrsim 20 \times 10^5 \text{ cm}^{-1}$ propagating with the limiting group velocity v_0 .

Applying the Bragg condition of Eq. 7.2, we can experimentally map out the spectral components of the magnon wavepacket, as well as extract the group velocity and propagation length of individual magnon modes. First, we vary the incidence angle γ of the probe pulse (inset Fig. 7.4b), and find that the central frequency of the oscillations is reduced upon increasing γ' (Fig. 7.4b), in perfect agreement with Eq. 7.2 and the magnon dispersion of Eq. 7.1. Next, upon decreasing the probe wavelength, we observe a systematic increase in the magnon frequency (Fig. 7.4c), once again in accordance with the Bragg condition.

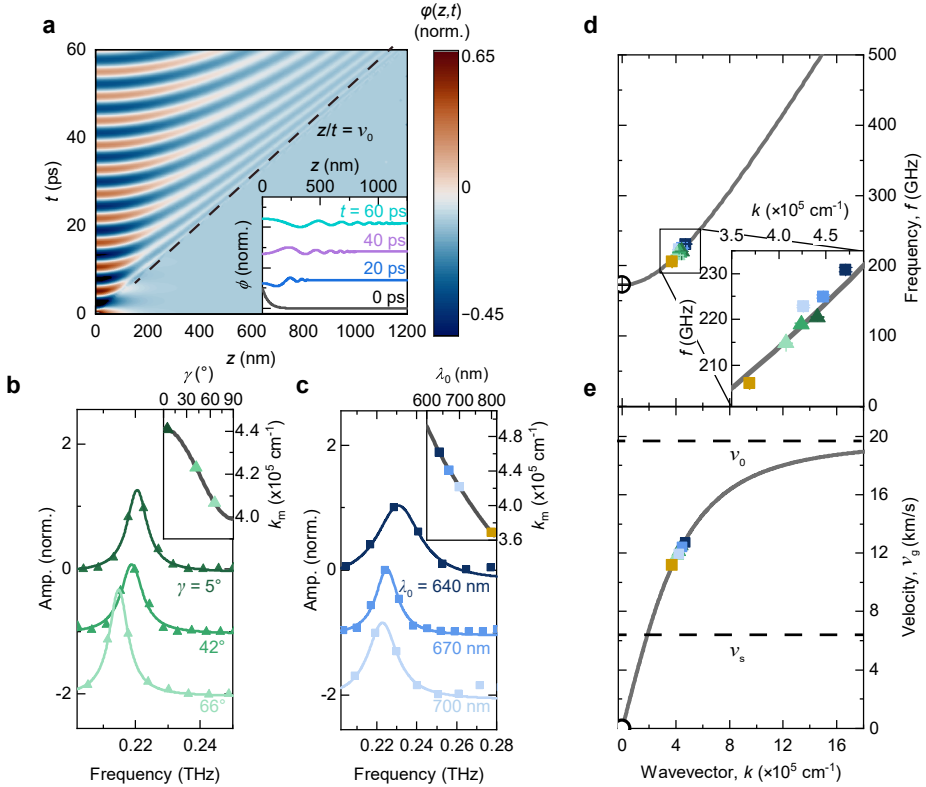


Figure 7.4: Revealing spectral components of the broadband antiferromagnetic magnon wavepacket. **a**, Simulation of the spatio-temporal evolution of the spin deflection $\phi(z, t)$ after optical excitation at 3.1 eV with a penetration depth of 50 nm, as determined by Eq. 7.4. Inset: Line cuts at different times t . **b, c**, Fourier spectra of the time-resolved polarization rotation in the reflection geometry ($T = 60 \text{ K}$) for different probe incidence angles γ ($\lambda_0 = 680 \text{ nm}$) (**b**) and probe wavelengths λ_0 ($\gamma = 5^\circ$) (**c**). The solid superimposed lines are Lorentzian fits of the Fourier peaks. Insets: The wavenumber k_m of the probed magnons, as a function of the angle γ (**b**) and probe wavelength λ_0 (**c**), with the measured points indicated by coloured markers. (**d, e**) The extracted central magnon frequencies (**d**) and the calculated group velocity (**e**) from the data in panel **b** and **c** at their respective calculated wavenumbers plotted with a best fit of the spin-wave dispersion curve (**d**) and the group velocity corresponding to the dispersion (**e**). The marker colours and shapes correspond to the measurements in panel **b** and **c**.

To summarize our observations, we plot the extracted central frequencies as a function of the corresponding wavenumbers k_m (see Fig. 7.4d). These points, fit to the dispersion relation ω_k given by Eq. 7.1, yield a limiting group velocity $v_0 = (19.0 \pm 0.7)$ km/s, in good agreement with the literature values [193]. Using this extracted value, we evaluate the group velocities $v_g = \left. \frac{\partial \omega}{\partial k} \right|_{k=k_m}$ of the optically detected magnons given by $v_g = v_0^2 \frac{k_m}{\omega_k}$. These values, shown in Fig. 7.4e, indicate that while the zone-center magnons do not support propagation, the shortest-wavelength components of the magnon wavepacket detected in our experiment propagate at a supersonic velocity of nearly 13 km/s ($v_s = 6$ km/s, see section 7.8.4 for a discussion on the broadband wavepacket of coherent acoustic phonons). We note that these magnons already approach the exchange wave regime characterized by the limiting group velocity v_0 . This remarkable feature, inherent to antiferromagnets, stands in sharp contrast with the situation in ferromagnets, where the quadratic dispersion relation dictates that the exchange value of the group velocity is reached only for magnons with $\lambda \lesssim 10$ nm. Although the shortest magnon wavelength detected in our experiments is 125 nm, magnons at even shorter wavelengths, down to the penetration depth limit of 50 nm, are anticipated, and could be detected using probe pulses at higher photon energies or other means to measure non-local ultrafast spin excitations [257–259].

7.5. SPIN-WAVE PROPAGATION DISTANCE

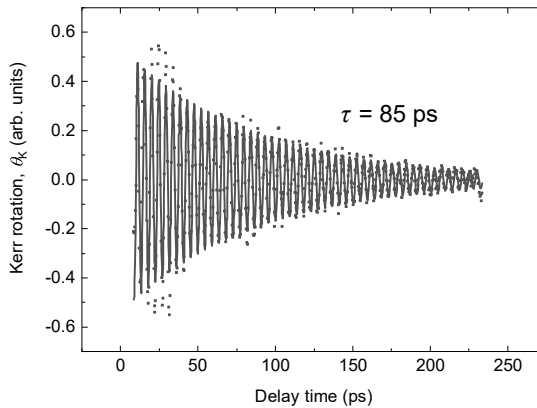


Figure 7.5: **Extracting the spin-wave propagation distance.** Time-resolved polarization rotation originating from a propagating magnon, as obtained in the reflection geometry. The solid line represents a best fit of a damped sine, giving a lifetime τ of about 85 ps. With the largest estimated group velocities v_g of the measured magnons of about 13 km/s, this gives a propagation distance $l_c = v_g \tau = 1.1 \mu\text{m}$.

Using the extracted lifetime of the oscillations $\tau = 85$ ps (see Fig. 7.5), we estimate the coherence length l_c of the spin-wave transport $l_c = v_g \tau = 1.1 \mu\text{m}$. We note that this length, dramatically enhanced as compared to metallic antiferromagnets [96, 180], also agrees with studies of diffusive spin transport in other insulating antiferromagnets [250, 260]. One can anticipate even longer propagation lengths for the coherent (ballistic) regime

reported here: our estimate of the coherence length is only a lower limit, as the propagating spin wave is likely to escape from the region that is probed by the reflected probe light ($\sim \lambda_0/2$). These striking observations make antiferromagnetic insulators such as DyFeO_3 a promising platform for the realization of high-speed wave-based magnonic devices.

7.6. CONCLUSIONS

Through optical pumping of above-bandgap electronic transitions, we have explored an efficient and virtually universal route for exciting coherent propagating spin waves in insulating antiferromagnets. The strong optical absorption provides an opportunity to spatially confine the light to a subwavelength scale, inaccessible by any other means, such as for example focusing [261–263], enabling the emission of a broadband continuum of short-wavelength antiferromagnetic magnons. The universal mechanism opens up prospects for terahertz coherent AFM magnonics and opto-spintronics [242] providing a long-sought source of coherent high-velocity spin waves. We anticipate even higher propagation velocities to be observed in the broad class of easy-plane antiferromagnets (e.g. hematite [260] and FeBO_3), in which the spin-wave gap ω_0 is reduced and the high-velocity exchange wave regime can be achieved at significantly smaller wavenumbers k . The demonstrated approach holds promise for a wide range of fundamental studies exploiting the excitation and propagation of nonlinear spin waves such as magnetic solitons [91, 264] as well as the investigation of the giant magneto-elastic coupling between antiferromagnetic magnons and acoustic phonons [265] directly in the time-domain.

7.7. METHODS

SAMPLE

A single crystal of DyFeO_3 , 63 μm thick, grown by a floating zone melting technique was used in this work. The sample is cut perpendicularly to the crystallographic z -axis.

TIME-RESOLVED EXPERIMENT

An amplified 1 kHz Ti:Sapphire laser system (Astrella, Coherent, central wavelength 800 nm, pulse energy: 7 mJ, pulse duration: 100 fs) forms the basis of the experimental setup. A large fraction of this output is used to pump a dual optical parametric amplifier (OPA, TOPAS-Twins, Light Conversion). The OPA delivers linearly polarized, 100 fs output pulses, with photon energies $h\nu$ in the range 0.45–1 eV ($\lambda_0 = 2.7$ – $1.4 \mu\text{m}$). The photon energy of these output pulses was doubled or tripled using a β -barium borate (BBO) single crystal in order to obtain tunable excitation pulses which cover the photon energies in the optical range of 1.55–3.1 eV (corresponding wavelength 400–800 nm). A small portion of the amplifier pulses was sent through a mechanical delay line and used as probe of the spin dynamics in the reflection and transmission geometries. Pump and probe pulse were focused onto the DyFeO_3 sample (pump spot diameter: 300 μm , typical fluence 2 mJ/cm², probe spot diameter: 80 μm), which was kept in a dry-cycle cryostat (Montana Instruments) that allowed to cool it down to 10 K and vary the temperature with high stability in a wide temperature range (10–250 K). The pump-induced changes in the polarization $\theta_{\text{K,F}}$ of the reflected or transmitted probe pulse were measured using an optical polar-

ization bridge (Wollaston prism) and a pair of balanced Si photodetectors. The optical setup is described in more detail, including a figure, in chapter 3.

EXPERIMENTAL DETERMINATION OF THE ABSORPTION COEFFICIENT.

The unpolarised absorption spectrum of DyFeO_3 was directly obtained with light propagating along the crystal z -axis in the spectral region 1–2.2 eV. The resulting absorption is shown in the inset of Figure 7.1a. In addition, we performed spectroscopic ellipsometry measurements using a Woollam M5000 ellipsometer over a wide energy range to obtain the real and imaginary parts of the refractive index. In the photon energy region 2.5–4 eV, where the transmission measurements are not possible for thick samples, we estimated the absorption using the acquired complex refractive index. These values are shown in the inset of Figure 7.1a. The real part of the complex refractive index is shown in Fig. 7.6.

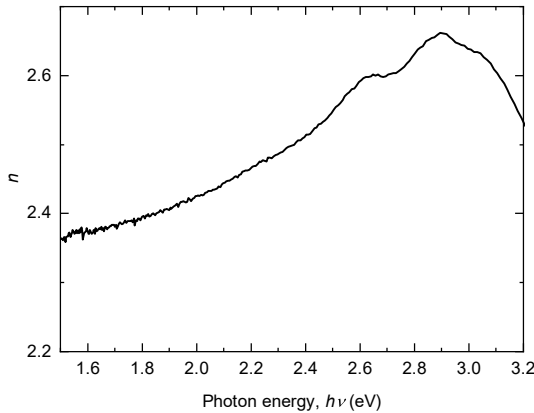


Figure 7.6: **Spectral dependence refractive index.** Real part n of the refractive index, as extracted using spectroscopic ellipsometry measurements.

7.8. SUPPLEMENTARY INFORMATION

7.8.1. TEMPERATURE-DEPENDENT SPIN-WAVE DETECTION

The time-resolved measurements of the polarization rotation in reflection and transmission geometry were performed at different temperatures (see Fig. 7.7). There is a pronounced difference in dynamics observed. The central frequencies of the oscillations in the reflection geometry were extracted and shown in Fig. 7.2.

7.8.2. MAGNETO-OPTICAL DETECTION OF PROPAGATING SPIN WAVES IN ANTI-FERROMAGNETS

MAGNETIC POTENTIAL

The antiferromagnetic order can be best described by introducing the antiferromagnetic Néel vector $\mathbf{L} = \mathbf{M}_1 - \mathbf{M}_2$ and net magnetization $\mathbf{M} = \mathbf{M}_1 + \mathbf{M}_2$, where $\mathbf{M}_{1,2}$ are the magnetizations of the antiferromagnetically coupled magnetic sublattices, such that $|\mathbf{M}_1| = |\mathbf{M}_2| = M_0$ and $|\mathbf{L}| \approx 2M_0 = L_0$. The density of magnetic energy in DyFeO_3 written

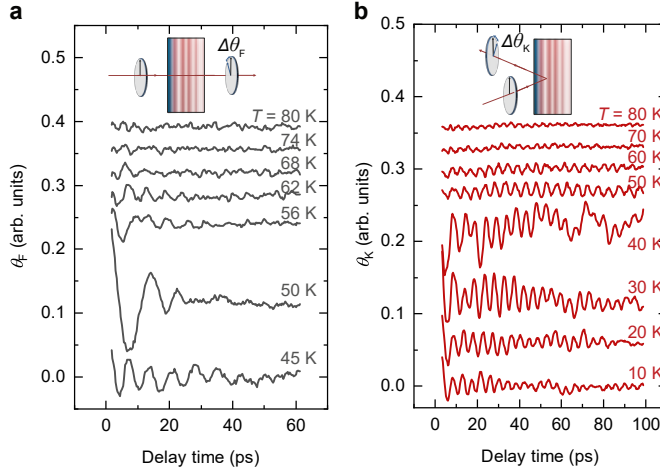


Figure 7.7: **Time-resolved spin-wave detection at different temperatures.** **a,b**, Time-resolved polarization rotation in the transmission **(a)** and reflection geometry **(b)** following excitation at $h\nu = 3.1$ eV for different temperatures. The probe-incidence angle is near-normal, with $\lambda_0 = 700$ nm.

in terms of \mathbf{M} and \mathbf{L} reads [91, 193]:

$$w(\mathbf{M}, \mathbf{L}) = \frac{H_{\text{ex}}}{4M_0} \mathbf{M}^2 - (\mathbf{H}_0 \cdot \mathbf{M}) - \frac{H_D}{2M_0} (\mathbf{e}_y \cdot [\mathbf{L} \times \mathbf{M}]) + w_a(\mathbf{L}). \quad (7.5)$$

In this expression, H_{ex} is the effective exchange field ($\omega_{\text{ex}} = \gamma H_{\text{ex}}$), with $\gamma = 1.76 \times 10^7$ (s/Oe) the gyromagnetic ratio, \mathbf{H}_0 is the external magnetic field, H_D is the magnitude of the effective Dzyaloshinskii-Moriya field ($\mathbf{H}_D = \frac{H_D}{2M_0} [\mathbf{e}_y \times \mathbf{L}]$, \mathbf{e}_y is the unit vector along the y -axis, which corresponds to the even C_2 crystal axis in DyFeO_3). The spontaneous spin-reorientation between the two competing magnetic states is governed by the temperature-dependence of the energy of the magneto-crystalline anisotropy [168, 169]:

$$w_a(\mathbf{L}) = \frac{1}{2} K_2(T) L_y^2 - \frac{1}{2} K_4 L_y^4, \quad (7.6)$$

with $K_{2,4}$ phenomenological parameters that describe the strength of the magnetic anisotropy.

Within the sigma-model approach, the dynamics of the Néel vector is described by a closed equation (sigma-model equation, see, e.g., review article [91] and section 7.8.3 for details), whereas the net magnetization \mathbf{M} is determined by this vector and its time derivative via the relation:

$$\mathbf{M} = \frac{M_0}{H_{\text{ex}}} \mathbf{H}_D + \frac{1}{2M_0\omega_{\text{ex}}} \left[\frac{\partial \mathbf{L}}{\partial t} \times \mathbf{L} \right], \quad (7.7)$$

In DyFeO_3 the ground state of the Néel vector as well as its dynamics corresponding to the quasi-antiferromagnetic mode (q-AFM) is restricted to the (xy) plane. For such dynamics, the Néel vector can be parametrized by introducing the angle ϕ_L that

the vector forms with the y -axis, $\mathbf{L} = L_0 (\sin \phi_L, \cos \phi_L, 0)$. In the magnetic ground state of DyFeO₃:

$$\phi_L = \begin{cases} 0, & T < T_M \\ \frac{\pi}{2}, & T > T_M, \end{cases} \quad (7.8)$$

with $T_M \approx 51$ K the Morin temperature.

For this planar dynamics of the Néel vector \mathbf{L} , the net magnetization M_z emerges along the z -axis, such that:

$$M_z = \frac{M_0}{H_{\text{ex}}} \left(-H_D \sin \phi_L + \frac{1}{\gamma} \frac{\partial \phi_L}{\partial t} \right), \quad (7.9)$$

At this point we introduce a variable ϕ to designate deviations of the vector \mathbf{L} from the equilibrium orientation, such that $\phi = \phi_L$ for the collinear AFM state and $\phi = \frac{\pi}{2} - \phi_L$ for the canted AFM state. For the case of small deviations of the Néel vector from equilibrium, we assume $\phi \ll 1$ and obtain:

$$M_z = \begin{cases} \frac{M_0}{H_{\text{ex}}} \left(-H_D \phi_L + \frac{1}{\gamma} \frac{\partial \phi}{\partial t} \right), & T < T_M \\ \frac{M_0}{H_{\text{ex}}} \left(-H_D - \frac{1}{\gamma} \frac{\partial \phi}{\partial t} \right), & T > T_M \end{cases} \quad (7.10)$$

MAGNETO-OPTICAL DETECTION MECHANISM FOR THE FINITE- k MAGNON MODES

Optical detection of magnetization dynamics in a reflection geometry is performed using the magneto-optical Kerr effect (MOKE). The phenomenon originates from a helicity-dependent refractive index in the material with broken time reversal symmetry. The refractive index differs for left-handed and right-handed circular polarized light, resulting in different reflection coefficients. To calculate the rotation of the plane of polarization after reflection, linearly polarized light is first decomposed into circular polarized components. For simplicity, it is assumed that the incident light is polarized along the x -axis, and the normalized electric field vector \mathbf{e}_i in the (x,y) plane is:

$$\mathbf{e}_i = \frac{1}{2} \begin{pmatrix} 1 \\ -i \end{pmatrix} + \frac{1}{2} \begin{pmatrix} 1 \\ +i \end{pmatrix} = \frac{1}{2} \mathbf{e}^+ + \frac{1}{2} \mathbf{e}^-, \quad (7.11)$$

where $\mathbf{e}^{\pm} = \begin{pmatrix} 1 \\ \mp i \end{pmatrix}$. Then the reflected field is

$$\mathbf{e}_r = \frac{1}{2} r^+ \mathbf{e}^+ + \frac{1}{2} r^- \mathbf{e}^- = \frac{1}{2} \begin{pmatrix} r^+ + r^- \\ i(r^- - r^+) \end{pmatrix} \quad (7.12)$$

Now the reflectivity is written as the sum of the static reflectivity r_0 and the dynamic part of the reflectivity Δr , which is induced by the spin wave:

$$\begin{aligned} r^+ &= r_0^+ + \Delta r^+ \\ r^- &= r_0^- + \Delta r^- \end{aligned} \quad (7.13)$$

We consider the experimental geometry schematically shown in Fig. 7.8a, in which a probe pulse enters the material at $z = 0$. To find the change in reflectivity, depending

on the light helicity, we take an approach similar to the ultrafast detection of acoustic phonons, where phonon-induced strain affects reflectivity [see Ref. [69], Eq. 32]. In Ref. [69] the change in reflectivity is derived as function of the time and space dependent change in permittivity $\Delta\epsilon(z, t)$ due to the strain modulation. Here, the same equation is employed to calculate the change of reflectivity induced by magnetization. The equation taken from Ref. [69] reads:

$$r = r_0 + \frac{ik_0^2}{2k} t_0 \tilde{t}_0 \int_0^\infty dz' e^{2ikz'} \Delta\epsilon(z', t), \quad (7.14)$$

where r_0 is the reflection coefficient in absence of perturbations in the permittivity, t_0 is the transmission coefficient of the light into the medium, and \tilde{t}_0 is the transmission coefficient from the medium into free space, k_0 is the wavenumber of the light in free space and k is the wavenumber of light in the medium.

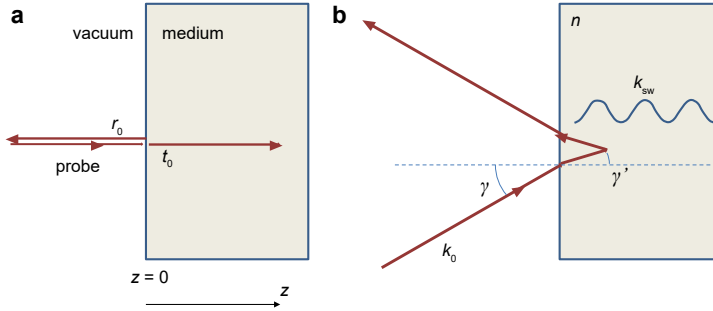


Figure 7.8: **Experimental geometry to probe spin-wave excitations.** a, Schematic diagram of the experiment considered. b, Schematic illustration of the detection condition from Eq. 7.2

Two electromagnetic eigenmodes exist in a magnetic material with (dynamical) magnetization along the z -axis, which have left-handed and right-handed circular polarization (\pm) and experience different refractive indices n_{\pm} [95]. From these effective refractive indices, the effective permittivity modulation $\Delta\epsilon$ can be obtained:

$$n_{\pm}^2 = \epsilon \pm g = \epsilon + \Delta\epsilon_{\pm}, \quad (7.15)$$

where g is the gyration term. Generally, this gyration term is proportional to the net magnetization: $g(M) = aM_z$, where a is a proportionality coefficient. From this it is found that:

$$\Delta\epsilon_{\pm}(z, t) = \pm aM_z(z, t). \quad (7.16)$$

Inserting the expression for $\Delta\epsilon(z, t)$ in Eq. 7.14 for right- and left-handed circular polarization we obtain:

$$\begin{aligned} r^+ &= r_0^+ - it_0^+ \tilde{t}_0^+ \frac{ak_0^2}{2k^+} \int_0^\infty dz' e^{2ik^+z'} M_z(z', t) \equiv r_0^+ + \Delta r^+ \\ r^- &= r_0^- + it_0^- \tilde{t}_0^- \frac{ak_0^2}{2k^-} \int_0^\infty dz' e^{2ik^-z'} M_z(z', t) \equiv r_0^- + \Delta r^-. \end{aligned} \quad (7.17)$$

For the sake of simplicity, we use the approximation of a pure antiferromagnet, such that the difference in reflection coefficients, transmission coefficients and wave vectors of light with opposite helicity in statics is negligible (we also neglect higher-order effects such as magnetic birefringence), simplifying the expression to:

$$\begin{aligned} r^+ &= r_0 - \Delta r \\ r^- &= r_0 + \Delta r, \end{aligned} \quad (7.18)$$

where

$$\Delta r = i \frac{ak_0^2}{2k} t_0 \tilde{t}_0 \int_0^\infty dz' e^{2ikz'} M_z(z', t) \quad (7.19)$$

Now the rotation angle θ_K is calculated from equation 7.12, by taking the ratio of the y - and x -components. Generally, the rotation angles are small such that $\tan \theta_K \approx \theta_K$ so that:

$$\theta_K \approx \frac{i(r^- - r^+)}{r^- + r^+} = \frac{i\Delta r}{r_0}. \quad (7.20)$$

As discussed in section 7.4 and 7.8.3, the optical pumping results in the excitation of a broadband spin-wave wave packet. We consider an arbitrary plane spin wave component of the packet with the frequency ω_s and the wavevector $k_m(\omega_s)$. We show below that the experimentally detected spin wave component is fully defined by the wavevector k of the probe pulse.

Following Eqs. 7.8, 7.9, spin dynamics in DyFeO₃ results in an oscillatory out-of-plane magnetization. The magnetization M_z associated with the propagating spin wave can thus be written as follows:

$$M_z(z, t) = M_k e^{i\omega_s t} e^{-ik_m(\omega_s)z}. \quad (7.21)$$

Here, M_k is the amplitude of the chosen spin wave component, determined by the amplitude of the spin deflection ϕ , (see Eqs. 7.8, 7.9) and $k_m(\omega_s)$ is the wave-vector of the spin wave, related to ω_s through the dispersion relation ω_k .

Substituting Eq. 7.21 in Eq. 7.19 and in Eq. 7.20 afterwards, results in the following expression for the rotation angle:

$$\theta_K = \frac{t_0 \tilde{t}_0}{r_0} \frac{ak_0^2}{2k} M_k \int_0^\infty dz e^{i\omega_s t} e^{i(2k - k_m(\omega_s)z)}. \quad (7.22)$$

Note that in a general case $k_m = \kappa_m - i\eta_m$, i.e. spin waves decay upon propagation from the sample boundary with a decrement η_m . For the case $\eta_m \neq 0$, the integral in Eq. 7.22 converges and the result is:

$$\theta_K = i \frac{t_0 \tilde{t}_0}{r_0} \frac{ak_0^2}{2k} M_k e^{i\omega_s t} \left(\frac{1}{2k - k_m(\omega_s)} \right). \quad (7.23)$$

The fraction $\left(\frac{1}{2k - k_m(\omega_s)} \right)$ can be expressed as:

$$\left(\frac{1}{2k - k_m(\omega_s)} \right) = \frac{2k - \kappa_m(\omega_s)}{(2k - \kappa_m(\omega_s))^2 + \eta_m^2} - \frac{i\eta_m}{(2k - \kappa_m(\omega_s))^2 + \eta_m^2}. \quad (7.24)$$

Now we can assume $\eta_m \ll \kappa_m$ and take the limit $\eta_m \rightarrow 0$. Taking into account one of the definitions of the Dirac function $\pi\delta(x) = \lim_{a \rightarrow 0} \frac{a}{x^2 + a^2}$ we obtain:

$$\lim_{\eta_m \rightarrow 0} \left(\frac{1}{2k - k_m(\omega_s)} \right) = \frac{1}{(2k - \kappa_m(\omega_s))} - i\pi\delta(2k - \kappa_m(\omega_s)). \quad (7.25)$$

Equations 7.23 and 7.25 select the spin waves with wave vectors satisfying the expression $2k - k_m(\omega_s) = 0$ to be detected as $\theta_K \sim \delta(2k - k_m(\omega_s))$, assuming $k_m = \kappa_m$ in the limit of no spin wave damping and taking the real part of θ_K , which corresponds to the polarization rotation. If one rewrites this expression in terms of the wavelengths $2\lambda_m = \lambda_{\text{probe}}$, with λ_m the wavelength of the spin wave and λ_{probe} the wavelength of the probe pulse in the medium, the well-known Bragg condition is obtained. In the specific case of our experiment, the gradient of the excitation is directed in the z -direction which, as discussed in section 7.8.3, results in spin waves with a wavevector in this particular direction. In the experiment, however, the incoming probe pulse can be directed under a certain angle γ . Taking refraction into account (see Fig. 7.8b), which leads to a refracted angle γ' for the incoming probe pulse, the detection expression becomes:

$$k_m = 2k_0 n \cos \gamma' \quad (7.26)$$

which equals Eq. 7.2 in section 7.2.

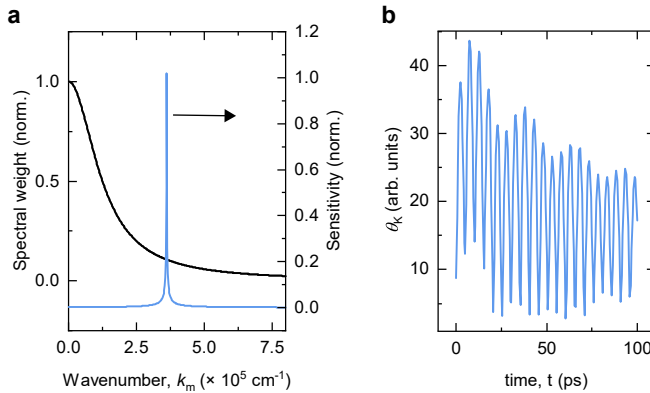


Figure 7.9: **Wavenumber selectivity.** **a**, Wavepacket distribution (black line, left axis) and the normalized sensitivity function as given Eq. 7.23 (blue line, right axis). **b**, The resulting time-resolved MOKE signal, given by the wavepacket distribution and the sensitivity function from panel **a**. Damping parameter $\eta_m = 0.001 \text{ nm}^{-1}$, wavepacket distribution: $a_k \sim \frac{1}{1+(k\delta)^2}$ (see section 7.8.3).

The result is the following. Assuming a spin wave packet distribution as discussed in section 7.8.3 (see Fig. 7.9a), the reflection geometry provides a sharp sensitivity to a single component, depending on the probe photon wavenumber. As a result, the oscillation emerging in the time-resolved probe polarization (Fig. 7.9b) has the frequency of the spin wave at that particular wavenumber.

7.8.3. FORMALISM ON THE GENERATION OF THE MAGNON WAVEPACKET

We describe the dynamics of the quasi-antiferromagnetic mode (q-AFM) in DyFeO₃ using the one-dimensional version of the sigma-model, which for the planar dynamics of the Néel vector can be obtained by the variation of the Lagrangian $L[\phi]$ [91]:

$$L[\phi] = \int dz \left\{ \frac{\alpha}{2} \left[\frac{1}{v_0^2} \left(\frac{\partial \phi}{\partial t} \right)^2 - \left(\frac{\partial \phi}{\partial z} \right)^2 \right] - w_a(\phi) \right\}, \quad (7.27)$$

where α is the non-uniform exchange constant, v_0 is the magnon speed at the linear region of the spectrum, $w_a(\phi)$ is the anisotropy energy, and the angle $\phi = \phi(z, t)$ describes the deflection of the antiferromagnetic vector \mathbf{L} from the equilibrium position (0° and 90° as measured from the y -axis in the collinear and canted AFM phase respectively, see section 7.8.2). Note that the characteristic speed $v_0^2 = \gamma \alpha \omega_{\text{ex}} / 2M_0$ contains only terms of exchange origin, the uniform exchange parameter $\omega_{\text{ex}} = \gamma H_{\text{ex}}$ and the non-uniform exchange constant α , which results in the large value of this speed.

The general equation obtained from Eq. 7.27 is the nonlinear Klein-Gordon equation (note that it transforms to the familiar sine Gordon equation for the variable 2ϕ for the simplest form of the anisotropy with only one constant, $w_a \propto \sin^2 \phi$). In the linear approximation over the small deviations of ϕ from its equilibrium value it takes the universal form

$$\frac{\partial^2 \phi}{\partial t^2} - v_0^2 \frac{\partial^2 \phi}{\partial z^2} + \omega_0^2 \phi = 0, \quad (7.28)$$

where ω_0 is the angular frequency of the spin-wave gap:

$$\omega_0^2 = \omega_{\text{ex}} \omega_a, \quad \omega_a = \frac{\gamma}{2M_0} \left. \frac{d^2 w_a}{d\phi^2} \right|_{\phi=0} \quad (7.29)$$

The derivative of the anisotropy energy is calculated at the equilibrium value of ϕ , see for more details Ref. [255]. Thus, all the parameters are represented by two well-known quantities: the limiting group velocity $v_0 \approx 20$ km/s [193] and the value of the magnon gap ω_0 , which is directly measured in our experiment. The characteristic space scale is given by the value v_0/ω_0 .

Ultrashort pulses of light with a corresponding broadband optical spectrum are routinely being used as an instantaneous excitation to generate high frequency spin dynamics [242]. We start with the assumption that at the time $t = 0$, the spin deflection $\phi(z, t)$ in the material is given by the spatial profile of the optical excitation, schematically shown in Fig. 7.10a, as the result of an instantaneous excitation (significantly shorter than the period of the spin precession):

$$\phi(z, t) = \begin{cases} \phi_0 e^{-z/\delta}, & z \geq 0 \\ 0, & z < 0 \end{cases} \quad (7.30)$$

Here, $z = 0$ forms the interface between the magnetic medium and vacuum, δ is the penetration depth of the excitation pulse and ϕ_0 the amplitude of the initial spin deflection, proportional to the pump fluence I and inversely proportional to δ ($\phi_0 \sim I/\delta$), as to conserve the total energy distributed among all the excited magnon modes.

In order to account for the boundary condition given by the surface of the sample, we consider the energy flow j_E ; from the Lagrangian (Eq. 7.27) it follows:

$$j_E = \frac{\partial L}{\partial(\partial\phi/\partial z)} \frac{\partial\phi}{\partial t} = -\alpha \frac{\partial\phi}{\partial z} \frac{\partial\phi}{\partial t} \quad (7.31)$$

The energy flow should vanish at the surface ($z = 0$) at all times t . This gives the boundary condition $\frac{\partial\phi}{\partial z}|_{z=0} = 0$ (free spins). The simplest way to find a solution obeying this boundary condition is to expand the problem symmetrically to $z < 0$, such that the solution of the symmetrical problem is $\tilde{\phi}(z, t) = \tilde{\phi}(-z, t)$ and can be found with the initial conditions:

$$\tilde{\phi}(z, t = 0) = \phi_0 e^{-\frac{|z|}{\delta}} \quad (7.32a)$$

$$\frac{\partial\phi}{\partial z}(z, t = 0) = \frac{\phi_0}{\delta} \begin{cases} -e^{\frac{z}{\delta}}, & z > 0 \\ 0, & z = 0 \\ +e^{\frac{z}{\delta}}, & z < 0 \end{cases} \quad (7.32b)$$

Using the dispersion relation of the material, which is obtained after solving Eq. 7.28, we obtain that for a given spin wave component ψ_k :

$$\psi_k(z, t) = A e^{ikz - i\omega_k t} + B e^{ikz + i\omega_k t}, \quad \omega_k = \sqrt{\omega_0^2 + (v_0^2 k)^2} \quad (7.33)$$

Here, as before, $\omega_0 = \sqrt{\omega_{\text{ex}}\omega_a}$ the spin wave gap and v_0 the characteristic speed. Having in mind the symmetry of the wanted solution, the only solution which is symmetric over inversion of the magnon eigenmodes, is:

$$\psi_k(z, t) = C \cos kz \cos \omega_k t \quad (7.34)$$

From Eq. 7.32a we can write the spin deflection $\tilde{\phi}(z, t = 0)$ in a material slab of thickness d using the Fourier expansion as:

$$\begin{aligned} \tilde{\phi}(z, t = 0) &= \phi_0 \sum_k a_k e^{ikz} \\ a_k &= \frac{1}{d} \frac{2\delta}{1 + (\delta k)^2} \end{aligned} \quad (7.35)$$

From this expression we find that the initial exponential distribution in spin-deflection in real-space corresponds to a broadband magnon wavepacket, as shown in Fig. 7.10.

Then in the continuous limit ($d \rightarrow \infty$), combining Eq. 7.30 and Eq. 7.35 we can easily obtain the final expression, given in section 7.4:

$$\begin{aligned} \phi(z, t) = \tilde{\phi}(z \geq 0, t) &= \frac{2\phi_0}{\pi} \int_{-\infty}^{\infty} dk \left[\frac{\delta}{1 + (\delta k)^2} \cos kz \cos \omega_k t \right]; & (z \geq 0), \phi_0 \sim \frac{I_0}{\delta} \\ &= \frac{2}{\pi} \int_{-\infty}^{\infty} dk [A_k \cos kz \cos \omega_k t]; & A_k = \frac{\phi_0}{d} \frac{\delta}{1 + (\delta k)^2} \end{aligned} \quad (7.36)$$

Eq. 7.36 describes the spin deflection as a function of space (z) and time (t) and therefore the dynamics of the broadband magnon wavepacket which will start propagating into the sample. This was shown in Fig. 7.4a in section 7.4.

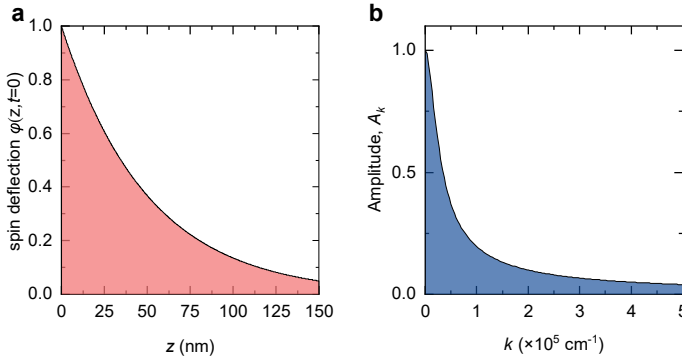


Figure 7.10: **Real-space spin deflection and momentum distribution.** **a, b,** Real-space distribution of the spin deflection $\phi(z, t)$ (**a**) and the corresponding wavevector distribution (**b**)

7.8.4. PROPAGATING COHERENT ACOUSTIC PHONON WAVEPACKET

Following the excitation with pump pulses at a photon energy of $h\nu = 3.1$ eV, the time-resolved polarization rotation signal θ_K reveals oscillatory dynamics at two distinct central frequencies (see Fig. 7.11). As argued in section 7.4, the high-frequency component corresponds to a finite- k magnon mode. The slow-varying component is caused by a broadband wavepacket of propagating acoustic phonons as in details described in Ref. [69]. The generation and detection of ultrafast light-induced coherent acoustic phonons in solids is a well-established research field known as picosecond acoustics [70]. Typically, the generation is based on a conversion of the energy of the strongly absorbed ultrashort pump pulse into photo-induced stress in vicinity of the material surface [70]. The stress leads to modulation of the intensity of light reflected from the sample as a consequence of modulation of refractive index due to optoacoustic effects. The propagating acoustic wavepacket then results in oscillations in the time-resolved probe pulse polarization rotation, which is also proportional to the intensity of reflected light.

More generally, the opto-acoustic conversion process can be described similarly to the magnon detection outlined in section 7.8.2, which causes the probe pulse to be specifically sensitive to an acoustic phonon with the wavenumber given by Eq. 7.26 [102]. The frequency of the resulting oscillation corresponds to the intrinsic frequency of the acoustic phonon. Therefore the measured oscillations can be used to map out the phonon dispersion, just like it is done for the magnon dispersion. We extract the central frequency of the slow oscillations for the different probing wavelengths that are also used in Figure 7.4. These frequencies are plotted for the wavenumber calculated using Eq. 7.26 and shown in Fig. 7.11b with a linear dispersion fit. The velocity of the sound waves extracted from this fit is $v_s = 6.2$ km/s. This agrees well with literature values of the longitudinal sound velocity in the orthoferrites, which all lie in the range of about 6.0–6.5 km/s at cryogenic temperatures [266–268]. We therefore conclude that optical excitation of the strongly-absorbing charge-transfer transitions excites both a propagating broadband magnon wavepacket and a propagating broadband acoustic phonon wavepacket.

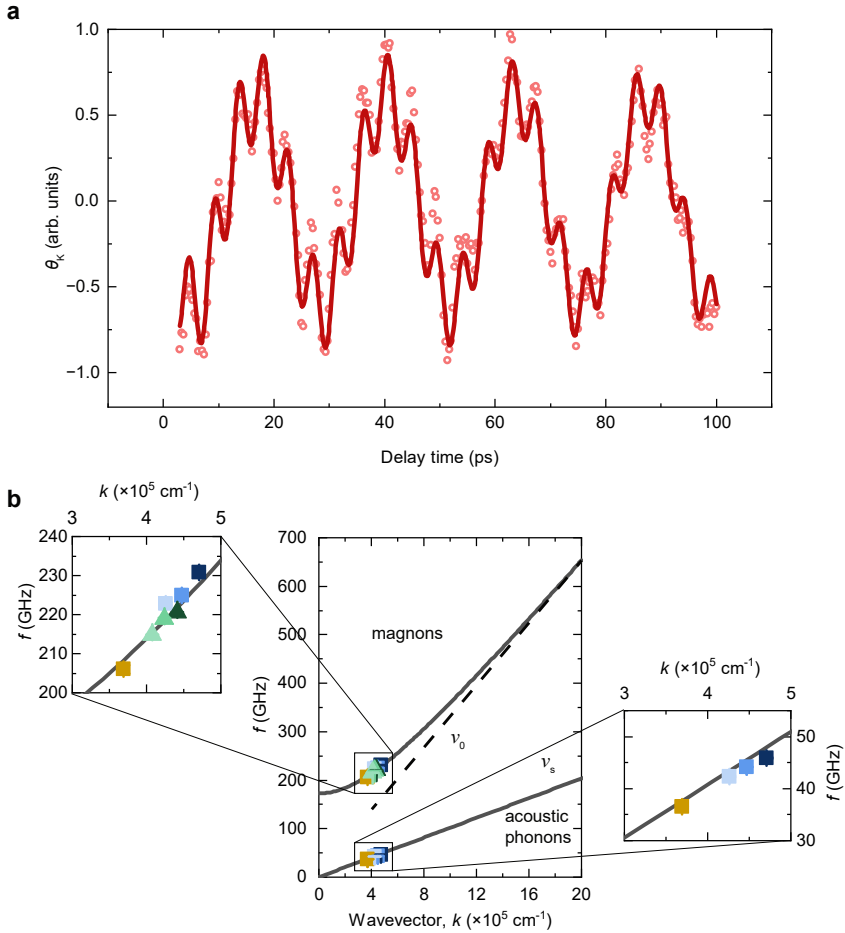


Figure 7.11: **Observation of a wavefront of propagating acoustic phonons.** **a**, Time resolved polarization rotation in the reflection geometry following excitation at $h\nu = 3.1$ eV, $T = 60$ K. The solid line represents a best fit using a double-sine function. The slower oscillations are the result of a finite- k phonon mode. The higher frequency oscillation corresponds to a finite- k magnon mode. **b**, Dispersion relation for the magnons, where the slope of the dispersion defines the (limiting) propagation speed of the waves, with the datapoints from Fig. 7.4. The extracted phonon frequencies are plot against the wavenumber calculated using Eq. 7.26 and fit with a linear dispersion, which then represents the (longitudinal) acoustic phonon branch in DyFeO₃.

7.8.5. TEMPERATURE AND MAGNETIC FIELD DEPENDENCE OF THE MAGNON AND PHONON MODES

To further investigate the behavior of the detected acoustic and magnetic finite- k waves, we studied their excitation at different temperatures across the Morin phase transition (see Fig. 7.12a). From the Fourier spectra of these signals (see Fig. 7.12b), we can distinguish clear contributions from the acoustic phonon mode (~ 40 GHz) and magnon mode (> 200 GHz) at all temperatures.

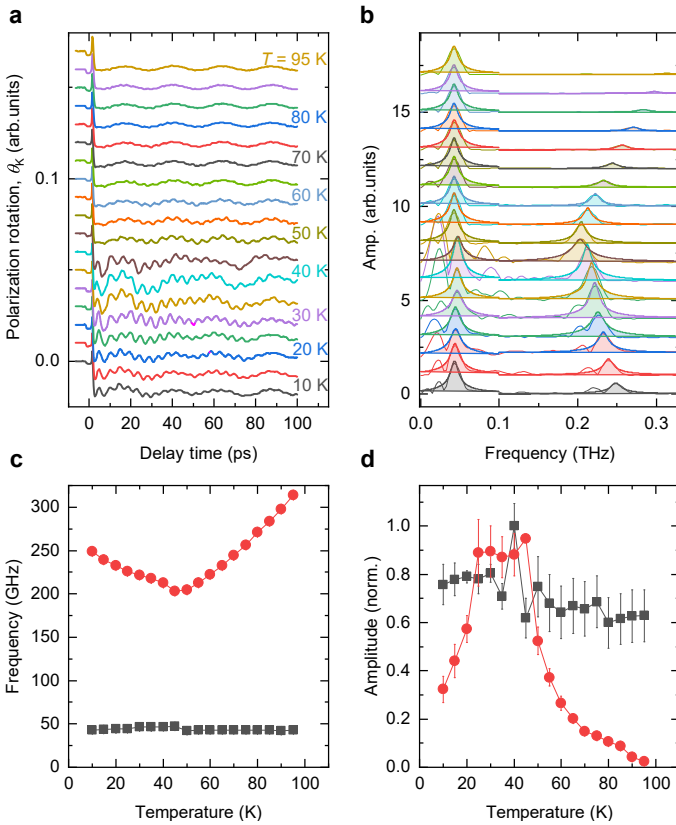


Figure 7.12: **Temperature dependence of the magnon and phonon modes.** **a**, Time-resolved measurements of the polarization rotation θ_K of a probe pulse ($\lambda_0 = 700$ nm) for different temperatures. **b**, The FFT spectra of the time-domain signals from panel **a**. The peaks corresponding to the phonon and magnon mode are fit with Lorentzians. **c,d**, The frequency (**c**) and amplitude (**d**) of the oscillatory components corresponding to the magnon and phonon mode, extracted with the Lorentzian fits in panel **b**. Red spheres: magnon data, black squares: phonon data.

Another way to confirm the attribution of the slow oscillation to an acoustic phonon mode and the fast oscillation to a magnon mode is to perform the measurements in a magnetic field. In the WFM phase, a magnetic field can bias the orientation of the small net magnetic moment of DyFeO_3 . As shown in Fig. 7.13, there is a strong dependence of the magnon amplitude on the polarity of the applied field in contrast to the phonon mode.

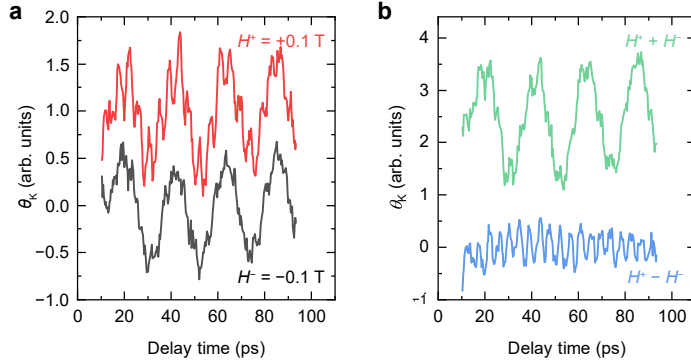


Figure 7.13: **Magnetic field dependence.** **a** Time-resolved measurements of the polarization rotation θ_k of a probe pulse ($\lambda_0 = 800$ nm) after excitation with pump pulses ($h\nu = 3.1$ eV) in magnetic fields with opposite polarity. **b**, The sum and difference of the signals from panel **a**, highlighting the phonon and magnon mode respectively.

7.8.6. POLARIZATION DEPENDENCE OF THE MAGNON AND PHONON MODES

The results of the measurements for different probe polarization orientations are summarized in Fig. 7.14. The polarization dependence of the amplitude of the measured oscillation corresponding to the magnon and phonon modes are substantially different. Whereas the phonon amplitude peaks for a probe polarization right in-between the crystal x - and y -axis ($\alpha = 45^\circ, 135^\circ$) and undergoes a 180° phase shift (see Fig. 7.14a), the magnon amplitude is less sensitive to the orientation and largest for the polarization oriented along the crystallographic x and y -axis. We also note that in vicinity of T_M the amplitude spectra reveal a probe polarization-dependent peak (mode 1) at a low frequency (~ 12 GHz), of which the origin remains to be identified.

The pump polarization of the excitation pulse has a profound effect on the amplitude and phase of the excited spin dynamics. As shown in Fig. 7.15, there is a slight change in phase as the pump polarization changes and a large change in the measured amplitude.

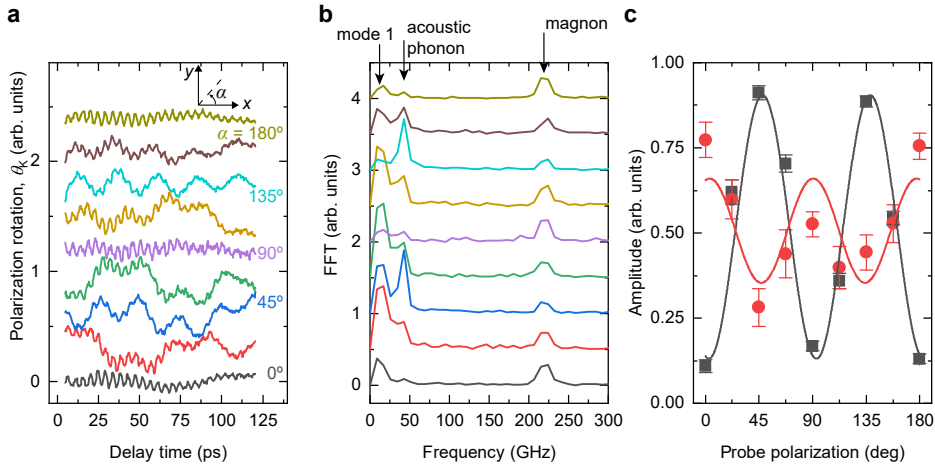


Figure 7.14: **Detection of finite- k magnon and phonon modes for different orientations of the probe polarization.** **a**, Time-resolved measurements of the polarization rotation $\Delta\theta_k$ of a probe pulse ($\lambda_0 = 690$ nm) for different orientations of the probe polarization plane w.r.t. the crystallographic x -axis. **b**, The Fourier spectra of the time-domain signals from panel **a**. **c**, The amplitude of the oscillatory components corresponding to the magnon and phonon mode for the different probe polarizations. The amplitudes are determined by fitting the data from panel **a** with a function with three sine functions with frequencies corresponding to the magnon, phonon and mode 1. The solid lines are guides to the eye to highlight the amplitude changes.

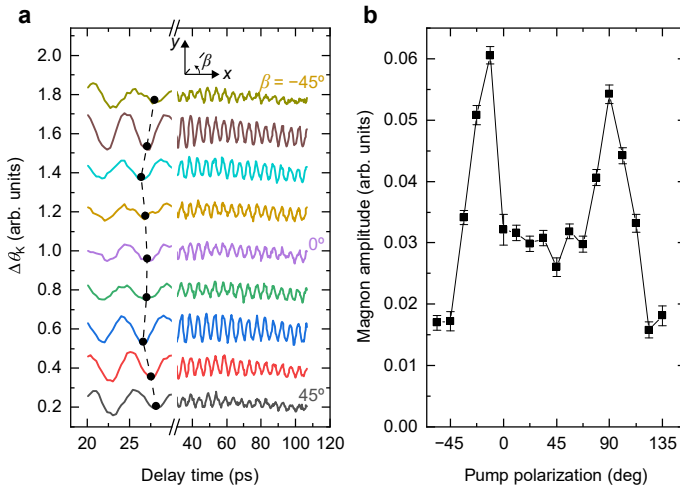


Figure 7.15: **Pump polarization dependence.** **a**, Time-resolved measurements of the polarization rotation $\Delta\theta_k$ of a probe pulse ($\lambda_0 = 800$ nm) for different orientations of the probe polarization plane ($h\nu = 3.1$ eV) w.r.t. the crystallographic x -axis. The connected points show the temporal position of the magnon minimum (phase) for each pump polarization. **b**, The amplitude of the oscillatory component corresponding to the magnon mode for the different orientations of the pump polarization plane. The amplitudes are determined by fitting the data from panel **a** with a sine function.

8

CONCLUSION AND OUTLOOK

“The important thing is not to stop questioning.”

Albert Einstein

The work presented in this thesis is diverse and explores the capabilities of resonant optical excitation to change (magnetic) materials on ultrashort timescales. It constitutes just a very small contribution to an immensely large research field. This contribution, however, does not just comprise the actual observations, it also consists of ‘potential’ for future experiments and directions of research. In this concluding chapter I provide the main conclusions of the work presented in this thesis and will reflect on unanswered questions and possible directions to extend this work.

Ultrashort pulses of electromagnetic radiation allow for materials to be driven strongly out of equilibrium. The purpose of studies on ultrafast control of material properties is usually two-fold. First of all, the ability to dynamically control macroscopic properties and steer systems into different states on short timescales is relevant for application in future technologies. In addition, these studies can visualize fundamental interactions between different degrees of freedom on their natural, picosecond timescales, which gives a unique insight in the different factors that determine the nature of a material's ground state.

This thesis covered experimental work on the ultrafast structural and magnetic dynamics in different material systems after selective excitation of optical resonances. In short, the main results of the work presented in this thesis concern: strain generation in an insulator (chapter 4) and control over magnetic interactions on picosecond timescales (chapter 5) after resonant lattice excitation, changing the anisotropy in a van der Waals antiferromagnet by excitation of orbital resonances (chapter 6) and the all-optical generation and detection of a broadband magnon wavepacket in an antiferromagnet using above-bandgap excitation (chapter 7). The most general and important conclusion one can make is that the importance of the ability to tune the frequency of the excitation can hardly be overestimated. Excitation of specific modes provides efficient routes to bring the system into otherwise inaccessible states and gives crucial insights in the microscopic mechanisms that underlie the macroscopic observations. Equally important is the side-effect that comes with this selectivity: the targeted dipole-active transition or vibration can be driven to large amplitude, while minimizing the dissipation of excess energy into unwanted channels. In the following, we summarize the main observations of the work from this thesis, and provide indications for future research directions.

8.1. NONLINEAR PHONONICS AND STRAIN GENERATION

In chapter 4 and 5 we explored resonant excitation of optical phonons in insulating materials in order to control material properties on ultrashort timescales. Selective driving of these low-energy lattice vibrations is a way to avoid the large heat-dissipation that typically comes with the excitation of the high-energy electronic degrees of freedom. In the insulator LaAlO_3 we observed coherent rotations of oxygen octahedra, corresponding to a Raman mode, after the excitation of an IR-active phonon mode. In the framework of nonlinear phononics, this impulsive excitation of Raman modes through ionic Raman scattering should be accompanied by a displacement along the Raman coordinate. This displacement is often invoked to explain the wide variety of phenomena observed after resonant lattice excitation. Our measurements serve as a confirmation of the presence of strong phonon-phonon coupling in wide bandgap insulating materials. In addition to coherent Raman oscillations, we observed the generation of transverse and longitudinal strain wavepackets. This indicates the presence of a strain gradient close to the material surface after excitation. The intimate relation between the excitation of optically-active lattice vibrations and macroscopic strain is still understudied. While different from the classical 'nonlinear phononics' mechanism [119], light-induced dynamical strain can also be used for material control. The presence of a tunable shear strain on ultrafast timescales can be exploited for control of many functional material properties such as ferroelectricity, including in ultrathin insulating oxide membranes.

8.2. CONTROLLING MAGNETIC PROPERTIES VIA RESONANT LATTICE EXCITATION

In chapter 5 we demonstrated that low-energy resonant lattice excitation can be used to manipulate fundamental magnetic interactions on the picosecond timescales. The time-evolution of the modified magnetic landscape was imprinted on the frequency of the relevant magnon mode, which softened with increased laser fluence. In the limit of large-amplitude phonon excitation, the modified Fe-Dy exchange interaction results in a coherent phase transition from an antiferromagnetic to a weakly ferromagnetic phase. Within a few picoseconds, the system is ballistically steered from its ground state into the competing magnetic phase. This striking observation strongly contrasts with the incoherent, heat-driven phase transition induced by exciting the electronic degrees of freedom, which is much slower.

The rare-earth ion plays a crucial role in this observation, as the strong exchange interaction between its orbital momentum and the ordered transition metal spins lead to a first-order spin reorientation transition in equilibrium. The rare-earth ion, with its large angular momentum, therefore provides the coupling of the magnetic system to the crystal lattice: a crucial component in this phonon-driven process. In this way it serves as an intermediate agent by connecting the transition metal spins to the crystal configuration. More generally, in order for the magnetic degree of freedom to be susceptible for resonant lattice excitation, there must be strong coupling to the crystal lattice, even in equilibrium. We therefore anticipate that very similar mechanisms or effects will be present in other rare-earth based compounds with similar anisotropic exchange interaction, such as manganites, vanadates, orthochromates and the other orthoferrites. In the specific case of the observations studied in chapter 5 there remain several open questions that could be answered by expanding the spectroscopy toolbox:

- Ultrafast X-ray diffraction can be used to experimentally establish the presence of transient lattice distortions after excitation.
- While the role of the rare earth ion has been established in our work through a phenomenological model, supported by DFT calculations, it would be highly interesting to conduct further experimental studies. An ultrafast THz probe could be used to establish the role of the configuration of the Dy electronic system on the observed changes in the magnetic interactions.
- Magneto-optical imaging can be used to visualize the nucleation of the weakly ferromagnetic phase [255], which will give general insight in the factors that determine the emergence speed and direction of photoinduced net magnetic moments.

It is only recently that selective excitation of optical phonons has been applied to steer magnetic systems into differently ordered phases [167, 269]. With the vast amount of insulating (anti)ferromagnets and the increased tunability of ultrashort pulses of light across the THz spectrum, these demonstrations only form the tip of the iceberg. In addition to applying the known technique to different material systems, future research can focus on electric field enhancement by integrating tailored antennas into the experimental setup [60] or to use cavities to enhance light-matter coupling [270]. Moreover

the concept can be extended to thin films and oxide heterostructures, as the resonant lattice excitation and the pump-induced effects are naturally confined to a small volume of less than a micrometer.

8.3. MAGNETIC EXCITATIONS IN A VAN DER WAALS ANTIFERROMAGNET

In chapter 6 we demonstrated that the selective excitation of orbital resonances in a van der Waals antiferromagnet can induce transient anisotropy and excite a previously unreported high-frequency magnon with a two-dimensional character. This work marks the capability of dynamical control experiments to uncover equilibrium properties in strongly correlated materials [216]. We anticipate to observe very similar effects on the magnetic system in the other antiferromagnetic thiophosphates FePS_3 and MnPS_3 . While the observation of pumping orbital resonances in order to control magnetic properties by itself is intriguing [61], the application in van der Waals antiferromagnets has the appeal of applicability in future, ultrafast and ultrathin devices. The first step towards this goal would be to perform pump-probe experiments on ultrathin flakes of these materials. This is a feasible scenario, as the thiophosphates can indeed be exfoliated down to the few-layer limit while preserving their magnetic properties [238, 271] which can be optically probed in atomically thin samples [272, 273].

8.4. PROPAGATING COHERENT ANTIFERROMAGNETIC SPIN WAVES

Impulsive excitation of coherent spin dynamics through various mechanisms has been one of the key topics within the field studying antiferromagnetic order manipulation ever since its first demonstration [34]. This uniform spin precession ($k = 0$) is limited to the optically excited volume, as the group velocity of these spin waves is nearly zero. Very recently several demonstrations of magnon-mediated spin-transport in antiferromagnets were reported. However, the spin transport is in these cases carried by incoherent magnons [250–252] or evanescent spin-waves [253]. In chapter 7 we demonstrated that confined impulsive excitation, using ultrashort pulses of light, can generate a coherent, broadband magnon wavepacket in an insulating antiferromagnet. We study this wavepacket using an optical detection method that relies on the Bragg reflection of the light as a result of interference between the probe pulse and the spin-wave packet.

This first demonstration of coherent propagating spin waves with nanometer wavelengths in an antiferromagnet is a crucial step towards terahertz antiferromagnetic magnonics. Phase-coherent ballistic spin-wave transport in an antiferromagnet is also interesting from a fundamental point of view and forms the starting point of many different future experiments. From the detection point of view, an unanswered question is whether these propagating antiferromagnetic spin waves can be detected in a non-local experiment. One could think of the experimental geometry shown in Fig. 8.1, where the volume where the spin waves are detected is physically separated from the optically excited volume. The detection could be performed in different ways:

- One option is to use near-infrared laser pulses, similar to the experiments described in this work (Fig. 8.1a).

- Another potential optical detection method relies on using AFM/heavy-metal bilayers to test whether the antiferromagnet propagating spin waves can result in THz emission from the heavy-metal film [257] (see Fig. 8.1b). This approach is inspired on the success of ultrafast spin-current generation in ferromagnet/heavy-metal bilayers in recent years [274].
- An important next step is to study the feasibility of electrical detection methods of the wavepacket of coherent phonons, similar to Refs. [68, 250–252, 260] (see Fig. 8.1b). Electrical detection is a crucial step towards the integration of the demonstrated concept in magnonic devices.

In terms of generation methods, future research could focus on generating propagating antiferromagnetic spin waves in-plane, possibly in thin films. This brings the research direction more in line with ferromagnetic magnonic studies that often use planar wave guides [66, 67]. This requires confinement of the excitation in the transverse direction, as compared to the lateral confinement provided by the penetration depth in our work.

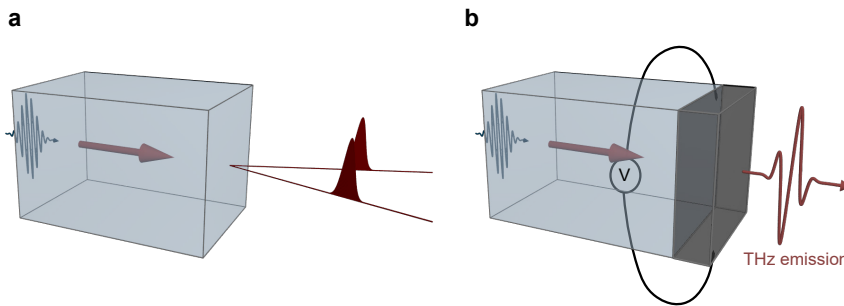


Figure 8.1: **Nonlocal detection of propagating spin waves.** **a,b**, Schematic of two potential experiments to measure the propagating antiferromagnetic spin waves nonlocally, after their propagation through the antiferromagnetic material: either by probing with laser pulses (**a**) or detection in a (heavy) metallic layer (black), using THz emission or a pump-induced voltage through spin-to-charge conversion using the inverse spin hall effect. (**b**)

8.5. CONCLUDING REMARKS

The results in this thesis are part of the large ongoing effort within condensed matter physics to steer (quantum) materials into competing groundstates and exert control over material properties on the fastest timescales [14]. Continuous progress in the generation of ultrashort (low)-THz pulses [275] and breakthroughs in temporal [276] and spectral pulse-shaping techniques [21] in the few-THz range, make that the possibilities for selective material control are almost endless.

REFERENCES

- ¹J. H. Nord, A. Koohang, and J. Paliszkievicz, *The Internet of Things: Review and theoretical framework*, [Expert Systems with Applications](#) **133**, 97 (2019).
- ²G. E. Moore et al., *Cramming more components onto integrated circuits*, [Electronics](#) **38**, 1 (1965).
- ³G. E. Moore et al., *Progress in digital integrated electronics*, International Electron devices meeting **21**, 11 (1975).
- ⁴T. N. Theis and H.-S. P. Wong, *The End of Moore's Law: A New Beginning for Information Technology*, [Computing in Science Engineering](#) **19**, 41 (2017).
- ⁵I. L. Markov, *Limits on fundamental limits to computation*, [Nature](#) **512**, 147 (2014).
- ⁶N. Jones, *How to stop data centres from gobbling up the world's electricity*, [Nature](#) **561**, 163 (2018).
- ⁷J. Shalf, *The future of computing beyond Moore's law*, [Philosophical Transactions of the Royal Society A](#) **378**, 20190061 (2020).
- ⁸S. Lathrop and T. Murphy, *High-performance computing education*, [Computing in Science & Engineering](#) **10**, 9 (2008).
- ⁹*A thin film approach to engineering functionality into oxides*, [Journal of the American Ceramic Society](#) **91**, 2429 (2008).
- ¹⁰J. Mannhart and D. G. Schlom, *Oxide interfaces—an opportunity for electronics*, [Science](#) **327**, 1607 (2010).
- ¹¹H. Hwang et al., *Emergent phenomena at oxide interfaces*, [Nature Materials](#) **11**, 103 (2012).
- ¹²D. G. Schlom et al., *Elastic strain engineering of ferroic oxides*, [MRS Bulletin](#) **39**, 118 (2014).
- ¹³Y. Tokura, M. Kawasaki, and N. Nagaosa, *Emergent functions of quantum materials*, [Nature Physics](#) **13**, 1056 (2017).
- ¹⁴D. Basov, R. Averitt, and D. Hsieh, *Towards properties on demand in quantum materials*, [Nature Materials](#) **16**, 1077 (2017).
- ¹⁵J. Zhang and R. D. Averitt, *Dynamics and control in complex transition metal oxides*, [Annual Review of Materials Research](#) **44**, 19 (2014).
- ¹⁶J. Ngai, F. Walker, and C. Ahn, *Correlated oxide physics and electronics*, [Annual Review of Materials Research](#) **44**, 1 (2014).
- ¹⁷R. A. Bartels et al., *Generation of spatially coherent light at extreme ultraviolet wavelengths*, [Science](#) **297**, 376 (2002).
- ¹⁸G. Cerullo and S. De Silvestri, *Ultrafast optical parametric amplifiers*, [Review of Scientific Instruments](#) **74**, 1 (2003).
- ¹⁹K. Reimann, *Table-top sources of ultrashort THz pulses*, [Reports on Progress in Physics](#) **70**, 1597 (2007).

- ²⁰A. Sell, A. Leitenstorfer, and R. Huber, *Phase-locked generation and field-resolved detection of widely tunable terahertz pulses with amplitudes exceeding 100 MV/cm*, *Optics Letters* **33**, 2767 (2008).
- ²¹B. Liu et al., *Generation of narrowband, high-intensity, carrier-envelope phase-stable pulses tunable between 4 and 18 THz*, *Optics Letters* **42**, 129 (2017).
- ²²A. de la Torre et al., *Nonthermal pathways to ultrafast control in quantum materials*, *Reviews of Modern Physics* **93**, 041002 (2021).
- ²³M. Buzzi, M. Först, R. Mankowsky, and A. Cavalleri, *Probing dynamics in quantum materials with femtosecond X-rays*, *Nature Reviews Materials* **3**, 299 (2018).
- ²⁴B. Lv, T. Qian, and H. Ding, *Angle-resolved photoemission spectroscopy and its application to topological materials*, *Nature Reviews Physics* **1**, 609 (2019).
- ²⁵T. L. Cocker et al., *An ultrafast terahertz scanning tunnelling microscope*, *Nature Photonics* **7**, 620 (2013).
- ²⁶M. Wagner et al., *Ultrafast and nanoscale plasmonic phenomena in exfoliated graphene revealed by infrared pump-probe nanoscopy*, *Nano letters* **14**, 894 (2014).
- ²⁷K. Miyano, T. Tanaka, Y. Tomioka, and Y. Tokura, *Photoinduced insulator-to-metal transition in a perovskite manganite*, *Physical Review Letters* **78**, 4257 (1997).
- ²⁸Y. X. Yan, E. B. Gamble, and K. A. Nelson, *Impulsive stimulated scattering: general importance in femtosecond laser pulse interactions with matter, and spectroscopic applications*, *The Journal of Chemical Physics* **83**, 5391 (1985).
- ²⁹E. Beaupaire, J.-C. Merle, A. Daunois, and J.-Y. Bigot, *Ultrafast spin dynamics in ferromagnetic nickel*, *Physical Review Letters* **76**, 4250 (1996).
- ³⁰F. Schmitt et al., *Transient electronic structure and melting of a charge density wave in $TbTe_3$* , *Science* **321**, 1649 (2008).
- ³¹S. Hellmann et al., *Ultrafast melting of a charge-density wave in the Mott insulator $1T-TaS_2$* , *Physical Review Letters* **105**, 187401 (2010).
- ³²M. F. Becker et al., *Femtosecond laser excitation of the semiconductor-metal phase transition in VO_2* , *Applied Physics Letters* **65**, 1507 (1994).
- ³³A. Cavalleri et al., *Femtosecond structural dynamics in VO_2 during an ultrafast solid-solid phase transition*, *Physical Review Letters* **87**, 237401 (2001).
- ³⁴A. V. Kimel, A. Kirilyuk, A. Tsvetkov, R. V. Pisarev, and T. Rasing, *Laser-induced ultrafast spin reorientation in the antiferromagnet $TmFeO_3$* , *Nature* **429**, 850 (2004).
- ³⁵D. Fausti et al., *Light-induced superconductivity in a stripe-ordered cuprate*, *Science* **331**, 189 (2011).
- ³⁶R. Mankowsky et al., *Nonlinear lattice dynamics as a basis for enhanced superconductivity in $YBa_2Cu_3O_{6.5}$* , *Nature* **516**, 71 (2014).
- ³⁷C. D. Stanciu et al., *All-optical magnetic recording with circularly polarized light*, *Physical Review Letters* **99**, 047601 (2007).
- ³⁸A. Stupakiewicz, K. Szerenos, D. Afanasiev, A. Kirilyuk, and A. V. Kimel, *Ultrafast nonthermal photo-magnetic recording in a transparent medium*, *Nature* **542**, 71 (2017).
- ³⁹A. Kirilyuk, A. V. Kimel, and T. Rasing, *Ultrafast optical manipulation of magnetic order*, *Reviews of Modern Physics* **82**, 2731 (2010).

- ⁴⁰E. Y. Vedmedenko et al., *The 2020 magnetism roadmap*, *Journal of Physics D: Applied Physics* **53**, 453001 (2020).
- ⁴¹C. Gong et al., *Discovery of intrinsic ferromagnetism in two-dimensional van der Waals crystals*, *Nature* **546**, 265 (2017).
- ⁴²K. F. Mak, J. Shan, and D. C. Ralph, *Probing and controlling magnetic states in 2D layered magnetic materials*, *Nature Reviews Physics* **1**, 646 (2019).
- ⁴³X. X. Zhang et al., *Gate-tunable spin waves in antiferromagnetic atomic bilayers*, *Nature Materials* **19**, 838 (2020).
- ⁴⁴B. Koopmans, *The ultimate view*, *Nature materials* **6**, 715 (2007).
- ⁴⁵M. van Kampen et al., *All-optical probe of coherent spin waves*, *Physical Review Letters* **88**, 227201 (2002).
- ⁴⁶N. P. Duong, T. Satoh, and M. Fiebig, *Ultrafast manipulation of antiferromagnetism of NiO*, *Physical Review Letters* **93**, 117402 (2004).
- ⁴⁷A. V. Kimel et al., *Ultrafast non-thermal control of magnetization by instantaneous photomagnetic pulses*, *Nature* **435**, 655 (2005).
- ⁴⁸A. M. Kalashnikova et al., *Impulsive generation of coherent magnons by linearly polarized light in the easy-plane antiferromagnet FeBO₃*, *Physical Review Letters* **99**, 167205 (2007).
- ⁴⁹A. V. Kimel and M. Li, *Writing magnetic memory with ultrashort light pulses*, *Nature Reviews Materials* **4**, 189 (2019).
- ⁵⁰J. Hohlfeld et al., *Fast magnetization reversal of GdFeCo induced by femtosecond laser pulses*, *Physical Review B* **65**, 1 (2002).
- ⁵¹T. Ostler et al., *Ultrafast heating as a sufficient stimulus for magnetization reversal in a ferrimagnet*, *Nature Communications* **3**, 666 (2012).
- ⁵²D. Afanasiev et al., *Laser excitation of lattice-driven anharmonic magnetization dynamics in dielectric FeBO₃*, *Physical Review Letters* **112**, 147403 (2014).
- ⁵³G. Ju et al., *Ultrafast generation of ferromagnetic order via a laser-induced phase transformation in FeRh thin films*, *Physical Review Letters* **93**, 197403 (2004).
- ⁵⁴J. U. Thiele, M. Buess, and C. H. Back, *Spin dynamics of the antiferromagnetic-to-ferromagnetic phase transition in FeRh on a sub-picosecond time scale*, *Applied Physics Letters* **85**, 2857 (2004).
- ⁵⁵T. Kampfrath et al., *Coherent terahertz control of antiferromagnetic spin waves*, *Nature Photonics* **5**, 31 (2011).
- ⁵⁶M. Först et al., *Driving magnetic order in a manganite by ultrafast lattice excitation*, *Physical Review B* **84**, 241104 (2011).
- ⁵⁷T. F. Nova et al., *An effective magnetic field from optically driven phonons*, *Nature Physics* **13**, 132 (2016).
- ⁵⁸S. F. Maehrlein et al., *Dissecting spin-phonon equilibration in ferrimagnetic insulators by ultrafast lattice excitation*, *Science Advances* **4**, eaar5164 (2018).
- ⁵⁹S. Baierl et al., *Nonlinear spin control by terahertz-driven anisotropy fields*, *Nature Photonics* **10**, 715 (2016).
- ⁶⁰S. Schlauderer et al., *Temporal and spectral fingerprints of ultrafast all-coherent spin switching*, *Nature* **569**, 383 (2019).

- ⁶¹R. V. Mikhaylovskiy et al., *Resonant pumping of $d-d$ crystal field electronic transitions as a mechanism of ultrafast optical control of the exchange interactions in iron oxides*, *Physical Review Letters* **125**, 157201 (2020).
- ⁶²V. V. Kruglyak, S. O. Demokritov, and D. Grundler, *Magnonics*, *Journal of Physics D: Applied Physics* **43**, 14 (2010).
- ⁶³A. V. Chumak, V. I. Vasyuchka, A. A. Serga, and B. Hillebrands, *Magnon spintronics*, *Nature Physics* **11**, 453 (2015).
- ⁶⁴A. Barman et al., *The 2021 Magnonics Roadmap*, *Journal of Physics: Condensed Matter* **33**, 413001 (2021).
- ⁶⁵P. Pirro, V. I. Vasyuchka, A. A. Serga, and B. Hillebrands, *Advances in coherent magnonics*, *Nature Reviews Materials*, 1 (2021).
- ⁶⁶A. A. Serga, A. V. Chumak, and B. Hillebrands, *YIG magnonics*, *Journal of Physics D: Applied Physics* **43**, 16 (2010).
- ⁶⁷B. Lenk, H. Ulrichs, F. Garbs, and M. Münzenberg, *The building blocks of magnonics*, *Physics Reports* **507**, 107 (2011).
- ⁶⁸L. J. Cornelissen, J. Liu, R. A. Duine, J. B. Youssef, and B. J. Van Wees, *Long-distance transport of magnon spin information in a magnetic insulator at room temperature*, *Nature Physics* **11**, 1022 (2015).
- ⁶⁹C. Thomsen, H. T. Grahn, H. J. Maris, and J. Tauc, *Surface generation and detection of phonons by picosecond light pulses*, *Physical Review B* **34**, 4129 (1986).
- ⁷⁰P. Ruello and V. E. Gusev, *Physical mechanisms of coherent acoustic phonons generation by ultrafast laser action*, *Ultrasonics* **56**, 21 (2015).
- ⁷¹M. Lejman et al., *Giant ultrafast photo-induced shear strain in ferroelectric BiFeO_3* , *Nature Communications* **5**, 4301 (2014).
- ⁷²D. Khomskii, *Transition metal compounds* (Cambridge University Press, 2014).
- ⁷³D. J. Griffiths and D. F. Schroeter, *Introduction to quantum mechanics* (Cambridge University Press, 2018).
- ⁷⁴J. Stöhr and H. C. Siegmann, *Magnetism, From fundamentals to nanoscale dynamics*, Vol. 5 (Springer, Berlin, Heidelberg, 2006).
- ⁷⁵S. Bewick, J. Edge, T. Forsythe, and R. Parsons, *Ck-12 chemistry* (CK-12 Foundation, 2009).
- ⁷⁶J. M. D. Coey, *Magnetism and magnetic materials* (Cambridge University Press, 2010).
- ⁷⁷S. Blundell, *Magnetism in condensed matter* (American Association of Physics Teachers, 2003).
- ⁷⁸D. Dai, H. Xiang, and M.-H. Whangbo, *Effects of spin-orbit coupling on magnetic properties of discrete and extended magnetic systems*, *Journal of computational chemistry* **29**, 2187 (2008).
- ⁷⁹J. Jensen and A. R. Mackintosh, *Rare earth magnetism* (Clarendon Press Oxford, 1991).
- ⁸⁰A. Moskvin, *Dzyaloshinskii interaction and exchange-relativistic effects in orthoferrites*, *Journal of Experimental and Theoretical Physics* **132**, 517 (2021).
- ⁸¹I. Dzialoshinskii, *Thermodynamic theory of "weak" ferromagnetism in antiferromagnetic substances*, *Soviet Physics - JETP* **5**, 1259 (1957), [Original: *Zh. Eksp. Teor. Fiz.*, **32**, 1547 (1957)].
- ⁸²T. Moriya, *Anisotropic superexchange interaction and weak ferromagnetism*, *Physical Review* **120**, 91 (1960).

- ⁸³N. D. Mermin and H. Wagner, *Absence of ferromagnetism or antiferromagnetism in one- or two-dimensional isotropic Heisenberg models*, *Physical Review Letters* **17**, 1133 (1966).
- ⁸⁴F. Bloch, *Zur Theorie des Ferromagnetismus*, *Zeitschrift für Physik* **61**, 206 (1930).
- ⁸⁵A. G. Gurevich and G. A. Melkov, *Magnetization oscillations and waves* (CRC press, 1996).
- ⁸⁶A. K. A.M. Kosevich B.A. Ivanov, *Magnetic Solitons*, *Physics Reports* **194**, 117 (1990).
- ⁸⁷V. Bar'yakhtar, M. Chetkin, B. Ivanov, and S. Gadetskii, *Dynamics of Topological Magnetic Solitons: Experiment and Theory*, Vol. 129 (Springer-Verlag Berlin Heidelberg, 1994), p. 187.
- ⁸⁸B. A. Ivanov, *Spin dynamics of antiferromagnets under action of femtosecond laser pulses*, *Low Temperature Physics* **40**, 119 (2014).
- ⁸⁹B. A. Ivanov, *Spin dynamics for antiferromagnets and ultrafast spintronics*, *Journal of Experimental and Theoretical Physics* **131**, 95 (2020).
- ⁹⁰S. M. Rezende, A. Azevedo, and R. L. Rodríguez-Suárez, *Introduction to antiferromagnetic magnons*, *Journal of Applied Physics* **126**, 151101 (2019).
- ⁹¹E. G. Galkina and B. A. Ivanov, *Dynamic solitons in antiferromagnets (Review Article)*, *Low Temperature Physics* **44**, 618 (2018).
- ⁹²A. V. Kimel et al., *Inertia-driven spin switching in antiferromagnets*, *Nature Physics* **5**, 727 (2009).
- ⁹³S. Backus, C. G. Durfee III, M. M. Murnane, and H. C. Kapteyn, *High power ultrafast lasers*, *Review of Scientific Instruments* **69**, 1207 (1998).
- ⁹⁴R. Paschotta, *Article on 'critical phase matching'*, in *RP Photonics Encyclopedia*, Accessed on 27-11-2021 ().
- ⁹⁵A. Zvezdin and V. Kotov, *Modern magnetooptics and magneto-optical materials*, *Condensed Matter Physics* (CRC Press, 1997).
- ⁹⁶S. A. Siddiqui et al., *Metallic antiferromagnets*, *Journal of Applied Physics* **128**, 040904 (2020).
- ⁹⁷J. A. Giordmaine and W. Kaiser, *Light scattering by coherently driven lattice vibrations*, *Physical Review* **144**, 676 (1966).
- ⁹⁸R. Merlin, *Generating coherent THz phonons with light pulses*, *Solid State Communications* **102**, 207 (1997).
- ⁹⁹J. Dil, *Brillouin scattering in condensed matter*, *Reports on Progress in Physics* **45**, 285 (1982).
- ¹⁰⁰C. Thomsen, H. T. Grahn, H. J. Maris, and J. Tauc, *Picosecond interferometric technique for study of phonons in the Brillouin frequency range*, *Optics Communications* **60**, 55 (1986).
- ¹⁰¹O. Matsuda, O. B. Wright, D. H. Hurley, V. E. Gusev, and K. Shimizu, *Coherent shear phonon generation and detection with ultrashort optical pulses*, *Physical Review Letters* **93**, 095501 (2004).
- ¹⁰²P. Babilotte et al., *Femtosecond laser generation and detection of high-frequency acoustic phonons in GaAs semiconductors*, *Physical Review B* **81**, 245207 (2010).
- ¹⁰³J. Hortensius, D. Afanasiev, A. Sasani, E. Bousquet, and A. Caviglia, *Ultrafast strain engineering and coherent structural dynamics from resonantly driven optical phonons in LaAlO₃*, *npj Quantum Materials* **5**, 95 (2020).
- ¹⁰⁴J. A. Mundy et al., *Atomically engineered ferroic layers yield a room-temperature magnetoelectric multiferroic*, *Nature* **537**, 523 (2016).
- ¹⁰⁵J. H. Haeni et al., *Room-temperature ferroelectricity in strained SrTiO₃*, *Nature* **430**, 758 (2004).
- ¹⁰⁶D. G. Schlom et al., *Strain tuning of ferroelectric thin films*, *Annual Review of Materials Research* **37**, 589 (2007).

- ¹⁰⁷D. Sando et al., *Crafting the magnonic and spintronic response of BiFeO₃ films by epitaxial strain*, *Nature Materials* **12**, 641 (2013).
- ¹⁰⁸H. Wen et al., *Electronic origin of ultrafast photoinduced strain in BiFeO₃*, *Physical Review Letters* **110**, 037601 (2013).
- ¹⁰⁹E. Baldini et al., *Exciton control in a room temperature bulk semiconductor with coherent strain pulses*, *Science Advances* **5**, eaax2937 (2019).
- ¹¹⁰A. A. Demenev et al., *Ultrafast strain-induced switching of a bistable cavity-polariton system*, *Physical Review B* **100**, 100301 (2019).
- ¹¹¹A. S. Kuznetsov, K. Biermann, and P. V. Santos, *Dynamic acousto-optical control of confined polariton condensates: From single traps to coupled lattices*, *Physical Review Research* **1**, 023030 (2019).
- ¹¹²E. J. Sie et al., *An ultrafast symmetry switch in a Weyl semimetal*, *Nature* **565**, 61 (2019).
- ¹¹³M. Y. Zhang et al., *Light-induced subpicosecond lattice symmetry switch in MoTe₂*, *Physical Review X* **9**, 021036 (2019).
- ¹¹⁴A. D. Caviglia et al., *Ultrafast strain engineering in complex oxide heterostructures*, *Physical Review Letters* **108**, 136801 (2012).
- ¹¹⁵I. A. Mogunov et al., *Ultrafast insulator-metal transition in VO₂ nanostructures assisted by picosecond strain pulses*, *Physical Review Applied* **11**, 14054 (2019).
- ¹¹⁶M. Rini et al., *Control of the electronic phase of a manganite by mode-selective vibrational excitation*, *Nature* **449**, 72 (2007).
- ¹¹⁷M. Först et al., *Spatially resolved ultrafast magnetic dynamics initiated at a complex oxide heterointerface*, *Nature Materials* **14**, 883 (2015).
- ¹¹⁸M. Först et al., *Multiple supersonic phase fronts launched at a complex-oxide heterointerface*, *Physical Review Letters* **118**, 027401 (2017).
- ¹¹⁹M. Först et al., *Nonlinear phononics as an ultrafast route to lattice control*, *Nature Physics* **7**, 854 (2011).
- ¹²⁰A. A. Maradudin and R. F. Wallis, *Ionic Raman effect. I. scattering by localized vibration modes*, *Physical Review B* **2**, 4294 (1970).
- ¹²¹R. F. Wallis and A. A. Maradudin, *Ionic Raman effect. II. the first-order ionic Raman effect*, *Physical Review B* **3**, 2063 (1971).
- ¹²²A. Subedi, A. Cavalleri, and A. Georges, *Theory of nonlinear phononics for coherent light control of solids*, *Physical Review B* **89**, 220301 (2014).
- ¹²³Y. Peter and M. Cardona, *Fundamentals of semiconductors: physics and materials properties*, 4th ed. (Springer Science & Business Media, 2010).
- ¹²⁴M. Dresselhaus, G. Dresselhaus, S. B. Cronin, and A. G. Souza Filho, *Solid state properties* (Springer-Verlag Berlin Heidelberg, 2018).
- ¹²⁵D. M. Juraschek, M. Fechner, and N. A. Spaldin, *Ultrafast structure switching through nonlinear phononics*, *Physical Review Letters* **118**, 054101 (2017).
- ¹²⁶P. G. Radaelli, *Breaking symmetry with light: Ultrafast ferroelectricity and magnetism from three-phonon coupling*, *Physical Review B* **97**, 085145 (2018).
- ¹²⁷T. Nova, *Nonequilibrium control of broken-symmetry phases in quantum materials - a low-energy approach*, PhD thesis (Universität Hamburg, Hamburg, 2020).

- ¹²⁸R. W. Wordenweber, *Growth of high- T_c thin films*, *Superconductor Science and Technology* **12**, 79339 (1999).
- ¹²⁹W. Prellier, P. Lecoeur, and B. Mercey, *Colossal-magneto-resistive manganite thin films*, *Journal of Physics Condensed Matter* **13**, 915 (2001).
- ¹³⁰S. Middey et al., *Physics of ultrathin films and heterostructures of rare-earth nickelates*, *Annual Review of Materials Research* **46**, 305 (2016).
- ¹³¹Z. M. Zhang, B. I. Choi, M. I. Flik, and A. C. Anderson, *Infrared refractive indices of LaAlO_3 , LaGaO_3 , and NdGaO_3* , *Journal of the Optical Society of America B* **11**, 2252 (1994).
- ¹³²M. V. Abrashev et al., *Comparative study of optical phonons in the rhombohedrally distorted perovskites LaAlO_3 and LaMnO_3* , *Physical Review B* **59**, 4146 (1999).
- ¹³³K. D. Fredrickson, C. Lin, S. Zollner, and A. A. Demkov, *Theoretical study of negative optical mode splitting in*, *Physical Review B* **93**, 134301 (2016).
- ¹³⁴S. G. Lim et al., *Dielectric functions and optical bandgaps of high- K dielectrics for metal-oxide-semiconductor field-effect transistors by far ultraviolet spectroscopic ellipsometry*, *Journal of Applied Physics* **91**, 4500 (2002).
- ¹³⁵E. Chernova et al., *Optical NIR-VIS-VUV constants of advanced substrates for thin-film devices*, *Optical Materials Express* **7**, 3844 (2017).
- ¹³⁶J. F. Scott, *Raman study of trigonal-cubic phase transitions in rare-earth aluminates*, *Physical Review* **183**, 823 (1969).
- ¹³⁷M. A. Carpenter, S. V. Sinogeikin, J. D. Bass, D. L. Lakshtanov, and S. D. Jacobsen, *Elastic relaxations associated with the $\text{Pm}\bar{3}m\text{-R}\bar{3}c$ transition in LaAlO_3 : I. single crystal elastic moduli at room temperature*, *Journal of Condensed Matter Physics* **22**, 035403 (2010).
- ¹³⁸C. Cancellieri et al., *Electrostriction at the $\text{LaAlO}_3/\text{SrTiO}_3$ interface*, *Physical Review Letters* **107**, 056102 (2011).
- ¹³⁹X. Gonze et al., *The Abinitproject: Impact, environment and recent developments*, *Computer Physics Communications* **248**, 107042 (2020).
- ¹⁴⁰M. Först et al., *Displacive lattice excitation through nonlinear phononics viewed by femtosecond X-ray diffraction*, *Solid State Communications* **169**, 24 (2013).
- ¹⁴¹T. Willett-Gies, E. DeLong, and S. Zollner, *Vibrational properties of bulk LaAlO_3 from Fourier-transform infrared ellipsometry*, *Thin Solid Films* **571**, 620 (2014).
- ¹⁴²T. F. Nova, A. S. Disa, M. Fechner, and A. Cavalleri, *Metastable ferroelectricity in optically strained SrTiO_3* , *Science* **364**, 1075 (2019).
- ¹⁴³V. Gusev, P. Picart, D. Mounier, and J. M. Breteau, *On the possibility of ultrashort shear acoustic pulse excitation due to the laser-induced electrostrictive effect*, *Optics Communications* **204**, 229 (2002).
- ¹⁴⁴D. Afanasiev, A. K. Zvezdin, and A. V. Kimel, *Laser-induced shift of the Morin point in antiferromagnetic DyFeO_3* , *Optics Express* **23**, 23978 (2015).
- ¹⁴⁵P. Zubko, G. Catalan, and A. K. Tagantsev, *Flexoelectric effect in solids*, *Annual Review of Materials Research* **43**, 387 (2013).
- ¹⁴⁶P. Hohenberg and W. Kohn, *Inhomogeneous electron gas*, *Physical Review* **136**, B864 (1964).
- ¹⁴⁷W. Kohn and L. J. Sham, *Self-consistent equations including exchange and correlation effects*, *Physical Review* **140**, A1133 (1965).

- ¹⁴⁸X. Gonze et al., *First-principles computation of material properties: the ABINIT software project*, *Computational Materials Science* **25**, 478 (2002).
- ¹⁴⁹M. Torrent, F. Jollet, F. Bottin, G. Zerah, and X. Gonze, *Implementation of the projector augmented-wave method in the ABINIT code: application to the study of iron under pressure*, *Computational Materials Science* **42**, 337 (2008).
- ¹⁵⁰D. R. Hamann, *Optimized norm-conserving Vanderbilt pseudopotentials*, *Physical Review B* **88**, 085117 (2013).
- ¹⁵¹M. van Setten et al., *The PseudoDojo: Training and grading a 85 element optimized norm-conserving pseudopotential table*, *Computer Physics Communications* **226**, 39 (2018).
- ¹⁵²J. P. Perdew et al., *Restoring the density-gradient expansion for exchange in solids and surfaces*, *Physical Review Letters* **100**, 136406 (2008).
- ¹⁵³X. Gonze and C. Lee, *Dynamical matrices, Born effective charges, dielectric permittivity tensors, and interatomic force constants from density-functional perturbation theory*, *Physical Review B* **55**, 10355 (1997).
- ¹⁵⁴X. Gonze, *First-principles responses of solids to atomic displacements and homogeneous electric fields: Implementation of a conjugate-gradient algorithm*, *Physical Review B* **55**, 10337 (1997).
- ¹⁵⁵T. Kohmoto, M. Masui, M. Abe, T. Moriyasu, and K. Tanaka, *Ultrafast dynamics of soft phonon modes in perovskite dielectrics observed by coherent phonon spectroscopy*, *Physical Review B* **83**, 064304 (2011).
- ¹⁵⁶P. G. Klemens, *Anharmonic decay of optical phonon in diamond*, *Physical Review B* **138**, 845 (1966).
- ¹⁵⁷A. J. Hatt and N. A. Spaldin, *Structural phases of strained LaAlO_3 driven by octahedral tilt instabilities*, *Physical Review B* **82**, 195402 (2010).
- ¹⁵⁸S. Geller and V. B. Bala, *Crystallographic studies of perovskite-like compounds. II. Rare earth aluminates*, *Acta Crystallographica* **9**, 1019 (1956).
- ¹⁵⁹K. A. Müller, W. Berlinger, and F. Waldner, *Characteristic structural phase transition in perovskite-type compounds*, *Physical Review Letters* **21**, 814 (1968).
- ¹⁶⁰P. Delugas, V. Fiorentini, and A. Filippetti, *Dielectric properties and long-wavelength optical modes of the high- κ oxide LaAlO_3* , *Physical Review B* **71**, 134302 (2005).
- ¹⁶¹P. Calvani et al., *Infrared optical properties of perovskite substrates for high- T_c superconducting films*, *Physica C: Superconductivity* **181**, 289 (1991).
- ¹⁶²D. Afanasiev et al., *Ultrafast control of magnetic interactions via light-driven phonons*, *Nature Materials* **20**, 607 (2021).
- ¹⁶³R. V. Mikhaylovskiy et al., *Ultrafast optical modification of exchange interactions in iron oxides*, *Nature Communications* **6**, 8190 (2015).
- ¹⁶⁴M. Först et al., *Melting of charge stripes in vibrationally driven $\text{La}_{1.875}\text{Ba}_{0.125}\text{CuO}_4$: assessing the respective roles of electronic and lattice order in frustrated superconductors*, *Physical Review Letters* **112**, 157002 (2014).
- ¹⁶⁵R. I. Tobey, D. Prabhakaran, A. T. Boothroyd, and A. Cavalleri, *Ultrafast electronic phase transition in $\text{La}_{1/2}\text{Sr}_{3/2}\text{MnO}_4$ by coherent vibrational excitation: evidence for nonthermal melting of orbital order*, *Physical Review Letters* **101**, 197404 (2008).
- ¹⁶⁶A. Melnikov et al., *Coherent optical phonons and parametrically coupled magnons induced by femtosecond laser excitation of the $\text{Gd}(0001)$ surface*, *Physical Review Letters* **91**, 227403 (2003).

- ¹⁶⁷A. S. Disa et al., *Polarizing an antiferromagnet by optical engineering of the crystal field*, *Nature Physics* **16**, 937 (2020).
- ¹⁶⁸A. K. Zvezdin and V. M. Matveev, *Theory of the magnetic properties of dysprosium orthoferrite*, *Soviet Physics-JETP* **50**, 1076 (1979).
- ¹⁶⁹A. Balbashov, A. Volkov, S. Lebedev, A. Mukhin, and A. S. Prokhorov, *High-frequency magnetic properties of dysprosium orthoferrite*, *Soviet Physics - JETP* **61**, 573 (1985), [Original: Zh. Eksp. Teor. Fiz. **88**, 974–987 (1985)].
- ¹⁷⁰K. P. Belov, A. K. Zvezdin, A. M. Kadomtseva, and R. Z. Levitin, *Spin-reorientation transitions in rare-earth magnets*, *Soviet Physics - Uspekhi* **19**, 574 (1976).
- ¹⁷¹T. Y. Khim et al., *Strain control spin reorientation transition in DyFeO₃/SrTiO₃ epitaxial film*, *Applied Physics Letters* **99**, 072501 (2011).
- ¹⁷²M. Fechner et al., *Magnetophononics: ultrafast spin control through the lattice*, *Physical Review Materials* **2**, 64401 (2018).
- ¹⁷³D. M. Juraschek, P. Narang, and N. A. Spaldin, *Phono-magnetic analogs to opto-magnetic effects*, *Physical Review Research* **2**, 043035 (2020).
- ¹⁷⁴M. Hase, M. Kitajima, S. ichi Nakashima, and K. Mizoguchi, *Dynamics of coherent anharmonic phonons in Bismuth using high density photoexcitation*, *Physical Review Letters* **88**, 67401 (2002).
- ¹⁷⁵K. Yamaguchi, T. Kurihara, H. Watanabe, M. Nakajima, and T. Suemoto, *Dynamics of photoinduced change of magnetoanisotropy parameter in orthoferrites probed with terahertz excited coherent spin precession*, *Physical Review B* **92**, 64404 (2015).
- ¹⁷⁶A. Berton and B. Sharon, *Specific heat of DyFeO₃ from 1.2° -80° K*, *Journal of Applied Physics* **39**, 1367 (1968).
- ¹⁷⁷D. L. Wood, J. P. Remeika, and E. D. Kolb, *Optical spectra of rare-earth orthoferrites*, *Journal of Applied Physics* **41**, 5315 (1970).
- ¹⁷⁸J. A. De Jong et al., *Coherent control of the route of an ultrafast magnetic phase transition via low-amplitude spin precession*, *Physical Review Letters* **108**, 157601 (2012).
- ¹⁷⁹Y. Tokura, S. Seki, and N. Nagaosa, *Multiferroics of spin origin*, *Reports on Progress in Physics* **77**, 076501 (2014).
- ¹⁸⁰V. Baltz et al., *Antiferromagnetic spintronics*, *Reviews of Modern Physics* **90**, 015005 (2018).
- ¹⁸¹A. Baltuška, T. Fuji, and T. Kobayashi, *Controlling the carrier-envelope phase of ultrashort light pulses with optical parametric amplifiers*, *Physical Review Letters* **88**, 133901 (2002).
- ¹⁸²P. E. Blöchl, *Projector augmented-wave method*, *Physical Review B* **50**, 17953 (1994).
- ¹⁸³X. Gonze et al., *Recent developments in the ABINIT software package*, *Computer Physics Communications* **205**, 106 (2016).
- ¹⁸⁴K. F. Garrity, J. W. Bennett, K. M. Rabe, and D. Vanderbilt, *Pseudopotentials for high-throughput DFT calculations*, *Computational Materials Science* **81**, 446 (2014).
- ¹⁸⁵M. Topsakal and R. M. Wentzcovitch, *Accurate projected augmented wave (PAW) datasets for rare-earth elements (RE = La-Lu)*, *Computational Materials Science* **95**, 263 (2014).
- ¹⁸⁶A. I. Liechtenstein, V. I. Anisimov, and J. Zaanen, *Density-functional theory and strong interactions: Orbital ordering in Mott-Hubbard insulators*, *Physical Review B* **52**, 15 (1995).
- ¹⁸⁷A. Togo and I. Tanaka, *First principles phonon calculations in materials science*, *Scripta Materialia* **108**, 1 (2015).

- ¹⁸⁸V. V. Eremenko and N. F. Kharchenko, *Magneto-optics of antiferromagnets*, *Physics Reports* **155**, 379 (1987).
- ¹⁸⁹A. Maziewski and R. Szymczak, *Visual observation of phase domains in dysprosium orthoferrite*, *Journal of Physics D: Applied Physics* **10**, L37 (1977).
- ¹⁹⁰S. L. Gnatchenko et al., *Magneto-optical studies of H-T phase diagram for DyFeO₃ (H || a)*, *Journal of Magnetism and Magnetic Materials* **81**, 125 (1989).
- ¹⁹¹R. Szymczak, *Domain structure in single crystal ferromagnetic oxide films near the phase transitions*, *Journal of Magnetism and Magnetic Materials* **35**, 243 (1983).
- ¹⁹²S. Gnatchenko, V. Eremenko, and N. Kharchenko, *Antiferromagnetic domain boundary as a line for nucleation of a weakly ferromagnetic phase from the antiferromagnetic one in dysprosium orthoferrite*, *Soviet Journal of Low Temperature Physics* **7**, 742 (1981).
- ¹⁹³V. G. Bar'yakhtar, B. A. Ivanov, and M. V. Chetkin, *Dynamics of domain walls in weak ferromagnets*, *Soviet Physics - Uspekhi* **28**, 563 (1985), [Original: *Zh. Eksp. Teor. Fiz.*, **78**, 1509–1522 (1980)].
- ¹⁹⁴M. Weber et al., *Raman spectroscopy of rare-earth orthoferrites RFeO₃ (R=La, Sm, Eu, Gd, Tb, Dy)*, *Physical Review B* **94**, 214103 (2016).
- ¹⁹⁵A. M. Glazer, *The classification of tilted octahedra in perovskites*, *Acta Crystallographica B* **B28**, 3384 (1972).
- ¹⁹⁶D. M. Korotin, V. V. Mazurenko, V. I. Anisimov, and S. V. Streltsov, *Calculation of exchange constants of the Heisenberg model in plane-wave-based methods using the Green's function approach*, *Physical Review B* **91**, 224405 (2015).
- ¹⁹⁷X. He, N. Helbig, M. J. Verstraete, and E. Bousquet, *TB2J: A python package for computing magnetic interaction parameters*, *Computer Physics Communications* **264**, 107938 (2021).
- ¹⁹⁸D. Afanasiev et al., *Controlling the anisotropy of a van der Waals antiferromagnet with light*, *Science Advances* **7**, eabf3096 (2021).
- ¹⁹⁹Y. Khan et al., *Recent breakthroughs in two-dimensional van der Waals magnetic materials and emerging applications*, *Nano Today* **34**, 100902 (2020).
- ²⁰⁰M. C. Wang et al., *Prospects and opportunities of 2D van der Waals magnetic systems*, *Annalen der Physik* **532**, 1900452 (2020).
- ²⁰¹K. S. Burch, D. Mandrus, and J. G. Park, *Magnetism in two-dimensional van der Waals materials*, *Nature* **563**, 47 (2018).
- ²⁰²B. Huang et al., *Layer-dependent ferromagnetism in a van der Waals crystal down to the monolayer limit*, *Nature* **546**, 270 (2017).
- ²⁰³M. Šiškins et al., *Magnetic and electronic phase transitions probed by nanomechanical resonators*, *Nature Communications* **11**, 2698 (2020).
- ²⁰⁴Y. Sun et al., *Effects of hydrostatic pressure on spin-lattice coupling in two-dimensional ferromagnetic Cr₂Ge₂Te₆*, *Applied Physics Letters* **112**, 072409 (2018).
- ²⁰⁵Y. Wang et al., *Strain-sensitive magnetization reversal of a van der Waals magnet*, *Advanced Materials* **32**, 2004533 (2020).
- ²⁰⁶B. Huang et al., *Electrical control of 2D magnetism in bilayer CrI₃*, *Nature Nanotechnology* **13**, 544 (2018).
- ²⁰⁷Z. Wang et al., *Electric-field control of magnetism in a few-layered van der Waals ferromagnetic semiconductor*, *Nature Nanotechnology* **13**, 554 (2018).

- ²⁰⁸K. Yosida, *The status of the theories of magnetic anisotropy*, *Journal of Applied Physics* **39**, 511 (1968).
- ²⁰⁹R. V. Mikhaylovskiy et al., *Terahertz magnetization dynamics induced by femtosecond resonant pumping of Dy^{3+} subsystem in the multisublattice antiferromagnet $DyFeO_3$* , *Physical Review B* **92**, 094437 (2015).
- ²¹⁰R. Iida et al., *Spectral dependence of photoinduced spin precession in $DyFeO_3$* , *Physical Review B* **84**, 64402 (2011).
- ²¹¹A. Stupakiewicz et al., *Selection rules for all-optical magnetic recording in iron garnet*, *Nature Communications* **10**, 612 (2019).
- ²¹²E. V. Boström et al., *Light-induced topological magnons in two-dimensional van der Waals magnets*, *SciPost Physics* **9**, 061 (2020).
- ²¹³M. J. Coak et al., *Tuning dimensionality in van-der-Waals antiferromagnetic Mott insulators $TMPS_3$* , *Journal of Physics Condensed Matter* **32**, 124003 (2020).
- ²¹⁴F. Wang et al., *New frontiers on van der Waals layered metal phosphorous trichalcogenides*, *Advanced Functional Materials* **28**, 1802151 (2018).
- ²¹⁵K. Z. Du et al., *Weak van der Waals stacking, wide-range band gap, and Raman study on ultrathin layers of metal phosphorus trichalcogenides*, *ACS Nano* **10**, 1738 (2016).
- ²¹⁶S. Y. Kim et al., *Charge-spin correlation in van der Waals antiferromagnet $NiPS_3$* , *Physical Review Letters* **120**, 136402 (2018).
- ²¹⁷S. Kang et al., *Coherent many-body exciton in van der waals antiferromagnet $NiPS_3$* , *Nature* **583**, 785 (2020).
- ²¹⁸K. Kim et al., *Suppression of magnetic ordering in XXZ -type antiferromagnetic monolayer $NiPS_3$* , *Nature Communications* **10**, 345 (2019).
- ²¹⁹A. Hashemi, H. P. Komsa, M. Puska, and A. V. Krasheninnikov, *Vibrational properties of metal phosphorus trichalcogenides from first-principles calculations*, *Journal of Physical Chemistry C* **121**, 27207 (2017).
- ²²⁰R. Brec, *Review on structural and chemical properties of transition metal phosphorus trisulfides MPS_3* , in *Intercalation in layered materials*, edited by M. S. Dresselhaus (Springer, Boston, MA, 1986), pp. 93–124.
- ²²¹A. R. Wildes et al., *Magnetic structure of the quasi-two-dimensional antiferromagnet $NiPS_3$* , *Physical Review B* **92**, 224408 (2015).
- ²²²P. A. Joy and S. Vasudevan, *Magnetism in the layered transition-metal thiophosphates MPS_3 ($M=Mn, Fe, \text{ and } Ni$)*, *Physical Review B* **46**, 5425 (1992).
- ²²³N. Chandrasekharan and S. Vasudevan, *Magnetism and exchange in the layered antiferromagnet $NiPS_3$* , *Journal of Physics: Condensed Matter* **6**, 4569 (1994).
- ²²⁴*Raman spectroscopy of two-dimensional magnetic van der Waals materials*, *Nanotechnology* **30**, 452001 (2019).
- ²²⁵J. Nishitani, K. Kozuki, T. Nagashima, and M. Hangyo, *Terahertz radiation from coherent antiferromagnetic magnons excited by femtosecond laser pulses*, *Applied Physics Letters* **96**, 221906 (2010).
- ²²⁶J. Nishitani, T. Nagashima, and M. Hangyo, *Terahertz radiation from antiferromagnetic MnO excited by optical laser pulses*, *Applied Physics Letters* **103**, 081907 (2013).

- ²²⁷S. T. Bramwell and P. C. Holdsworth, *Magnetization and universal sub-critical behaviour in two-dimensional XY magnets*, *Journal of Physics: Condensed Matter* **5**, L53 (1993).
- ²²⁸S. T. Bramwell and P. C. Holdsworth, *Magnetization: A characteristic of the Kosterlitz-Thouless-Berezinskii transition*, *Physical Review B* **49**, 8811 (1994).
- ²²⁹A. Taroni, S. T. Bramwell, and P. C. Holdsworth, *Universal window for two-dimensional critical exponents*, *Journal of Physics Condensed Matter* **20**, 275233 (2008).
- ²³⁰J. F. Scott, *Soft mode spectroscopy: experimental studies of structural phase transitions*. *Reviews of Modern Physics* **46**, 83 (1974).
- ²³¹B. A. Ivanov, *Mesoscopic antiferromagnets: Statics, dynamics, and quantum tunneling (Review)*, *Low Temperature Physics* **31**, 635 (2005).
- ²³²X. Wang et al., *Spin-induced linear polarization of photoluminescence in antiferromagnetic van der Waals crystals*, *Nature Materials* **20**, 964 (2021).
- ²³³G. A. Smolenskii, R. V. Pisarev, and I. G. Siniĭ, *Birefringence of light in magnetically ordered crystals*, *Soviet Physics - Uspekhi* **18**, 410 (1975).
- ²³⁴D. Lançon, R. A. Ewings, T. Guidi, F. Formisano, and A. R. Wildes, *Magnetic exchange parameters and anisotropy of the quasi-two-dimensional antiferromagnet NiPS₃*, *Physical Review B* **98**, 134414 (2018).
- ²³⁵F. Atoneche et al., *Large ultrafast photoinduced magnetic anisotropy in a cobalt-substituted yttrium iron garnet*, *Physical Review B* **81**, 214440 (2010).
- ²³⁶A. M. Kalashnikova, A. V. Kimel, and R. V. Pisarev, *Ultrafast opto-magnetism*, *Physics-Uspekhi* **58**, 969 (2015).
- ²³⁷D. Bossini and T. Rasing, *Femtosecond optomagnetism in dielectric antiferromagnets*, *Physica Scripta* **92**, 024002 (2017).
- ²³⁸C. T. Kuo et al., *Exfoliation and Raman spectroscopic fingerprint of few-layer NiPS₃ van der Waals crystals*, *Scientific Reports* **6**, 20904 (2016).
- ²³⁹F. Junginger et al., *Single-cycle multiterahertz transients with peak fields above 10 MV/cm*, *Optics Letters* **35**, 2645 (2010).
- ²⁴⁰J. R. Hortensius et al., *Coherent spin-wave transport in an antiferromagnet*, *Nature Physics* **17**, 1001 (2021).
- ²⁴¹T. Jungwirth, X. Marti, P. Wadley, and J. Wunderlich, *Antiferromagnetic spintronics*, *Nature Nanotechnology* **11**, 231 (2016).
- ²⁴²P. Němec, M. Fiebig, T. Kampfrath, and A. V. Kimel, *Antiferromagnetic opto-spintronics*, *Nature Physics* **14**, 229 (2018).
- ²⁴³V. V. Kruglyak and R. J. Hicken, *Magnonics: Experiment to prove the concept*, *Journal of Magnetism and Magnetic Materials* **306**, 191 (2006).
- ²⁴⁴D. Sander et al., *The 2017 magnetism roadmap*, *Journal of Physics D: Applied Physics* **50**, 363001 (2017).
- ²⁴⁵T. Giamarchi, C. Rüegg, and O. Tchernyshyov, *Bose-Einstein condensation in magnetic insulators*, *Nature Physics* **4**, 198 (2008).
- ²⁴⁶Ø. Johansen, A. Kamra, C. Ulloa, A. Brataas, and R. A. Duine, *Magnon-mediated indirect exciton condensation through antiferromagnetic insulators*, *Physical Review Letters* **123**, 167203 (2019).
- ²⁴⁷Y. M. Bunkov et al., *High- T_c spin superfluidity in antiferromagnets*, *Physical Review Letters* **108**, 177002 (2012).

- ²⁴⁸S. Takei, B. I. Halperin, A. Yacoby, and Y. Tserkovnyak, *Superfluid spin transport through anti-ferromagnetic insulators*, *Physical Review B* **90**, 94408 (2014).
- ²⁴⁹A. Qaiumzadeh, H. Skarsvåg, C. Holmqvist, and A. Brataas, *Spin superfluidity in biaxial antiferromagnetic insulators*, *Physical Review Letters* **118**, 137201 (2017).
- ²⁵⁰R. Lebrun et al., *Tunable long-distance spin transport in a crystalline antiferromagnetic iron oxide*, *Nature* **561**, 222 (2018).
- ²⁵¹J. Li et al., *Spin current from sub-terahertz-generated antiferromagnetic magnons*, *Nature* **578**, 70 (2020).
- ²⁵²P. Vaidya et al., *Subterahertz spin pumping from an insulating antiferromagnet*, *Science* **368**, 160 (2020).
- ²⁵³M. Dabrowski et al., *Coherent transfer of spin angular momentum by evanescent spin waves within antiferromagnetic NiO*, *Physical Review Letters* **124**, 217201 (2020).
- ²⁵⁴D. Bossini et al., *Macrospin dynamics in antiferromagnets triggered by sub-20 femtosecond injection of nanomagnons*, *Nature Communications* **7**, 10645 (2016).
- ²⁵⁵D. Afanasiev et al., *Control of the ultrafast photoinduced magnetization across the Morin transition in DyFeO₃*, *Physical Review Letters* **116**, 1 (2016).
- ²⁵⁶P. A. Usachev et al., *Optical properties of thulium orthoferrite TmFeO₃*, *Physics of the Solid State* **47**, 2292 (2005).
- ²⁵⁷H. Qiu et al., *Ultrafast spin current generated from an antiferromagnet*, *Nature Physics* **17**, 388 (2021).
- ²⁵⁸I. Razdolski et al., *Nanoscale interface confinement of ultrafast spin transfer torque driving non-uniform spin dynamics*, *Nature Communications* **8**, 15007 (2017).
- ²⁵⁹A. Melnikov et al., *Ultrafast transport of laser-excited spin-polarized carriers in Au/Fe/MgO(001)*, *Physical Review Letters* **107**, 076601 (2011).
- ²⁶⁰R. Lebrun et al., *Long-distance spin-transport across the Morin phase transition up to room temperature in ultra-low damping single crystals of the antiferromagnet α -Fe₂O₃*, *Nature Communications* **11**, 6332 (2020).
- ²⁶¹Y. Hashimoto et al., *All-optical observation and reconstruction of spin wave dispersion*, *Nature Communications* **8**, 15859 (2017).
- ²⁶²T. Satoh et al., *Directional control of spin-wave emission by spatially shaped light*, *Nature Photonics* **6**, 662 (2012).
- ²⁶³Y. Au et al., *Direct excitation of propagating spin waves by focused ultrashort optical pulses*, *Physical Review Letters* **110**, 097201 (2013).
- ²⁶⁴S. Bonetti et al., *Direct observation and imaging of a spin-wave soliton with p-like symmetry*, *Nature Communications* **6**, 8889 (2015).
- ²⁶⁵V. I. Ozhogin and V. L. Preobrazhenskii, *Anharmonicity of mixed modes and giant acoustic non-linearity of antiferromagnetics*, *Soviet Physics - Uspekhi* **31**, 713 (1988).
- ²⁶⁶G. Gorodetsky and B. Luthi, *Sound-wave soft-mode interaction near displacive phase transitions: spin reorientation in ErFeO₃*, *Physical Review B* **2**, 3688 (1970).
- ²⁶⁷G. Gorodetsky, S. Shaft, and B. M. Wanklyn, *Magnetoelastic properties of TmFeO₃ at the spin reorientation region*, *Physical Review B* **14**, 2051 (1976).
- ²⁶⁸L. Tsymbal and A. Isotov, *Features of acoustic properties of ErFeO₃ in second-order phase transitions*, *Soviet physics - JETP* **75**, 525 (1992).

- ²⁶⁹A. Stupakiewicz et al., *Ultrafast phononic switching of magnetization*, *Nature Physics* **17**, 489 (2021).
- ²⁷⁰D. M. Juraschek, T. Neuman, J. Flick, and P. Narang, *Cavity control of nonlinear phononics*, *Physical Review Research* **3**, L032046 (2021).
- ²⁷¹G. Long et al., *Isolation and characterization of few-layer manganese thiophosphite*, *ACS nano* **11**, 11330 (2017).
- ²⁷²H. Chu et al., *Linear magnetoelectric phase in ultrathin MnPS₃ probed by optical second harmonic generation*, *Physical Review Letters* **124**, 027601 (2020).
- ²⁷³Q. Zhang et al., *Observation of giant optical linear dichroism in a zigzag antiferromagnet FePS₃*, *Nano Letters* **21**, 6938 (2021).
- ²⁷⁴T. Seifert et al., *Efficient metallic spintronic emitters of ultrabroadband terahertz radiation*, *Nature photonics* **10**, 483 (2016).
- ²⁷⁵M. Jazbinsek, U. Puc, A. Abina, and A. Zidansek, *Organic crystals for THz photonics*, *Applied Sciences* **9**, 882 (2019).
- ²⁷⁶M. Budden, T. Gebert, and A. Cavalleri, *Hybrid CO₂-Ti:sapphire laser with tunable pulse duration for mid-infrared-pump terahertz-probe spectroscopy*, *Optics Express* **29**, 3575 (2021).

ACKNOWLEDGEMENTS

As it is the last one to be written, and often the first one to be read, this section holds a special place in every thesis. The PhD journey is not one of solitude. In the past four years I have had the privilege and pleasure to work with and meet many different people. Without them, this thesis could not have existed in its present form and I might very well have followed completely different paths, both in life and in my professional career. It is a challenge to acknowledge everyone that helped shape me and the thesis in just a few pages. I have accepted this challenge and I apologize in case I have forgotten anyone.

First and foremost I would like to thank my promotor **Andrea Caviglia** for giving me the opportunity to perform my PhD research in his lab. **Andrea**, you have created a research environment where everyone is entrusted with the freedom to work independently and explore research directions and projects that seem fruitful and interesting. At the same time, you provide the opportunity and stimulate all group members to collaborate with many people, both inside and outside our university, for which I am grateful. I wish you all the best with your new position in Geneva and I look forward to see many new discoveries and exciting results come from the lab! Next, I would like to thank my other promotor **Kobus Kuipers**. Having your own research group in combination with the duties as head of the department results in a busy schedule. I highly appreciate your quality to run effective meetings and your critical, insightful questions, both in personal and department meetings. It was always refreshing to hear your opinion on the general progress and the future steps.

I would like to extend my gratitude to the members of my PhD defence committee: **Yaroslav Blanter**, **Roberta Citro**, **Tobias Kampfrath**, **Alexey Kimel**, **Jean-Marc Triscone** and **Peter Steeneken**. Thank you for being part of the doctoral committee and for taking the time to read my thesis.

During my PhD I had the pleasure to collaborate with researchers from many different groups outside TU Delft. The work presented in this thesis is the result of team efforts. I want to thank **Alireza Sasani** and **Eric Bousquet** from the University of Liège for the detailed theoretical calculations and for sharing their knowledge on symmetry groups that resulted in the great collaboration in two projects. I also would like to thank **Roberta Citro**, **Ruben Leenders**, **Rostislav Mikhaylovskiy** and **Alexey Kimel** for their crucial help to unravel all mysteries that DyFeO_3 offers. I want to thank **Boris Ivanov** for sharing his magnetism knowledge, his detailed theoretical support and for detailed feedback on every draft that we provided. I am grateful for the collaboration with **Samuel Mañas**, **Eugenio Coronado** in the thiophosphate projects. Finally, I want to thank **Yaroslav Blanter** for the pleasant collaboration in different projects and his endless efforts to find every typo in drafts.

I joined the CavigliaLab as a master student more than five years ago. My first task was to join a new post-doc, who had just started a few months before me, in his efforts to build an optics lab from the ground up. At the start, five years ago, I could never have imagined the long, amazing and intense collaboration that lay ahead of us. **Dima**, it might be safe to say that I will never again work together with anyone as closely as we did. We spent hours and hours together in the lab during my master project to build and align the setup, find and improve this mysterious thing called ‘the overlap’, analyze the peaks, look for oscillations and measure in the darkness. From the first day you tried to teach me everything you know about experiments, optics, magnetism and science in general. When I continued in the lab as PhD student our collaboration only intensified. We obtained amazing results in different projects and we went to wonderful places to tell the world about our work. Unfortunately, it took us a long time and a lot of effort to convince the rest of the world that these results were indeed amazing. It took even beyond your time in Delft, which meant that our live discussions turned into endless discussions over the phone. But we managed to bring all the projects to completion and the hard work was rewarded after all. Despite, and maybe because of, the many differences in the way we like to organize our work, we made a great team. I admire your unmatched dedication and work ethic, and am very happy to see that it paid off in the form of a position in Nijmegen. I want to thank you for being a great colleague, a true friend and for the rollercoaster ride of the past four years, which resulted in our shared work presented in this thesis.

A few months after I started my PhD, the *femtolab* was expanded with the arrival of a talented master student who became the third of the Three Musketeers and turned out to be an excellent addition to our lab. **Mattias**, you are a true experimentalist, skilled both in the optics lab and the cleanroom, a good writer, and the new master of the LabVIEW code. Already during your master project you showed that you can work independently and that if something does not work, you just try a different approach. I appreciate your creativity and optimism (“Good news, we have now two well-performing THz crystals”) and I am sure that with the current, amazing, setup you will find that ‘golden trace’. A large part of the content in this thesis has been created together with you, for which I want to thank you. I wish you all the best!

From optics we move to transport. **Thierry**, ‘the champ’, king of the transport lab and the third floor (and the Oostblok?). We started and finished our master projects in CavigliaLab a few months apart, and now we have (almost) done the same with our PhD projects. During these years we had many lunch breaks (me: sandwiches, you: one apple), worked together on several projects and went to some beautiful places for conferences. The trip to the USA in 2020 was an unforgettable experience and surely one of the highlights of my PhD. I admire your relaxed, optimistic and energetic approach to science and life. As one of the last holders of the true ‘MED-spirit’ it has been your mission to keep the MED traditions (midnight measurements, graduation songs) going and tell the newer generations about the good old days. Based on the quality of the songs in the past year, I believe this mission has been successful.

Yildiz, you were working on a truly interdisciplinary project, split between two different labs. Despite many setbacks in your first years you always remained the most cheerful

person in the department. I am very happy that you found a nice position at ASML and wish you all the best!

Patrick: The Irish (or British?) member of the lab. With your (gym) routines you are an exception in a department where irregularity is rife. Your dedication to learn Dutch is exceptional and you even try to blend in society with your Swapfiets. I appreciate that you use 'plain English' when speaking to us non-Irish and I thank you for trying to teach me some Irish words (most of which I have forgotten unfortunately...). I wish you all the best in exfoliating and stretching those bloody membranes!

Ulderico: As Thierry's protégé you became a skilled experimentalist in no time. The first year was one with many setbacks and you seem to be in an eternal fight. You have been fighting with the sun in the office (Dima's aula food trays!), the light in the office (who needs proper office lighting anyway?), failing equipment, the Basware-Alusta ordering system and HR. Even though I am glad to have met a fellow pessimist, I hope that you see the bright sight of those fights: you have gained a lot of valuable experience and knowledge. Thank you for all the interesting discussions in the office and being our Italian tour guide in Genoa!

Part-time CavigliaLab member **Martin** deserves a place in this paragraph, as we consider him adopted by our group. You have a passion for science accompanied by a remarkable drive and creativity. I wish you all the best in Munich and in your future (academic) career!

The lab existed long before I started my PhD (and will continue to do so after I am gone), which means that there are people that started before me and left during my presence. In anti-chronological order these people are:

Victoria, you joined the lab a few months before Covid kicked in, which must have made your stay a special experience. Thank you for being the mature person in an otherwise immature group. I am glad to see that you found a job at a tech company in this part of the country and wish you and your family all the best. **Edouard**, you brought a lot of experience to the lab at times when it was really needed. Aside from managing your own projects, you were always helping others with theirs. I wish you all the best in your future career! **Dirk:** With your efficiency and success in your research you set an example for me. You were always willing to help or share your experience when needed. I am sure you will thrive in the rest of your career! One of the other PhDs working hard to learn Dutch was **Mafalda**, I am sure that by now you are fluent. Thank you for your advice and cheerfulness and I hope you still enjoy the semi-'ballenclub'! **Nicola**, thank you for the excellent organization of iWOE27 in Genoa! A final word goes to the first generation of PhD students of the lab **Giordano** and **Emre**. Giordano it was great to meet you again in Genoa. I wish you both the best of luck in your future scientific careers! A final thanks to the master students in the group **Niels**, **Hélène**, **Amber** and **Ludwig** for their hard work and contributions!

CavigliaLab is part of the QN department, full of wonderful people that are always in for a chat or willing to help and share their knowledge. Throughout the last four years, office F190 always felt like a warm and welcoming home. I want to thank my office mates: (Dr.) **Luigi**, for his defence advice and his (occasionally funny) word play. From now on

you can arrive earliest in the office again; **Joris**, for his optimism, energy and the discussions on the Dutch housing market and the PhD salary; **Brecht** for discussions about terrible neighbours and the superiority (or inferiority) of the Randstad compared to the Achterhoek; **Maarten** for being an example of how to properly organize your work and workplace and being a constant and reliable supplier of office supplies and finally **Ulderico** for forgiving the rest of the office members for speaking Dutch so often.

Iacopo, thanks for the shared love for spin waves (although in my humble opinion THz > GHz, MOKE > NV-centers) and shared hatred for slow editors. When coming all the way from Leiden, in between writing your next spin-wave paper, you are always in for an occasional chat and present at Friday afternoon drinks. The trip to Denver and New York was an amazing experience, we managed to make the best of it, despite the cancellation of the APS. I wish you all the best in that future consultancy/academica/something else career! Thanks **Adrian**, for taking part in that same memorable trip to the USA. I have never heard anyone talk so passionately about chess matches! One day you will become a grand master yourself. **Rasa** (RasRas), I apologize once again for my inappropriate wild skiing in Courchevel, I hope you can forgive me. Thank you for your endless enthusiasm, your optimism, your amazing proofreading and writing skills¹ and your continuous interest in Pauli and Newton (the rabbits, not the Nobel-prize winning physicists). **Maikel**, fellow optics enthusiast, thank you for sharing (free) optics with our lab! Thanks **Samer**, for showing the world that happy postdocs exist. Keep up the good spirit! Thank you **Makars**, for introducing the world of thiophosphates to us and thanks **Irina** for discussions on the Montana and the matching coffee mug! I want to thank the continuously changing QMIII TA-team, for the good teaching times: **Nikos**, **Marios**, **Rasa** (grading with donuts, great idea), **Marc** (Noordam(!)), **Tom** (great IT-support, hardcore exam question) and **Patrick** (very,very last, but not the least).

I want to thank the members of the OtteLab, **Rasa**, **Lukas**, **Robbie**, **Alex**, **Laëti** (Pauli and Newton say hi to Nap-Nap), **Rik**, **Hester** and **Evert** for the many shared lunches. I am happy to see an increasing amount of sandwiches in your group during lunch.

Thanks to all other people at QN that I have interacted with over the years!

The research contained in this thesis would not have been possible without the support from the team of technicians **Tino**, **Tom**, **Ronald**, **Nico** and **Tim**. A special thanks goes to the QN and Casimir Research School support staff, **Marijke**, **Lizzy**, **Heleen**, **Maria**, **Erica**, **Marije** and **Etty** for the excellent organization of the QN events, support with all administrative matter and the many things within the department that we are not aware of. I am grateful that the door to your offices was always open.

I want to thank all PIs for creating a department full of interesting, world-leading research, your inspirational courses taught at the bachelor and master level, many interesting discussions throughout the years and for your work behind the scenes to keep the labs accessible in times of a pandemic.

Vele, vele vrienden buiten de universiteit hebben de afgelopen jaren interesse getoond in mijn werk (wat ik meestal omschrijf als “Met laserstralen op magnetische materialen

¹This acknowledgement section has not been proofread by Rasa; she cannot be held responsible for the banal text, the mediocre grammar and the potential spelling errors

schieten en kijken wat er gebeurt"). Ik ben hen dankbaar voor de interesse, de steun en voor de welkome afleiding in de vorm van voetbaltrainingen en wedstrijden, weekenden weg, kerstdiners, online pubquizen en whatsappgesprekken over uiteenlopende onderwerpen als files, politieke polarisatie en Feyenoord.

Daarnaast heb ik heel veel steun en hulp gekregen van familie. **Petra, Kees, Thom** en **Laura**, ik mag mezelf gelukkig prijzen met zo'n fijne schoonfamilie. Ik heb me altijd welkom gevoeld en ben daarnaast heel erg dankbaar voor alle hulp afgelopen zomer met de verhuizing.

Oma, ik ben nog steeds heel dankbaar dat ik tijdens mijn stage bij Philips drie maanden mocht 'logeren'. Ik hoop dat dit proefschrift een mooi plekje krijgt in het rijtje op de boekenkamer. **Ruben**, je zult altijd de eerste zijn om mijn problemen te relativiseren en me vervolgens met een optimistischere blik naar het geheel te laten kijken. Bedankt voor je inzichten, adviezen en ongezouten mening, ik waardeer het om een broer te hebben waar ik altijd bij terecht kan. **Papa** en **Mama**, van jongs af aan hebben jullie me geholpen en alle mogelijkheden geboden om te leren en te studeren, en me tegelijkertijd altijd gemotiveerd om het beste uit mijzelf te halen. Ik weet dat ik altijd bij jullie terecht kan voor advies en wijze raad op vrijwel elk vlak en dat jullie altijd voor mij klaar staan. Bedankt voor alle steun!

De laatste, en belangrijkste, plaats in de lijst is gereserveerd voor de allerbelangrijkste persoon in mijn leven. Lieve **Sanne**, door de manier waarop ik bezig was met het onderzoek, was het onvermijdelijk dat mijn PhD ook deel uitmaakte van jouw leven. Met je vertrouwen, je geduld, je hulp in vele vormen en je onvoorwaardelijke steun heb je een enorme bijdrage geleverd aan dit proefschrift. Het afgelopen jaar bracht vele uitdagingen en kende helaas ook dieptepunten. Deze scriptie vormt hopelijk het slotstuk van deze bewogen periode en ik kijk enorm uit naar het volgende hoofdstuk in ons leven samen.

Delft, January 2022

CURRICULUM VITÆ

Jorrit Rutger HORTENSIUS

11-04-1994 Born in Schiedam, The Netherlands.

EDUCATION

- 2006–2012 Secondary School
Het Lyceum Vos
Vlaardingem, the Netherlands
- 2012–2015 Bachelor of Science in Applied Physics
Delft University of Technology
Delft, The Netherlands
- 2015–2017 Master of Science in Applied Physics
Delft University of Technology
Delft, The Netherlands
Thesis: Nonlinear optical probing of oxide interfaces and
their ultrafast structural and electron dynamics
Supervisor: Dr. A.D. Caviglia
- 2018–2022 Ph.D. in Applied Physics
Delft University of Technology
Delft, The Netherlands
Thesis: Resonant optical control of magnetism on ultrashort
timescales
promotors: Dr. A.D. Caviglia
Prof. dr. L. Kuipers

LIST OF PUBLICATIONS

10. **J. R. Hortensius**, D. Afanasiev, L. Vistoli, M. Bibes, and A. D. Caviglia, *Ultrafast magnetization in manganite parent compound CaMnO_3* , (in preparation)
9. C. A. Perroni, **J. R. Hortensius**, D. Afanasiev, Y. M. Blanter, G. De Filippis, V. Cataudella, and A. D. Caviglia, *Ultrafast polaron excitation in $\text{LaAlO}_3/\text{SrTiO}_3$* , (in preparation)
8. M. Matthiesen, D. Afanasiev, **J. R. Hortensius**, S. Mañas-Valero, M. Šiškins, H. S. J. van der Zant, B. A. Ivanov, E. Coronado, and A. D. Caviglia, *Selective control of magnetism via resonant excitation of phonons and orbitals in a zero orbital moment antiferromagnet*, (in preparation)
7. T. C. van Thiel, W. Brzezicki, C. Autieri, **J. R. Hortensius**, D. Afanasiev, N. Gauquelin, D. Jannis, N. Janssen, D. J. Groenendijk, J. Fratermans, S. van Aert, J. Verbeeck, M. Cuoco, and A. D. Caviglia, *Coupling charge and topological reconstructions at polar oxide interfaces*, *Physical Review Letters* **127**, 127202 (2021).
6. **J. R. Hortensius***, D. Afanasiev*, M. Matthiesen, R. Leenders, R. Citro, A. V. Kimel, R. V. Mikhaylovskiy, B. A. Ivanov, and A. D. Caviglia, *Coherent spin-wave transport in an antiferromagnet*, *Nature Physics* **17**, 1001 (2021).
5. D. Afanasiev, **J. R. Hortensius**, M. Matthiesen, S. Mañas-Valero, M. Šiškins, M. Lee, E. Lesne, H. S. J. van der Zant, P. G. Steeneken, B. A. Ivanov, E. Coronado, and A. D. Caviglia, *Controlling the anisotropy of a van der Waals antiferromagnet with light*, *Science Advances* **7**, eabf3096 (2021).
4. D. Afanasiev*, **J. R. Hortensius***, B. A. Ivanov, A. Sasani, E. Bousquet, Y. M. Blanter, R. V. Mikhaylovskiy, A. V. Kimel, and A. D. Caviglia, *Ultrafast control of magnetic interactions via light-driven phonons*, *Nature Materials* **20**, 607 (2021).
3. **J. R. Hortensius***, D. Afanasiev*, A. Sasani, E. Bousquet, and A. D. Caviglia *Ultrafast strain engineering and coherent structural dynamics from resonantly driven optical phonons in LaAlO_3* , *npj Quantum Material* **5**, 95 (2020).
2. D. J. Groenendijk, C. Autieri, T. C. van Thiel, W. Brzezicki, **J. R. Hortensius**, D. Afanasiev, N. Gauquelin, P. Barone, K. H. W. van den Bos, S. van Aert, J. Verbeeck, A. Filippetti, S. Picozzi, M. Cuoco, and A. D. Caviglia, *Berry phase engineering at oxide interfaces*, *Physical Review Research* **2**, 023404 (2020).
1. M. Matthiesen, D. Afanasiev, **J. R. Hortensius**, T. C. van Thiel, R. Medapalli, E. E. Fullerton, and A. D. Caviglia, *Temperature dependent inverse spin Hall effect in Co/Pt spintronic emitters*, *Applied Physics Letters* **116**, 212405 (2020).

*equal contribution